Imperial College London

Universidade de São Paulo

Spectral/hp large eddy simulation of vortex-dominated automotive flows around bluff bodies with diffuser and complex front wing geometries

Filipe Fabian Buscariolo

January 8, 2021

Supervisors: Prof. Spencer Sherwin
Prof. Gustavo Assi
Prof. Denis Doorly

Department of Aeronautics / Mechanical Engineering
Imperial College London / University of São Paulo

This thesis is submitted for the Doctor of Philosophy joint-degree
between Imperial College London and University of São Paulo





Copyright © Filipe Fabian Buscariolo
PhD Student, Department of Aeronautics, Imperial College London and Department of Mechanical Engineering, University of São Paulo
All rights reserved.

Copyright declaration

The copyright of this thesis rests with the author and is made available under a Creative Commons Attribution Non-Commercial No Derivatives licence. Researchers are free to copy, distribute or transmit the thesis on the condition that they attribute it, that they do not use it for commercial purposes and that they do not alter, transform or build upon it. For any reuse or redistribution, researchers must make clear to others the licence terms of this work.

Declaration of originality

The work presented hereafter is based on research carried out by the author at the Department of Aeronautics of Imperial College London and it is all the author's own work except where otherwise acknowledged. No part of the present work has been submitted elsewhere for another degree or qualification.

Filipe Fabian Buscariolo

London, September 2019

Acknowledgement

Firstly, I would like to thank my supervisors, Prof. Spencer J. Sherwin and Prof. Gustavo Roque da Silva Assi for their advice and guidance through this research. I am deeply grateful for their trust in my work and research capabilities. I must thank Spencer for pushing and supporting me whenever necessary and needed but also for the friendship, patience and great experiences shared during my time in the UK.

Mr. Yuanbo Nie, I can't thank you enough for all support, friendship and leanings during my time in the UK. Thanks for making me feel both at home and part of your family! I am also very thankful to your wife Li Yi for being so nice and patient. You are already part of my family.

Additionally, I would like to acknowledge and thank many colleagues and friends I made at NDF-USP, namely Lucia Messa, Prof. Bruno Carmo, Dr. Rafael Gioria and Prof. Julio Meneghini; at Imperial, namely Dr. Dave Moxey, Dr. Chris Cantwell, Dr. Jean-Eloi Lombard, Karim Shawki, Dr. Giovanni Fantuzzi, Dr. John Alan Pascoe, Dr. Paul Bruce, Dr. Oliver Buxton, Dr. Giacomo Castiglioni, Andrea Cassinelli, Omar Mahfoz, Brenda (Xingchen Zhou), Yu Pan and Walid Hambli; at McLaren Racing, namely Dr. Julien Hoessler, Dr. John Baker, Dr. Adam Swift, Dr. Petros Akridis, Dr. Giampaolo Cetraro, Dr. Jon Pegrum, Dr. Laurent Dalla Longa and Dr. Francesco Bottone. I must also include my Brazilian friends at Imperial Dr. Douglas Serson, Dr. Rodrigo Moura, Dr. Ricardo Amigo, Robin Basso (pseudo-Brazilian) and Murilo Cicolin. Thanks for all the support and friendship during my time at Imperial.

I also acknowledge CNPq (National Council for Research and Development) for the scholarship 202578/2015-1 and both ExaFLOW and McLaren Racing for the partnership research.

Outside the academia, I would like to thank my all my friends and people who supported me during my PhD, especially Andre Lino, Marcelo Massad, Marcos Belga, Fabio Yamasaki, Renato Ghiro, Dr. Cecilia Chirenti, Roberto Ramos, Julio Cesar Lelis Alves, Leonardo Volpe, Flavio Maruyama and Felipe Magazoni.

Finally, I am deeply grateful to all my family, especially my fiancé Taluana, my mother Vera, my father Celso, my sister Fernanda and my brother Fabio who always supported me on the decision of taking this joint PhD Program. Thanks for always being with me, allow me to study and reach my dreams. I couldn't do it without you all by my side! Additional thanks to my niece Paola and our dogs for cheering up the days during my writing up!

'Friends are the family you choose.'

Jess C. Scott

Abstract

In this research project, it is demonstrated the use of spectral/hp element method for simulations of fully 3D complex geometries. Such solutions at high Reynolds numbers and with higher order polynomials were previously intractable due to numerical stability issues affecting the convergence of the scheme. For this approach, we have employed the latest development of continuous Galerkin spectral vanishing viscosity (CG-SVV) with a discontinuous Galerkin (DG) mimicking kernel. Together with dealiasing techniques, the numerical stability and convergence characteristics of the spectral/hp element method have been greatly improved. These advances in numerical methods are also supported by novel meshing strategies, taking advantage of the additional flexibility in changing the uniform polynomial orders of the mesh and the solution. As a result, efficient simulations can be formulated with consistent and highly accurate solutions obtainable.

Specific for this work, the focus is on complex geometries often found in automotive engineering. To reduce the computational demands, this research explored the use of symmetry boundary conditions for large eddy simulations *(LES)* using a half model. It is found that if only the average flow properties near the body are of interest, such an approach can provide more than 50% reduction in simulation time while maintaining the solution quality. In terms of improving the solution resolution, as one might expect from a p-type method we have observed that increasing the polynomial order can be a more effective approach in comparison to conventional mesh refinement. In the three test cases, we have successfully exploited the use of polynomial accuracy of 4^{th}, 5^{th} and 6^{th} order. This is the first comprehensive study using polynomials of such high orders, and the corresponding solutions are obtained for fully 3D geometries using spectral/hp element method.

Three test cases have been considered, the first being the simulations of the original Ahmed Body serves as a validation study for 3D simulations of the spectral/hp element method. The Ahmed Body is one of the most widely studied bluff bodies used for automotive conceptual studies and computational fluid dynamics *(CFD)* software validation. For this validation study, the differences in results obtained using various polynomial orders for the mesh as well as for the solution interpolation have been examined in detail. With the proposed approach, we were able to obtain fairly good correlations with the aerodynamic quantities for polynomial orders of 5 and above. Regarding the flow features around the body, solutions from the 6^{th} order polynomial showed clear advantage in the slant vortex intensity. With the computational facilities, further increase of solution polynomial order is not feasible; however, the required solution resolution can also be obtained via the use of local mesh refinement.

We determine that this level of solution accuracy, after comparing with various studies in the literature, cannot be obtainable using steady-state simulations such as the very popular Reynolds averaged Navier-Stokes *(RANS)* method.

Based on the validation result, the second test case involved the simulations of Ahmed Body geometries with a simplified diffuser using the proposed method. This case serves as an independent study examining the suitability of the method for design analysis. Using the same 6^{th} order polynomial and *Refined* mesh, the solution successfully identified the flow features consistent with to past literature on underbody diffusers. Additionally, we have found that the geometry of the reference body imposes a quite significant influence on the performance of the diffuser, as well as identified some strong interplay between the lower-side vortex and the diffuser flow. The toolchain has clearly demonstrated its capability in assisting integrated design analysis for a simplified road vehicle equipped with a diffuser.

In the final test case, a new benchmark study case for aerodynamic design of high-performance vehicles and racing cars, the Imperial front wing is proposed. This study consists of a multi-element front-wing based on a Formula One front wing design. It generates complex flow features including ground effects, and multiple vortex system development and interaction. We used this test case as a challenging examination of our proposed method and simulation strategy using the spectral/hp element method. The simulations were also supported by an independent experimental study and results obtained for comparison achieved a high level of agreement. Using a polynomial order of 4^{th} and above have successfully correlated the flow velocity fields at various planes downstream, while increasing the polynomial order to 5^{th} will further result in a good matching of flow visualization details.

From all three test cases, the spectral/hp element method when applied to suitable meshes at reasonably polynomial orders has been able to accurately and consistently yield reliable solutions in good agreement with experiment. The benefits of using high order polynomials for mesh generation of complex geometries, and for solution interpolation of higher accuracy have enabled the use of much coarser meshes than would typically be applied in commercial CFD codes. The progress made in this research is a solid step forward for the adaptation of the spectral/hp element for industrial level applications.

Resumo

Neste projeto de pesquisa, demonstramos o uso do método espectral/hp aplicado a simulações totalmente 3D de geometrias complexas. Esse tipo de solução aplicada à problemas com valor de número de Reynolds e ordem polinomial ambos elevados eram impraticáveis anteriormente devido a problemas de estabilidade que comprometiam a convergência da solução. Aplicamos os últimos desenvolvimentos do operador de spectral vanishing viscosity para o método de Garlerkin contínuo (CG-SVV) combinado com uma aproximação do método de Garlerkin descontínuo. Junto com técnicas de dealising, a estabilidade e convergência de simulações utilizando o método de elemento espectral/hp foi consideravelmente melhorada. Os novos avanços neste método numérico se devem em parte à uma nova estratégia de geração de malha, aproveitando-se da flexibilidade de aumentar a ordem polinomial da malha e da solução. Como resultado, simulações podem ser eficientemente geradas, produzindo resultados de alta-fidelidade.

Especificamente neste trabalho, o foco é em superfícies complexas, frequentemente presente no ramo da engenharia automotiva. Visando reduzir o poder computacional, exploramos o uso da condição de simetria em simulações do tipo *LES*, utilizando meio-modelo. Concluímos que se o objetivo principal do estudo são as propriedades do escoamento médio próximos do corpo, essa metodologia é capaz de reduzir o tempo computacional em mais de 50%, mantendo a qualidade dos resultados. A melhora na acurácia da solução utilizando refino do polinômio (tipo p) da solução se prova mais eficiente quando comparado com o refino do tamanho de malha (tipo h). Em três casos, exploramos o uso de polinômios de acurácia de 4^{th}, 5^{th} e 6^{th} ordem. Este é um dos estudos pioneiros do uso de tais ordens polinomiais de solução em casos totalmente 3D utilizando o método de elemento espectral/hp.

Três casos foram considerados, sendo o primeiro estudo a simulação do corpo de Ahmed original, sendo o mesmo também utilizado como validação da metodologia do método de elemento espectral/hp a ser usada para casos posteriores. O corpo de Ahmed é um dos corpos rombudos automotivos mais utilizados para desenvolvimento de novas tecnologias e validação de códigos de *(CFD)*. Para o estudo de validação, as diferenças nos resultados obtidos utilizando diversas ordens polinomiais para malha e também solução são analisados em detalhes. Com a metodologia proposta, conseguimos obter boa correlação com as quantidades aerodinâmica, utilizado polinômio de ordem 5 e superior para solução. Para estruturas do escoamento, polinômio de 6^{th} ordem mostra-se superior aos demais resultados em termo de capturar a intensidade do vórtice traseiro. Com a estrutura computacional utilizada neste trabalho, não foi possível aumentar a ordem da solução, entretanto, o grau de refinamento

necessário pode ser obtido por meio de refino de malha. Verificando estudos anteriores, este nível solução não pode ser obtido utilizando soluções de regime permanente como o popular método Reynolds averaged Navier-Stokes *(RANS)*.

Baseado no caso anterior de validação, o segundo estudo se concentra na aplicação dessa metodologia em um corpo de Ahmed equipado com um difusor traseiro simplificado. Este caso serve como um estudo independente para verificar a aplicabilidade do método para predição de um comportamento aerodinâmico não-conhecido. Utilizando o caso de malha *Refined*, com elementos de 6^{th} ordem, a solução foi capaz de identificar diferentes tipos de escoamento nos difusores. Adicionalmente, verificamos que a superfície exterior do corpo influencia a performance do difusor e identificamos uma grande influência do vórtice-lateral inferior no escoamento na região do difusor. A metodologia claramente demonstra sua capacidade em predizer o escoamento e ajudar no projeto de veículos simplificados equipados com difusor.

O último caso testado é a proposta de um novo caso de teste para validação aerodinâmica de veículos de alta performance e carros de corrida: a Imperial front wing. O estudo consiste em uma asa frontal de um carro de Fórmula 1, composta por diversos elementos. Estruturas de fluxo complexas são geradas, incluindo efeito-solo e geração de múltiplos sistemas de vórtices com interação entre os mesmos. Utilizamos este caso como um desafio para a metodologia proposta utilizando o método de elemento espectral/hp. O estudo numérico conta ainda com um estudo experimental, onde um nível alto de correlação foi atingido. Utilizando polinômio de 4^{th} ordem ou superior para a solução, obtém-se boa correlação com os campos de velocidade extraídos em diversos planos a jusante da asa, entretanto, aumentando a solução para 5^{th} ordem resulta em melhor correlação em termos de visualização de fluxo sobre a asa.

Para os três casos, o método de elemento espectral/hp quando aplicado à malhas projetadas para o método e utilizando-se de polinômios de solução adequados, conseguem capturar as nuances do escoamento, com excelente correlação aos experimentos físicos. Os benefícios de utilizar polinômios de alta ordem para malha e solução de escoamento em torno de superfícies complexas permite o uso de malhas relativamente grosseiras, utilizadas em métodos numéricos de CFD simplificados. Os desenvolvimentos aqui apresentados mostram um consistente avanço para o uso do método de elemento espectral/hp em aplicações de nível industrial.

Contents

Copyright declaration i

Declaration of originality iii

Acknowledgement v

Abstract vii

Resumo ix

I Introduction and Background Information 1

1 Road vehicles aerodynamics 3

1-1 Background 3

1-2 Aerodynamics development and analysis techniques 7

2 Objectives, Aims and Goals 11

2-1 Motivation 11

2-2 Main objectives 12

2-3 Goals 13

3 Numerical Methods 15

3-1 Computational methods for fluid flows 15

3-1-1 Methods based on Reynolds Averaged Navier-Stokes 15

3-1-2 Scale-resolving simulation methods 18

3-2 iLES simulations with half (symmetric) models for exterior aerodynamics 20

4 Main contributions and organization of the thesis **25**
4-1 Main contributions . . . 25
4-2 Organization of the thesis . . . 27

II Spectral/hp Method **29**

5 Spectral/hp method **31**
5-1 Introduction . . . 31
5-2 Partial differential equation solution - the Galerkin method . . . 32
5-3 One-dimensional implementation . . . 34
5-3-1 The h-type discretization . . . 34
5-3-2 The p-type discretization . . . 35
5-3-3 Local expansion basis . . . 36
5-4 Multiple-dimensional implementation . . . 37
5-4-1 Quadrilateral *2D* elements and hexahedral *3D* elements . . . 38
5-4-2 Triangular *2D* elements and tetrahedral *3D* elements . . . 39
5-5 Mesh element mapping . . . 40
5-6 Incompressible Navier-Stokes equation . . . 41
5-6-1 High-order splitting Scheme . . . 42
5-7 Spectral dealiasing . . . 44

6 Stabilization Techniques and Meshing Strategy **45**
6-1 Spectral-vanishing viscosity - SVV . . . 45
6-1-1 SVV operator concept . . . 46
6-1-2 Continuous Galerkin SVV with discontinuous Galerkin mimicking kernel . . . 48
6-2 Mesh generation . . . 49
6-2-1 Mesh parameter estimation for spectral/hp simulation . . . 49
6-2-2 High-order mesh generation pipeline . . . 50
6-2-3 NekMesh high-order mesh generation . . . 50
6-2-4 Hybrid meshing approach . . . 54
6-3 Naming convention for higher order spectral/hp element mesh . . . 55
6-4 Summary . . . 56

III Ahmed Body **59**

7 The Original Ahmed Body **61**
7-1 Automotive bluff bodies . . . 61
7-1-1 Windsor body . . . 62
7-1-2 Morel bluff body . . . 65

7-1-3 The Ahmed body . . . 70
7-1-4 Geometry details . . . 73
7-2 Past studies for the Ahmed body . . . 74
7-2-1 Ahmed body experimental references . . . 74
7-2-2 Ahmed body correlation studies . . . 80
7-2-3 Wake dynamics and flow structures . . . 88
7-3 Numerical Simulation of Ahmed Body with Spectral/hp Element Method . . . 88
7-3-1 Objectives . . . 88
7-3-2 Simulation configuration . . . 89
7-3-3 Results and analysis . . . 95
7-4 Conclusions . . . 112
7-5 List of publications . . . 113
7-5-1 Paper contributions . . . 113
7-5-2 Presentations and poster sessions . . . 113

8 Ahmed Body with Diffuser 115
8-1 Background . . . 115
8-1-1 Introduction . . . 117
8-1-2 Literature review . . . 123
8-1-3 Objectives . . . 129
8-1-4 Geometry . . . 130
8-2 Simulation configuration . . . 130
8-3 Results and analysis . . . 132
8-3-1 Aerodynamic quantities results . . . 133
8-3-2 Flow Features Analysis . . . 135
8-4 Conclusions . . . 155
8-5 List of publications . . . 157
8-5-1 Paper contributions . . . 157
8-5-2 Presentations and poster sessions . . . 157

IV Imperial Front Wing 159

9 Imperial Front Wing 161
9-1 Background . . . 161
9-1-1 Introduction . . . 162
9-1-2 Geometry . . . 163
9-1-3 Literature review . . . 166
9-1-4 Objectives . . . 172
9-2 Experimental test configuration . . . 173

9-2-1 Domain parametrisation . . . 174
9-2-2 Measurements . . . 174
9-3 Simulation configuration . . . 177
9-3-1 Boundary Conditions . . . 177
9-3-2 Mesh Generation . . . 178
9-3-3 Load case configuration . . . 180
9-4 Results and analysis . . . 180
9-4-1 Wing loading resolution sensitivity . . . 181
9-4-2 Flow Visualization . . . 183
9-4-3 Comparison with PIV data . . . 185
9-4-4 Additional flow features . . . 195
9-5 Conclusions . . . 196
9-6 List of publications . . . 197
9-6-1 Paper contributions . . . 197

V Conclusions and recommendations 199

10 Conclusions and recommendations for future work 201
10-1 Application of spectral/hp element method in 3D cases . . . 202
10-1-1 Ahmed body validation . . . 203
10-1-2 Ahmed body with diffuser . . . 204
10-1-3 Imperial front wing . . . 205
10-2 Recommendations and further work . . . 206

Bibliography 209

List of Figures

1-1 Influence of the drag coefficient on the final velocity, considering a fixed amount of power. Reproduction from [Barnard, 2001] 4

1-2 Influence of the drag coefficient on the acceleration time to reach certain speed. Reproduction from [Barnard, 2001] 5

1-3 Downforce and drag coefficient versus ground clearance for an inverted LS(1)-0413 aerofoil. Reproduction from [Zerihan and Zhang, 2000] 6

1-4 Influence of the downforce (negative C_L) on the braking distance of a vehicle. Reproduction from [Katz, 1995] 7

1-5 Five examples of automotive bluff bodies. Representation of Huminic and Huminic [2010] 8

1-6 General Motors full-scale Wind Tunnel [Kelly et al., 1982] 9

1-7 TMG wind tunnel test section. Reproduction from www.toyota-motorsport.com . 10

3-1 Comparison between experimental results (left) and *RANS* simulations with SST model (middle) and $k-\epsilon$ model (right) for the vertical velocity V on the plane $X/L = 0$ of the Ahmed body with slant angle of 25°. 17

3-2 Distribution of resolved and modelled turbulent scales in a *LES* simulation. . . . 18

3-3 Summary of the most used numerical methods in CFD simulations in terms of resolved and modelled turbulent scales. 19

3-4 Surface mesh of Ahmed body with slant angle of 30°. Reproduction of Makowski and Kim [2000]. 21

3-5 Contours of time-averaged normalised streamwise velocity U for planes downstream of the Ahmed body with slant angle of 25°. Reproduction from Pagliarella [2009]. 22

5-1 Schematic explaining the finite element, finite volume, finite difference and spectral methods and how both h and p refinements combine to form the spectral/hp element method Hoessler [2011]. 32

5-2 Local and global expansions coefficients for a three-element split of the calculus domain. Reproduction from Karniadakis and Sherwin [2013]. 35

5-3 Modal expansion shape function as defined in Equation (5-20) for a polynomial order $P_N = 5$. Reproduction from Karniadakis and Sherwin [2013]. 38

5-4 Mapping of a standard quadrangle to a standard triangle. Reproduction from Karniadakis and Sherwin [2013]. 39

5-5 Construction of a fourth order ($P_N = 4$) triangular expansion using the product of two modified principal functions $\psi_p(\eta_1(\xi_1, \xi_2))$ and $\psi_{pq}(\eta_2(\xi_2))$, reproduction from Karniadakis and Sherwin [2013] and Hoessler [2011]. 40

6-1 Normalised dissipation curves in log-log scale for CG-based advection-diffusion at very large Peclet number with $P_N = 3$ (left) and $P_N = 7$ (right) compared against DG dissipation curves for P_N (blue), $P_N - 1$ (orange) and $P_N - 2$ (yellow). [Moura, 2017] 49

6-2 A sequence of meshes obtained by splitting macro-elements into $N_{BL} = 8$ elements using a geometric progression and various values of growth rate GR. (a) The macro-element mesh; (b) $GR = 1$; (c) $GR = 3/2$; (d) $GR = 2$. Reproduction courtesy of Moxey et al. [2015] 53

6-3 Close detail of boundary layer mesh near the shoulder of the Boeing RLG wheel case, comparing linear mesh (left) with 4$^{\text{th}}$ order mesh from NekMesh (right). Reproduction from Turner et al. [2017]. 54

6-4 Representation of the linear mesh generated by Star-CCM+ on the IFW case. . . 55

6-5 High-order mesh generation process for Nektar++ simulations. 57

7-1 Side view of the Howell or Windsor body (top) and the Ahmed body (bottom). . 62

7-2 Detailed view of the Rover/Windsor body used for automotive studies. Howell et al. [2003] 63

7-3 Drag coefficient of an axis symmetric cylinder with inclined slanted back. Reproduction from Morel [1978]. 65

7-4 Types of separated flows patterns on a slanted back verified by Morel: (a) behaviour verified on Regime I condition; (b) and (c) behaviours verified on Regime II condition. Reproduction from Morel [1978]. 66

7-5 Effect of free-stream turbulence on drag coefficient behaviour of a slanted cylinder. Reproduction from Morel [1978]. 66

7-6 Geometry details and main dimensions of the vehicle-like model proposed by Morel. Reproduction from Morel [1978]. 67

7-7 Drag and lift coefficient values on the proposed baseline Morel body. Reproduced from Morel [1978]. 68

7-8 Drag coefficient comparative results for reduced ground height case and rounded upper edge, against baseline Morel body (dashed line). Reproduction from Morel [1978]. 69

7-9 Drag coefficient results for different slant angles comparing rounded upper edge (light continuous line and white dots), rounded upper edge combined with ground height reduction (darker continuous line and black dots) against baseline Morel body (dashed line). Reproduction from Morel [1978]. 69

7-10 Ahmed body schematic drawing considering its main dimensions. 70

7-11 Flow visualization on an Ahmed body with slant angle inclination of 12.5° with flow moving from top to bottom. Reproduction from Ahmed et al. [1984] 71

7-12 Flow visualization on an Ahmed Body with slant angle inclination of 25° and 35° from experimental measurements of Lienhart et al. [2002]. Reproduction from Lienhart et al. [2002]. 72

7-13 Break down of the main drag coefficient components on an Ahmed body: frontal (C_K), slant (C_S) and back (C_B). Reproduction from Ahmed et al. [1984]. . . . 72

7-14 Drag coefficient measurements for the different slant angles (φ) evaluated in the original Ahmed body. C_W indicates the total drag coefficient and C_R represents the drag coefficient of other components excluding the frontal part (C_K), the slant (C_S) and the back (C_B). Reproduction from Ahmed et al. [1984]. 73

7-15 Schematic Ahmed body drawing considering all evaluated slant angles. Reproduction from Ahmed et al. [1984]. 74

7-16 Summary of downstream planes for LDA measurements over the Ahmed Body in Lienhart et al. [2002] experiments. Reproduction from Lienhart et al. [2002]. . . 75

7-17 Schematic setup for the Ahmed Body in moving ground conditions with upper fixation support. Reproduction from Strachan et al. [2007]. 76

7-18 Lift and drag coefficient comparison chart. Reproduction from Strachan et al. [2007]. 77

7-19 Comparative plots of normalized vertical velocity V on $X/L_l = 0$ plane for the Ahmed Body with slant angle of 25° for Lienhart et al. [2002] (top) and Strachan et al. [2007] (bottom). Reproduction from Strachan et al. [2007] 78

7-20 Plots of normalized vertical velocity V on plane $X/L_l = 0.048$ showing the presence of counter-rotating vortex close to the underbody. Results for the Ahmed body with 40° slant angle are on the left and for 0° slant angle on the right. Reproduction from Strachan et al. [2007]. 79

7-21 Flow patterns over the slant of an Ahmed body with slant angle of 25°. Reproduction from Pagliarella [2009]. 80

7-22 Plots of turbulent kinetic energy and streamlines at $X/L_l = 0.077$ for the Ahmed body with slant angle of 35°, showing simulation results for EARSM turbulence model (left) and experiment (right); Reproduction from Guilmineau [2008] 81

7-23 Plots of iso-velocity and streamlines at $X/L_l = 0.077$ for the Ahmed body with slant angle of 25° showing simulation results for Spalart-Allmaras turbulence model (left) and $K-\omega$ SST turbulence model (right); Reproduction from Guilmineau [2008] 82

7-24 Drag coefficient for 3 mesh refinement cases and time-averaged streamlines in the symmetry plane Y equals 40 mm. (a) EARSM, (b) DES-SST, (c) DES-SST-F1, (d) DES-SST-F2, (e) experiments. Guilmineau et al. [2011] 83

7-25 Iso-contours of the streamwise velocity U in YZ-planes the wake of the Ahmed body with slant angle of 35°. From top to bottom, the rows correspond to normalized X location $X/L_l = 0$, $X/L_l = 0.077$, $X/L_l = 0.191$ and $X/L_l = 0.479$, respectively. Reproduction from Guilmineau et al. [2017] 84

7-26 Iso-contours of the streamwise velocity U in YZ-planes the wake of the Ahmed body with slant angle of 25°. From top to bottom, the rows correspond to normalized X location $X/L_l = 0$, $X/L_l = 0.077$, $X/L_l = 0.191$ and $X/L_l = 0.479$, respectively. Reproduction from Guilmineau et al. [2017] 85

7-27 Comparison of surface flow visualization from Lienhart et al. [2002] experiments (left) with time-averaged flow lines on the surface of the body from Krajnović and Davidson [2004] (right). Reproduction from Krajnović and Davidson [2004] . . . 85

7-28 Comparison of time-averaged streamlines projected onto planes: a) $X/L_l = -0.749$, b) $X/L_l = -0.251$, c) $X/L_l = 0.047$ and d) $X/L_l = 0.096$. Front view of the lower-left edge of the body where the direction of the vortex rotation is clockwise. Reproduction from Krajnović and Davidson [2004] 86

7-29 Contours of the mean streamwise velocity U in YZ-planes in the wake of the Ahmed body with slant angle of 25°. From left to right the experimental measurements of Lienhart et al. [2002] and the results of LES-NWR, LES-SVV, DES-SST and LES-NWM, respectively. From top to bottom, the rows correspond to the locations $X/L_l = 0.036$, $X/L_l = 0$, $X/L_l = 0.074$, $X/L_l = 0.190$, $X/L_l = 0.48$, respectively, with the origin x = 0 located at the slant end of the body. Serre et al. [2013] 86

7-30 Top views showing iso-surfaces of the Q-criterion (Q = 60) indicating the vortex development over the slant: (a) DES-SST, (b) LES-NWR, (c) LES-SVV. Reproduction of Serre et al. [2013] 87

7-31 Plane view $Z = 0$ indicating the location of the refinement boxes on the Ahmed body model for the *Original* mesh case. The Ahmed body refinement region is indicated in yellow and the wake refinement region is indicated in black. 91

7-32 Plane view $Z = 0$ indicating the location of the refinement boxes on the Ahmed body model for the *Refined* mesh case. The Ahmed body refinement region is indicated in yellow and the wake refinement region is indicated in black. 93

7-33 Mesh discretization considering normalized length of $1L$ for the body. 95

7-34 Comparison of normalized time-averaged U velocity for the symmetric model (left) against full model (right) on planes $X/L_l = 0$ (top) and $X/L_l = 0.096$ (bottom). 97

7-35 Comparison of normalized V velocity for the symmetric model (left) against full model (right) on planes $X/L_l = 0$ (top) and $X/L_l = 0.096$ (bottom). 98

7-36 Comparison of normalized W velocity for the symmetric model (left) against full model (right) on planes $X/L_l = 0$ (top) and $X/L_l = 0.096$ (bottom). 99

7-37 Drag coefficient comparison for *Original* and *Refined* mesh cases, considering proposed high-order meshes and polynomial basis. 101

7-38 Lift coefficient comparison for *Original* and *Refined* mesh cases, considering proposed high-order meshes and polynomial basis. 102

7-39 Instantaneous drag coefficient convergence for the *Original* and the *Refined* mesh cases, considering all high-order meshes and polynomial expansions evaluated. . . 103

7-40 Instantaneous lift coefficient convergence for the *Original* and the *Refined* mesh cases, considering all high-order meshes and polynomial expansions evaluated. . . 104

7-41 Comparison of normalized vertical velocity (V) between experiments of Lienhart et al. [2002] (top) and computational simulations on plane ZY at $X/L_l = 0$. . . 105

7-42 Comparison of normalized streamwise velocity U between experiments of Lienhart et al. [2002] (top) and computational simulations on plane ZY at $X/L_l = 0.077$. 106

7-43 Wall shear stress lines experimental results on the slanted surface on the Ahmed body, with highlighted regions: vortex (purple) and flow separation (orange). Adaptation from Lienhart et al. [2002]. 107

7-44 Comparison of wall shear stress lines over the slanted surface on the Ahmed body using the *Original* mesh with different P orders. 108

7-45 Comparison of wall shear stress lines over the slanted surface on the Ahmed body using the *Refined* mesh with different P orders. 109

7-46 Simulation resolution comparison by iso-contours 3D plots of Q-Criterion (Q-Crit $= 100$) coloured by U velocity, for *Original* and *Refined* meshes at different polynomial expansion proposed. 111

8-1 The Chaparral 2E car, designed by Jim Hall. Reproduction from https://www.gettyimages.ie/ 116

8-2 The Chaparral 2J car designed by Jim Hall considering the dual-fan on the rear and side skirts scheme. Reproduction from http://www.grandprixhistory.org/ . . 117

8-3 Lotus John Player Special 78 (top) and Lotus John Player Special 79 (bottom) Formula One cars. Reproduction from https://racingengineering.tumblr.com/ . . 118

8-4 Rear view of the McLaren MCL-33 Formula One car, highlighting its rear underbody diffuser. Reproduction from www.motorsport.com 118

8-5 Automotive bluff body proposed by Cooper et al. [1998] for proposed diffuser studies. Reproduction from Cooper et al. [1998]. 119

8-6 The pumping effect is demonstrated by Cooper et al. [1998] on the middle plane for diffuser angle of 9.64° and at different ground heights and moving ground. Reproduction from Cooper et al. [1998]. 120

8-7 Lift coefficient values at different ground heights h/H and moving ground condition for proposed diffuser angles from Cooper et al. [1998] study. Reproduction from Cooper et al. [1998]. 121

8-8 Drag coefficient values at different ground heights h/H and moving ground condition for proposed diffuser angles from Cooper et al. [1998] study. Reproduction from Cooper et al. [1998]. 121

8-9 Lift coefficient comparative analysis between moving and fixed ground condition at different ground heights h/H. Reproduction from Cooper et al. [1998]. 122

8-10 Rear view of the McLaren P1 hyper-car, highlighting its rear underbody diffuser. 122

8-11 Generic rounded-front bluff body used for automotive studies, considering diffuser. Ruhrmann and Zhang [2003] 123

8-12 Lift coefficient and proposed performance region division based on the ground height h/Wd for a generic automotive bluff body equipped with 17° diffuser. Reproduction from Senior and Zhang [2001]. 124

8-13 Diffuser flow analysis considering four performance regions as proposed by Senior and Zhang [2001]. Reproduction from Senior and Zhang [2001]. 125

8-14 Lift coefficient and proposed performance region division by Ruhrmann and Zhang [2003]. Reproduction from Ruhrmann and Zhang [2003]. 126

8-15 Surface flow visualization on the diffuser surface at maximum downforce region for 5°, 10° and 15° diffuser angles. Flow from up to down at $h/Wd = 0.584$. Reproduction from Ruhrmann and Zhang [2003]. 127

8-16 Aerodynamic coefficient results in function of diffuser angle. Reproduction from Moghimi and Rafee [2018]. 128

8-17 Half Ahmed body scale model proposed by Moghimi and Rafee [2018] in a reference with a ruler. Reproduction from Moghimi and Rafee [2018]. 129

8-18 Schematic drawing of the Ahmed body squared-back equipped with rear underbody diffuser. 130

8-19 Schematic drawing of the Ahmed body with slant angle of 25° equipped with rear underbody diffuser. 131

8-20 Mesh refinement regions on both Ahmed bodies squared back (top) and with slant angle of 25° (bottom). Refinement region highlighted in yellow is defined as the Ahmed Body refinement and region highlighted in black is defined as Wake Refinement. 132

8-21 Drag coefficient comparative results for Ahmed Body squared-back (blue line) and 25° slant inclination (orange line), considering baseline configuration and evaluated diffuser angles: 5°, 10°, 20°, 30°, 40° and 50°. 133

8-22 Lift coefficient comparative results for the Ahmed Body squared-back (blue line) and 25° slant inclination (orange line) considering standard configuration and evaluated diffuser angles: 5°, 10°, 20°, 30°, 40° and 50°. 134

8-23 Contours of Q-Criterion for the Ahmed body squared-back considering diffuser angle of 5° (DA5), 10° (DA10), 20° (DA20), 30° (DA30), 40° (DA40) and 50° (DA50) for planes $X/L_l = 0$ and $X/L_l = 0.096$. 137

8-24 Contours of normalized streamwise velocity U for the Ahmed body squared-back considering diffuser angle of 5° (DA5), 10° (DA10), 20° (DA20), 30° (DA30), 40° (DA40) and 50° (DA50) for planes $X/L_l = 0$ and $X/L_l = 0.096$. 139

8-25 Contours of normalized vertical velocity V for the Ahmed body squared-back considering diffuser angle of 5° (DA5), 10° (DA10), 20° (DA20), 30° (DA30), 40° (DA40) and 50° (DA50) for planes $X/L_l = 0$ and $X/L_l = 0.096$. 140

8-26 Contours of normalized spanwise velocity W for the Ahmed body squared-back considering diffuser angle of 5° (DA5), 10° (DA10), 20° (DA20), 30° (DA30), 40° (DA40) and 50° (DA50) for planes $X/L_l = 0$ and $X/L_l = 0.096$. 141

8-27 Time-averaged wall shear stress lines (black) on the diffuser surface for the Ahmed body squared-back considering the proposed diffuser angles: 5° (DA5), 10° (DA10), 20° (DA20), 30° (DA30), 40° (DA40) and 50° (DA50), bottom view, incoming flow direction from top. 142

8-28 Pressure coefficient (C_p) distribution for proposed diffuser angles though the whole Ahmed body squared-back length. 143

8-29 Contours of Q-Criterion (QCrit = 100) for the Ahmed body with slant angle of 25° considering diffuser angle of 5° (DA5), 10° (DA10), 20° (DA20), 30° (DA30), 40° (DA40) and 50° (DA50) for planes $X/L_l = 0$ and $X/L_l = 0.096$. 145

8-30 Contours of normalized streamwise velocity U for the Ahmed body with slant angle of 25° considering the proposed diffuser angles: 5° (DA5), 10° (DA10), 20° (DA20), 30° (DA30), 40° (DA40) and 50° (DA50) for planes $X/L_l = 0$ and $X/L_l = 0.096$. 146

8-31 Contours of normalized vertical velocity V for the Ahmed body with slant angle of 25° considering the proposed diffuser angles: 5° (DA5), 10° (DA10), 20° (DA20), 30° (DA30), 40° (DA40) and 50° (DA50) for planes $X/L_l = 0$ and $X/L_l = 0.096$. 148

8-32 Contours of normalized spanwise velocity W for the Ahmed body with slant angle of 25° considering the proposed diffuser angles: 5° (DA5), 10° (DA10), 20° (DA20), 30° (DA30), 40° (DA40) and 50° (DA50) for planes $X/L_l = 0$ and $X/L_l = 0.096$. 149

8-33 Time-averaged wall shear stress lines (black) on the diffuser surface for the Ahmed body with slant angle of 25° considering the proposed diffuser angles: 5° (DA5), 10° (DA10), 20° (DA20), 30° (DA30), 40° (DA40) and 50° (DA50), bottom view, incoming flow direction from top. 150

8-34 Pressure coefficient (C_p) distribution for proposed diffuser angles though the whole length of the Ahmed body with 25° slant. 151

8-35 Contours of Q-Criterion on the plane $X/L_l = 0$ for the proposed Ahmed body with slant angle of 25° simulation resolutions without diffuser. The lower side vortex is observed at approximate coordinates $Y = 0.05$ and $Z = 0.2$ for cases with enough resolution. 153

8-36 Lower side vortex origin by iso-surface contours of Q-Criterion (QCrit = 100) coloured by U. 153

8-37 Iso-contours of Q-Criterion (QCrit = 100), coloured by U, of the bottom view of the Ahmed body squared-back. The following proposed diffuser angles are presented: 5° (DA5), 10° (DA10), 20° (DA20), 30° (DA30), 40° (DA40) and 50° (DA50). . 154

8-38 Iso-contours of Q-Criterion (QCrit = 100), coloured by U, of the bottom view of the Ahmed body with slant angle of 25°. The following proposed diffuser angles are presented: 5° (DA5), 10° (DA10), 20° (DA20), 30° (DA30), 40° (DA40) and 50° (DA50). 156

9-1 Inverted rear wing profile and reduced front wing configuration on the 1968 Lotus 49B. Reproduction from www.favcars.com 162

9-2 Dual wing configuration on the 1968 McLaren M7A, where the front wing is assembled on the front suspension. Reproduction from www.pinterest.com 163

9-3 Topology of the complex vortex system downstream of the front wing with the three main vortices rotation direction. Reproduced from Pegrum [2007]. 164

9-4 Front wing detail of the McLaren MCL-33 (2018). Reproduction from www.motorsport.uol.com.br164

9-5 McLaren MP4-17D Formula One car. Reproduction from www.somefoi.com . . . 165

9-6 Schematic drawing of the IFW with main dimensions (in mm). 165

9-7 Tyrrell 026 race car. Reproduction of www.motorsport.com. 166

9-8 Lift coefficient results in ground effect for the Tyrrell 026 front wing at $AoA = 1°$, for the two proposed configurations: fixed transition and transition free wing. Reproduction of Zerihan and Zhang [2000]. 167

9-9 Lift coefficient results in ground effect for different AoA on the transition free wing. Reproduction of Zerihan and Zhang [2000]. 167

9-10 Front wing geometry and lift coefficient variation with main front wing element AoA. Reproduction of Katz and Garcia [2002]. 168

9-11 Double-element front wing assembly. Reproduction of Zhang and Zerihan [2003]. 169

9-12 Pressure distribution on the surface of the NACA4412 aerofoil at AoA of 10°. Reproduction of Ahmed et al. [2007]. 170

9-13 Drag coefficient results for the NACA4412 aerofoil at different ground clearances (h/c) for varying AoA. Reproduction of Ahmed et al. [2007]. 171

9-14 Open wheel and inverted wing profile setup configuration of Diasinos and Gatto [2008] experiment. Reproduction of Diasinos and Gatto [2008]. 171

9-15 Laser smoke visualisation behind the endplate, courtesy of Jonathan Pegrum. (Pegrum [2007]). 172

9-16 Imperial Front Wing assembly on Imperial College London 10 × 5 wind tunnel. . 173

9-17 Imperial Front Wing geometry with its coordinate axis definition. 174

9-18 Imperial Front Wing geometry. Nomenclature: ride height h (light blue line), chord c (yellow line), main plane (dark orange), moving belt (dark grey), nose cone (A), Gurney flap (B), canard (C), endplate (D) and footplate (E). 175

9-19 Imperial Front Wing geometry and selected PIV planes. 176

9-20 Complete PIV setup of the IFW at the 10 × 5 wind tunnel in the Department of Aeronautics at Imperial College London. 177

9-21 PIV calibration grid used for the IFW measurements at the 10 × 5 wind tunnel in the Department of Aeronautics at Imperial College London. 178

9-22 Detailed view of the macro prism layer. 179

9-23 Details of the three proposed refinement boxes on the plane $Y/c = -2$. Far-field refinement box (red), wing refinement box (light blue) and endplate refinement box (orange). 179

9-24 Comparative lift trend line for 3rd (NM36 - blue line) and 4th (NM46 - red-dashed line) polynomial expansions obtained from the same NM36 restart file from the 2nd to the 5.5 CTU 182

9-25 Drag (top) and Lift (bottom) coefficients history on the IFW comparing NM46 and NM56 results. 183

9-26 Drag (top) and Lift (bottom) coefficients history on the IFW for the NM56 results. 184

9-27 Flow visualization of IFW at velocity of 15m/s using Formula 1 standard aerodynamic paint. 185

9-28 Comparison of the flow visualization and wall shear stress results for IFW (bottom view) 186

9-29 Comparison of the flow visualization and wall shear stress results for IFW (top view) 187

9-30 Flow visualization results for IFW simulation considering 3rd polynomial expansion (NM36) 188

9-31 Comparative flow visualization results for IFW simulation considering 3rd (NM36), 4th (NM46) and 5th (NM56) polynomial expansion in order to highlight the major differences in resolution. 189

9-32 IFW vortices nomenclature definition on the V velocity plot. From top to bottom: endplate vortex (partially represented), canard vortex and main vortex. 189

9-33 Time-averaged normalized V and W velocity results from Nektar++ for 4th (NM46) and 5th (NM56) order polynomial expansion compared with experimental results for plane 1. 190

9-34 Time-averaged normalized V and W velocity results from Nektar++ for 4th (NM46) and 5th (NM56) order polynomial expansion compared with experimental results for plane 2. 191

9-35 Time-averaged normalized V and W velocity results from Nektar++ for 4th (NM46) and 5th (NM56) order polynomial expansion compared with experimental results for plane 3. 192

9-36 Time-averaged normalized V and W velocity results from Nektar++ for 4th (NM46) and 5th (NM56) order polynomial expansion compared with experimental results for plane 4. 193

9-37 Time-averaged normalized V and W velocity results from Nektar++ for 4th (NM46) and 5th (NM56) order polynomial expansion compared with experimental results for plane 5. 194

9-38 Comparison of time averaged iso-contours of $CP0 = 0$ coloured by pressure. . . 195

9-39 Comparison of instantaneous iso-contours of $CP0 = 0$ coloured by pressure. . . . 196

List of Tables

5-1 Coefficients for stiffly-scheme time integration. 42

7-1 Resolution of the proposed simulations, showing total number of DOF (in Million) for each case evaluated, at different polynomial expansions accuracy P_N. 94

7-2 Drag and lift averaged coefficient for the half symmetric and full body models, comparing with experimental values obtained from Strachan et al. [2007]. 96

7-3 Drag and lift averaged coefficient for the *Original* and *Refined* meshes considering evaluated P_M and P_N high-order, comparing with experiments from Strachan et al. [2007]. 100

7-4 Required computational time in hours for different Ahmed body simulations to reach 7 CTUs at Imperial College CX2 cluster with 432 CPUs. 109

9-1 Plane locations for PIV measurements 176

9-2 EDR Infiniband technical specifications on HP cluster. 181

9-3 Intel Omni-Path Cluster technical specifications on HP cluster. 181

9-4 Simulation time for one convective length using Nektar++, considering NM36, NM46 and NM56. 182

Part I

Introduction and Background Information

Chapter 1

Road vehicles aerodynamics

1-1 Background

Aerodynamics is the field of study which focuses on the physics of objects moving through the air and how the object shape affect this movement. Today, aerodynamics is one of the key areas for road vehicle development, directly shaping the geometry and overall performance. Aerodynamics studies have gone way beyond the purpose of generating trendy designs, now playing a crucial role in ensuring the vehicle's fuel economy, low wind noise and other environmental footprints such as emissions.

The first studies of aerodynamics applied to vehicles began around 1920, when engineers realized that a significant portion of power dissipated from cars in motion was a result of its high resistance against the air, as referred by Hucho and Sovran [1993]. In the 1930s, automakers noted the effect of aerodynamic drag and intensified their researches to develop vehicles with improved aerodynamics. This development continues until the present day, with vast investments in studies and innovative designs in order to decrease the resistance of the vehicle into the air.

Some of the key vehicle performance criteria are highlighted in the list below:

- fuel economy
- top speed
- control and stability in high speeds
- engine, powertrain, cabin and brake cooling
- wind noise
- air conditioning
- aerodynamics and surface design

Improve drag coefficient (C_D) performance is the major motivation for road vehicles to have aerodynamically engineered and optimized geometries. A lower C_D means less energy required to overcome air resistance, therefore, fuel consumption is reduced. An example of the influence of the drag coefficient is illustrated in Figure 1-1, which present the curves of the required power to reach certain velocity overcoming the aerodynamic drag, with three vehicles of drag coefficients valued at 0.45, 0.35 and 0.25 respectively.

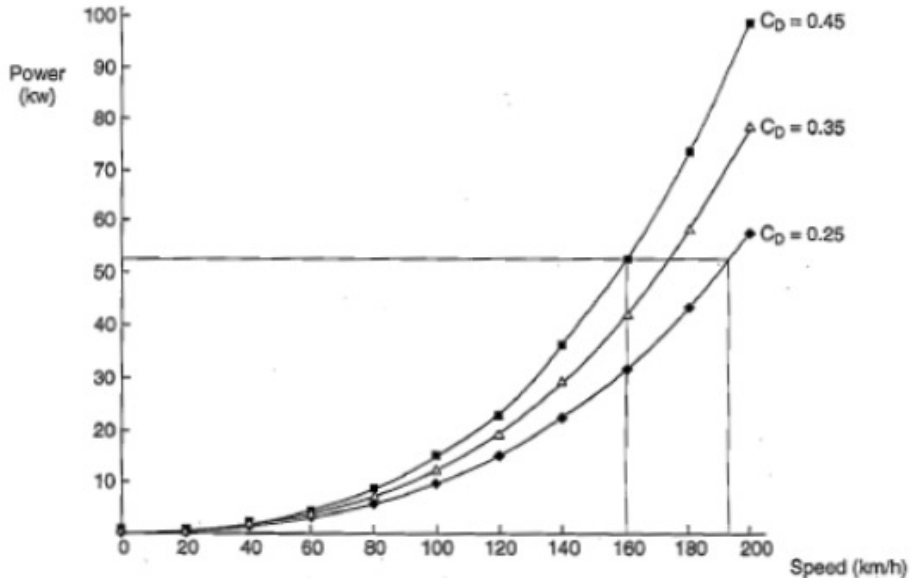


Figure 1-1: Influence of the drag coefficient on the final velocity, considering a fixed amount of power. Reproduction from [Barnard, 2001]

For the vehicle with drag coefficient value of 0.45, power required to reach the speed of 160 km/h is around 52 kW. In contrast, the vehicle with the lowest drag coefficient (0.25) requires 40% less power to reach the same speed. This effect can be more significant at high speeds as the forces acting on the vehicle increase with the square of the velocity, (Jowsey [2013]). With current social policies focusing on a significant reduction in greenhouse emissions in combination with pressures on environmentally friendly initiatives, a reduction in fuel consumption and hence carbon emissions are of utmost importance to the automotive industry as a whole.

Performance and acceleration are also areas in which vehicles will benefit from aerodynamic optimisation. Figure 1-2 presents a comparison between the acceleration performance for the same three vehicles with different drag coefficient values, from the study performed by [Barnard, 2001]. To reach the speed of 120 km/h, the vehicle with lowest drag coefficient has an acceleration around 3 seconds faster than the vehicle with drag coefficient of 0.45.

The improvements in acceleration time are also dependent on another aerodynamic quantity: the lift coefficient C_L. The lift coefficient is a flow parameter related to normal force component of the flow, acting on the object. Airplanes are designed to provide a positive lift component, as a convention, to counteract the weight. Considering road and race vehicles, it is desirable to have a negative lift component in order to improve tire grip. The additional tire grip is desirable for acceleration in limited traction zones and braking conditions, as well

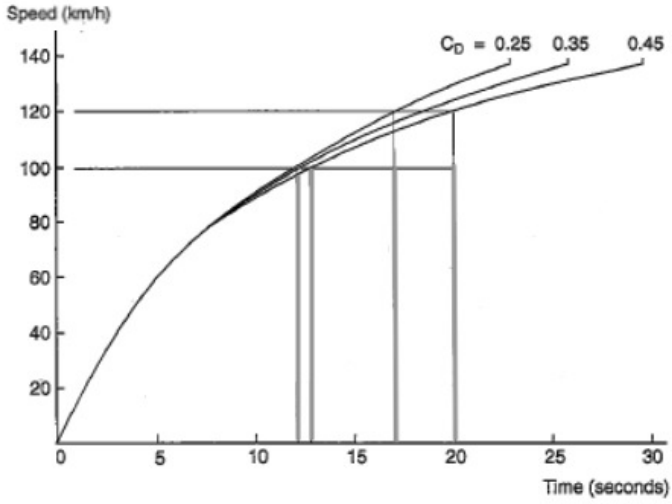


Figure 1-2: Influence of the drag coefficient on the acceleration time to reach certain speed. Reproduction from [Barnard, 2001]

as to provide extra stability for the vehicle when driving into curves. Negative lift is referred to colloquially as downforce in automotive and racing industries. On an aerofoil-like geometry, downforce can be generated by slowing the air on the top of the profile and accelerating it on the lower part, resulting in a downward force. The mechanism is identical to the lift generation of aircraft wing however in the opposite direction.

The application of inverted wing profiles on vehicles started by implementing front and rear wings on racing cars. Both wings as well as curved or tunnelled underbody geometries are the most common methods to increase downforce for both racing and road cars. The downforce increment also depends on the ground clearance between the vehicle and the ground as evaluated by Zerihan and Zhang [2000]. One typical example of this dependency for an inverted wing profile is presented in Figure 1-3, where the highest values of downforce and drag coefficient are obtained when the ground clearance is smaller than a quarter of the aerofoil chord. It is stated by Katz [2006] that most race cars, especially with open wheels, are designed to have front wings mounted in the maximum downforce increment range found for ground clearance h normalized by the wing profile chord length c between $h/c = 0.1$ and $h/c = 0.3$. Below $h/c = 0.1$, it was found that most automotive wing profiles stalls, losing downforce efficiency.

Figure 1-4 presents braking performance comparison illustrating braking curves for the same vehicle geometry but with three different negative C_L or downforce values: 0, -1 and -2. The outcome shows that by increasing downforce, the required braking distance reduces.

Another important point to be considered regarding the downforce is the load distribution between rear and front axles. This force distribution influences the cornering dynamics, as the relationship between the centre of pressure with the centre of gravity determines aerodynamic sensitivity and sign of aerodynamic moments in yaw and crosswind conditions. Unbalanced downforce distribution will cause problems on the controlling the vehicle, so aerodynamic parts should be carefully designed to work as a system and offer the flexibility to change their parameters. One such example is the angle of attack of front and rear wings, which can be

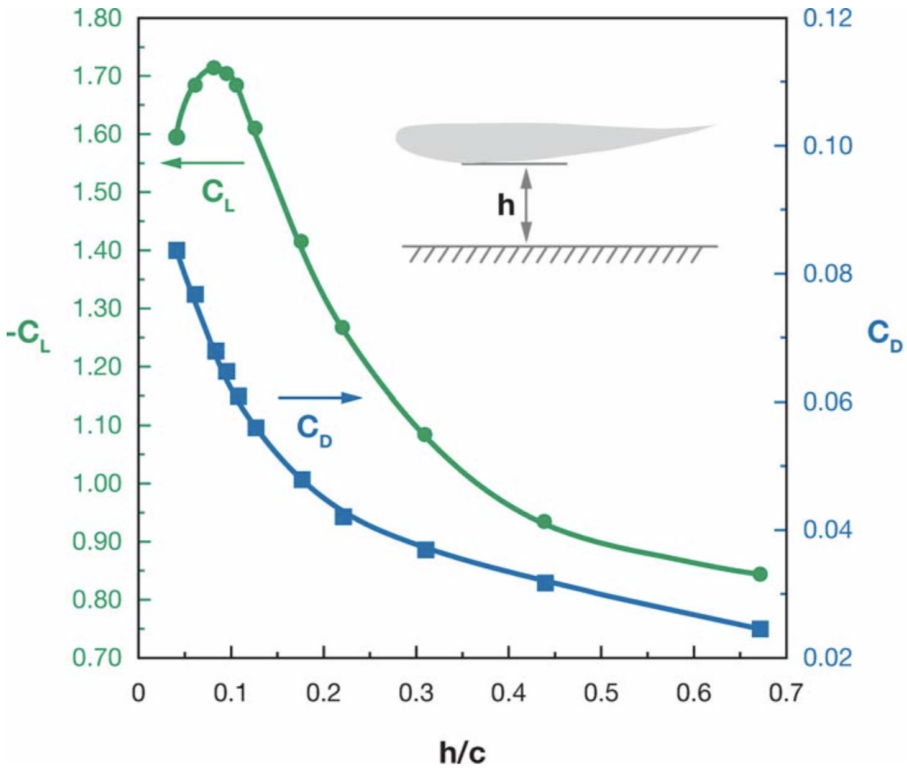


Figure 1-3: Downforce and drag coefficient versus ground clearance for an inverted LS(1)-0413 aerofoil. Reproduction from [Zerihan and Zhang, 2000]

fine-tuned according to calibration parameters or the driver's preference on a racing car.

Wide understanding of downforce and drag generation and their behaviour on vehicles was constrained, as most of the automotive companies consider their geometry models copyrighted and only offer the aerodynamic community limited access. Due to the lack of an open source vehicle test case or similar model able to represent a road vehicle in its fundamental behaviour, academics and industrial researchers proposed different types of bluff bodies, with lower ground height and common automotive body features. One example of such feature would be to have fixed flow separation points, which was first proposed by Morel [1978].

Morel [1978] and Ahmed et al. [1984] introduced the most widely studied variants of automotive bluff bodies. These are due to the specific flow characteristics that are replicated, such as flow separation and reattachment. The generation of different flow features are due to the angle of upper slanted back, which can be modified, replicating different automotive body styles flow behaviours. However, as shown in Figure 1-5, a wider array of bluff bodies are available to replicate a larger variety of flow structures present in automotive geometries.

Generic automotive bluff bodies also provide a reliable base case for research and development of active and passive aerodynamic devices such as synthetic jet, spoilers and rear underbody diffusers, with specific automotive focuses. Once the generic automotive bluff body base has a widely understood and characterized aerodynamic behaviour, the changes in flow field and aerodynamic quantities values due to the addition of an aerodynamic part are easier to

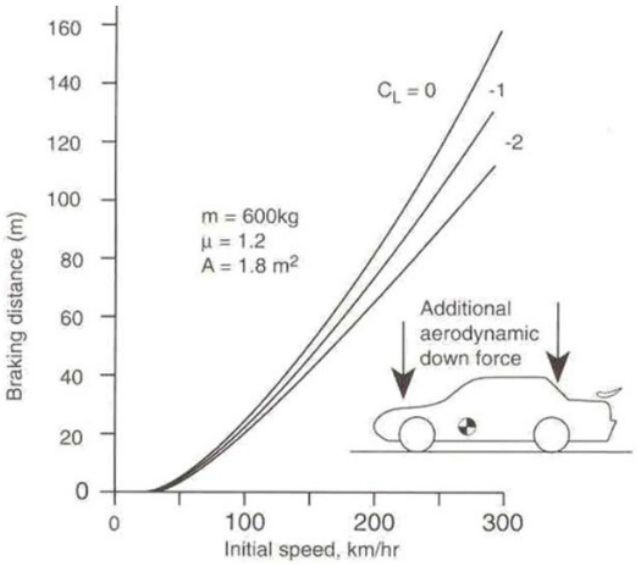


Figure 1-4: Influence of the downforce (negative C_L) on the braking distance of a vehicle. Reproduction from [Katz, 1995]

identify and understand. As a consequence, when applying those aerodynamic parts to real world vehicles geometries, it's easier to understand the flow characteristics and to improve the vehicles' performance.

For optimizing road vehicles' aerodynamic performance in terms of drag and lift, the main tools used in the industry are wind tunnel tests and Computational Fluid Dynamics (CFD) simulations. The main advantage of using wind tunnel test is the fast response time to obtain the aerodynamic properties, once the model is available and faster small design iterations when using clay model. However, the operational costs of these structures are very high, also requiring a complex electric power structure. Wind tunnel tests are only possible once a prototype is available, usually at an advanced stage of a road vehicle development and very costly to produce even for racing car. CFD simulations can be performed on vehicles even at very early stages of development, guiding the design by showing the aerodynamic performance and avoiding further re-work, which can be costly in a road vehicle development pipeline. Both CFD and wind tunnel test are complementary to each other, where the computational study feeds-back the test with the flow field analysis. The main goal of this approach is to drive the iterations to improve the most sensitive areas in terms of aerodynamic performance and maximise the experimental window. Aerodynamic development techniques for road and racing vehicles are introduced in next section.

1-2 Aerodynamics development and analysis techniques

In the 1930's, when the aerodynamic performance of road vehicles started to be studied and optimized, only empirical tests were available as stated by Hucho and Sovran [1993]. Same conditions for all tests were difficult to be kept as the vehicle had to be moving in an

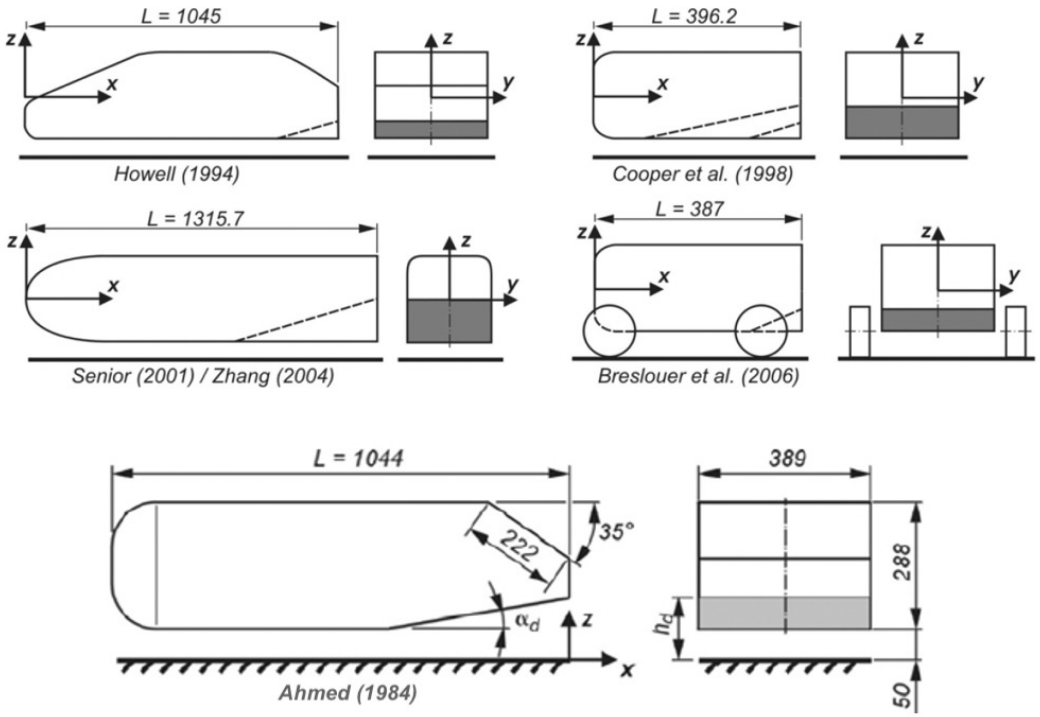


Figure 1-5: Five examples of automotive bluff bodies. Representation of Huminic and Huminic [2010]

open environment, so the aerodynamic properties results were influence by different weather and wind conditions. To overcome this difficulty, engineers moved the aerodynamic test to controlled facilities, which were named wind tunnels.

Wind tunnels are environment-controlled facilities for aerodynamic tests of different objects. The object is assembled in the test section, usually connected to a force balance. Air is driven through the test section where the object is fixed, simulating its movement while evaluating its aerodynamic behaviour and properties. Classification of wind tunnels can be made according to the Mach number on the test section, temperature control, type of test section and the path taken by air. For automotive and racing applications, wind tunnels are mostly subsonic with temperature control, in order to keep air properties constant. In terms of test section, it can be designed either to be open, without side and top walls or to fully closed.

Considering the path taken by the air to reach the test section, we have two types of wind tunnel: closed or open circuit. In the Göttingen wind tunnel, or closed-circuit tunnel, the fan re-circulates the air within a closed ducts, without air intake from the environment outside the circuit. This type of construction tends to have a better temperature control, keeping similar gas properties for the air reaching the test section, as well as having lower energy consumption compared to open circuit wind tunnels. This is the main reason why the closed type is the preferred one in the automotive and racing industries. The second type of wind tunnel is the Eiffel type, or open circuit, in which air is extracted from the external environment, pass through the test section and then return to the outside.

In the automotive industry, one of the largest and most important wind tunnels is the General Motors (GM) wind tunnel, located in Warren, Michigan. According to Kelly et al. [1982], the GM's tunnel is a closed-circuit wind tunnel which presents a cross section at the final nozzle of 56.16 m^2 and approximate length of 21.3 m. It is built of coated metal with a thick 600 mm concrete layer to prevent sound waves propagation. The air flow is driven by a powerful fan with approximate power of 3000 kW and 13 m diameter blades, able to reach a top speed of 250 km/h for 15 minutes. GM's wind tunnel scheme is shown in Figure 1-6.

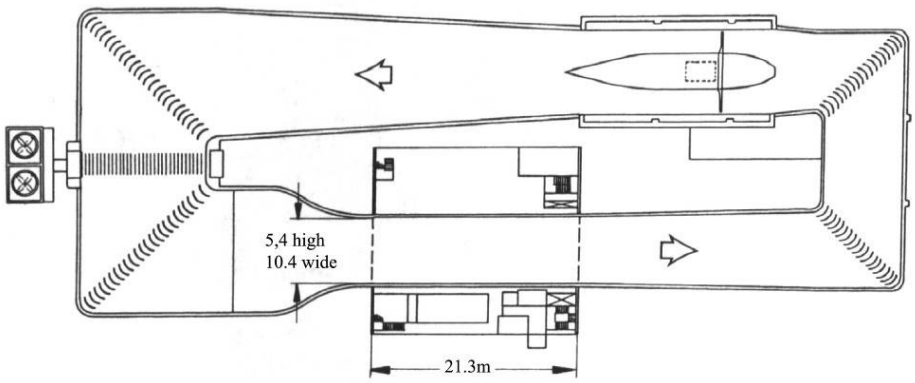


Figure 1-6: General Motors full-scale Wind Tunnel [Kelly et al., 1982]

The representation of the ground is one of the most important parts of the tunnel when it comes to automotive vehicles testing, as its configuration influences the flow over the tested vehicle and both drag and lift coefficients. To remove flow perturbation and large boundary layer development of the floor, combinations of different ground configuration together with a boundary layer suction system are employed, aiming to reproduce real operation condition, however with a significant investment increase for the tunnel construction. The most common automotive wind tunnel floor configurations on the test section are: static floor, raised platform and moving belt. These configurations aim to reproduce the ground-vehicle interaction, providing a closer approximation to real conditions of the vehicle operation.

In Newtonian Mechanics and within an inertial reference frame, engineers can keep the vehicle stationary whilst passing air over the object. In static ground wind tunnels, the model is assembled on the floor of the tunnel either by supports or over its surface and connected to the balance, placed below the test section. The force balance is responsible to measure the main aerodynamic quantities, such as drag and lift forces. For wind tunnels with moving ground capabilities the assembly process changes, as the movement of the ground makes impossible to place the model directly on the floor. The model is, in most circumstances, fixed by a rod, shaped in a symmetrical aerofoil profile to reduce form drag influences.

State-of-the-art automotive and racing wind tunnels, such as the TMG, presented in Figure 1-7, employ moving ground, boundary layer control techniques, force measurement balance attached to the moving ground and wheel model fixing. These measures together provide conditions closer to the real operative environment of the vehicle. The tunnel also incorporates particle image velocimetry (PIV) for off-surface flow visualization, aiming to provide a comprehensive dataset for aerodynamic evaluation.



Figure 1-7: TMG wind tunnel test section. Reproduction from www.toyota-motorsport.com

Due to the substantial costs and resource requirements of wind tunnel operations, Computational Fluid Dynamics (CFD) is used to compliment tunnel tests in the design phase. Studies such as Buscariolo and Mariani [2010], Magazoni et al. [2015], Gupta et al. [2015], highlight the reliability and correlation between physical test and virtual simulations, which are in order of 97% for the drag coefficient which is the most common and one of the most important parameter reported for vehicles.

Currently, the CFD simulation methodologies that can be used to evaluate the aerodynamic behaviour of an object would be, in ascending order of computational cost and accuracy, Reynolds Averaged Navier-Stokes ($RANS$), unsteady ($RANS$), Detached Eddy Simulation (DES), Large Eddy Simulation (LES) and Direct Numerical Simulation (DNS), this later one current unfeasible for automotive applications. Within the LES methodology, we have explicit LES, also referred as wall modelled Large Eddy Simulation ($WMLES$) and implicit Large Eddy Simulation ($iLES$), sometimes referred to as under-resolved Direct Numerical Simulation ($uDNS$).

CFD simulations and Wind Tunnel test are currently the main tools used for road and race cars aerodynamic development. Both approaches work together to deliver the best aerodynamic performance by understanding the flow behaviour around the vehicle. The CFD simulations provide aerodynamic insights at early stages of the project, aiming to optimize the performance of the vehicle's systems such as the underbody. The development of new Computer Processing Units - CPUs and cost reduction of the clusters, complex flow solutions became feasible in a reliable time for production. The computational power upgrades also made possible the use of high-order codes, thanks to the capacity of scaling the simulation in parallel processes almost linearly. A brief summary of the most used numerical methods for CFD applications are presented in the next chapter.

Chapter 2

Objectives, Aims and Goals

The main objective of this research project is to benchmark and analyse the use of high-fidelity CFD simulations, the spectral/hp element method, for complex automotive geometries. It focuses on the necessary development required to bridge the gap between academic research and industrial level application studies, allowing academic software to be rather straight-forwardly deployed in engineering activities. Specifically, this project focuses on the evaluation, use and development of spectral/hp element CFD suite, Nektar++, to obtain reliable 3D simulations of external aerodynamics. The geometries considered in this project consists of a standard-type automotive bluff body, the Ahmed body, a derived version of it, the Ahmed body with diffuser, and a Formula One car front wing design, the Imperial front wing.

In this chapter, information regarding the motivation (Section 2-1) will be given, identifying the gaps in the state-of-the-art which this project will bridge. This is followed by the presentation of the main objectives in Section 2-2. To reach the objective, detailed goals and project milestones are identified and presented in Section 2-3.

2-1 Motivation

Generally, research can be conducted following various motivations, resulting them being categorised as basic or fundamental research, applied research, among many others. Basic research advances fundamental knowledge, focusing on creating, refuting or supporting theories of observed phenomena. Applied research can be defined as the implementation or development of some technology towards practical applications, bridging the gap between the academia and the industry.

Collaboration between the academia and the industry in the form of applied research is being increasingly emphasised in recent years. Novel computational methods for many fields have already proved their validity and benefits in terms of efficiency and accuracy in various established canonical test cases. However, these academic codes lack the consistency of handle a whole range of different cases and comprehensiveness, such as an user-interface, that would be required for new tools to be accepted and widely appreciated in industry. Applied research

fulfils this gap, bringing together the in-depth knowledge of academic researches and detailed requirements from the engineer based on decades of experiences. As the result, novel methods and new tools may become much more accessible for a wider group of researchers and engineers in the field.

In fluid dynamics, canonical test cases are usually characterized by simplified geometries and boundary conditions, and often with 2D geometries at low-moderate Reynolds number. Although they have played a key role in validating newly proposed methodologies or problem formulations, they failed to capture the challenges often confronted with engineers working on CFD simulations of real-world geometries. One example is the slow adoption of spectral methods on CFD simulations.

Spectral methods, such as the spectral/hp element method, offer highly desirable properties for CFD codes, with high-fidelity solution and exponential convergence. Such method is currently widely applied in *LES* and *DNS* simulations for 2D geometries at moderate values of Reynolds number. Although, conceptually, simulations with higher Reynolds numbers and 3D geometry would be a straight-forward step, results from previous studies have shown that this might not be the case. Due to low-dissipation characteristic of spectral methods using Continuous Galerkin approach, high-frequency modes start to rise quickly when the Reynolds number increases, causing the simulation to be unstable and leading to divergence. As result, most published work on the simulation of a 3D geometry with spectral method at higher Reynolds number are using the quasi-3D (also known as the 2.5D) simulation, with the 3D result extracted from 2D solutions. In addition, complex geometries found in real-world 3D models also pose a challenge for spectral methods: traditional approach of increasing the mesh density to capture surface details would lead to very large-scale problems that are computationally intractable.

This research is motivated by enhancing the resolution and accuracy of 3D automotive and racing flows using the spectral/hp element method. It would require the necessary enhancements to conventional spectral/hp element simulations, such as meshing and solution design in order to establish the support for flow simulations of fully 3D complex geometries. In addition, conventional experiences and meshing strategies may not be suitable for the use of spectral/hp method, with the additional capability to change the polynomial order. Development of suitable guidelines and best practices may become essential in conducting efficient meshing and simulations that can take full advantage of the spectral/hp element method. This is the first step towards full capability application of a spectral method for a wider range of problems. For this work, we focus on the use and development of the CFD software Nektar++, with the main objectives of the research are presented as follows.

2-2 Main objectives

The main objectives of this research are determined to be:

To obtain reliable and highly accurate results using fully 3D incompressible flow simulations with the spectral/hp element method for complex geometries, by incorporating latest developments on numerical stabilization technique and the development of new meshing strategies. The obtained result should be validated with both existing and newly proposed test cases that represent challenging geometries in automotive aerodynamics.

The detailed research objectives to be accomplished are as follows:

- Determine configurations of the solver to deliver stable and converged results for fully 3D complex geometries.
- Develop a meshing strategy for efficient simulations, with the spectral/hp element method.
- Demonstrate results accuracy and high-resolution on capturing flow physics on an existing automotive bluff body.
- Application of the same methodology to evaluate the influence of rear underbody diffuser mounted on same automotive bluff body.
- Proposing of a new standard test case representing flow features of high-performance cars and racing applications based on a Formula One front wing.

To reach the main objectives presented, we've established some goals and milestones presented as follows.

2-3 Goals

From the main objectives, it can be observed that the first point, to obtain stable and converged simulations, will be the foundation for the fulfilment of all subsequent items. To stabilize the simulation and improve the convergence characteristics, the following goals have been proposed:

- Stabilization of the solution high-frequency modes which are known to prohibit the convergence of spectral methods at high-Reynolds numbers.
- Avoid aliasing issues when inappropriate quadrature orders are used.
- For the stabilized scheme, evaluate the efficiency when simulating fully 3D complex geometries at relatively high Reynolds numbers.
- Development of warm start practices for high order simulations, assisting convergence under constraint computational wall time.

Meshing strategy development is another objective complementing the previous development, exploiting the flexibility of adjusting mesh and solution polynomial orders.

- Determination of a guideline on how to translate traditional designs of linear mesh into suitable higher order mesh designs.
- Evaluate the effectiveness of h-typed mesh refinement on high order polynomial meshes.
- For complex 3D geometries with smooth curvatures, exploit the benefit of using curved mesh with high-order polynomials, instead of traditional way of approximating the curvature with a dense mesh.

With a mesh strategy and solution setup defined, we evaluate the influence of different polynomials for the solution on an automotive bluff body, which the main goals are:

- Provide a comparative study to examine the feasibility of iLES simulations using half model with symmetry boundary condition, when only the averaged flow is of interest.
- Correlate aerodynamic quantities and flow structure results with experimental references.
- Quantify the influence of increasing solution polynomial expansion orders when combined with different high-order meshes, and determine the most reliable configuration.
- Identify particular flow features that an accurate solution needs to capture.

Next step is to apply all findings previous reported to a modified version of the automotive bluff body, in which a diffuser without endplates is assembled on the rear underbody. The goals of this study are:

- Evaluate the changes in aerodynamic quantities and flow structures when adding a diffuser with different angles.
- Compare the performance and flow behaviour differences when the diffuser is applied to different body geometries.
- Discuss the generation and trajectory of the lower side vortex at the presence of the diffuser.

Unlike automotive bluff bodies for road vehicles, currently there exists few benchmark test cases representing high-performance and racing cars often with some wing elements located at the front and/or the rear of the vehicle. In collaboration with McLaren Racing, we propose to use a complex Formula One front wing geometry, the Imperial front wing, to establish a new test case representing the design and simulation challenges in racing cars. The main goals are:

- Establish the Imperial front wing as a standard test case for automotive and motorsport CFD validation.
- Obtain experimental data set with open access for the fluid dynamics community.
- Validation of previously developed tools, meshing strategy and other guidelines in obtaining accurate results for 3D simulation of a much more complex geometry with the spectral/hp element method.
- Identify the added benefit of running simulations with higher polynomial orders for a complex geometry.

Chapter 3

Numerical Methods

Based on the project objective and goals identified in Chapter 2, this Chapter focuses on analysing relevant numerical methods that will be selected to help achieve these goals. A brief explanation of each method is provided as well as the main differences between each. A brief introduction to the spectral/hp element method is also presented in this chapter, however the aim is just to motivate the design choices. Full details will be presented further in Chapter 5. Lastly, the concept of symmetric CFD models is discussed for both *RANS* and *LES* solutions. Results of an Ahmed body iLES-SVV simulation comparing half and full model is presented in Chapter 7.

3-1 Computational methods for fluid flows

3-1-1 Methods based on Reynolds Averaged Navier-Stokes

Among the most popular simulation methodologies presented on Section 1-2, we will first evaluate the *RANS* case, which is currently used in the automotive industry, according to Buscariolo et al. [2016] and Magazoni et al. [2015]. It can be defined as a statistical-averaged method which assumes that the flow is ergodic (statistically stationary), therefore using a time-averaged estimator. The Navier-Stokes equations are applied in order to describe the fluid flow motion, in which a quantity is decomposed into its time-averaged and fluctuation quantities (Reynolds decomposition) for turbulent flow conditions. Within this decomposition, a new stress source from the convective acceleration is introduced, referred as the Reynolds stress, adding a second order tensor of unknown variables. To obtain a system of equations containing only the time-averaged velocity and pressure, it is necessary to model the Reynolds stress term, eliminating the fluctuating part of the quantity and this is the so-called closure problem.

The closure problem was first studied by Boussinesq, in which he stated that the momentum transfer caused by turbulent eddies can be modelled with an eddy viscosity (Boussinesq [1877]). The concept of eddy viscosity states that the Reynolds stresses tensor should be

proportional to the mean strain rate tensor in order to generate a appropriate condition to solve the system of equations. This approach was defined as the eddy viscosity model (EVM), which might be combined with additional equations or turbulence models to estimate its value. Whenever no additional PDE is used to estimate the eddy viscosity value, these models are referred as Algebraic turbulence or zero-equation models. These models are often simple and might not be able to account history effects on the turbulence for complex geometries, however they are still suitable for simplified cases and some examples are the Cebeci-Smith (Smith and Cebeci [1967]) and Baldwin-Lomax (Baldwin and Lomax [1978]) models.

We now highlight the most used turbulence models in the industry for $RANS$ simulations, based on the EVM. The Spalart–Allmaras model, proposed by Spalart and Allmaras [1992], is a one-equation model that solves a modelled transport equation for the kinematic eddy turbulent viscosity. The model was designed focusing on aerospace turbo-machinery applications involving wall-bounded flows where boundary layers are subjected to adverse pressure gradients.

The most common model, especially for road and racing vehicles simulations, is the $k-\epsilon$ two-equation turbulence model, proposed by Jones and Launder [1972]. The two equations come directly from the differential transport equations, where k represents the turbulent kinetic energy, determining the energy in turbulence and ϵ represents the turbulence dissipation rate. This model demonstrated good agreement for free-shear layer flows with small pressure gradients.

Another common two-equation turbulence model is the $k-\omega$ proposed by Wilcox [1988], where ω refers to a specific dissipation rate of the turbulent kinetic energy k into internal thermal energy. In this model, the turbulence prediction is performed by additionally solving the turbulent kinetic energy k equation and ω transport equation,

A widely used and robust two-equation turbulence model is the Menter's Shear Stress Transport (SST), originally proposed by Menter [1994], combining both $k-\epsilon$ and $k-\omega$ models. The use of the $k-\omega$ model formulation applies to the inner parts of the boundary layer, making the model directly usable all the way down to the wall through the viscous sub-layer. The SST formulation switches to the $k-\epsilon$ model in the free-stream and thereby avoiding sensitive issues of the $k-\omega$ model due to the inlet free-stream turbulence properties.

Simulations employing the $RANS$ methodology usually have good correlation with experimental results in terms of the aerodynamic quantities, especially for the drag coefficient value, such results presented by Buscariolo [2009] and Fu et al. [2018]. For most of the cases in the automotive industry, drag coefficient is the main aerodynamic quantity to be pursued for fuel economy and emission performance. The $RANS$ methodology would be sufficient for those cases, offering a cost and time effective solution. For other aerodynamic quantities, such as the lift coefficient and for flow topology and structures when analysing complex geometries with abrupt flow separation and vortex dominated, relevant for high-performance and racing vehicles and many other industrial applications, this methodology is still unable to correctly predict these phenomena.

In order to give basis to previous statement, we selected one of the cases of this research, the Ahmed body with slant angle of 25°, to evaluate the $RANS$ methodology on a commercial code within two turbulence models: the $k-\epsilon$ and the SST turbulence models, both solving two transport equations. Although the Ahmed body has a simplified bluff body shape, this

slant angle is still a challenge for CFD codes to correctly predict its flow behaviours. The domain has same dimensions of the wind tunnel test section from the reference experimental work of Strachan et al. [2007] with moving ground simulation and inlet velocity of 25 m/s. The mesh was created on the same commercial code with 10 prismatic layers and growth rate $GR = 1.6$, also incorporating volumetric refinements over the Ahmed body surface and on the wake as will be detailed in Section 7-3-2. The total number of prism and tetrahedra elements are around 5 million, considering half model approach, which will be later discussed.

Results for the drag of coefficient considering both turbulence models have similar numerical results, both with a slight under-prediction of the experimental result in around 2%, indicating good correlation level for this aerodynamic quantity. When comparing the flow structures on the edge of the slant on plane $X/L = 0$ by showing contours of vertical velocity V, presented in Figure 3-1, it is possible to notice that the flow structures are captured however we observe a clear under-prediction when comparing to the experimental results. Both positive and negative parts of the vortex are indicating only two contours when in the experimental results, we observe at least three contours on the positive portion and six for the negative part. On the middle portion of the slant, the *RANS* simulation with $k - \epsilon$ turbulence model correlates closer to experiments as the velocity profile has a smoother transition, compared with the SST model where close to the symmetry plane, the velocity gradient is stronger.

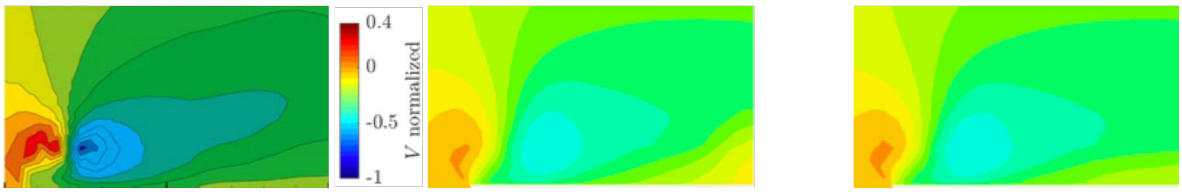


Figure 3-1: Comparison between experimental results (left) and *RANS* simulations with SST model (middle) and $k - \epsilon$ model (right) for the vertical velocity V on the plane $X/L = 0$ of the Ahmed body with slant angle of 25°.

Within previous simulation, we verified that *RANS* methodology might be insufficient to capture the correct flow physics, although some aerodynamic quantity values indicate that the correlation level is high. *RANS* methods have shown their strength essentially for wall-bounded flows, where the calibration according to the law-of-the-wall provides a sound foundation for further refinement. For free shear flows, the performance of *RANS* models is much less uniform and represent the flow with lower accuracy. For such complex problems, the flow field solution is better represented by models in which at least part of the turbulence spectrum. Such methods are termed scale-resolving simulation (*SGS*) models.

Considering cases where the vehicle geometry presents several separation areas and vortex generation and those critical areas need to correctly predicted, such as in Formula One cars, *RANS* solutions might not be fully able to reproduce the reality, requiring more accurate solutions, increasing costs and computational time. The next step in order to improve the confidence level of those complex case is applying simulations using *LES* and *DES* methodologies.

3-1-2 Scale-resolving simulation methods

LES can be defined as a methodology that allows large eddies to be explicitly solved and small eddies are taken into account by a modelling technique (Smagorinsky [1963]). Most practical implementations of *LES* use the grid size as a filter size to define which turbulent scales are solved and which are unresolved and will be modelled, illustrated in Figure 3-2. An estimation of the size of turbulent scales to be solved follow the Kolmogorov's $-5/3$ power law (Kolmogorov [1941]). *SGS* and resolved sub-filter scales (*SFS*) are the two possible ways of modelling the unresolved scales, where *SGS* is the most common technique used. The resolution of *LES* simulation is higher compared to similar *RANS* cases, however computational time increases, as the number of grid points also increases.

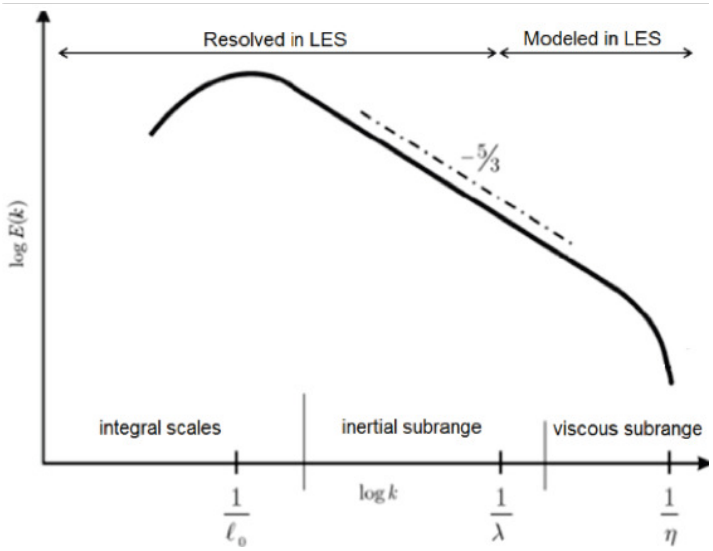


Figure 3-2: Distribution of resolved and modelled turbulent scales in a *LES* simulation.

DES is a hybrid methodology that combines both *RANS* and *LES* solutions in the same domain in order to solve the difficulties in near-wall regions when using pure *LES* methods (Spalart [1997]). Regions near solid boundaries and where the turbulent length scale is smaller than the maximum grid dimension are assigned the *RANS* methodology. The *LES* methodology is applied where the turbulent scales exceed the grid dimension and scales are explicitly solved. Different turbulence models can be combined for the *RANS* methodology, similar to the ones presented for pure *RANS* simulations.

The *DNS* is a methodology use to solve the Navier-Stokes equations without any turbulence model, consequently requiring to resolve the entire range of turbulent scales (Orszag [1970]). Resolving an entire range of turbulent scales implies resolving the Kolmogorov microscales up to the integral scales. The integral scales are related to the eddies motion which also have most of the kinetic energy. The Kolmogorov microscales are associated with the smallest dissipative scales and also define the minimum grid distance in a *DNS* simulation. Mesh requirements for *DNS* simulations are very demanding, requiring $Re^{9/4}$ grid points for a three-dimensional ($3D$) simulation and the required operations for the solution grows as Re^3, where Re is the Reynolds number (Pope [2001]). As a consequence of the extreme mesh

and operation requirements, *DNS* is currently not applicable for industrial complex geometry problems.

A methodology between *DNS* and *LES* methods is referred as uDNS/iLES. The uDNS/iLES methodology is characterized by solving the Navier-Stokes equations without any explicit subgrid-scale model. The mesh is not sufficient refined to resolve the full turbulent spectrum, mainly the smaller scales. Thus, the subgrid-scale modelling is left to numerical truncation error (Garnier et al. [1999]). This truncation error might turn the simulation unstable, specially at high Reynolds number as high-frequency modes appear on the solution.

For most iLES solution methods, alternatives to artificial dissipation schemes are used to stabilize the solution. The artificial dissipation schemes however might have excessive damping on the small scales, compromising subgrid effects accuracy (Adams and Hickel [2009]). Some proposals to improve the accuracy are presented by different schemes, such as flux-corrected transport method (FCT) (Grinstein and Fureby [2004]), adaptive local deconvolution method ($ALDM$) (Adams et al. [2004]) and spectral-vanishing viscosity (SVV) (Tadmor [1989] and Karamanos and Karniadakis [2000]) for spectral methods. Within this advances, uDNS/iLES prove to be a suitable option for high-fidelity simulations.

To summarize the most used simulation methodologies in CFD, we present a comparative chart in terms of turbulent scales solved in Figure 3-3.

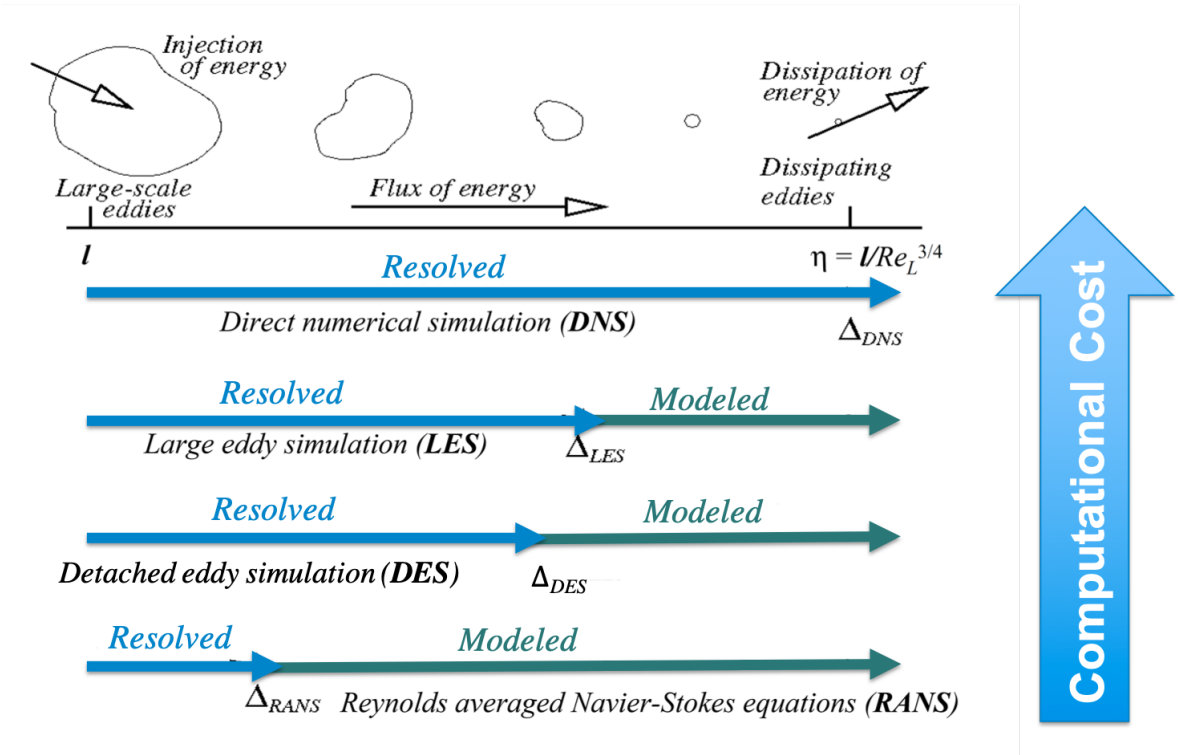


Figure 3-3: Summary of the most used numerical methods in CFD simulations in terms of resolved and modelled turbulent scales.

With the advancements of computing capability, an emerging trend in CFD methodology is the application of high-order methods, such as spectral/hp element methods. This dis-

cretisation takes advantage of the high accuracy and advantageous convergence properties of spectral (p) methods, while retaining the flexibility of the classical finite element (h) methods allowing complex geometries to be efficiently captured. It also provides an attractive higher-precision approximation to solve $PDEs$ and dissipation rates compatible to the one observed in experiments when compared to traditional solutions, reproducing better the flow features (Xu et al. [2018]). After decades of developments, significant progress has been made to its technological readiness. CFD software suites, such as Nektar++ (Cantwell et al. [2015]), have already made high-order spectral/hp element method widely accessible to a broader community of users.

We propose using the spectral/hp element method with an uDNS/iLES simulation for the computational studies performed in this research. The spectral/hp element method allows the use of relatively coarse mesh combined with a high-order polynomial. The high-order polynomial is used to adapt the coarse linear mesh to accurately reproduce the surface curvature of the object. The flow solution is approximated by a high-order polynomial, which can be changed, influencing the resolution of the simulation.

3-2 iLES simulations with half (symmetric) models for exterior aerodynamics

In Formula One and other motor sports, design iterations and improvements are required in the extremely time constrained schedule between races. This pushes the development of techniques and practices that would allow fast response in order to obtain reliable results in the required time. One of these common practices is the partial modelling of an symmetric on plane geometry, such as the exterior surface of most of road and race vehicles.

At the symmetry axis, symmetry boundary conditions need to be imposed to preserve the flow behaviour. The basic concept of the symmetry boundary condition is a set of zero flux constrains, with zero velocity and zero gradient of any flow quantity in the direction normal to this boundary. This is also known as an inviscid wall condition.

Such application of symmetry boundary conditions is widely used in the CFD simulation of racing, automotive and aeronautical industries. Makowski and Kim [2000] worked on the numerical aerodynamics simulation around an Ahmed body and other automotive geometries using $RANS$ methodology. The turbulence models employed for the $RANS$ methodology were $k - \epsilon$ and Reynolds stress model (RSM). Unstructured mesh for the half Ahmed body is presented in Figure 3-4, with a symmetry boundary condition imposed on the spanwise direction at the symmetry plane. The simulation of the half body was able to demonstrate all the salient flow features observed in the experiments on the full body.

Kapadia et al. [2004] performed CFD simulations on an Ahmed body with slant angle of 25° and 35° using DES and $RANS$ methodologies. Spalart-Allmaras turbulence model was selected and applied to both methodologies evaluated. Mesh was generated over half of the body for $RANS$ simulations, with symmetry boundary condition. Results indicated that for the half body, DES methodology still provided better agreement with experimental results. It is noted that for such unsteady methodologies, the symmetry boundary conditions must be applied at every instant.

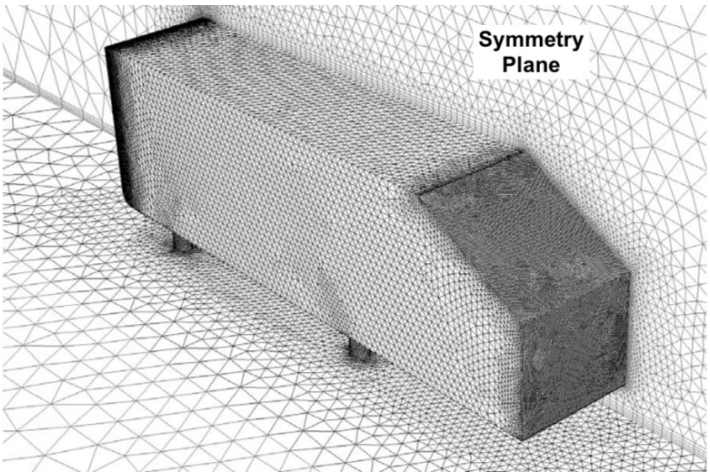


Figure 3-4: Surface mesh of Ahmed body with slant angle of 30°. Reproduction of Makowski and Kim [2000].

When applied to *LES* methods, special attention must be taken with the symmetry boundary conditions which could make the instantaneous flow result less accurate, as turbulence fluctuations are temporarily asymmetric (Schlüter [2004]). Schlüter [2004] performed a comparative study between *LES* jet simulations using symmetry boundary conditions. The influence of using this boundary condition was assessed, comparing with a full modelled domain for swirl and no-swirl conditions. Results indicated a remarkable computational cost improvement, however due to the error introduced, this approach is not suitable for swirl dominated flows. The error source is connected to the absence of the turbulence radial component, as the model used represents only 1/4 of the jet full domain. Thus, Schlüter [2004] highlights that this approach might be suitable for cases with low turbulence crossing the symmetry plane.

The study of the Ahmed body and many automotive geometries can be considered as such cases, when the information of interest is related to the average flow field. In an experimental study, Pagliarella [2009] investigated the wake behaviour at different positions downstream from the Ahmed body. Despite doing the experiment on a full model, the wake data was only presented for half of the model as in Figure 3-5. Although the author points out that the wake is slightly asymmetric in the spanwise direction, this influence can only be observed at $X/L = 1$. For all other planes closer to the slant, when averaging the flow, there are only negligible influences from the asymmetry.

Following the recommendation by Schlüter [2004] as well as based on our past experiences, we think that the influences of symmetry boundary conditions on *LES* simulations should not become an obstacle for external aerodynamics automotive applications when the averaged flow is desired. To verify this observation, we proposed to evaluate the symmetry boundary condition for an Ahmed body with slant angle of 25°, comparing with the full model approach.

Symmetry conditions are imposed on the mid-span of the body and we selected the spectral/hp element method (Chapter 5) to perform *iLES* simulations for both full and half model cases. The h-mesh uses same setting as the *Refined* case, combined with a polynomial of 6^{th} order is used for curvature representation as presented in Section 7-3-2. For the solution expansion, we considered a high-order polynomial of 6^{th} order accuracy.

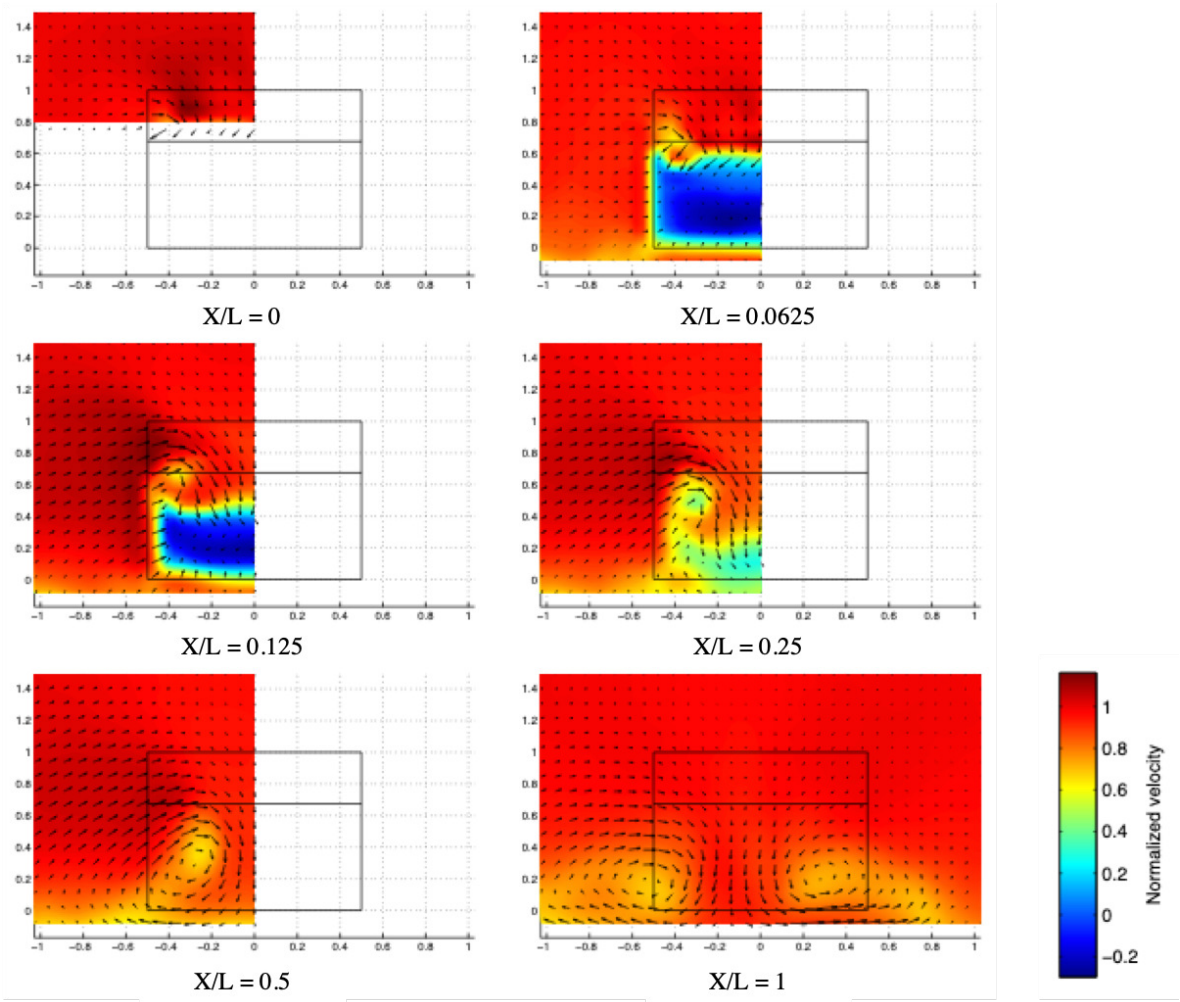


Figure 3-5: Contours of time-averaged normalised streamwise velocity U for planes downstream of the Ahmed body with slant angle of 25°. Reproduction from Pagliarella [2009].

Results for this study are presented under Section 7-3-3 in detail, where the mains findings in terms of flow structures, aerodynamic coefficients and computational time are discussed. In short, we have obtained very similar results for aerodynamic quantities (lift and drag coefficients) and the velocity field close to the body. Further downstream from the body, especially for V and W velocities, the effects of asymmetric flow features are becoming more noticeable. Since the design focus of automotive geometries are mainly related to the time-averaged flow features adjacent to the body, for fast design iterations, this level of accuracy is well suitable. In addition, as improving computational efficiency for a *LES* simulation is one of the key factors for promoting high-fidelity CFD simulations in a wider industry field, a computation time reduction of more than 50% (as shown in Section 7-3-3) can be very attractive.

Symmetric model is a very common practice in the automotive and racing industries as attested by the ten-year experience of the author. Applications of the symmetric vehicle models for aerodynamic quantity predictions can be found in a wide range of *RANS*, *DES* and *LES* simulation studies. We believe that the downside of implementing symmetry boundary conditions are mainly related to instantaneous flow behaviour, thus full model is required for complex turbulent-dependent calculations, such as aero-acoustics, as well as, for far wake analysis. Our observation is that the flow asymmetry close to the body are related to small scale turbulence crossing the symmetry plane, which will have very little influence in the averaged field of most vehicles. Based on the outcome of this comparative study, we have decided to employ the half body models for all simulations in this research, including the original Ahmed body (Chapter 7), the Ahmed body with diffuser (Chapter 8) and the Imperial front wing (Chapter 9).

Chapter 4

Main contributions and organization of the thesis

4-1 Main contributions

The main contributions of this research start by implementing the meshing generation procedure and simulation parameters configuration for an academic CFD code based on the spectral/hp element method to be applied on complex three-dimensional industrial applications. This is achieved by evaluating and developing meshing strategies and applying suitable stabilization techniques for spectral methods. Application of high-order methods for canonical problems are typically common but can be challenging for other geometries.

- Applying the continuous Galerkin spectral-vanishing viscosity (CG-SVV) method with discontinuous Galerkin (DG) mimicking kernel in 3D complex flow simulations. This allows, for the first time, high-Reynolds number simulation solution to be successfully computed with the spectral/hp element method. (Section 6-1)

- Development of suitable 3D meshing strategies for spectral/hp element method with uDNS/iLES, exploiting the flexibility of adjusting mesh and solution polynomial orders. This has led to efficient computations of high accuracy solution with significantly coarser mesh. (Section 6-2)

  - Exploited 3D mesh generation with Nekmesh (Section 6-2-3, with application in Part III), as well as a hybrid approach using Nekmesh together with other commercial mesh generator allowing highly complex geometries that are beyond the native capability of Nekmesh (Section 6-2-4, with application in Part IV).
  - Development of a guidance for initial mesh generation in terms of the number of required h-element and the choice of polynomial degrees of freedom.

The research presents a correlation study for the proposed methodology using a well-established automotive bluff body, the Ahmed body. The Ahmed body literature is widely available for results full comparison.

- Validating the performance of spectral/hp element method in bluff body geometry, showing good agreement in flow physics and aerodynamic quantities, when compared to previous wind-tunnel measurements and numerical simulations.
- For the first time with a fully 3D simulation, polynomial expansion of orders higher than 5^{th} for accuracy is implemented for representing the solution, showing benefits in improving the solution resolution for a given coarse mesh.
- Demonstrating that it is possible to exploit the symmetry property of geometries to execute LES simulations using half models, when the averaged flow characteristics are of interest for exterior aerodynamics analysis.

Following the correlation study, the next contribution is related to a parametric computational study on an Ahmed body equipped with underbody diffuser. Although this bluff body is being widely studied in the automotive community, this is the first study it is proposed with a simplified diffuser.

- The study presents drag and lift coefficient, as well as flow visualization results, which are subsequently used to characterize the flow. It can also be considered as a standard case for automotive applications, focusing on the underbody flow.
- Highlighting the development of a lower vortex near the underbody, and the influence of its trajectory by the presence of a diffuser.

The final contribution is to propose a new test case that considers a complex Formula one front wing geometry. Experimental measurements are performed to extract surface flow lines and velocity components on selected PIV planes downstream of the wing, tracking important vortical structures, critical in motor racing applications.

- Presented a novel benchmark case for race and automotive aerodynamics, with high-complex Formula One geometry.
- Comprehensive experimental data obtained in this research and made publicly available for validation of CFD codes.
- Demonstrate the benefit of spectral/hp element method in capturing the complex vortex system generated by the front wing elements, and maintain relative high resolution downstream, where classical CFD codes become increasing diffusive.
- Show that the workflow designed, as well as the toolchain selected and developed in this research project is capable of successfully handling complex geometries commonly found in industrial case studies.

4-2 Organization of the thesis

In this thesis, an introduction of road vehicles aerodynamics is first presented, presenting the first developments in automotive aerodynamics, the main concepts and the importance of the aerodynamics on road and race vehicles in connection with flow behaviour and drag and lift coefficients. As follows, the concept of wind tunnel tests in the automotive industry is presented, highlighting the main aspects and characteristics. The work follows by introducing some generic automotive bluff bodies, used as well-established test cases for automotive application. The Ahmed body is presented as the focus of this research and briefly described. Moving further, numerical methods for CFD simulations are presented, where the main methodologies used in the industry are discussed. The spectral/hp element method concept is introduced and its application for complex geometries and industrial CFD cases is highlighted as focus of this research. A study on the influence of using half model and symmetry boundary condition is presented in sequence.

A more rigorous discussion on spectral/hp element method is provided in the second part presents an introduction to the spectral/hp element method, presenting an introduction of the methodology, providing a comparison with classical methodologies. The methodology is applied in an example for solving a classical partial differential equation (PDE) the Helmholtz Equation, using the Galerkin method, setting its approximate solution. The next step presented is implementing this approximation using the spectral/hp element method, first defining the h-type discretization, then the p-type discretization.

The third part refers to the Ahmed body, in which an introduction with its main characteristics, geometry and literature review is presented. A correlation study follows, presenting a comparison between reference and current spectral/hp element techniques using the code Nektar++. The first correlation study focus on the Ahmed Body with slant angle of 25°, in which two mesh cases are proposed considering different h-refinements and evaluated in a combination of three high-order mesh schemes for curvature: 4^{th}, 5^{th} and 6^{th} order. Each of the six meshes proposed are three different polynomial orders expansion for the solution: 4^{th}, 5^{th} and 6^{th} order for accuracy, in a total set of eighteen load cases. Meshing and simulation setup are presented and discussed for each case. Results are compared in terms of drag and lift coefficient prediction, flow structures, velocity distribution and consistency with experimental results.

Following correlation studies, the next chapter concerns the investigation of mechanisms for drag and lift generation, flow characterization and surface topology by considering wake interactions between the backlight and diffuser. The rear underbody diffuser is defined and literature review on diffusers is summarized. The first Ahmed body study with diffuser is the Squared-back or 0° slant angle, followed by the 25° slant angle. The diffuser was designed to have the same dimension of the slant and six diffuser angles are proposed: 5°, 10°, 20°, 30°, 40° and 50°. Meshing and simulation setup are presented and discussed for each case. Results are compared in terms of drag and lift coefficient prediction, flow structures around the body and flow characterization on the diffuser region.

The final portion of this research relies on the application of spectral/*hp* method and the iLES-SVV solver methodology both proposed on Nektar++ to identify and characterize vortex intensity and wall shear stress on a real industrial case: The Imperial Front Wing - IFW. We discuss some references on Formula One front wings as well as previous experiments. Mov-

ing forward, we present the physical test definition, simulation setup and meshing strategy. Results are presented as comparison for Wall Shear Stress - WSS and plane velocity contours between updated experimental results also performed in this research and spectral/hp simulations proposed.

The thesis closes with general conclusions of the studies presented and presents suggestions for future and complementary work for this research.

Part II

Spectral/hp Method

Chapter 5

Spectral/hp method

This chapter provides a brief introduction to the most popular numerical methods used to solve Partial Differential Equations, highlighting the spectral/hp method. Then a solution for the PDEs based on the Galerkin Method with an implementation to one-dimensional ($1D$) problems for a single element, explaining the $h-type$ discretization and then the $p-type$ discretization. Once those concepts are established, it will be extended to two and three dimensions for quadrilateral/hexahedral and tri/tetrahedral elements, which are employed for this study.

The next topic is the application of the methodology to solve the Incompressible Navier-Stokes Equations, presenting the high-order splitting scheme. Following, we present stabilization techniques used on the spectral/hp element method for the solution of high Reynolds numbers problems such as the dealiasing and spectral-vanishing viscosity.

The last topic relies on the high-order mesh generation process for the spectral/hp element method, which can be fully created within the software pipeline or can convert a linear mesh from a third-part software.

5-1 Introduction

Considering the field of fluid dynamics, the most important differential equations are the Navier-Stokes. Numerical methods are widely used to find approximate solutions to differential equations and are basically divided into four major groups as suggested by Hoessler [2011] and shown in Figure 5-1; finite difference methods, finite volume methods, finite element methods and spectral methods. Due to their accuracy and exponential convergence properties, spectral methods have been used to simplify DNS and large eddy simulations. For complex geometries and relatively high Reynolds numbers cases, such as motorsports and other complex industrial problems, which imply the use of unstructured meshes, low order finite element or finite volume methods are currently preferred.

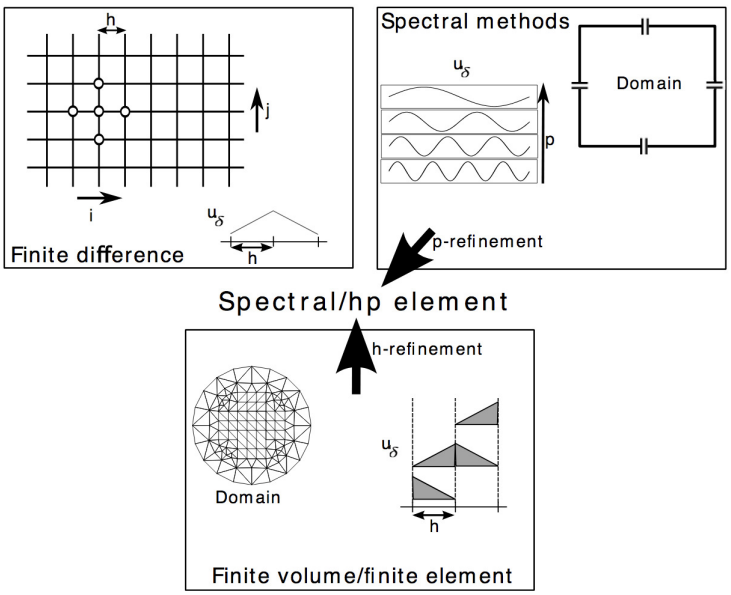


Figure 5-1: Schematic explaining the finite element, finite volume, finite difference and spectral methods and how both h and p refinements combine to form the spectral/hp element method Hoessler [2011].

In the spectral/hp element method, the domain is first divided into non-overlapping elements, in the same way as in the finite element method (FEM), so it offers geometric flexibility and allows for local refinement. The solution in each element is then approximated by high order polynomials, giving the method an exponential spatial convergence. The steps will be explained in the following chapters.

The present numerical study focuses on high fidelity simulation models applied to an Ahmed body at high Reynolds number. This study employs the code Nektar++ to solve the incompressible Navier-Stokes Equations in which an implicit LES simulation has been performed using a highly accurate spectral/hp method. The spectral/hp element method works as a combination of both FEM with spectral methods, giving the capability of handling complex geometries with high order accuracy. The solution using spectral/hp element method is stabilized by using dealiasing and spectral-vanishing viscosity techniques.

5-2 Partial differential equation solution - the Galerkin method

CFD software aims to solve a set of Partial Differential Equations or PDEs in order to find flow behaviour. Similar to Serson [2017] and Hoessler [2011], the Helmholtz Equation will be considered in order to demonstrate the method. The Helmholtz Equation is given by Equation (5-1).

$$\nabla^2 \boldsymbol{u} - \mu \boldsymbol{u} - \boldsymbol{f} = 0 \tag{5-1}$$

where $\boldsymbol{u}$ is the unknown, μ is a constant and $\boldsymbol{f}$ is the forcing term.

The objective is to obtain the solution $\boldsymbol{u}$ considering the domain Ω, under appropriate boundary conditions Γ. To have the exact solution of the equation, it would require the values of $\boldsymbol{u}$ for each point of the domain, which, from a numerical point of view, is impossible. Considering this limitation previously stated, the first step is to approximate $\boldsymbol{u}$ by a linear combination of a finite number of basis functions. We now have:

$$\boldsymbol{u}^{\delta} = \sum_{i=1}^{DOF_{total}} \hat{\boldsymbol{u}}^{i} \Phi^{i} \tag{5-2}$$

where $\boldsymbol{u}^{\delta}$ is the approximate solution, DOF_{total} is the number of degrees of freedom considered in the approximation, $\hat{\boldsymbol{u}}^{i}$ are the expansion coefficients and Φ^{i} are the basis functions.

In order to implement the boundary conditions of the equation, it is recommended to split the solution $\boldsymbol{u}^{\delta}$ into a part that satisfies the Dirichlet boundary condition, demoted by $\boldsymbol{u}^{D}$, where the basis functions are now zero. The second term $\boldsymbol{u}^{H}$ is a homogeneous solution, vanishing on those boundaries, leading to

$$\boldsymbol{u}^{\delta} = \boldsymbol{u}^{D} + \boldsymbol{u}^{H} \tag{5-3}$$

$$\boldsymbol{u}^{\delta} = \boldsymbol{u}^{D} + \sum_{i=1}^{DOF_{H}} \hat{\boldsymbol{u}}^{i} \Phi^{i} \tag{5-4}$$

with DOF_H the number of degrees of freedom on the boundary condition. Considering a given set of coefficients, $\boldsymbol{u}^{\delta}$ will not necessarily satisfy Equation (5-1). This will happen only if the exact solution is $\boldsymbol{u}^{\delta}$, and if it belongs to the function space spanned by the basis functions.

In order to obtain an approximate solution, once the exact solution is difficult to be obtained, a set of conditions to be imposed on $\boldsymbol{u}^{\delta}$, also defining the residual of Equation (5-1) by $\boldsymbol{R}(\boldsymbol{u}^{\delta}) = \nabla^2 \boldsymbol{u}^{\delta} - \mu \boldsymbol{u}^{\delta} - \boldsymbol{f}$, one set of conditions widely employed is denoted by

$$\int_{\Omega} \boldsymbol{R}(\boldsymbol{u}^{\delta}) \boldsymbol{v}^{j} \boldsymbol{d\Omega} = 0 \tag{5-5}$$

where $\boldsymbol{v}^{j}$ are the test functions, denoting the weighted residuals method. The choice of some specific test functions leads to different numerical methods.

The Galerkin method is used to denote the spectral/hp element method. Basically, the Galerkin method assumes the test functions to be the same as the basis functions denoted by Φ^{i}. Applying this concept to the Helmholtz Equation (5-1), it becomes:

$$\int_{\Omega} (\nabla^2(\boldsymbol{u}^{\delta}) - \mu(\boldsymbol{u}^{\delta}) - \boldsymbol{f}) \Phi^{j} \boldsymbol{d\Omega} = 0, 1 \leq j \leq N_{dof,H} \tag{5-6}$$

A determined system is obtained, since the index j should be considered in the whole range from 1 to $N_{dof,H}$, representing a set of $N_{dof,H}$ equations for $N_{dof,H}$ unknowns.

Applying the divergence theorem to Equation (5-6), in other to simplify, it becomes:

$$\int_{\Omega} \nabla \boldsymbol{u}^{\delta} \cdot \nabla \Phi^{j} + \mu \boldsymbol{u}^{\delta} \Phi^{j} \boldsymbol{d\Omega} = \int_{\Omega} -\boldsymbol{f} \Phi^{j} \boldsymbol{d\Omega} + \int_{\Gamma} \Phi^{j} \nabla \boldsymbol{u}^{\delta} \cdot \boldsymbol{n} \boldsymbol{dS} \tag{5-7}$$

where the last term of the equation, which can be obtained from the Neumann boundary conditions, vanishes on the boundaries with Dirichlet conditions. Replacing $\boldsymbol{u}^{\delta}$ by the definition on Equation (5-6), it is now possible to represent the equation into matrix form, such as:

$$(L + \mu M)\hat{u} = F \tag{5-8}$$

with the left-hand side of the equation being:

$$L_{ij} = \int_{\Omega} \nabla \Phi^{i} \cdot \nabla \Phi^{j} \boldsymbol{d\Omega} \tag{5-9}$$

$$M_{ij} = \int_{\Omega} \Phi^{i} \Phi^{j} \boldsymbol{d\Omega} \tag{5-10}$$

where L_{ij} is the weak Laplacian matrix and M_{ij} is the mass matrix. The right-hand side of the matrix equation is written as:

$$F_{j} = -\int_{\Omega} (\boldsymbol{f} \Phi^{j} + \nabla \boldsymbol{u}^{D} \cdot \nabla \Phi^{j} + \mu \boldsymbol{u}^{D} \Phi^{j}) \boldsymbol{d\Omega} + \int_{\Gamma} \Phi^{j} \nabla \boldsymbol{u}^{\delta} \cdot \boldsymbol{n} \boldsymbol{dS} \tag{5-11}$$

This section provides the tools to determine the approximate solution for a PDE. At this point, the type of trial functions to be used for the spatial decomposition of the domain has not been chosen and a single domain has been considered. The next step is the implementation to $1D$ problems.

5-3 One-dimensional implementation

Now that the approximate solution for a set of PDEs is set, it will be implemented for a 1-D problem considering the spectral/hp element method. In the spectral/hp element method, the computational domain is divided in non-overlapping elements, which is the classical h-type discretization presented in both finite element and finite volume element methods. The difference from the two previous methods to the spectral/hp is that the solution is represented by a high-order expansion inside each element. Major part of the operations is performed in the element level, with an assembly operation being used to obtain a global solution from these local expansions.

5-3-1 The h-type discretization

Considering the Helmholtz problem stated in Equation (5-1), the domain is subdivided into 3 non-overlapping finite elements, as in h-type discretization, which is illustrated in Figure 5-2. The division of the domain into 3 elements can be written as:

$$\Omega_{i} = \{x | x_{i} \leq x \leq x_{i+1}\} \quad i = 0...2 \quad \text{and} \quad \Omega = \cup_{i=0}^{i=2} \Omega_{i}, \cap_{i=0}^{i=2} \Omega_{i} = \emptyset \tag{5-12}$$

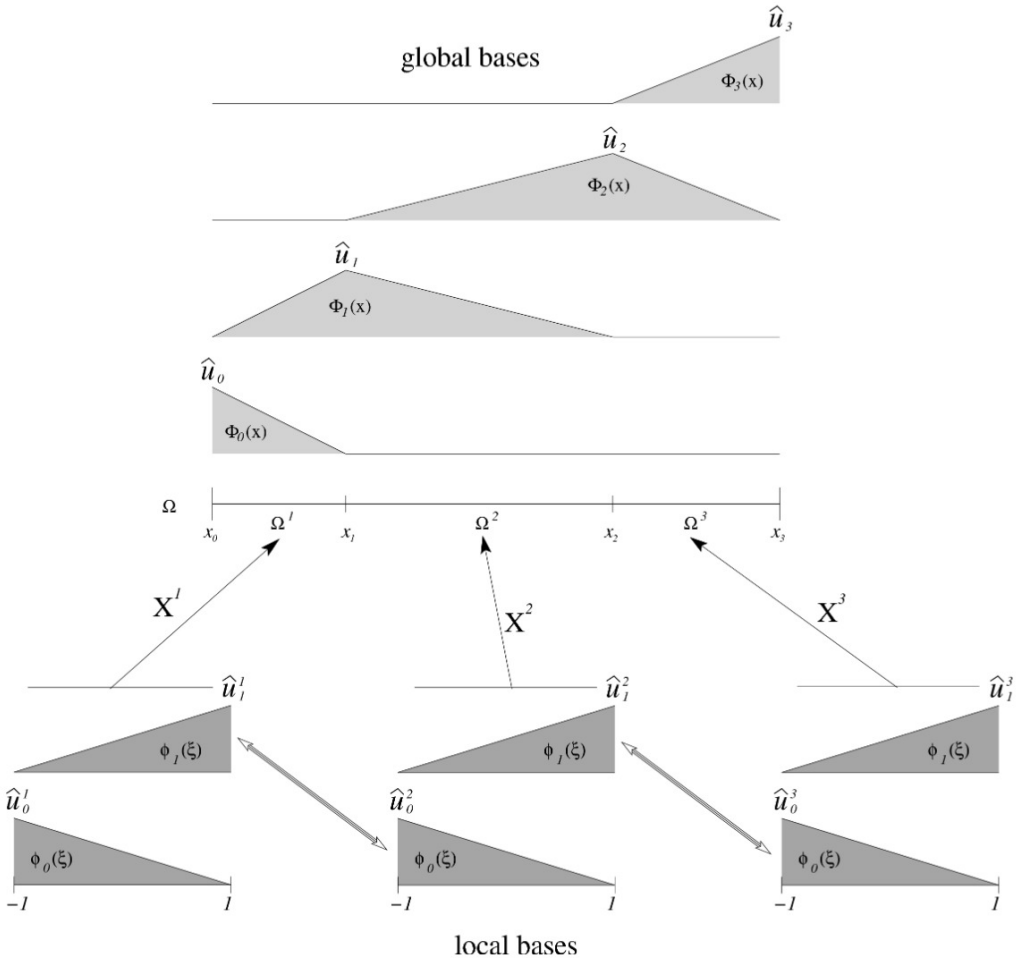


Figure 5-2: Local and global expansions coefficients for a three-element split of the calculus domain. Reproduction from Karniadakis and Sherwin [2013].

5-3-2 The p-type discretization

The next stage of the spectral/hp element method is to define a standard region $\Omega_{std} = \{\xi | -1 \leq \xi \leq 1\}$ which is mapped by a transformation function $\chi_i(\xi)$ in each physical element Ω_i. This step is necessary once the global expansion basis Φ_k is built from a combination of the local expansion modes ϕ_p defined within each of the elements with mode number $p \in \{0, \ldots, P_N\}$. P_N is the order of polynomial used for the element. For now, we first consider the case as illustrated in Figure 5-2 with $P_N = 1$.

The transformation functions can also be described as the mapping functions, as they express the global coordinates x as a function of the local coordinate ξ, as expressed for a one-dimensional case:

$$\forall x \in \Omega_i, x(\xi) = \chi_i(\xi) = \frac{1-\xi}{2}x_i + \frac{1+\xi}{2}x_{i+1}, \xi \in \Omega_{std} \tag{5-13}$$

The inverse mapping function expressing the local coordinates in terms of the global counterparts is:

$$\forall \xi \in \Omega_{std}, \xi(x) = \chi_i^{-1}(x) = 2\frac{x - x_i}{x_{i-1} - x_{i+1}} - 1, x \in \Omega_i \tag{5-14}$$

A local expansion basis can be defined as $\phi_p = \phi_p(\xi)$ within the standard region Ω_{std}. The basis chosen, in order to match with notations of Figure 5-2, is a first-order polynomial expansion defined as:

$$\phi_p(\xi) = \begin{cases} \frac{1-\xi}{2} & \text{for } p = 0 \\ \frac{1+\xi}{2} & \text{for } p = 1 \end{cases} \tag{5-15}$$

with the local basis functions of zero value outside the element considered. Expressing the mapping defined in Equation (5-13) by means of the local expansion basis, it becomes:

$$\forall x \in \Omega_i, x(\xi) = \phi_0(\xi) + \phi_1(\xi)x_{i+1} \tag{5-16}$$

After calculating for a single element, it's possible to generalise the process to all the elements in the domain. The global expansion basis Φ_k is expressed in terms of the local expansions to approximate a function u by u_δ along the domain Ω:

$$u^\delta(x) = \sum_{i=0}^{DOF_{total}-1} \hat{u}_i \Phi_i(x) = \sum_{e=0}^{2} \sum_{p=0}^{1} \hat{u}_p^e \phi_p^e(\xi) \tag{5-17}$$

where $\hat{u}_i$ and $\hat{u}_p^e$ are respectively the global and local coefficients of the expansion. The number of global degrees of freedom (DOF_{total}) is lower than the number of local degrees of freedom, as seen in Figure 5-2. This is due to the C^0 continuity enforced at x_1 and x_2.

5-3-3 Local expansion basis

Accuracy of the approximation and numerical efficiency are the most important properties when selecting a high-order expansion basis. In the calculations, the conditions which require the matrix inversion directly affect the accuracy as well as the efficiency of iterative inversion techniques. In order to simplify this procedure, the expansion bases are selected such that they are orthogonal. Hierarchical schemes also facilitate efficient computations due to their ability to allow for adaptive operations.

Expansion bases are generally classified as nodal or modal. Nodal expansions evaluate the approximate solution at a fixed set of points, or nodes, inferring that the unknown coefficients $\hat{u}_i$ have a physical meaning and are the values at these nodes. Nodal expansion bases, like the Lagrange Polynomials, are not hierarchical as stated by Karniadakis and Sherwin [2013].

In order to describe the concept of modal expansion, the concept is introduced for one-dimension cases. The expansion basis is formed from Jacobi polynomials such as $P_p^{\alpha,\beta}(x)$, which are a family of solutions of the singular Sturm-Liouville problem as follows:

$$\forall x \in]-1,1[, \frac{d}{dx}[(1-x)^{1+\alpha}(1+x)^{1+\beta}\frac{d}{dx}P_p^{\alpha,\beta}(x)] = \lambda_p(1-x)^{\alpha}(1+x)^{\beta}P_p^{\alpha,\beta}(x) \tag{5-18}$$

where α and β two constants, and $\lambda_p = -p(\alpha+\beta+p+1)$. This type of polynomial satisfies the following orthogonality condition:

$$\int_{-1}^{1}(1-x)^{\alpha}(1+x)^{\beta}P_p^{\alpha,\beta}(x)P_q^{\alpha,\beta}(x)dx = C\delta_{pq}, \text{ for } q<p \tag{5-19}$$

where δ_{pq} is the Kronecker delta. This implies that, when integrated with respect to the function $(1-x)^{\alpha}(1+x)^{\beta}$, $P_p^{\alpha,\beta}$ is orthogonal to all polynomials of order less than p. The Legendre and Chebyshev polynomials are subsets of the family of Jacobi polynomials, for $\alpha=\beta=0$ for Legendre and $\alpha=\beta=-1/2$ for Chebyshev polynomials.

The spectral/hp element allows the boundary interior decomposition, a concept that divides the basis into boundary and interior elements, which are respectively unity at the element boundaries and are zero at the boundaries. These conditions allow C^0 continuity to be imposed at the interface between elements and also keeps most of the orthogonality. Generalising the modal expansion defined in Equation (5-15) to higher order, i.e. with $P_N > 1$, one possibility would be:

$$\psi_p(\xi) = \begin{cases} \frac{1-\xi}{2} & \text{for } p=0 \\ \frac{1-\xi}{2}\frac{1+\xi}{2}P_{p-1}^{1,1}(\xi) & \text{for } 0<p<P_N \\ \frac{1+\xi}{2} & \text{for } p=P_N \end{cases} \tag{5-20}$$

where $\psi_p(\xi)$ is a modified principal function $\phi_p(\xi)$ as proposed by Karniadakis and Sherwin [2013].

This expansion is illustrated for $P_N = 5$ in Figure 5-3. As previously stated, this basis is hierarchical and contains the first order base defined in Equation (5-15). Under the boundary interior decomposition principle, the modes $p=0$ and $p=P_N$ are boundary modes and the remaining are interior modes. These bases will now be generalised to multiple dimensions.

5-4 Multiple-dimensional implementation

After outlining the expansion basis for one-dimensional ($1D$) cases, these concepts are extended to multiple dimensions. The expansion bases are extended basically to two and three-dimensional (*2D* and *3D*) standard regions. The local expansion bases are extended for quadrangle and triangles in two-dimensions and into hexahedron and tetrahedron for the three-dimensional elements as they are employed in this research.

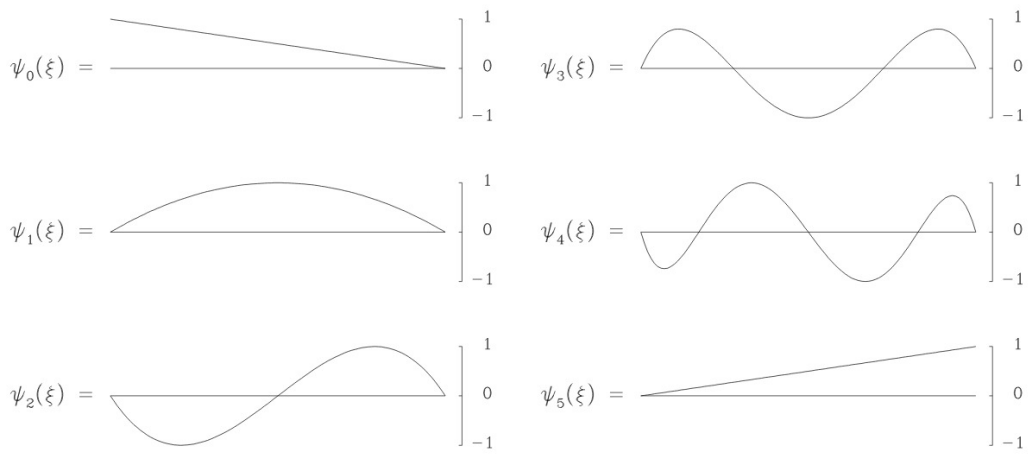


Figure 5-3: Modal expansion shape function as defined in Equation (5-20) for a polynomial order $P_N = 5$. Reproduction from Karniadakis and Sherwin [2013].

5-4-1 Quadrilateral *2D* elements and hexahedral *3D* elements

The extension to quadrangles and hexahedral elements from the basis presented in Equation (5-20) is relatively straightforward. The standard regions Q^{2D}_{std} for *2D* quadrilateral elements and Q^{3D}_{std} for *3D* hexahedral elements are defined:

$$Q^{2D}_{std} = \{(\xi_1, \xi_2) | -1 \leq \xi_1, \xi_2 \leq 1\} \tag{5-21}$$

$$Q^{3D}_{std} = \{(\xi_1, \xi_2, \xi_3) | -1 \leq \xi_1, \xi_2, \xi_3 \leq 1\} \tag{5-22}$$

where ξ_i generates a Cartesian coordinate system in two-dimensions for $i = 2$ and three-dimensions for $i = 3$. The corresponding *2D* and *3D* expansion bases $\phi_{pq}(\xi_1, \xi_2)$ and $\phi_{pqr}(\xi_1, \xi_2, \xi_3)$ can be formed as the tensor product of one dimensional expansion bases. This is defined in Equation (5-20) along each coordinate ξ_i, as follows:

$$\phi_{pq}(\xi_1, \xi_2) = \phi_p(\xi_1)\phi_q(\xi_2), \text{ for } 0 \leq p \leq P_{N,1}, 0 \leq q \leq P_{N,2} \tag{5-23}$$

$$\phi_{pqr}(\xi_1, \xi_2, \xi_3) = \phi_p(\xi_1)\phi_q(\xi_2)\phi_r(\xi_3), \text{ for } 0 \leq p \leq P_{N,1}, 0 \leq q \leq P_{N,2}, 0 \leq r \leq P_{N,3} \tag{5-24}$$

with $P_{N,i}$ the expansion orders along each dimension for a i dimensional problem.

5-4-2 Triangular *2D* elements and tetrahedral *3D* elements

Due to the geometric complexity of a lot of industrial problems, triangles or tetrahedral elements offer greater flexibility for the mesh generation. First proposed by Sherwin and Karniadakis [1995], the triangular element expansion basis requires a new standard region and a new coordinate system η_i, related to the Cartesian coordinates system ξ_i following this new mapping function

$$\eta_1 = 2\Big(\frac{1-\xi_1}{1-\xi_2}\Big) - 1, \eta_2 = \xi_2 \tag{5-25}$$

$$\Omega^T_{std} = \{(\eta_1, \eta_2) | -1 \leq \eta_1, \eta_2 \leq 1\} \tag{5-26}$$

The mapping defined by Equations 5-25 and 5-26 collapses the standard quadrilateral region into a unit triangle and (η_1, η_2) are hence described as the collapsed coordinates, illustrated in Figure 5-4.

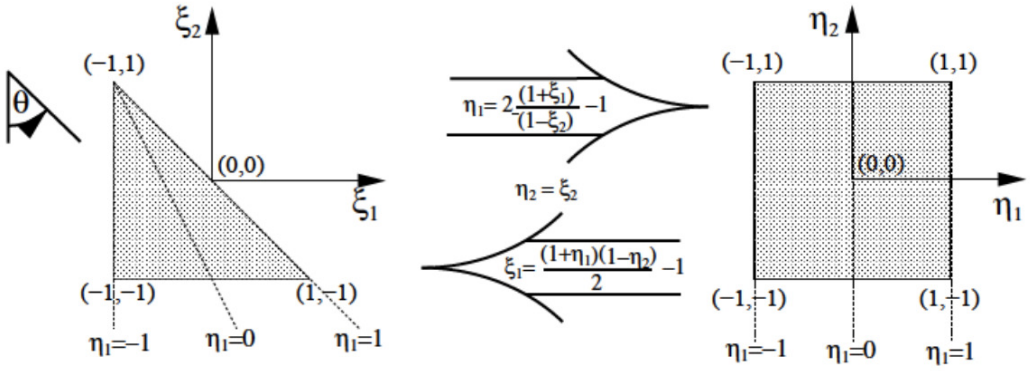


Figure 5-4: Mapping of a standard quadrangle to a standard triangle. Reproduction from Karniadakis and Sherwin [2013].

The boundary interior decomposition must be kept and in order to do so, the expansion basis cannot directly be obtained by a tensor product of principal functions. It must be the product of a one-dimensional tensor $\psi_p(\eta_1(\xi_1, \xi_2))$ with a two-dimensional tensor $\psi_{pq}(\eta_2(\xi_2))$. As previously presented, these two tensors are the modified principal functions. The bi-dimensional expansion $\phi_{pq}(\xi_1, \xi_2)$ on the standard region Ω^T_{std} is shown in Figure 5-5.

The previous formulation defined the triangular element in the collapsed coordinate system. Extending this to the tetrahedral element, the standard region can be defined for the same

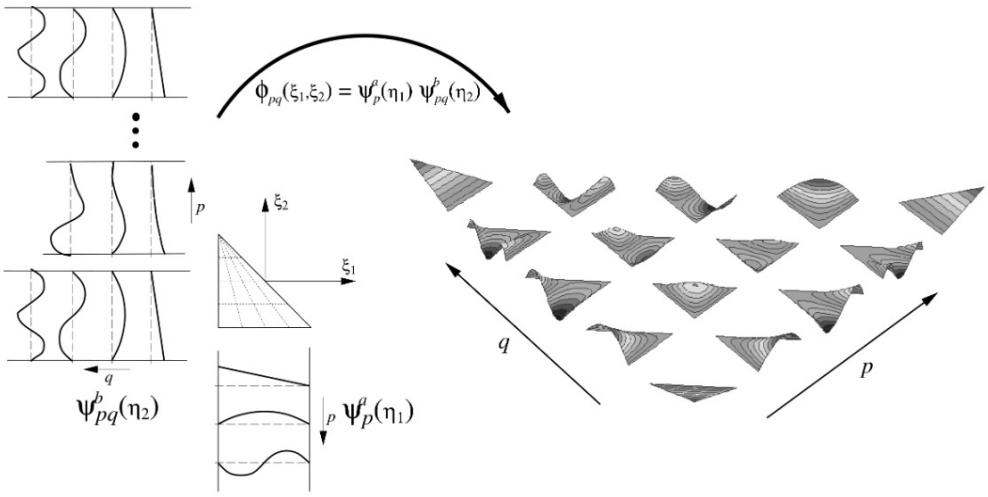


Figure 5-5: Construction of a fourth order ($P_N = 4$) triangular expansion using the product of two modified principal functions $\psi_p(\eta_1(\xi_1, \xi_2))$ and $\psi_{pq}(\eta_2(\xi_2))$, reproduction from Karniadakis and Sherwin [2013] and Hoessler [2011].

collapsed coordinate system as:

$$\eta_1 = 2\Big(\frac{1+\xi_1}{-\xi_2-\xi_3}\Big) - 1 \tag{5-27a}$$

$$\eta_2 = 2\Big(\frac{1+\xi_2}{1-\xi_3}\Big) - 1 \tag{5-27b}$$

$$\eta_3 = \xi_3 \tag{5-27c}$$

The local 3D expansion basis $\phi_{pqr}(\xi_1, \xi_2, \xi_3)$ can be defined in terms of the modified principal functions $\phi_p(\eta_1(\xi_1, \xi_2, \xi_3))$, $\psi_{pq}(\eta_2(\xi_2, \xi_3))$ and $\psi_{pqr}(\eta_3(\xi_3))$ and further details are found in Karniadakis and Sherwin [2013].

5-5 Mesh element mapping

It is required a mapping between physical element Ω_i and the standard region Ω_{std} when using the spectral/hp element method. We will first define the function of a 2-D straight-sided quadrangular element to be mapped back to the standard square region. The standard square region is defined by $(\xi_1, \xi_2) \in [-1, 1]^2$ and its mapping is:

$$\begin{aligned}\chi(\xi_1,\xi_2) = &\frac{(1-\xi_1)(1-\xi_2)}{4}\mathrm{x}^1 + \frac{(1+\xi_1)(1-\xi_2)}{4}\mathrm{x}^2 \\ &+\frac{(1-\xi_1)(1+\xi_2)}{4}\mathrm{x}^3 + \frac{(1+\xi_1)(1+\xi_2)}{4}\mathrm{x}^4\end{aligned} \tag{5-28}$$

For high-order elements with known curved edges, the mapping of each can be represented by a function $f^{kn}(\xi_i)$, where kn represents each curve edge. Proving that these mappings are consistent at the edges, Gordon and Hall [1973] proposed the following blending function to define the elemental mapping:

$$\begin{aligned}\chi(\xi_1,\xi_2) = f^{k1}(\xi_1)\frac{(1-\xi_2)}{2} + f^{k3}(\xi_1)\frac{(1+\xi_2)}{2} + f^{k4}(\xi_2)\frac{(1-\xi_1)}{2} + f^{k2}(\xi_2)\frac{(1+\xi_1)}{2} \\ -f^{k1}(-1)\frac{(1-\xi_1)(1-\xi_2)}{4} - f^{k1}(1)\frac{(1+\xi_1)(1-\xi_2)}{4} \\ -f^{k3}(-1)\frac{(1-\xi_1)(1+\xi_2)}{4} - f^{k3}(1)\frac{(1+\xi_1)(1-\xi_2)}{4}\end{aligned} \tag{5-29}$$

We now present the application of the spectral/hp element method to solve the incompressible Navier-Stokes equations, applied to all simulations in this research.

5-6 Incompressible Navier-Stokes equation

After considering the spectral/hp spatial discretization on the domain, it's necessary to define a time integration scheme to fully solve the problem, since the equations considered are time dependant. For this work, the focus is to solve the unsteady Navier-Stokes Equations considering an incompressible flow over complex automotive geometries and bluff body. Nektar++ has several modules and the one used is the incompressible Navier-Stokes solver, which allows the solution of the governing Navier-Stokes equations. The momentum and continuity equations are presented (Equation (5-30a)) as follows:

$$\frac{\partial \boldsymbol{u}}{\partial t} = -(\boldsymbol{u}\cdot\nabla)\boldsymbol{u} - \nabla p + \nu\nabla^2\boldsymbol{u} \tag{5-30a}$$

$$\nabla\cdot\boldsymbol{u} = 0 \tag{5-30b}$$

where $\boldsymbol{u}$ is the velocity, p is the specific pressure (including density) and ν the kinematic viscosity. Given a reference length L and a reference velocity U, the Reynolds number can be written as $Re = \frac{LU}{\nu}$.

The Navier-Stokes Equations need to be solved in the domain Ω, subject to an initial condition $\boldsymbol{u}^0$ and to the following boundary conditions:

$$\boldsymbol{u} = \boldsymbol{u}_{\mathfrak{D}} \text{ on } \Gamma_{\mathfrak{D}} \tag{5-31a}$$

$$\frac{\partial \boldsymbol{u}}{\partial n} = \boldsymbol{u}_{\mathfrak{N}} \text{ on } \Gamma_{\mathfrak{N}} \tag{5-31b}$$

where $\Gamma_{\mathfrak{D}}$ is the the boundary region where Dirichlet boundary conditions are imposed on the velocity, while on $\Gamma_{\mathfrak{N}}$ the Neumann boundary conditions are imposed.

In order to abbreviate the equations, the convective and viscous terms are defined as:

$$\boldsymbol{N}(\boldsymbol{u}) = -(\boldsymbol{u} \cdot \nabla)\boldsymbol{u} \tag{5-32}$$

$$\nu \boldsymbol{L}(\boldsymbol{u}) = \nu \nabla^2 \boldsymbol{u} \tag{5-33}$$

The momentum Equation (5-30a) now becomes:

$$\frac{\partial \boldsymbol{u}}{\partial t} = -\boldsymbol{N}(\boldsymbol{u}) - \nabla p + \nu \boldsymbol{L}(\boldsymbol{u}) \tag{5-34}$$

5-6-1 High-order splitting Scheme

In the original approach of Karniadakis et al. [1991], a stiffly-stable time integration was proposed which was then later fully re-analysed in the work of Guermond and Shen [2003]. A high-order splitting scheme was originally proposed in three steps involving explicit advection of the non-linear terms, followed by the solution of the pressure Poisson system and finally the solution of a Helmholtz problem to enforce the viscous terms and velocity boundary conditions. The non-linear advection terms are treated explicit via an Adam-Bashforth-type approximation of order J_e. Diffusion terms implicit considering an Adam-Moulton family of integration order J_i, in order to avoid very low time step and numerical stability issues.

The first step to solving this problem is to discretise the momentum equation in time by approximating the time derivative by a backward differentiation formula (BDF) and by representing the convective term using a polynomial extrapolation from the previous time-steps. Using these approximations, the momentum equation at time-step $n+1$ is now:

$$\frac{\tilde{c}_0 \boldsymbol{u}^{n+1} - \sum_{q=0}^{J_i-1} \tilde{a}_q \boldsymbol{u}^{n-q}}{\Delta t} = \sum_{q=0}^{J_e-1} \tilde{b}_q \boldsymbol{N}(\boldsymbol{u}^{n-q}) - \nabla p^{n+1} + \nu \boldsymbol{L}(\boldsymbol{u}^{n+1}) \tag{5-35}$$

where J_e and J_i are the integration orders of the explicit and implicit terms, previously mentioned, respectively, and the coefficients $\tilde{a}$, $\tilde{b}$ and $\tilde{c}$ for orders up to 3 are presented in table 5-1.

Table 5-1: Coefficients for stiffly-scheme time integration.

Coefficient	1^{st} order	2^{nd} order	3^{rd} order
$\tilde{a}_0$	1	2	3
$\tilde{a}_1$	0	-1/2	-3/2
$\tilde{a}_2$	0	0	1/3
$\tilde{b}_0$	1	2	3
$\tilde{b}_1$	0	-1	-3
$\tilde{b}_2$	0	0	1
$\tilde{c}_0$	1	3/2	11/6

To simplify Equation (5-35), it is presented the following summations definitions:

$$\sum_{q=0}^{J_i-1} \tilde{a}_q \boldsymbol{u}^{n-q} = \boldsymbol{u}^+ \tag{5-36}$$

$$\sum_{q=0}^{J_e-1} \tilde{b}_q \boldsymbol{N}(\boldsymbol{u}^{n-q}) = \boldsymbol{N}^* \tag{5-37}$$

The new arrangement of Equation (5-35) is now:

$$\frac{\tilde{c}_0 \boldsymbol{u}^{n+1} - \boldsymbol{u}^+}{\Delta t} = \boldsymbol{N}^* - \nabla p^{n+1} + \nu \boldsymbol{L}(\boldsymbol{u}^{n+1}) \tag{5-38}$$

To solve the Equation (5-38), Karniadakis et al. [1991] propose to split the right-hand-side of the equation into three steps demonstrated as follow:

$$\frac{\hat{\boldsymbol{u}} - \boldsymbol{u}^+}{\Delta t} = \boldsymbol{N}^* \tag{5-39a}$$

$$\frac{\hat{\hat{\boldsymbol{u}}} - \hat{\boldsymbol{u}}}{\Delta t} = -\nabla p^{n+1} \tag{5-39b}$$

$$\frac{\tilde{c}_0 \boldsymbol{u}^{n+1} - \hat{\hat{\boldsymbol{u}}}}{\Delta t} = \nu \boldsymbol{L}(\boldsymbol{u}^{n+1}) \tag{5-39c}$$

where $\hat{\boldsymbol{u}}$ and $\hat{\hat{\boldsymbol{u}}}$ are intermediate fields. When applying the spatial discretization, the first step would lead to a projection problem, which can be costly since it requires the inversion of the global mass matrix. The analytical expression for $\hat{\boldsymbol{u}}$ is substituted in the second equation, so the first step only involves the direct calculation of $\hat{\boldsymbol{u}}$ in the physical space, without performing the projection to the solution space.

In the previous formulation, the pressure gradient is rewritten as the discrete gradient between two consecutive time steps and expressed by:

$$\nabla p^{n+1} = \frac{1}{\Delta t} \int_{t_n}^{t_{n+1}} \nabla p dt \tag{5-40}$$

Returning to the second step, the pressure is then calculated by taking the divergence of the equation and imposing a condition in which $\nabla \cdot \hat{\hat{\boldsymbol{u}}} = 0$, that becomes:

$$\nabla^2 p^{n+1} = \nabla \cdot (\frac{\hat{\boldsymbol{u}}}{\Delta t}) \tag{5-41}$$

We conclude that Equation (5-41) is a Poisson Equation that requires appropriate boundary conditions. Karniadakis et al. [1991] proposed a pressure boundary condition denoted by:

$$\frac{\partial p^{n+1}}{\partial \boldsymbol{n}} = \boldsymbol{n} \cdot [\boldsymbol{N}^* - \nu(\nabla \times \nabla \times \boldsymbol{u})^*] \tag{5-42}$$

Finally, once the pressure is retrieved from Equation (5-41) and the third and last step is a Helmholtz Equation for the velocity, which can be solved by the same methodology presented on Section 5-2.

With respect to solution stability, further stabilisation techniques need to be introduced - for example, spectral-vanishing viscosity (SVV) - in order to damp erroneous solution oscillations. The novel solution stabilization techniques are presented in next section.

5-7 Spectral dealiasing

On spectral methods, a common source of instability is the aliasing effects arising from the non-linearity of the underlying problem. The aliasing error for the Navier-Stokes Equations appears when handling its quadratic non-linearity term by using the Gauss integration order Q similar to the solution polynomial order P as stated by Kirby and Karniadakis [2003]. This is usually present in simulations considering under-resolved turbulence, such the iLES (also called uDNS), which leads to a significant error increment in high-frequency modes of the solution and cause it to diverge. To avoid those, we employed a quadrature order consistent with the polynomial order of the expansion and non-linearities of the equation.

For complex curved geometries, such the IFW and the frontal part of the Ahmed body both studied in this work, where we have non-linear geometry deformation, we also must be mindful of aliasing effects, arising from the geometric mapping. The projection of a standard element into the Cartesian space, taken by the Jacobian of the isoparametric mapping, is a non-constant, non-linear polynomial for curved elements, introducing another aliasing source called geometrical aliasing. The geometrical aliasing can corrupt the solution in a similar manner as the aliasing of the non-linearity of the PDE and eventually increase the overall degree of the non-linearity. Currently implemented dealiasing technique used is based on the work of Mengaldo et al. [2015] where we refer the reader for more details.

Although the dealiasing techniques alone are not always capable of stabilizing the solution, they are important as they potentially improve the accuracy of the solution by consistently integrating the non-linear terms. They also allow reduction of the amount of SVV used in the simulation, since it can have a significant impact on the accuracy of under resolved simulations and is discussed in the next chapter.

Chapter 6

Stabilization Techniques and Meshing Strategy

Despite decades of development, directly implementing the spectral/hp element method for a 3D simulation of complex geometries at high Reynolds number is still very challenging. A key aspect is to stabilize the solution within the high frequency modes so that numerical errors do not grow unbounded causing the scheme to diverge. A commonly used technique to stabilize the solution for spectral/hp element method is SVV, introducing artificial dissipation to the smallest scales of the solution. The fundamental concept of SVV, together with the latest development using the discontinuous Galerkin (DG) mimicking kernel is presented in Section 6-1.

Another important aspect is the meshing strategy. Conventional workflow and design traditions developed for h-type meshes are found unsuitable for spectral/hp element method, which has the extra flexibility in changing the polynomial orders for the geometry mesh as well as for the solution representation. The guidelines presented in Section 6-2 is specifically developed to address this issue, allowing the benefit of spectral/hp element method to be fully exploited.

6-1 Spectral-vanishing viscosity - SVV

High-order methods present low numerical diffusion, as discussed by Karniadakis and Sherwin [2013] and simulations with marginal spatial resolution become numerically unstable, especially in the presence of turbulence at high Reynolds numbers, condition in which most of engineering problems are. The spectral-vanishing viscosity (SVV) is a technique that adds artificial dissipation to the smallest scales of the solution and this modern strategy has been proven to effectively stabilise the simulation.

The SVV technique was first proposed by Tadmor [1989] as a stabilisation technique for classical spectral methods in Fourier space. Essentially, an artificial diffusion term is added

to the governing equations. The fundamental idea behind is that the SVV dissipation can be set to affect mainly the polynomial modes of highest order in each element. The high-frequency polynomial modes comprise the most oscillatory part of the solution and represent the smallest turbulent scales captured by the DOFs employed in the solution.

Within the implicit LES (iLES) context, SVV has been used in place of an explicit turbulence model. The assumption arises from the fact that the action of subgrid scales on the resolved scales is equivalent to strictly dissipative effect. Even though the SVV operator is not explicitly designed as a subgrid-scale model, this concept is widely adopted inside the CFD community.

The present work considers a relatively high Reynolds number of approximately $Re = 1.7 \times 10^6$, consequently the SVV is a significant enabler of simulations of this type. We will present the concept of the SVV, with different approximation. The SVV operator proposed by Moura et al. [2017] is used for the spectral/hp element method simulations in this work.

6-1-1 SVV operator concept

The main idea of SVV consists in expanding the Navier-Stokes Equations to include an artificial dissipation operator, leading to:

$$\frac{\partial \boldsymbol{u}}{\partial t} = -(\boldsymbol{u} \cdot \nabla)\boldsymbol{u} - \nabla p + \nu \nabla^2 \boldsymbol{u} + S_{VV}(\boldsymbol{u}) \tag{6-1a}$$

$$\nabla \cdot \boldsymbol{u} = 0 \tag{6-1b}$$

and the original operator SVV is:

$$S_{VV}(\boldsymbol{u}) = \epsilon \sum_{i=1}^{N_{dim}} \frac{\partial}{\partial x_i}[Q_i * \frac{\partial u}{\partial x_i}] \tag{6-2}$$

with N_{dim} being the spatial dimension of the problem, ϵ a constant coefficient, and $*$ representing the application of the filter Q_i through a convolution operation. The implementation of SVV depends on obtaining the matrix form of the operator from Equation (6-2), and defining the filter Q_i. Once the SVV matrix is obtained, it can be incorporated into the velocity-correction scheme by adding it to the Laplacian matrix in the solution of the velocity fields. The work of Kirby and Sherwin [2006] shows that the SVV operator in a single element can be obtained by:

$${S_{VV}}^e = \epsilon \sum_{i=1}^{N_{dim}} \tilde{\boldsymbol{S}_i^T} \hat{\boldsymbol{Q}} \boldsymbol{M}^{-1} \tilde{\boldsymbol{S}_i} \tag{6-3}$$

with $\tilde{\boldsymbol{S}_i}$ being

$$\tilde{\boldsymbol{S}_i} = \tilde{\boldsymbol{B}^T} \boldsymbol{W} \boldsymbol{D}_i \boldsymbol{B} \tag{6-4}$$

where for quadrilateral elements the matrices with a tilde correspond to the basis formed by the tensor product of Legendre polynomials, while the other matrices correspond to the basis employed in the solution.

For Equations 6-3 and 6-4, $\boldsymbol{M}$ is the mass matrix, $\boldsymbol{W}$ is a diagonal matrix containing the quadrature weights, $\boldsymbol{B}$ contains the values of the basis functions at the quadrature nodes, $\boldsymbol{D}_i$ is the matrix representing numerical differentiation in the i^{th} direction, $\hat{\boldsymbol{Q}}$ represents the filter in modal space, and $\tilde{\boldsymbol{B}}$ is the analogous of $\boldsymbol{B}$ using a basis formed by the tensor product of Legendre polynomials.

Although the matrices $\tilde{\boldsymbol{B}}$ and $\tilde{\boldsymbol{M}}$ could correspond to any polynomial basis spanning the same space as the one representing the solution, one of the motivations for using the Legendre basis is to make the operator symmetric positive-definite, similarly to the original Laplacian operator, as demonstrated in Kirby and Sherwin [2006]. However, this is only true when $\tilde{\boldsymbol{M}}$ is diagonal, which is only true if the element h as a constant Jacobian.

For elements that do not satisfy this previous condition, the diagonal nature of the mass matrix, which corresponds to the tensor-product of Legendre basis, can be recovered by projecting this basis in the standard element. The projection, however, breaks the symmetry of the operator because the quadrature weights for this operation would be different. To understand this last point, we denote the quadrature weights in the standard element as $\boldsymbol{W}_{std}$, and thus the full form of the operator in this case becomes:

$$S_{VV}{}^{e} = \epsilon \sum_{i=1}^{N_{dim}} (\tilde{\boldsymbol{B}}^T \boldsymbol{W} \boldsymbol{D}_i \boldsymbol{B})^T \hat{\boldsymbol{Q}} (\tilde{\boldsymbol{B}}^T \boldsymbol{W}_{std} \tilde{\boldsymbol{B}})^{-1} (\tilde{\boldsymbol{B}}^T \boldsymbol{W}_{std} \boldsymbol{D}_i \boldsymbol{B}) \tag{6-5}$$

Although in this case the mass matrix $\tilde{\boldsymbol{B}}^T \boldsymbol{W}_{std} \tilde{\boldsymbol{B}}$ is diagonal, the operator is not symmetric because the terms in the first and last brackets use different forms of $\boldsymbol{W}$. To recover the symmetry of the operator, the previous formulation was modified using the element Jacobian. By noting that $\boldsymbol{W} = \boldsymbol{J}\boldsymbol{W}_{std}$, where $\boldsymbol{J}$ is the diagonal matrix with the absolute value of the Jacobian in the quadrature points, we can obtain a symmetric positive-definite operator by using:

$$S_{VV}{}^{e} = \epsilon \sum_{i=1}^{N_{dim}} (\tilde{\boldsymbol{B}}^T \boldsymbol{J}^{-\frac{1}{2}} \boldsymbol{W} \boldsymbol{D}_i \boldsymbol{B})^T \hat{\boldsymbol{Q}} (\tilde{\boldsymbol{B}}^T \boldsymbol{W}_{std} \tilde{\boldsymbol{B}})^{-1} (\tilde{\boldsymbol{B}}^T \boldsymbol{J}^{\frac{1}{2}} \boldsymbol{W}_{std} \boldsymbol{D}_i \boldsymbol{B}) \tag{6-6}$$

This corresponds to a multiplication by the square root of the Jacobian before projecting to the Legendre basis, and a division by the same factor after projecting the filtered values back to physical space. Also, we note that when the Jacobian is constant, this form becomes equivalent to Equation (6-3). By modifying the exponents in the newly introduced Jacobian terms, we could also obtain a formulation of the SVV which scales with a power of the Jacobian in each element.

The other point that needs to be defined is the form of the filter determined by $\hat{\boldsymbol{Q}}$. A popular SVV filter function, known as the exponential kernel, is given by:

$$\hat{\boldsymbol{Q}}[i(p,q)][i(p,q)] = \begin{cases} 0 & p+q \leq P_{cut} \\ e^{-\frac{(p+q-P_N)^2}{(p+q-P_{cut})^2}} & p+q > P_{cut} \end{cases} \tag{6-7}$$

where $i(p,q)$ represents the index of the modes, $\Phi_i = L_p(\xi_1)L_q(\xi_2)$ and P_{cut} represents a threshold after which the modes start to be filtered, and is usually given as a percentage of the polynomial order P_N.

6-1-2 Continuous Galerkin SVV with discontinuous Galerkin mimicking kernel

Traditional SVV operators are based on constant ϵ magnitude while Moura et al. [2016] proposed that the ϵ is proportional to the product of local velocity with the mesh spacing, turning the Péclet number, which can be understood as a numerical Reynolds number based on local velocity and mesh spacing, to be constant and controlled all over the domain. It was also shown by [Moura et al., 2016] that this approach also avoids undesirable non-smooth dissipation characteristics at very high Péclet numbers.

This new proposed SVV operator concept is also combined with new power kernel function proposed by Moura et al. [2017] and presented on Equation (6-8). This new power kernel function i proposed to enforce that SVV dissipation is distributed monotonically across wavenumber space. It also features a user-defined parameter P_{SVV} that, when increased, further confines SVV damping to the smaller scales.

$$\mathcal{Q}(k) = \hat{k}^{P_{SVV}}; \quad 0 \leq \hat{k} = \frac{k}{P_N} \leq 1 \tag{6-8}$$

where k is the polynomial mode index and P_N is the overall solution polynomial order. This kernel also guarantees that when raising P_N, it automatically increases the resolution power per DOF.

On the spatial context, where boundary conditions are inlet-outlet type, it is not possible to match the dissipation levels of the continuous Galerkin ($CG-SVV$) with the discontinuous Galerkin (DG) for the same polynomial order. This mismatch happens because the DG dissipation curves are too steep due to super-convergence properties in frequency space. Also due to the existence of dissipation bubbles on the numerical diffusion curves of CG. The SVV operator proposed by Moura et al. [2017] considers a DG-based CG-SVV approach, in which the dissipation curves of CG with SVV stabilization of order P_N are match to those of DG with order $P_N - 2$. Figure 6-1 shown log-log plots of axis dissipation vs. frequency considering CG dissipation curves at a very large Péclet number - Pe^* without SVV for P_N =3 (left) and P_N =7 (right), both presented in colour black. For comparative purposes of the dissipation level, P_N (blue), $P_N - 1$ (orange) and $P_N - 2$ (yellow) dissipation curves for the standard upwind DG are also presented for the case considering solution order P_N =3 (left) and P_N =7 (right).

From Figure 6-1, it is possible to observe that DG order $P_N - 2$ offers the best match to CG order P_N as it remove the CG dissipative bubbles and spikes, compared to other DG orders.

According to Moura et al. [2017], numerical diffusion curve fitting study was performed via Matlab's optimisation toolbox and consisted of tuning SVV's kernel entries presented in Moura et al. [2016] for each given polynomial order. The final agreement was found to be very good, with the optimised CG-SVV approach yielding a smooth DG-like dissipative behaviour which holds a good balance between robustness and accuracy at high polynomial orders.

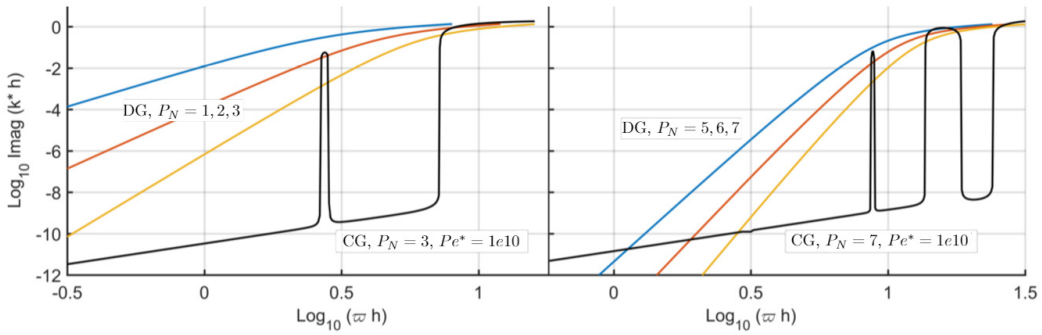


Figure 6-1: Normalised dissipation curves in log-log scale for CG-based advection-diffusion at very large Peclet number with $P_N = 3$ (left) and $P_N = 7$ (right) compared against DG dissipation curves for P_N (blue), $P_N - 1$ (orange) and $P_N - 2$ (yellow). [Moura, 2017]

The CG-SVV with DG mimicking Kernel operator applied to a solution with fixed number of DOFs, recovers superior eddy-resolving capabilities of high-order DG schemes when increasing the polynomial order. It can also be combined with meshing coarsening approaches to use high-order polynomials for the solution. The CG's order of accuracy is not expected to change in the proposed formulation, once the CG and DG dissipation curves were matched in the super-convergent frequency region. This is hardly a concern for under-resolved simulations, such the one presented here.

This novel DG-based CG-SVV approach, is referred on Nektar++ framework as CG-SVV with DG mimicking Kernel and it is considered as the SVV operator for all simulations in this research.

6-2 Mesh generation

The high-order mesh generation for the simulation cases presented are based on the work developed by Turner [2017] on NekMesh, a high-order mesh generator inside the Nektar++ package. The high-order mesh generation on NekMesh for this work is divided in different stages: CAD interface, linear mesh generation and high-order mesh generation. This research presents two different mesh strategies: the first using NekMesh high-order mesh generation complete pipeline and a second case using a hybrid approach where NekMesh is used to convert a low-order mesh from a commercial software into high-order mesh. The first mesh strategy is initially presented and explained followed by the second case.

6-2-1 Mesh parameter estimation for spectral/hp simulation

Traditional *LES* and *DNS* meshes are very demanding in terms of computational resources to have a high-quality solution as they require elevated number of elements. The spectral/hp element method allows that any mesh increases its resolution by using high-order polynomials to approximate the solution on each element. We propose an initial sizing guide for spectral/hp meshes for 3D geometries and high Reynolds numbers. Our main objective is to

make use of the advantages of this higher order method by designing a relatively coarse and efficient mesh for the required accuracy level.

The initial step is to define which turbulent scales are going to be solved. Based on our experience, we have found that if the design of a traditional h-typed finite volume *LES* mesh, including sizing refinement zones for regions of interest, would end up with a total number of mesh elements of N_h. Then the corresponding number of elements for a spectral/hp mesh (N_{hp}) necessary for obtaining results of similar accuracy at the mesh points (i.e. excluding the influences caused by different interpolation methods) can be estimated based on the choice polynomial order P_N as follows:

$$N_{hp} = \frac{4.8 \times N_h}{P_N \times (P_N + 1) \times (P_N + 2)}, \text{ for } P_N \leq 6 \tag{6-9}$$

Proposed equation 6-9 presents an estimated number of mesh elements required for Nektar++, including the macro prism layer. The factor 4.8 is related to the author experience from meshing design, aiming to correct capture the flow physics and it represents 80% of the total number of DOFs from tetrahedra elements.

In this way, an initial guideline for the mesh generation of simulations with higher order spectral/hp element method is available, avoiding the tendency for early adaptors to design meshes based on their past experiences with traditional finite volume *LES* mesh generation. These past practices often lead to an excessive number of elements, making the spectral/hp element simulation unnecessarily expensive or even computationally prohibitive.

6-2-2 High-order mesh generation pipeline

With an estimation of the required mesh size available, we now focus on the mesh generation process. First presented is a strategy in which only NekMesh is used to generate the high-order mesh from the CAD geometry. Then a hybrid approach will be presented where the linear mesh is generated by other commercial CFD suites for ease of operation and better handling of complex geometries and converted to a higher order mesh with NekMesh.

6-2-3 NekMesh high-order mesh generation

The pipeline is divided into CAD interface, linear mesh generation based on the CAD information and final high-order mesh generation, detailed as follows. This strategy is the one used for the Ahmed body validation cases and on the Ahmed body diffuser study. For further info on NekMesh, please refer to Turner [2017].

CAD interface

The process begins with the definition of the geometries for the computational simulations on a Computer Aided Design (CAD) software. All Ahmed body geometries presented were developed on the commercial CAD package Inventor 2017, available for Imperial College students, and the Imperial Front Wing geometry was created on commercial CAD package Catia available at McLaren Racing. The CAD geometry input required for NekMesh should

support a boundary representation description, since it needs to ensure geometrical accuracy and geometrical enquires. We selected the CAD exporting format ISO 10303 standard, also referred as Standard for the Exchange of Product (STEP) 203, for the model geometry data as it fulfils the software requirements.

NekMesh performs geometrical queries and checks the CAD at a basic level by using interfaces to CADfix and OpenCascade. OpenCascade is a large open-source library encapsulating a vast range of CAD operations and manipulations. The correction of any errors is performed by CADfix which provides several tools for fixing geometrical inconsistencies that can be found in CAD data. The use of CADfix and its interface presented here as CFI, is motivated by the CAD quality requirements for high-order meshing generation as stated by Turner et al. [2017] in which the distortion levels on the surfaces might be perfectly acceptable for generating linear meshes however they might induce poor quality or invalid elements in high-order meshes. The pipeline used for the main Ahmed body meshes follows the one presented by Turner et al. [2017] and uses the NekMesh Cad engine, which consists in using the CFI for the CAD geometry queries, followed by a linear mesh generated by CADfix, which are used to generate the final high-order mesh. For the IFW and full Ahmed body, the linear mesh is generated on a commercial mesh software, the Star-CCM+. The linear mesh generation is explained as follows.

Linear mesh generation

The initial step on the high-order mesh creation process is the generation of a linear mesh. The linear mesh is built in a bottom-up approach to ensure geometric accuracy is maintained for coarse mesh, once the curvature information is not eliminated as in most commercial mesh generators. The first step according to Turner et al. [2016] is to fix mesh vertices to the vertices of the model geometry from CAD. The following step starts by meshing the curves in 1D parameter space using the end vertices as boundaries and the 3D real distances to decide the distribution in compliance with the mesh spacing. Next, the 2D parameter spaces of the surfaces are then meshed using a third-party library, namely Triangle (Shewchuk [2002]), considering previous curve meshes as boundaries. The final step is the interior volume generation using 3D constrained meshing by using TetGen library (Si [2015]). This approach is used to ensure that all CAD information associated with all the vertices, edges and faces and can be used in the high-order mesh generation.

Linear mesh generation on NekMesh also incorporates an optimisation step after the 3D surface mesh is created to avoid irregular and low quality meshes once the surface mesh is projected into its 3D form using the CAD surface. The optimization step uses both edge swapping and point relaxation are used to maximise the quality of the surface mesh, breaking the Delaunay mesh characteristics, however improving the high-order mesh generation process, according to Turner et al. [2016].

We are also evaluating in this research the linear mesh generation capabilities on NekMesh in terms of robustness on all Ahmed body cases, which are close to current cases employed on the automotive industry. This is an important evaluation once the current pipeline for complex industrial cases require a commercial software for linear mesh generation, with is explained on 6-2-4 and was employed on the IFW evaluation.

High-order mesh generation

The final step on the mesh configuration process is the generation of the high-order mesh from a previously created linear mesh, following the same bottom-up approach from 6-2-3, following the idea proposed by Sherwin and Peiró [2002]. The generation of the high-order mesh requires the addition of extra points to represent the polynomial discretization (with order P_M), which are added respectively along the curves, followed by the surfaces of the CAD geometry and in the interior of the domain. The generation of points for each part are further detailed on Sherwin and Peiró [2002], Turner et al. [2017] and Turner [2017]. The processes are divided in three stages which are: the high-order surface mesh generation, followed by the generation of both boundary layer high-order mesh on selected wall surfaces and volumetric high-order mesh on rest the domain, finishing with the boundary layer split.

The most important stage on the high-order mesh generation is the optimisation of the high-order surface, which should be able to overcome the CAD geometry distortions, since even small inaccuracies on the geometric boundary have a large impact on the flow effects and solution. The most common inaccuracies include, according to Turner et al. [2017] highly distorted surface elements, linear mesh nodes being distant from the CAD surface and under-representation of the geometric curvature by using low polynomial order mesh combined with a large linear mesh element.

To generate the high-order surface mesh that fully represents the CAD geometry, according to Turner et al. [2016] and Turner et al. [2017], NekMesh approach considers vertex locations of the linear surface mesh fixed and use affine mapping of the triangle in the 2D parameter plane to the reference triangle of a high-order element to generate the high-order surface. This is also used to locate the new high-order nodes in the parameter space and project into 3D using the CAD engine. To avoid low quality high-order meshes, entities are modelled as a spring networks system. By minimising the spring energy, the high-order nodes location is optimized, improving geometric distortion (Sherwin and Peiró [2002]).

Following the spring network modelling, mesh edges that lie on curves are the first to be optimized, which can be simplified as a 1D spring system optimization problem, with the vertices of the linear mesh fixed. Edges lying on surfaces are the next entities to be optimized and can be modelled similarly to the previous case however now in 2D plane, aiming to reduce the distortion found in the high-order edges by minimising the length of the edge. The final optimisation step is on the interior triangle faces on CAD surfaces which is modelled as a set of freely movable nodes, consisting of those nodes lying on the interior of the triangle and a set of fixed nodes which lie on the edges. Each of the free nodes is connected to a system of six surrounding nodes by springs, and this is the system which is minimised. To optimise the energy of the system a bounded version of the BFGS algorithm is used as proposed by Turner et al. [2016] and Turner et al. [2017].

The next stage is the generation of the boundary layer, which might be extremely complicated for simulations at high Reynolds, such the ones presented in this research, due to low y^+ requirement on the elements in the wall-normal direction in order to fully represent the boundary layer behaviour.

The process requires the generation of a macro boundary-layer mesh, consisting of a single layer of prismatic elements near the walls. For the rest of the domain tetrahedra elements are generated using the top surface of the prisms as a pseudo-surface to mesh from. The

generation of the high-order surface will curve one of the triangular faces of the prism. To avoid generating invalid elements, the height of the macro prisms layer H_{BL} should be able to accommodate the wall surface curvature. With this requirement fulfilled, the boundary-layer mesh can be transformed into valid high-order elements by using the isoparametric approach proposed by Moxey et al. [2015], where the number of layers N_{BL} and growth rate GR are specified by the user on the Mesh Configure File (MCF) script. An example of the method is presented in Figure 6-2, where different growth rates are evaluated for 8 layers. The isoparametric approach allows the creation of very thin boundary layer elements without self-intersection, respecting some restrictions discussed on Moxey et al. [2015].

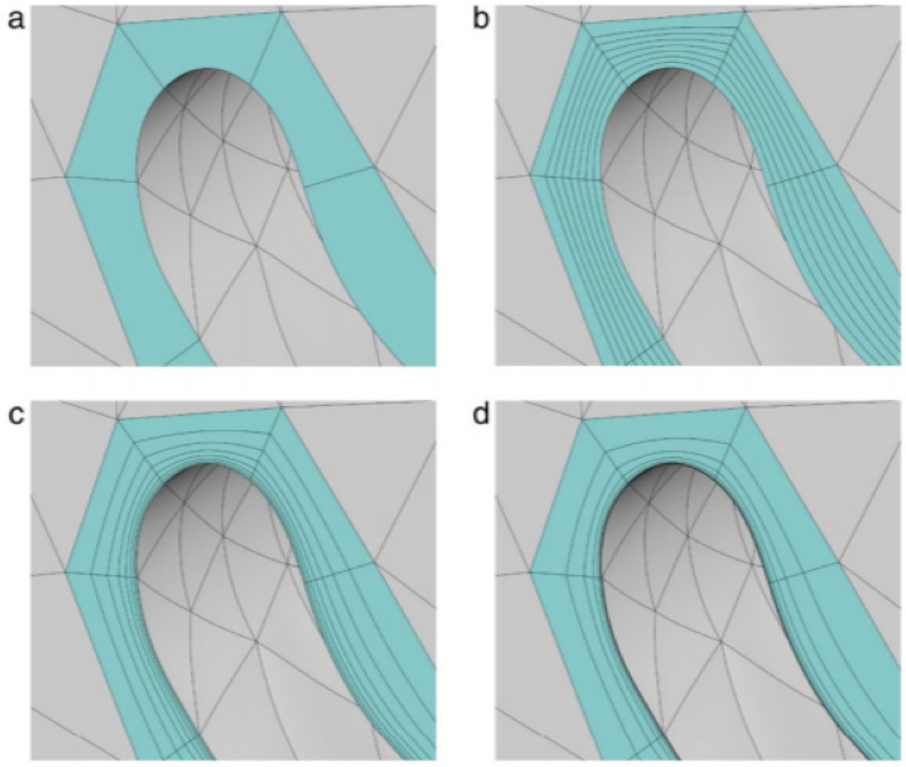
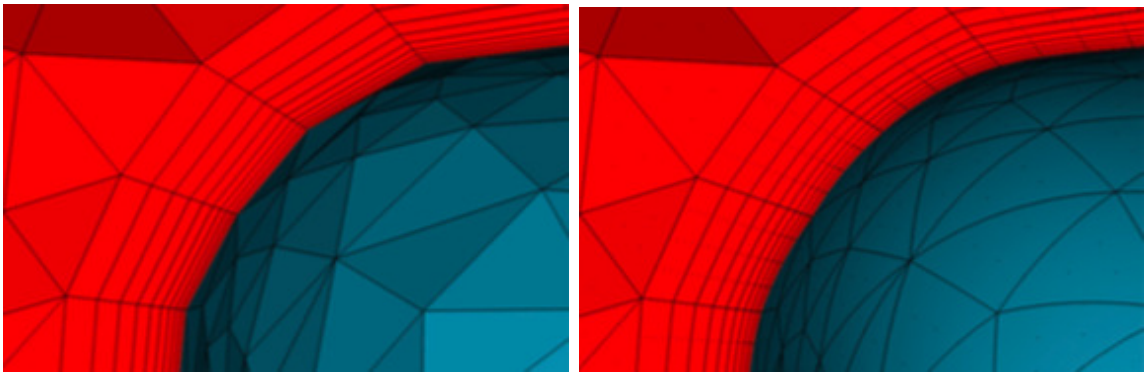


Figure 6-2: A sequence of meshes obtained by splitting macro-elements into $N_{BL} = 8$ elements using a geometric progression and various values of growth rate GR. (a) The macro-element mesh; (b) $GR = 1$; (c) $GR = 3/2$; (d) $GR = 2$. Reproduction courtesy of Moxey et al. [2015]

The final high-order results on a curved linear mesh in order to represent the CAD geometry, a curved boundary layer, with the last face of the prism layer being straight in order to easily generate the volumetric mesh. A comparison with the traditional linear mesh and the high-order mesh generated on NekMesh on a test case is presented in Figure 6-3 from Turner et al. [2017], where is possible to conclude that the projected high-order elements with P_m using 4^{th} order represent the real geometry with higher accuracy.



(a) Linear mesh **(b)** High-order mesh

Figure 6-3: Close detail of boundary layer mesh near the shoulder of the Boeing RLG wheel case, comparing linear mesh (left) with 4^{th} order mesh from NekMesh (right). Reproduction from Turner et al. [2017].

6-2-4 Hybrid meshing approach

Although NekMesh is capable of generating reliable meshes for relatively complex automotive geometries, such as the Ahmed body, the software itself is still relatively difficult to use compared to other commercially available CFD packages. Additionally, it still has some limitations in handling complex geometries. As the result, direct mesh generation of industrial geometries using NekMesh alone is potentially time consuming and inefficient. Inspired by the study of Lombard et al. [2015], we propose a second high-order meshing strategy as a possible walk-around, combining the meshing capabilities of different software. In this case we utilize Star-CCM+, together with NekMesh, to produce a high-order mesh for an industrial level geometry, the Imperial front wing.

The linear mesh is generated on Star-CCM+, by loading the CAD geometry, followed by creating a fine triangulation representing the boundary of the computational domain within a given tolerance. The linear mesh is then built using this approximate representation before the original CAD information is removed. The boundary layer mesh is generated as one macro prismatic layer on critical wall surfaces, then tetrahedra elements are generated on the rest of the domain which can also incorporate volumetric refinement regions. We present in Figure 6-4 a mesh generation example on Star-CCM+ for the IFW, which is further detailed in chapter 9.

The next step is the conversion of the low-order mesh generated on the commercial software into a high-order mesh using NekMesh. One critical issue for the high-order mesh generation rises with this way of generating the linear mesh: the lack of information relating the mesh to the original CAD definition, once the linear mesh was based on a fine triangulation definition, which is not available. The conversion process of low-order mesh into high-order mesh on NekMesh starts with the projection of the commercial software linear mesh onto the CAD surfaces to reconstruct the missing information. The surface mesh nodes are processed to obtain their parametric coordinates in the CAD surface followed by an auxiliary triangulation of the geometry. This additional information is stored on the CAD model in order to allow

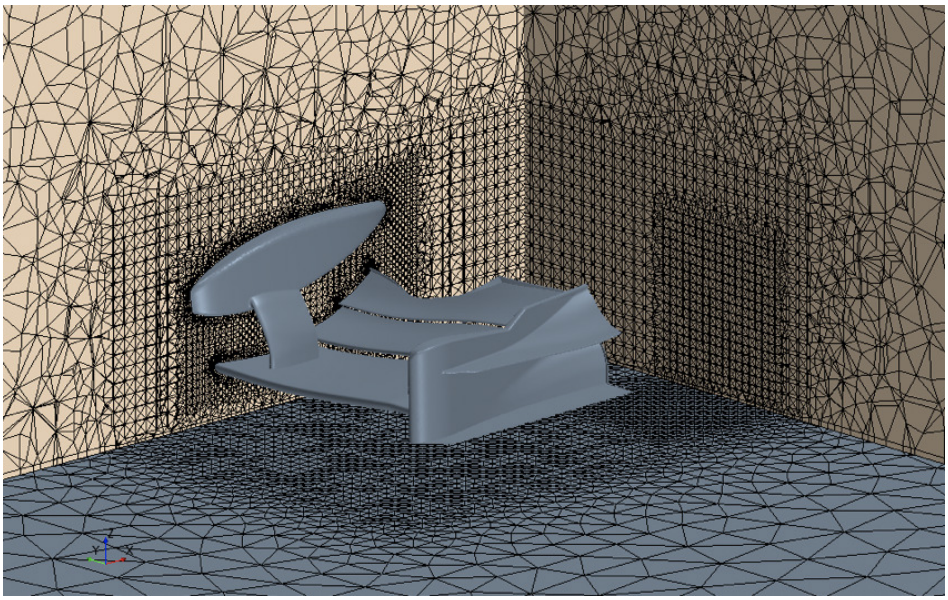


Figure 6-4: Representation of the linear mesh generated by Star-CCM+ on the IFW case.

the high-order mesh generation process. Next, NekMesh performs an operation to find the nearest vertex in the auxiliary triangulation on the CAD surface. It uses the parametric coordinates of the vertex as the initial guess for projecting the node onto the surface. The node can also be moved up to 10% of the length of the edges in the local mesh if the node does not lie on the CAD surface. If any nodes are above this 10% limit for the node adjustment, it will cause the entity connected to it, such as a face, edge to not be curved on the high-order mesh. An example of this procedure is presented for the Imperial front wing case in chapter 9.

Once we now have reconstructed the CAD information necessary to generate a high-order mesh, the process follow the similar pipeline as presented on 6-2-3, where high-order nodes will be placed along the linear mesh entity producing a high-order but straight sided entity. To curve the mesh entity the nodes are then projected onto the CAD surface and moved to the surface. This process is also applied to curve prismatic element on the boundary layer and tetrahedra elements on the rest of the domain. The high-order meshing process finishes by splitting the macro boundary layer.

6-3 Naming convention for higher order spectral/hp element mesh

As noted before, in comparison to conventional h-type method, the simulation settings for the spectral/hp element method additionally require the definition of the maximum order for polynomial expansion P_N and the polynomial order for the mesh (P_M). P_N may be referred as the solution polynomial order or the order of accuracy, when the exact solution is sufficiently smooth.

In this work, we also define a simplified notation when both parameters are mentioned together: NM46 would indicate $P_N = 4$ and $P_M = 6$. Additional settings will be appended to this notation: for example in the Ahmed body mesh study, NM46-A would represent NM46 with the *Original* mesh.

6-4 Summary

In this chapter we introduced and presented the main aspects of the spectral/hp element method applied to solve an incompressible Navier-Stokes problem. Spectral methods are currently being used for a wide range of 2D or quasi-3D canonical problems, proving to be a reliable solution method for CFD problems. However, for 3D geometries at high Reynolds numbers, the use of spectral methods is very challenging. Unstable high-frequency modes appear on the solution of high Reynolds cases causing the solution to diverge. The main solution stabilization technique for spectral methods, the SVV, was presented and discussed. We also presented the CG-SVV with DG mimicking kernel operator (Moura et al. [2017]) and proposed to use this novel SVV operator for 3D geometries at relatively high Reynolds number.

Next, we introduce the full mesh generation process for Nektar++ simulations. Based on a CAD surface, the process starts with linear mesh generation and its conversion to high-order mesh elements. The last step of the process is the macro boundary-layer splitting. The mesh generation process presented may follow two different pipelines: complete mesh generation process on NekMesh or hybrid generation process. The later process combines a commercial CFD software with the high-order mesh capabilities of NekMesh. The full pipeline for high-order mesh generation to be used on Nektar++ is summarized in Figure 6-5.

We now present a 3-dimensional validation study for an automotive bluff body referred as the Ahmed body, in order to evaluate the capabilities of the Nektar++ code on industrial cases.

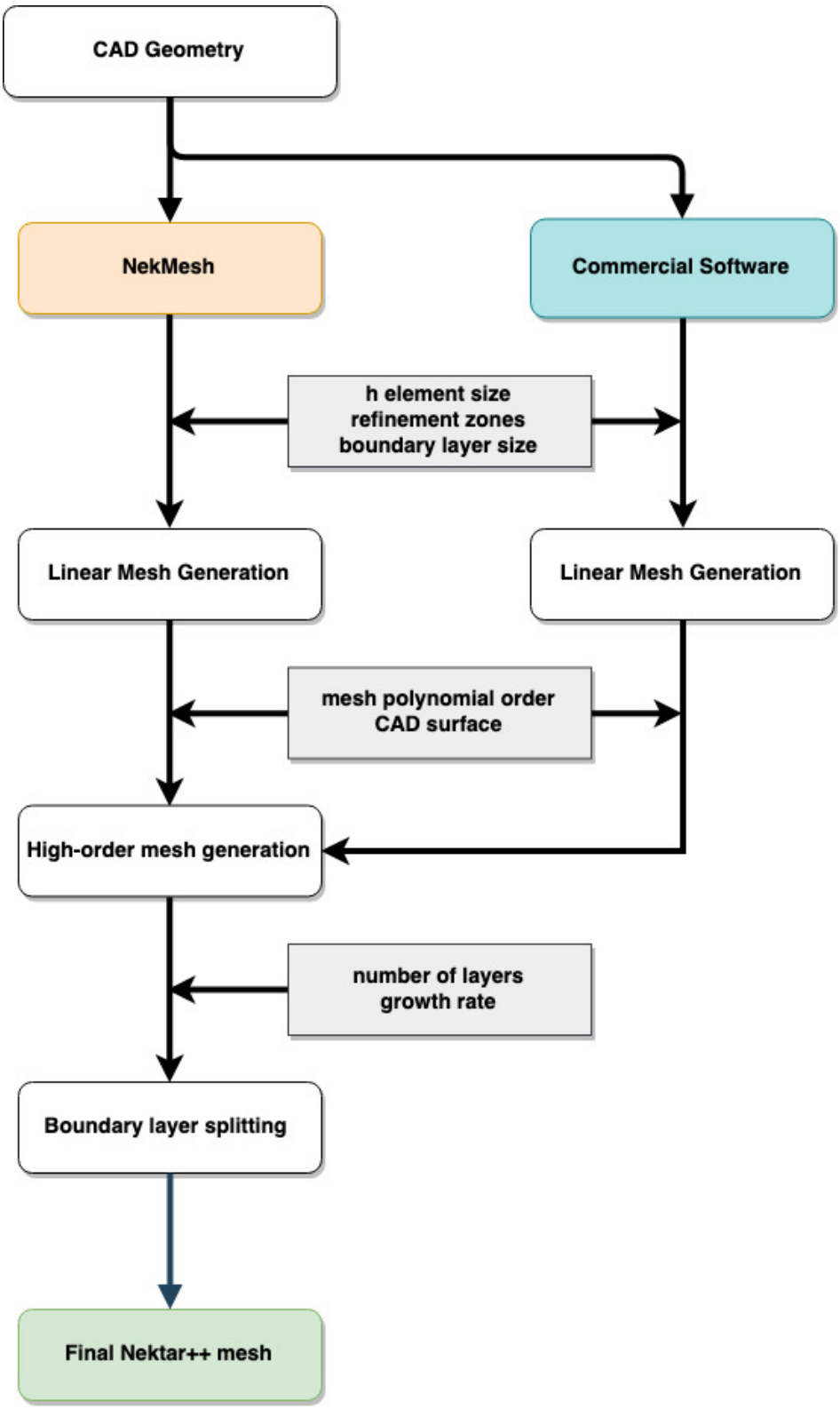


Figure 6-5: High-order mesh generation process for Nektar++ simulations.

Part III

Ahmed Body

Chapter 7

The Original Ahmed Body

The automotive bluff body selected for this research is the Ahmed body. In this chapter, we first present a literature review for various type of automotive bluff bodies, before introducing the details regarding the Ahmed body. Then we present a correlation study for the Ahmed body with 25°, with moving ground condition imposed in a uDNS/iLES simulation employing the spectral/hp element method. The simulation results are compared with experimental references and previous computational studies of the Ahmed body in terms of aerodynamic quantities and flow features. We also analyse various possible configurations of the proposed method to establish best practices.

7-1 Automotive bluff bodies

Road vehicles can be considered similar as bluff bodies geometries, with the flow around being highly turbulent and complex due to the high Reynolds number combined with fixed separation points, frontal stagnation, low ground height and complex geometries such as the underbody and engine vault.

The automotive models' chart is divided into several types of models, based on body style such as sedans, hatchbacks, Sport Utility Vehicle (SUV), Pick-up Trucks, performance and race cars. Each car manufacturer has its own designs, engine types, frontal area, grille openings, ground height and several other details that turn out to be impossible to apply a single common vehicle in a reliable study for all companies and universities.

As the shape and design change from each automaker, even though the body style is the same, it would be very complicated to perform fundamental studies that could be shared along the automotive aerodynamic community. It's also restricted by confidential policies inside the companies, in which vehicle's geometries can't be made available publicly. Only after a certain period, some companies make the models available for studies, however not representing the latest trend in car design.

In order to make it possible to share research results and possibly attract people to complement the work, generic automotive bluff bodies were developed by different authors and made available to anyone interested, by sharing both the study results and body geometric dimensions. The most common automotive bluff bodies such as the Howell or Windsor Body squared-back and the Ahmed body are presented in Figure 7-1.

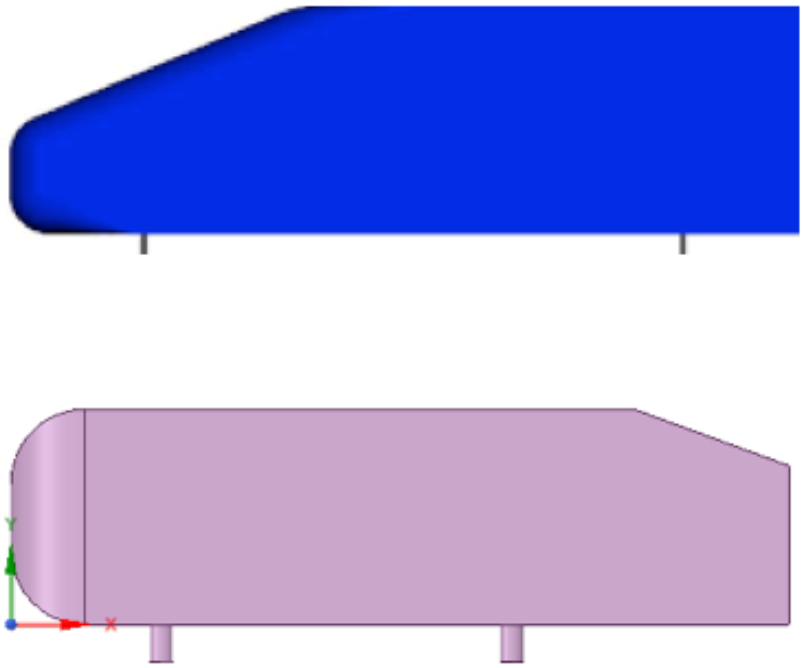


Figure 7-1: Side view of the Howell or Windsor body (top) and the Ahmed body (bottom).

The geometries aim to represent the behaviour of a real ground vehicle, in order to understand fundamental fluid phenomena, such as separation and flow reattachment, rear wake and base pressure fluctuations.

The most common automotive bluff bodies used on the literature are briefly discussed such as generic rounded-front bluff bodies, the Windsor body, the Morel body and the most used one, based on the previous case: the Ahmed Body. Their details and some of the main studies are exposed in the next sections.

7-1-1 Windsor body

An automotive bluff body called both Rover or Windsor has been in use by Rover (including Land Rover) for many years for basic internal aerodynamic studies, such as effects of rear end shape and ground simulation, according to Howell et al. [2003]. The interchangeable rear allows a wide range of lift and drag characteristics and wake structures to be evaluated. The model, which has the dimensions of a 1/4 scale small hatchback, is connected to an underfloor balance via four thin legs in the position of the wheels, with a ground clearance of 50 mm. All leading edges are rounded with a radius of 50 mm except for the roof leading edge, which

has a radius of 0.20m. The longitudinal and trailing edges are sharp, and this kind of body was studied mainly by Howell et al. [2003], Howell and Le Good [2005], Howell and Le Good [2008], Littlewood and Passmore [2010], Littlewood et al. [2011], Littlewood and Passmore [2012] and Perry et al. [2016]. A detailed sketch of the bluff body is shown in Figure 7-2.

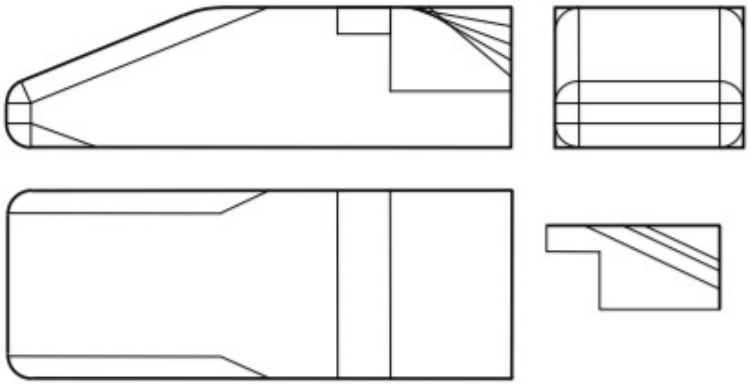


Figure 7-2: Detailed view of the Rover/Windsor body used for automotive studies. Howell et al. [2003]

As shown in Figure 7-2, the Rover/Windsor body has the following principal dimensions, similar to the ones of the Ahmed body:

- Length 1,045 mm;
- Width 390 mm;
- Height 290 mm;
- Frontal Area 0.112m^2;

The experimental study of Howell et al. [2003] was conducted on Squared-back Windsor body model, to investigate drag reduction opportunities from injecting low velocity air into the base region, called base bleed. In all injection cases studied drag is reduced with increasing bleed rate. It was also studied the influence of the inner rear cavity size by using a porous wall on its boundary. The porous wall was evaluated in fully open and fully closed condition and the main outcome is a drag reduction as the wall remains open as well as the Re number increases.

In the other study from Howell and Le Good [2005], the parabolic relationship between drag due to the lift was investigated, in which is referred as vortex drag. The same Windsor Body from square back to 40° slant angle, with a variation of 5° for each case, with low ground clearance is the focus of the study. The wind tunnel tests were performed considering both moving and stationary ground simulations. Results show that vortex drag factor, KV, reduces as the ground clearance reduces. At small ground clearances it is approximately proportional to ground clearance. At small ground clearance, the vortex drag factor was reduced with a

moving belt ground simulation in comparison with a stationary belt. This effect is small at ground clearances relevant to passenger cars.

Continuing the work from 2005, Howell and Le Good [2008] showed for a Windsor body that the backlight surface is a significant source of vortex drag and he studied the backlight aspect ratio on both vortex and base drag. The vortex drag factor is found to be independent of aspect ratio, while the base drag component is shown to be dependent on the ratio of base to frontal area.

In the study of Littlewood and Passmore [2010], the authors worked to understand how an optimized roof trailing edge, in the form of a chamfer, can reduce wake size, increase base pressures and reduce drag. The focus was an experimental study using PIV, balance measurements and static pressure measurements was performed in order to investigate the flow and wake structure behind a simplified car model. Significant reductions in C_D are demonstrated and directly related to the measured base and slant pressures. The PIV data shows both the time averaged structure of the wake and the unsteady shedding associated with the upper separation.

Littlewood et al. [2011] shows changes in drag coefficient and lift coefficient for both cases, of a square-back simplified vehicle body style as a result of physically small passive modifications. The proposed modifications consist on adding slats to the base surface of both a quarter scale Windsor body and at full scale SUV. The full-scale vehicle was tested with and without a flat floor. The low profile, horizontal slats proposals were created mainly to disrupt any steady wake structures acting close to the vehicle base surface. Force balance, static pressure and PIV measurements have been used to investigate the flow structures in the vehicle wake. For the Windsor body, the best drag coefficient improvement is around 8 counts for 4 slats at 40 m/s and for lift coefficient around 32 counts for 3 slats at 30 m/s. For the full-scale SUV, the best demonstrated drag reduction was 4 counts, by adding 6 slants equally spaced on the rear at speed of 31.3 m/s and the best lift coefficient reduction was 11 counts for the condition with 3 slants on the lower rear portion of the car at 31.3 m/s.

On the study presented by Littlewood and Passmore [2012], it was investigated the effect of active flow control by using synthetic jets on the slant of a squared-back Windsor Body. The flow control was analysed for the jet in 4 cases, which were perpendicular upwards to the flow direction, 45° upwards to flow direction, parallel to flow direction and 45° downwards to flow direction. The only configuration that improved the drag coefficient during the 1/4 scale tests was the 45° downwards to flow direction attributed to a reduction in wake size via a deflection of the upper shear layer downwards and reduction in the velocities observed in the lower vortex structure located at close proximity to the base surface. Further studies were conducted for a Re=3.01×10^6 for this case only and the main conclusion is that the jet velocity ratio with free stream should be very high to deliver a reasonable drag improvement and the cost of implementing such method would be prohibitive.

The most recent study on the Windsor body, Perry et al. [2016] applied large scale tomographic PIV to study the wake region of this model. This forms part of a larger study intending to understand the mechanisms that drive drag force changes when rear end optimizations are applied. For the first time, tomographic PIV has been applied to an airflow volume able to capture the near wake. The model evaluated is a 25% scale Windsor model and PIV were made in a single measurement with speed ranging from 10 m/s to 40 m/s. The tomographic results are shown to produce high quality data with the setup used, but further improvements

such as increase seeding density and tests at higher Reynolds number could be conducted to improve the confidence level. Proper Orthogonal Decomposition (POD) was applied to both the 2D and tomographic data and indicate the presence of a bi-stable wake structure mainly on the 2D case and the topographic was not directly seen due to misalignment of the model during the measurements. Bi-stable wake is usually found on bluff bodies squared-back, as presented in the work of Grandemange et al. [2013] and will be further discussed in this work.

7-1-2 Morel bluff body

The first study regarding the influence of the slant angle on an automotive bluff body was performed by Morel [1978]. Drag coefficient measurements were performed on an axis symmetric cylinder with slanted back for slant angles φ from 20° to 90°, as shown in Figure 7-3.

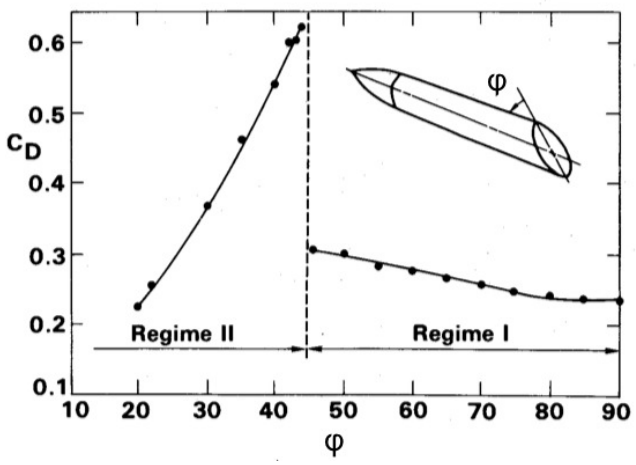


Figure 7-3: Drag coefficient of an axis symmetric cylinder with inclined slanted back. Reproduction from Morel [1978].

Considering the drag measurements, Morel also observed two different phenomena happening on the slant region up to a limit slant angle and were called Regime I and Regime II. For Regime I, which ranges from 45° to 90° of the slant angle, the time-mean of the flow separation pattern is quasi-axis-symmetric. For Regime II, from 20° to 45°, flow separation pattern observed is strongly three-dimensional, with edge vortex been formed along each of the side edges. The rolled-up vortices have a low-pressure zone on their cores, influencing the nearby surfaces, changing wake profile and increasing the drag coefficient as observed in Figure 7-3, resulting in strong suction effect on the slant. Figure 7-4 illustrates these effects and flow structures observed by Morel.

The conclusion for this first study was that the slant angle inclination influenced the drag coefficient of the cylinder. Some questions rose regarding some factors that might influence separation patterns such as free-stream turbulence, Reynolds number, ground proximity or clearance, rounding the upper edge transition, spoiler addition and the aspect ratio of the slanted surface. These doubts led Morel to perform one additional experiment using the same slanted cylinder in order to evaluate free stream turbulence. Two conditions were evaluated in this new experiment: smooth flow considering 0.1% of turbulence intensity (u'/U, where

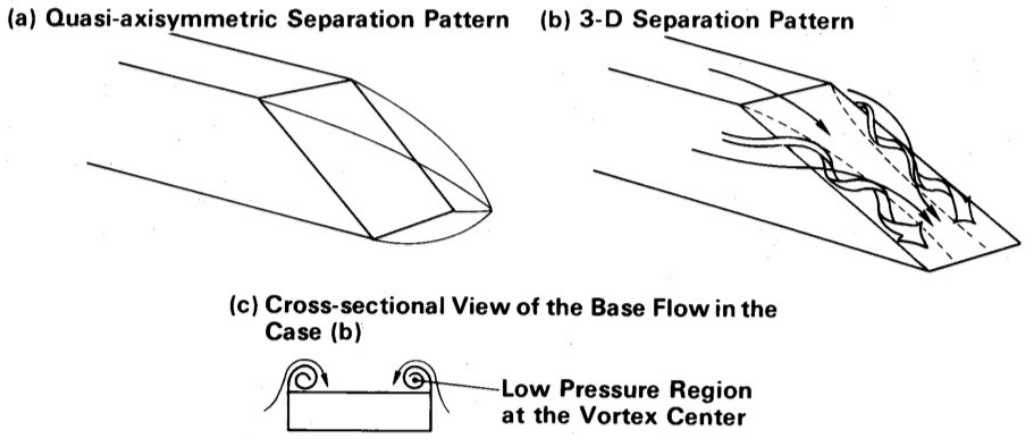


Figure 7-4: Types of separated flows patterns on a slanted back verified by Morel: (a) behaviour verified on Regime I condition; (b) and (c) behaviours verified on Regime II condition. Reproduction from Morel [1978].

U is the streamwise velocity and u' is the perturbation on the velocity field) and turbulent flow, considering 6% of turbulence. For both cases, drag coefficient measurement were taken and evaluated. The conclusion is that the turbulence level raised the drag coefficient values, compared to the ones with smooth flow. The critical behaviour in which the flow regime abruptly changes was basically unaffected as shown in Figure 7-5.

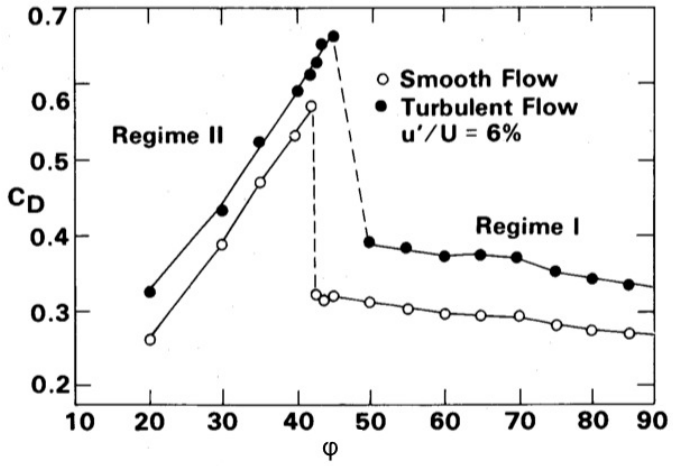


Figure 7-5: Effect of free-stream turbulence on drag coefficient behaviour of a slanted cylinder. Reproduction from Morel [1978].

The cylinder case tested by Morel [1978], considered a Reynolds number of 94,000 based on the diameter, which is around 25 times lower than a full-scale vehicle. The boundary layer on the body was found to be fully turbulent by the time it reached the base area, so Morel concluded that by increasing the Re number, the boundary layer height will thin down and would not affect the overall drag behaviour. Experiments on the slanted cylinder, ranging

the Re number from 15,000 to 112,000, confirmed this trend and the critical angle remained fixed. Only for the case of 22,000 the value moved a little lower compared to the other cases. The fact that the critical angle remained fixed over a Reynolds number range 5:1 showed that the critical behaviour is not too dependent on this parameter.

Ground proximity was also studied, especially for the Regime II, since in this case the flow in the mid-portion of the slanted surface follows the base slant, shoots down towards the ground, and may impinge. The interference caused by this impingement could have an upstream influence strong enough to modify the flow and the drag behaviour.

The upper edge of the slant was rounded in order to smooth the separation and it would produce significant changes in drag. In addition to the previous cases, Morel studied the influence of adding spoilers and the influence of changing the aspect ratio of the slanted surface.

Aiming to further study the Reynolds number dependence, as well as to investigate the other factors such as the ground proximity, rounded upper edge, spoilers and aspect ratio change, Morel proposed a larger and more realistic model in terms of an automobile, known as the Morel body, shown in Figure 7-6.

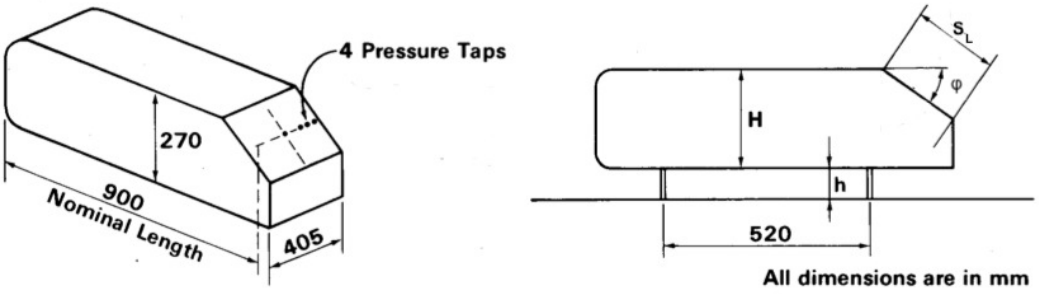
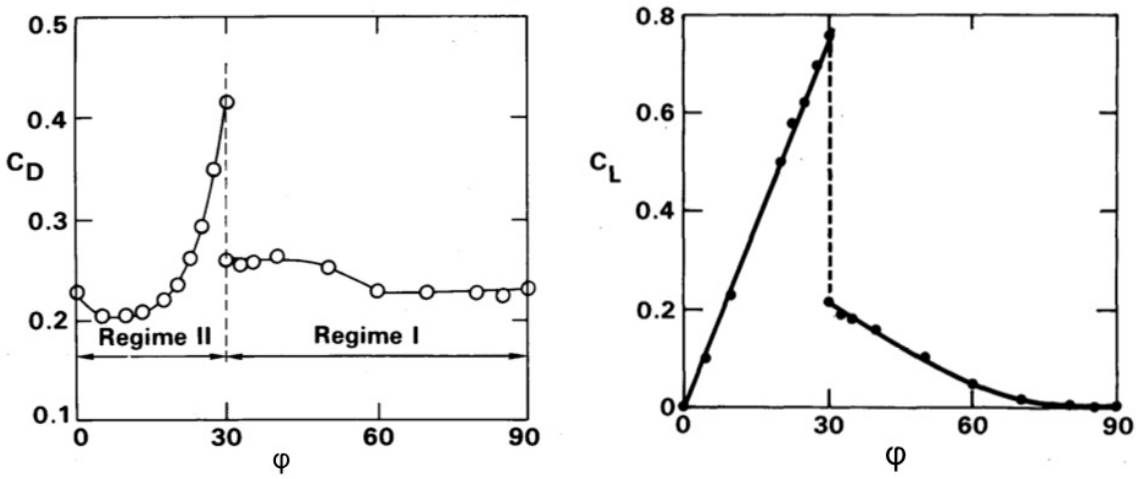


Figure 7-6: Geometry details and main dimensions of the vehicle-like model proposed by Morel. Reproduction from Morel [1978].

The new model was meant to have its overall dimensions in the same proportion as the envelop of a typical full-size vehicle, length: width: height being 3.33 : 1.5 : 1.0, although its size corresponds to 1/4 scale of a typical road vehicle. The Morel's proposed bluff body model was tested in a different wind-tunnel from the previous study, with $Re = 1.4 \times 10^6$ and we will be referred as the baseline Morel body model.

Results for the drag shows that the maximum drag coefficient value of 0.41 was reached for the slant angle of 30° on Regime II zone, followed by a suddenly drop to 0.25 at higher angles in the Regime I zone, demonstrated in Figure 7-7a. The lift coefficient values are positive at all non-zero slant angles φ, once the base slant exposes an upward projection of the low-pressure base surface. The curve behaviour is demonstrated in Figure 7-7b.

In order to study the influence of the ground clearance, Morel set one case reducing the ground height to a corresponding value of 180 mm on a real vehicle and compared with baseline results. For the drag coefficient values, the critical angle and flow behaviour didn't change, however the drag increases for φ above 50°, as shown in Figure 7-8a.



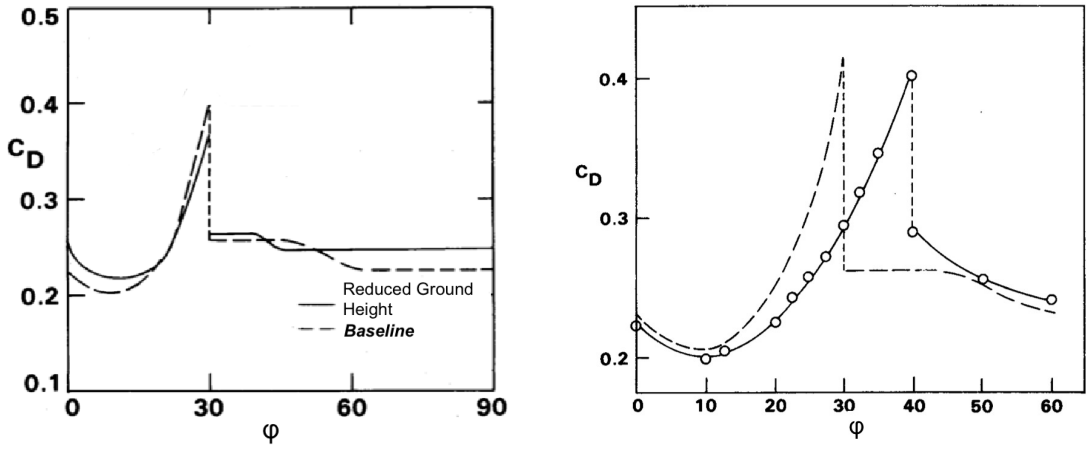
(a) Drag **(b)** Lift

Figure 7-7: Drag and lift coefficient values on the proposed baseline Morel body. Reproduced from Morel [1978].

By rounding the upper edge of the slant, Morel selected a large round radius of 200 mm, which corresponds to 0.74 times the body height for thirteen cases, ranging the slant angle from 10° to 50°. In addition to those cases, the 60° case was rounded with a 170 mm radius and the 70° one with a 140 mm radius. The test concluded that by rounding the sharp edge on the upper slant, the critical high-drag angle was shifted in 10°, as shown in Figure 7-8b. The shifting on the maximum drag can be explained by the fact that flow remains attached longer when the rounded radius is applied on the slant transition.

The combination of rounding the upper edge with ground height reduction to 180 mm reduce the maximum drag increment and its critical angle, which can be explained by a resultant of upstream influence of downwash impingement on the ground plane. Results for this configuration using different slant angles φ is shown in Figure 7-9 comparing with baseline results.

Morel summarized his studies by concluding that the peak drag value is around 30°, even considering the changes in the Reynolds number, ground height and upper edge rounding studies. This was also the motivation study for Ahmed in 1984 to generate a similar bluff body to this one, however considering a smaller frontal stagnation area and flow transition on the side of the body.



(a) reduced height (continuous line)

(b) rounded upper edge (continuous line and white dots)

Figure 7-8: Drag coefficient comparative results for reduced ground height case and rounded upper edge, against baseline Morel body (dashed line). Reproduction from Morel [1978].

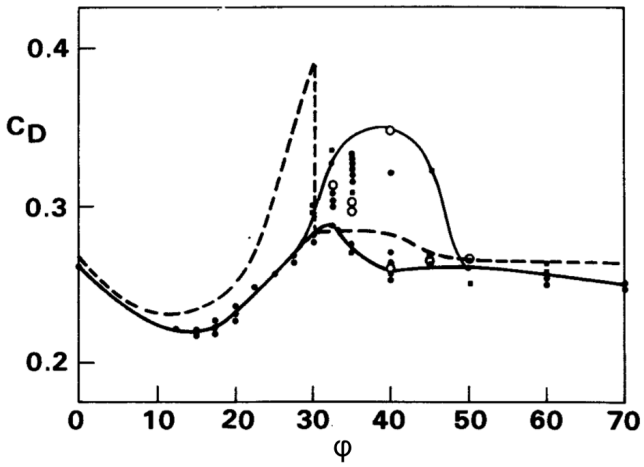


Figure 7-9: Drag coefficient results for different slant angles comparing rounded upper edge (light continuous line and white dots), rounded upper edge combined with ground height reduction (darker continuous line and black dots) against baseline Morel body (dashed line). Reproduction from Morel [1978].

7-1-3 The Ahmed body

The Ahmed body is another type of automotive bluff body and the most used for theoretical and computational aerodynamic research in the automotive community. It was first proposed by Ahmed in 1984 (Ahmed et al. [1984]) in which he proposed a bluff body with characteristics similar as a road vehicle, considering a frontal stagnation, side area and a transition at the rear back to the wake. The schematic drawing of a classical Ahmed body is presented in Figure 7-10, with its main dimensions.

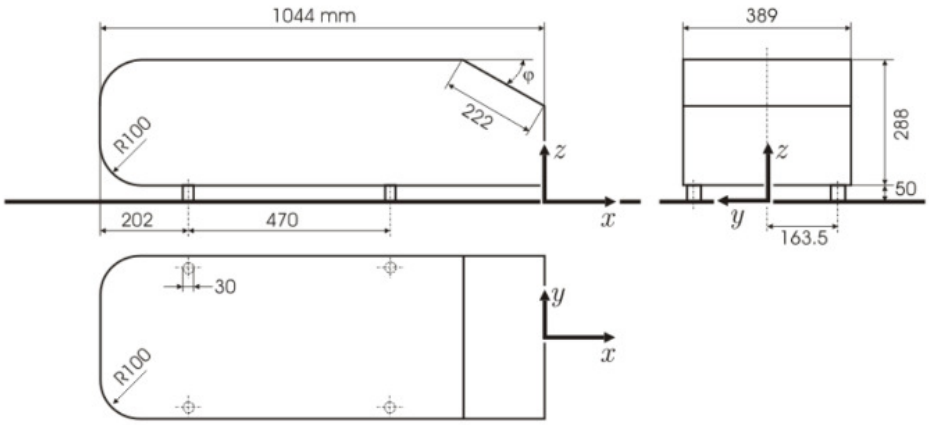


Figure 7-10: Ahmed body schematic drawing considering its main dimensions.

According to (Huminic and Huminic [2010]), it has been shown that the flow over the angled upper back section is dependent on the specific slant angle. There have been found to be two critical angles, 12.5° and 30°, at which the flow structure changes significantly, revealed also by changing of curvature of the drag variation.

Angles below 12.5°, the airflow over the angled surface remains fully attached before separating from the model when it reaches the vertical surface of the back end. The flow from the angled section and the side walls produces a pair of counter rotating vortices, which continue downstream. The attached flow on an Ahmed Body with slant angle of 12.5° is shown in Figure 7-11.

For angles between 12.5° and 30°, the flow over the angled section becomes highly three-dimensional. Two increased counter-rotating lateral vortices are shed from the sides of the angled section with increased size, which affects the flow over the whole back end, causing a three-dimensional wake. These vortices are also responsible for maintaining attached flow over angled surface up to an angle of 30°, and it have been shown that they are extended up to half of the length of the model beyond the trailing edge, according to Strachan et al. [2007] and Lienhart et al. [2002]. Close to the second critical angle, a separation bubble is formed over the backlight. The flow separates from the body, but re-attaches before reaching the vertical back section. At this point, the flow again separates from the model, as shown in Figure 7-12a.

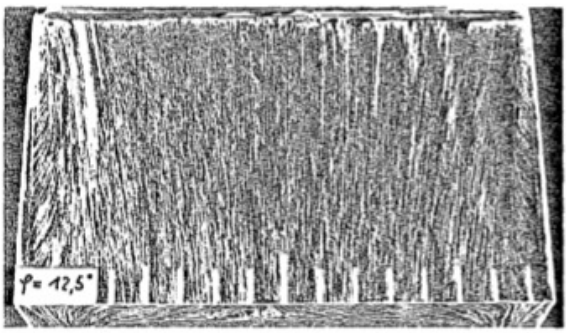


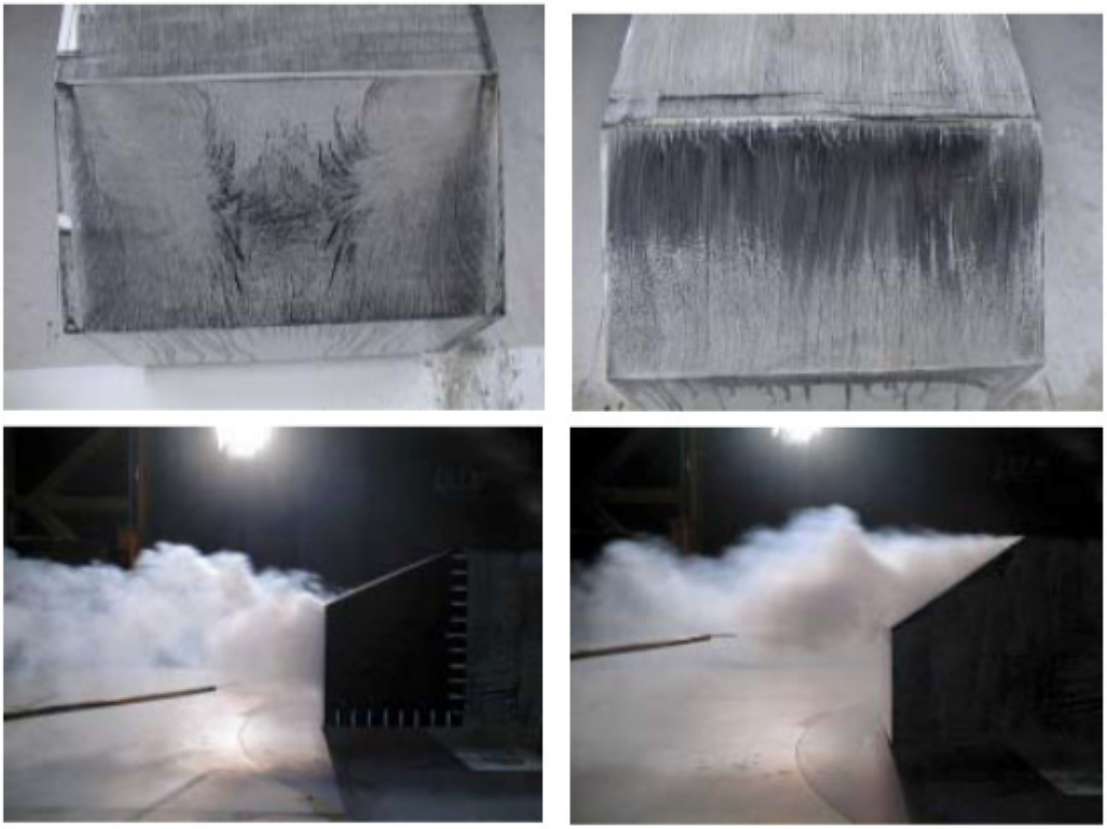
Figure 7-11: Flow visualization on an Ahmed body with slant angle inclination of 12.5° with flow moving from top to bottom. Reproduction from Ahmed et al. [1984]

Above 30° (Figure 7-12b), flow over the angled section is fully separated. There remains though a weak tendency of the flow to turn around the side edge of the model, a result of the relative separation positions of the flow over model top and that over the backlight side edges. When the flow is in this state, a near constant pressure is found across that region.

In his study, Ahmed et al. [1984] focused on measurements of the drag coefficient for ten different slant angles configurations, reporting the individual contribution of the main parts: frontal (C_K), slant (C_S) and back (C_B), as shown in Figure 7-13. The main objective was to understand the influence of each part and how the slant and back components behave when the angle changes.

During the drag coefficient measurements, it was noticed that, at the slant angle of 30° the drag coefficient was the highest value measured but it suddenly drops by adding a splitter plate vertically on the ground board in the plane behind the model. For this specific case, there is a high and a low drag case, indicating that it is the critical angle, transitioning from a partially separated 3-D flow to a fully separated quasi-2D flow. Measurements for angles higher than 30° presented lower drag coefficient tendencies, as shown in Figure 7-14.

The effects noticed by Ahmed et al. [1984] were in accordance with results previously reported by Morel [1978], reporting the same drag coefficient trend increment and peak value at 30°. This work was the start point of several complementary researches, focusing in several different aspects, such as flow structures characterization, drag reduction by active and passive flow control, moving ground and ground height influences, application of aerodynamic part such as underbody diffusers and many others.



(a) 25° **(b)** 35°

Figure 7-12: Flow visualization on an Ahmed Body with slant angle inclination of 25° and 35° from experimental measurements of Lienhart et al. [2002]. Reproduction from Lienhart et al. [2002].

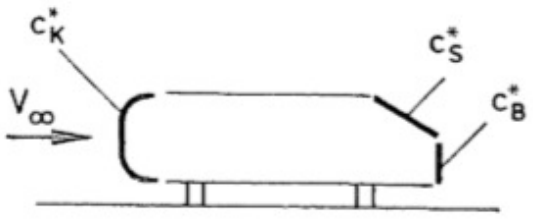


Figure 7-13: Break down of the main drag coefficient components on an Ahmed body: frontal (C_K), slant (C_S) and back (C_B). Reproduction from Ahmed et al. [1984].

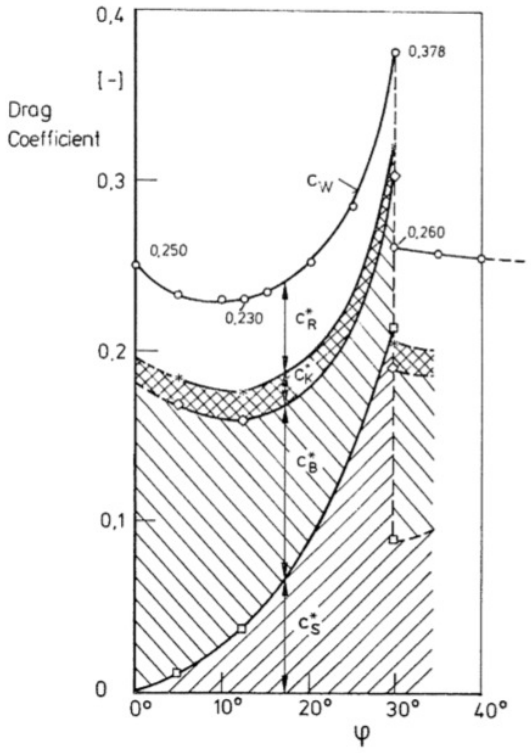


Figure 7-14: Drag coefficient measurements for the different slant angles (φ) evaluated in the original Ahmed body. C_W indicates the total drag coefficient and C_R represents the drag coefficient of other components excluding the frontal part (C_K), the slant (C_S) and the back (C_B). Reproduction from Ahmed et al. [1984].

7-1-4 Geometry details

In terms of geometry, the Ahmed body is an open source test case, which main dimensions are presented as follows:

- Total length (L_l): 1,044 mm;
- Total width (L_w): 389 mm;
- Total height (L_h): 288 mm;
- Slant length (L_s): 222 mm;
- Ground height (h): 50 mm;
- Frontal area (A_f): 0.112m^2;

The model's dimensions ratio for length, width and height are 3.36 : 1.37 : 1.00, similar to the one proposed by Morel [1978]. For the back portion, the slant length was fixed in 222 mm with sharp edges in all cases. Nine inclination angles were evaluated starting from 0° to

40° in increments of 5° at a Reynolds number of 4.29 million based on the body length of 1,044mm in the original experiment of Ahmed et al. [1984]. A tenth measurement was made in the slant angle of 12.5°, as detailed in Figure 7-15.

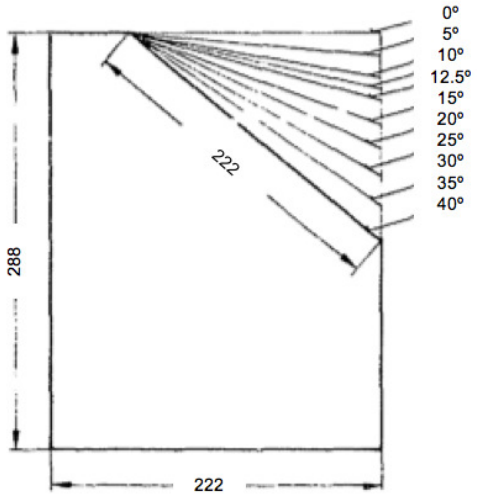


Figure 7-15: Schematic Ahmed body drawing considering all evaluated slant angles. Reproduction from Ahmed et al. [1984].

7-2 Past studies for the Ahmed body

Most relevant publications on the Ahmed body are now presented and discussed. This section is divided into experimental references (Section 7-2-1), complementing the original study of Ahmed et al. [1984]. The second part (Section 7-2-2) presents computational studies on the Ahmed body, focusing on comparison against experiments. The computational studies presented considers both simplified and currently state-of-the-art methodologies.

7-2-1 Ahmed body experimental references

The Ahmed Body original study provided significant amount of data but, due to technical limitations, flow characterization was performed only over the slant of the body by ink contours. Measurements in the wake and over the body itself were performed slightly later by Lienhart et al. [2002], which also became a complementary study associated to the original case, since the same flow conditions, such as the Reynolds number, fixed ground and tunnel conditions were reproduced, focusing only on flow characterization.

From Ahmed et al. [1984] and Morel [1978] studies, it was concluded that the slant provide three flow behaviours, which the most interesting for automotive applications are the 3-D flow, ranging from slant angles above 12.5° up to 30° and the fully separated flow, for slant angles above 30° which is also the critical drag coefficient angle. In order to evaluate both

conditions and not reach the critical angle region, which is also unstable, the slant angle of 35° was selected to represent the fully separated flow condition and the slant angle of 25° represents the 3-D flow condition, which is the case studied in this research.

Lienhart et al. [2002] performed a study using laser doppler anemometry (LDA), hot-wire anemometry (HWA) and static pressure measurements in order to investigate the flow and turbulence structure around the Ahmed Body model for two slant angle conditions: 25° and 35°. The main scope was to supply a detailed data set acquired under well-defined boundary conditions, similar to Ahmed's test, to be used as reference data for numerical simulations. The test conditions considered a slightly smaller Reynolds number, changing the velocity from 60 m/s to 40 m/s but maintaining the static ground condition, as performed by Ahmed et al. [1984]. A summary of the measurements in four normal planes to the flow direction: 0, 80, 200 and 500 mm and in the parallel plane to the flow at the middle portion of the body, made to both slant angles, is presented in Figure 7-16.

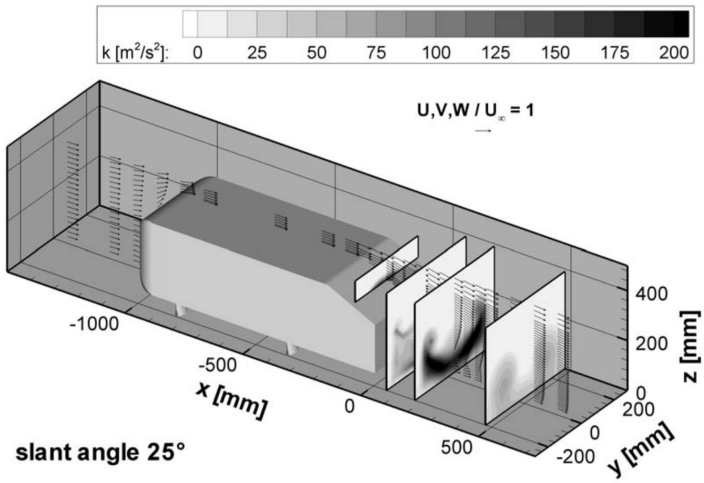


Figure 7-16: Summary of downstream planes for LDA measurements over the Ahmed Body in Lienhart et al. [2002] experiments. Reproduction from Lienhart et al. [2002].

The study of Lienhart et al. [2002] is one of the most important in terms of flow topology and structures identification on the Ahmed body, as it provides a complete data set for the most common slant angles configuration and it is acknowledged as a complementary work of Ahmed's original experiment from 1984.

Another important contribution to flow characterization was the work of Strachan et al. [2007], in which the Ahmed Body was tested in moving road conditions and both the aerodynamic forces and flow characteristics were recorded. In order to have the rolling road condition, the supports on the ground were replaced by a fixing system on the top of the tunnel, as demonstrated in Figure 7-17.

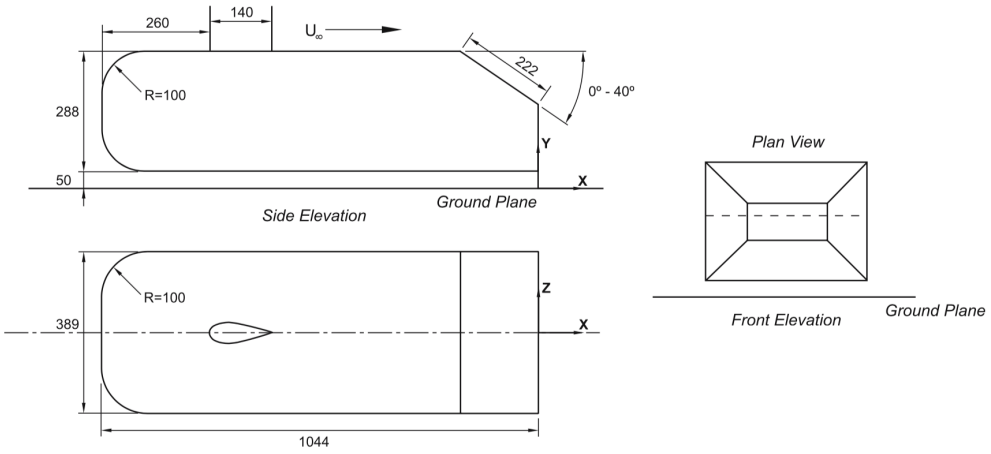


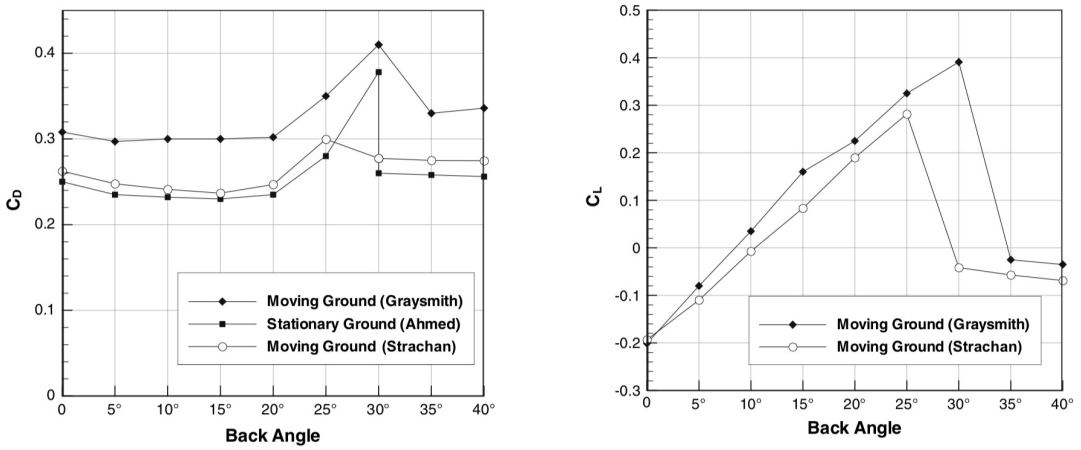
Figure 7-17: Schematic setup for the Ahmed Body in moving ground conditions with upper fixation support. Reproduction from Strachan et al. [2007].

Flow conditions were slightly different from the ones used on Ahmed's test, by reducing the flow velocity to 25 m/s due to the rolling road simulation limitations, resulting in a Reynolds number of $Re = 1.7 \times 10^6$ based on its length. Drag and Lift coefficient measurements and time-averaged LDA in the transverse planes at 0, 80, 500 and 1,004 mm were recorded and compared with the literature of Lienhart et al. [2002] and Graysmith et al. [1994].

Figure 7-18a shows the drag coefficient values from Strachan's experiments compared with previously published experimental data, considering both fix and moving ground cases. It can be seen the two overall drag coefficients for the 30° case, as recorded by Ahmed, which is found to be the critical and unstable slant angle for flow regime change. The 30° slant angle has two behaviours: the high drag case, following the drag rising trend of previous slant angles; and low drag case, this latter being achieved by fixing a vertical splitter plate behind the model. Due to the unstable nature of the flow at this slant angle, a small perturbation triggers the flow regime change. For slant angles above and below 30°, there is no evidence of flow change when the splitter plate is added. Graysmith et al. [1994] tested only the high drag case while Strachan et al. [2007] tested the low drag version. For the later, it can be concluded from the results that at the critical 30° angle, there is an interference from the overhead supporting structure which may cause the separation bubble to burst between the 25° and 30° slant measurements. The trend is similar for the three cases, with a maximum offset of 10% between Ahmed and Strachan's experiments.

Lift coefficient data were not measured in the Ahmed original experiment and a comparison was performed with Graysmith et al. [1994] data in Figure 7-18b. The comparison shows similar lift coefficient trend for both studies, with a maximum offset of 20% between both studies.

A comparison between vertical velocity V from these two LDA investigations, displaying a plane of data at the top end of the trailing edge for the 25° back angle is shown in Figure 7-19. The plots are of the V velocity component non-dimensionalised with respect to the free-stream velocity, showing both the two counter-rotating vortices being shed from the back end. Although the free stream velocity in Lienhart et al. [2002] experiments was higher than



(a) Drag coefficient **(b)** Lift coefficient

Figure 7-18: Lift and drag coefficient comparison chart. Reproduction from Strachan et al. [2007].

Strachan et al. [2007], the overhead struts seems to be the main cause of the reduction on the intensity of the slant vortices in the latter case, which turns Lienhart et al. [2002] flow visualization image on the upper portion more reliable.

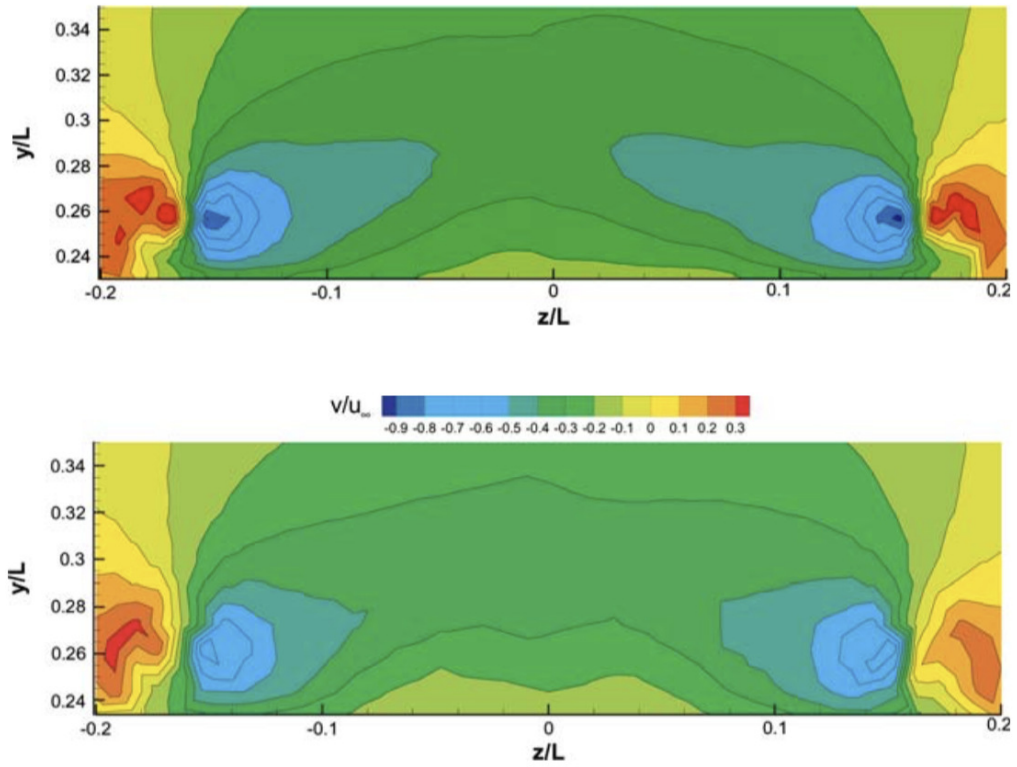


Figure 7-19: Comparative plots of normalized vertical velocity V on $X/L_l = 0$ plane for the Ahmed Body with slant angle of 25° for Lienhart et al. [2002] (top) and Strachan et al. [2007] (bottom). Reproduction from Strachan et al. [2007]

Strachan et al. [2007] made additional measurements on the 0° and 40 ° cases and identified lower vortices being shredded from the underbody of the Ahmed body. This finding was not previously reported by other authors mainly because the use of fixing studs to place the Ahmed body on the balance in fixed ground conditions. The study, however, don't identify where those structures are generated from and will be assessed in next Section of this Ahmed body work. Contour of normalized vertical velocity V on plane $X/L_l = 0.048$, are shown in Figure 7-20 for two different slant angles: 40° (left) and 0° (right). Comparative results shows that the lower vortex on the left (slant angle of 40°) is more intense and have bigger core than the right one (slant angle of 0°). This should be related to the flow at the base of the Ahmed body, where the left case has smaller wake compared to the right case. The smaller wake leads the vortex to develop downstream, whereas the bigger wake seems to drag it inwards.

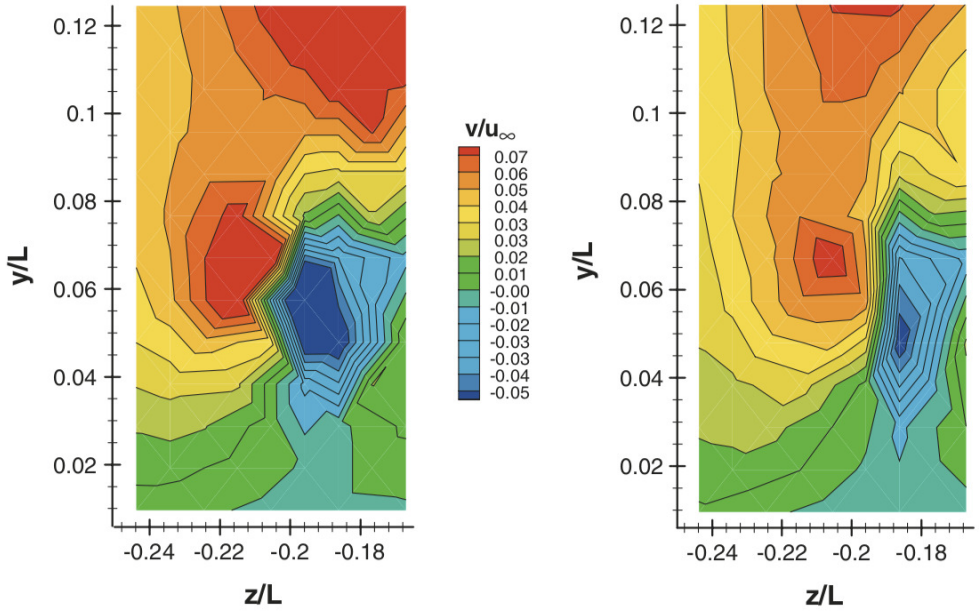


Figure 7-20: Plots of normalized vertical velocity V on plane $X/L_l = 0.048$ showing the presence of counter-rotating vortex close to the underbody. Results for the Ahmed body with 40° slant angle are on the left and for 0° slant angle on the right. Reproduction from Strachan et al. [2007].

The conclusion for flow structure near the slant, is that Lienhart et al. [2002] plots are the most accurate in terms of the real flow physics, as the upper support is not installed, conclusion also highlighted in Strachan et al. [2007] work, so it will be the benchmark for correlation results here presented. The vortex shedding phenomena on the lower portion of the Ahmed Body mainly due to the absence of the fixing studs on the floor and because of the ground simulation, however there is still no indication where those structures rise from. Drag and lift coefficient results show similar trend for the experimental data presented, considering fixed and moving ground, where the slant angle of 30° is the critical angle for maximum drag and lift and by adding a splitter plate, it suddenly drops.

Pagliarella [2009] investigated the aerodynamic performance of the Ahmed body platoons, using both slant angles of 25° and 35°. These two slant angles are considered the pre and post-critical slant angles, where the aerodynamic properties and flow regime suddenly change. Before studying the platoons, both isolated Ahmed bodies were validated in the RMIT wind tunnel, as the test section has elevated turbulence intensity levels when compared to previous experiments, reaching 1.8%. Tests were performed with 75% scale models and results are reported for a Reynolds number of $Re = 1.8 \times 10^6$ and static ground condition. Qualitative and quantitative results corroborated with previous literature. Focusing on the results for the slant angle of 25°, surface plot over the slant, shown in Figure 7-21 confirms presence of the side vortex, consistent with results from Ahmed et al. [1984], Lienhart et al. [2002] and Strachan et al. [2007].



Figure 7-21: Flow patterns over the slant of an Ahmed body with slant angle of 25°. Reproduction from Pagliarella [2009].

We've presented the main experimental references for the Ahmed body studies and which are also going to be employed throughout this work as a comparison for validation studies. The following section presents correlation studies using computational CFD simulations for the Ahmed body to pursue latter references results.

7-2-2 Ahmed body correlation studies

For the two most popular slant angles, 35° and 25°, several correlation studies have been published, in which the first case, due to its flow topology, presents good correlation between CFD and physical tests. The case considering slant angle of 25° is still a challenge for the computational community due to the flow complexity.

Considering the correlation cases, Guilmineau [2008] considered a Reynolds Average Navier-Stokes (RANS) simulation considering different turbulence models over an Ahmed body with both 35° and 25° angles, considering the same static ground and Reynolds number as Lienhart et al. [2002]. For the first case, all turbulence models, except Spalart-Allmaras predicted the drag coefficient results with a 10% difference from experiments without the ground fixing support. By considering the ground fixing support only performed for the 35° slant angle, the Explicit Algebraic Reynolds Stress Model (EARSM) model gave the best estimate of the drag. Flow structures were not fully reproduced for both cases, as presented in Figure 7-22 for the case considering slant angle of 35° in contours of turbulent kinetic energy, in which the rear wake intensity is clearly under-predicted even for the case considering turbulence EARSM with the fixing studs, which has the best agreement for drag coefficient. When analysing the flow results for the case considering slant angle of 25° by iso-velocity plots on the same plane $X/L_l = 0.077$, the RANS methodology predicts most of the structures, however the location and intensity are not matching with experimental results, as presented in Figure 7-23, which lead most of the research on this type of bluff body to move to DES and LES methodologies.

Another correlation example is shown on Huminic and Huminic [2010] studies where the main focus is the effect of underbody diffusers on an Ahmed Body with slant angle of 35° and moving ground simulations. In this section, the focus is only on the correlation study proposed,

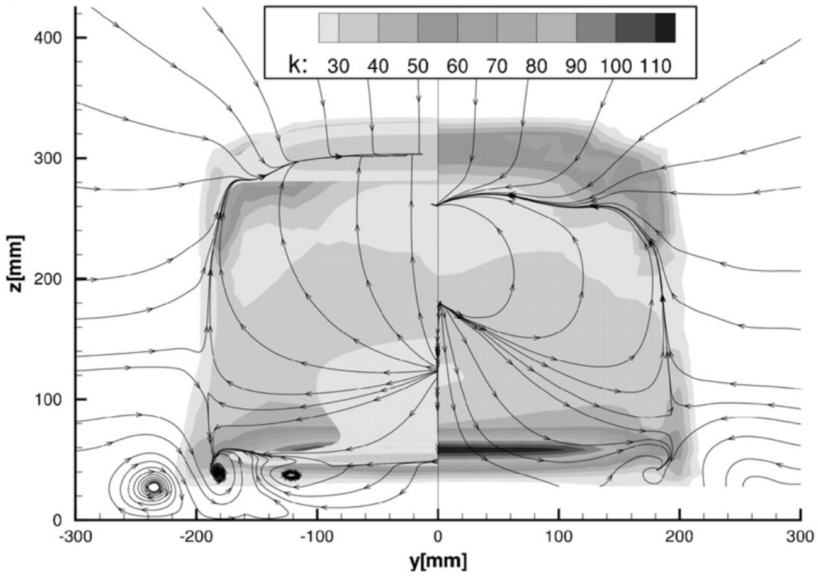


Figure 7-22: Plots of turbulent kinetic energy and streamlines at $X/L_l = 0.077$ for the Ahmed body with slant angle of 35°, showing simulation results for EARSM turbulence model (left) and experiment (right); Reproduction from Guilmineau [2008]

where the model is first validated with experimental results provided by Strachan et al. [2007] wind tunnel test. It was considered a higher Reynolds number than the comparison case, claiming that the mesh methodology and the commercial code CFX, combined with a $K-\omega$ SST turbulence model, presented excellent results in terms of drag coefficient but the lift coefficient presented results around 5 times smaller than experimental reference. Due to this fact, results from the variation of the diffuser angles studied were reported in increments rather than absolute values. Authors claim that the correlation in terms of flow structures matches with experiments, however no metrics are provided.

Considering new computational approaches and methodologies aiming to reproduce the flow around the Ahmed Body with slant angle of 25°, Guilmineau et al. [2011] first employed a Detached Eddy Simulation (DES) solution combined with $k-\omega$ turbulence model on an Ahmed body. Two modified versions of the DES approach, adding extra functions were also evaluated and referred as $F1$ and $F2$. The author wanted to reproduce same conditions as used on Lienhart et al. [2002] experiment, employing the ISIS-CFD academic code, same as employed on his previous work of Guilmineau [2008]. A comparison with the EARSM RANS model was also considered in order to take the best outcome from the previous study. Results shows that the DES-Shear Stress Transport (SST) model, give a better solution compared with the RANS solution in terms of flow behaviour. The rear wake profile at $Y = 0$, is presented in Figure 7-24, where most flow structures are observed although their intensity are under-predicted or in different position when comparing to experimental reference. The drag coefficient value is not correctly predicted by the DES approaches, over-predicting the experimental results in 20-30% and first highlight the trade-off between capturing the flow physics or predicting the correct drag coefficient for this complex Ahmed body style.

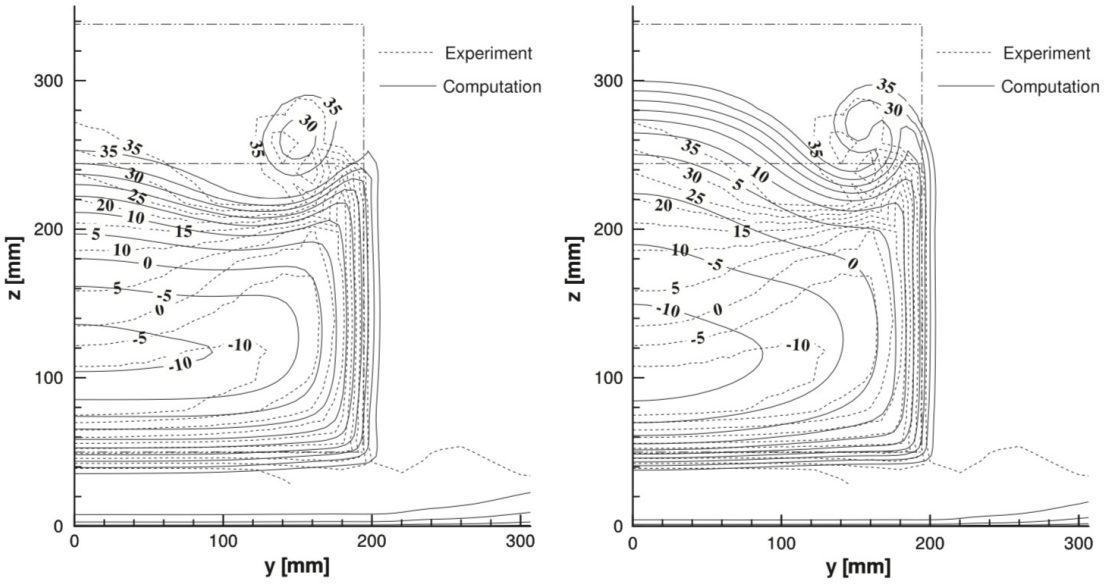


Figure 7-23: Plots of iso-velocity and streamlines at $X/L_l = 0.077$ for the Ahmed body with slant angle of 25° showing simulation results for Spalart-Allmaras turbulence model (left) and $K-\omega$ SST turbulence model (right); Reproduction from Guilmineau [2008]

Following his previous work considering hybrid RANS-LES simulations, Guilmineau et al. [2017] performed a new study for the Ahmed Body with both 35° and 25° slant angles, considering a comparison between RANS methodology with $K-\omega$ SST model, the EARSM model (both from Guilmineau [2008], the DES model (Guilmineau et al. [2011] and a new approach named Improved Delay Detached Eddy Simulation (IDDES) also based on $K-\omega$ SST model. The results for the slant angle of 35° suggested that all model predicted well the behaviour and values, with slight advantage for the IDDES model, as presented in Figure 7-25. The aerodynamic quantities for this Ahmed body slant angle still show better agreement with RANS solutions, where the new IDDES case is 34% higher than Ahmed et al. [1984] reference for the drag coefficient.

For the 25° cases, only the IDDES model was able to represent the recirculation bubble, providing a good agreement with the experimental data from Lienhart et al. [2002]. We highlight the correlation level on plane $X/L_l = 0.077$, as presented in Figure 7-26, achieved by using a h-type refined mesh. Drag and lift coefficient values presented maximum variation around 33% between the studies, however additional experimental references were considered, reaching a better agreement with the IDDES quantitative results. We understand that the authors presented additional references to point out differences in experimental results. The aerodynamic quantities results differences might be related to scale of the model evaluated, different wind tunnel conditions, equipment's uncertainty, which are not presented.

Moving to pure LES studies, Krajnović and Davidson [2004] was the pioneer of LES simulation the Ahmed Body. In his study, it was considered a Smagorinsky-LES model in order to model the flow around the Ahmed body with slant angle of 25° with similar conditions proposed by Lienhart et al. [2002]. The Reynolds number however, was reduced to $Re = 2.0 \times 10^5$ for the simulation. Flow results showed that the LES approach is able to predict a wide range in size

	Coarse mesh	Medium mesh	Fine mesh
C_D	0.4120	0.4159	0.4201

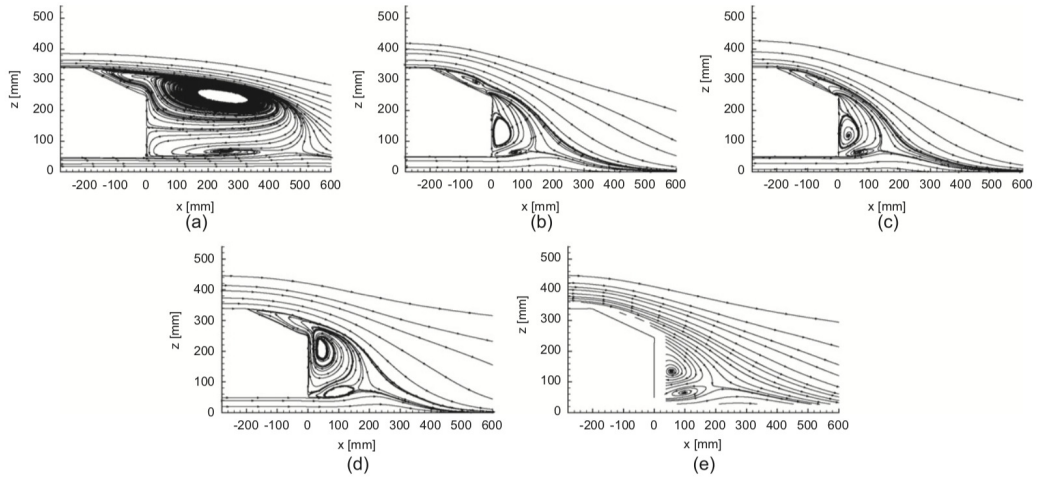


Figure 7-24: Drag coefficient for 3 mesh refinement cases and time-averaged streamlines in the symmetry plane Y equals 40 mm. (a) EARSM, (b) DES-SST, (c) DES-SST-F1, (d) DES-SST-F2, (e) experiments. Guilmineau et al. [2011]

of the turbulent scales around the rear slant surface. Shear stress lines on the slant surface, illustrated in Figure 7-27, shows good agreement with results found by Lienhart et al. [2002]. The vortical structure on the side of the body is clearly observed, while the flow over the slant is slightly different.

One of the most interesting features identified by the study of Krajnović and Davidson [2004] is the identification of a pair of vortices on the lower side portion of the body. This new flow structure appeared as the model doesn't have the fixing studs, even though it has fixed ground condition. It is claimed that the vortex first grow and later shrink in diameter and is presented in Figure 7-28. This flow structure is of great interest in the present work, due to the proximity of the rear underbody diffusers and is presented on next Chapter.

The latest achievements in the high fidelity turbulence models around an Ahmed Body with slant angle of 25° are summarized in the compilation work presented by Serre et al. [2013], in which a comparative analysis of recent simulations is presented. The research was conducted in the framework of a French-German collaboration using LES simultions with Reynolds number of 768,000, similar conditions as the original Ahmed body experiment (Ahmed et al. [1984] and Lienhart et al. [2002]) for comparative reasons. It presents results obtained with different four eddy-resolving modelling approaches, with two LES on body-fitted curvilinear grids: LES with Smagorinsky model and wall function (LES-NWM) and Wall-resolving LES with dynamic Smagorinsky model (LES-NWR), a stabilized spectral method with SVV (LES-SVV), similar to the one used in this present work, and a DES-SST approach. Results of the flow field shows good agreement with results measured by Lienhart et al. [2002] for the case LES-NWM, as presented in Figure 7-29.

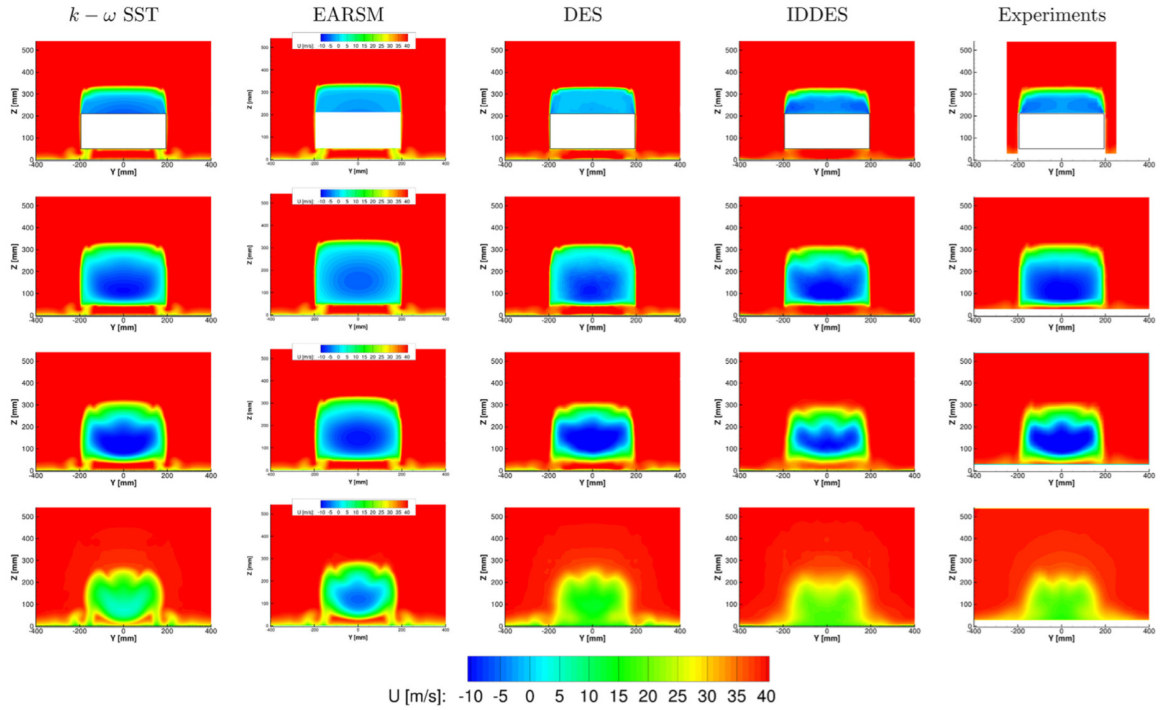


Figure 7-25: Iso-contours of the streamwise velocity U in YZ-planes the wake of the Ahmed body with slant angle of 35°. From top to bottom, the rows correspond to normalized X location $X/L_l = 0$, $X/L_l = 0.077$, $X/L_l = 0.191$ and $X/L_l = 0.479$, respectively. Reproduction from Guilmineau et al. [2017]

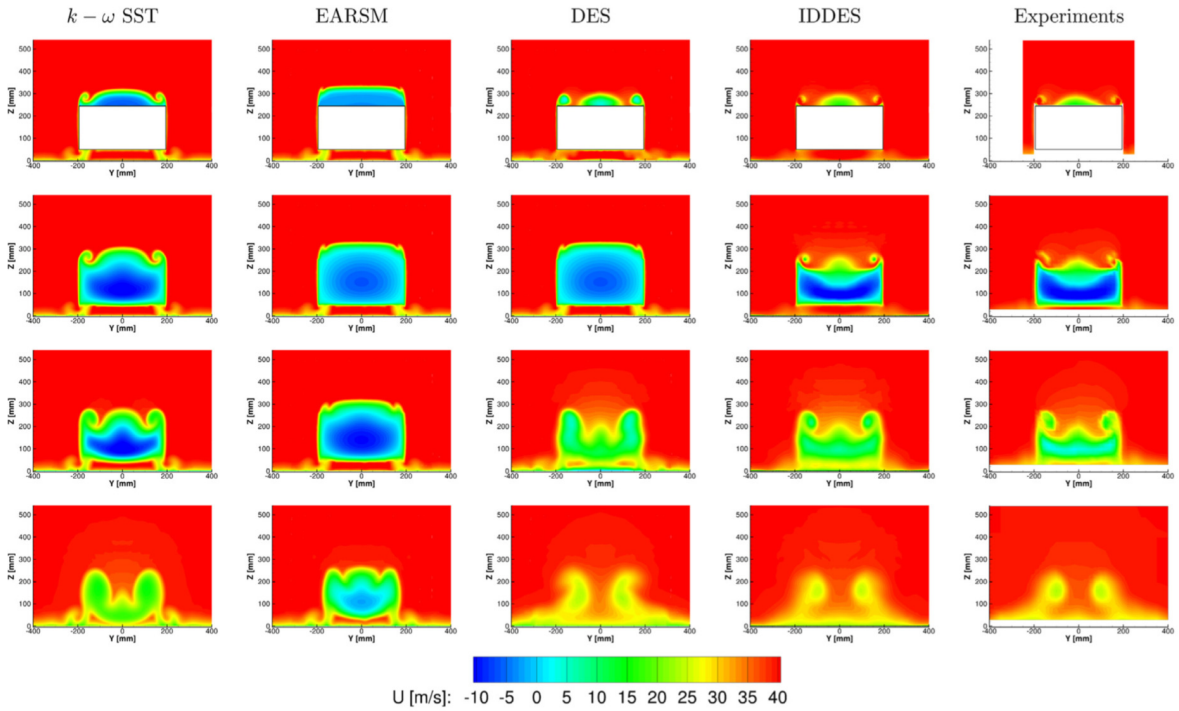


Figure 7-26: Iso-contours of the streamwise velocity U in YZ-planes the wake of the Ahmed body with slant angle of 25°. From top to bottom, the rows correspond to normalized X location $X/L_l = 0$, $X/L_l = 0.077$, $X/L_l = 0.191$ and $X/L_l = 0.479$, respectively. Reproduction from Guilmineau et al. [2017]

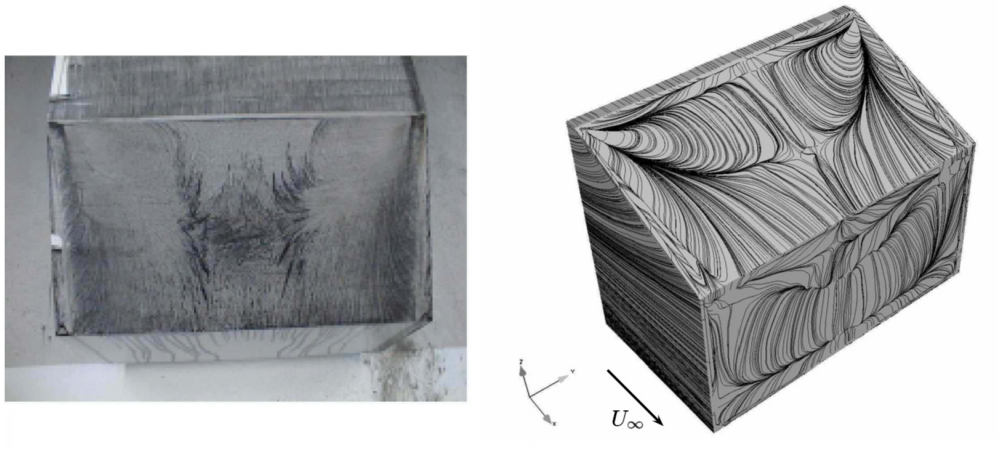


Figure 7-27: Comparison of surface flow visualization from Lienhart et al. [2002] experiments (left) with time-averaged flow lines on the surface of the body from Krajnović and Davidson [2004] (right). Reproduction from Krajnović and Davidson [2004]

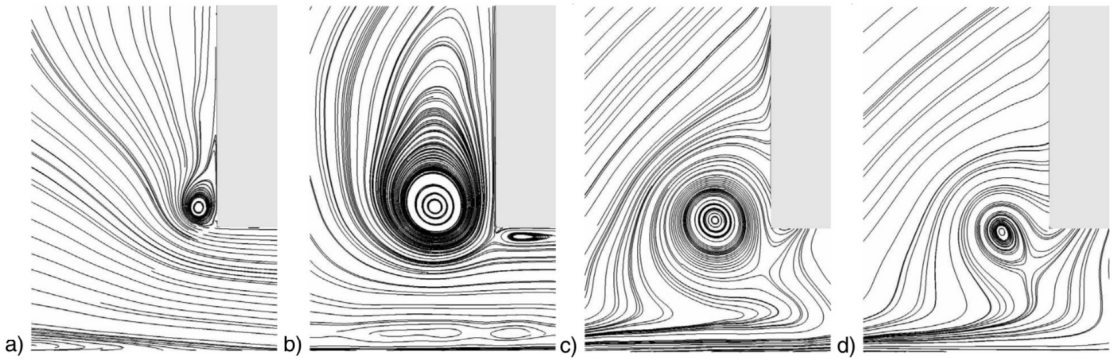


Figure 7-28: Comparison of time-averaged streamlines projected onto planes: a) $X/L_l = -0.749$, b) $X/L_l = -0.251$, c) $X/L_l = 0.047$ and d) $X/L_l = 0.096$. Front view of the lower-left edge of the body where the direction of the vortex rotation is clockwise. Reproduction from Krajnović and Davidson [2004]

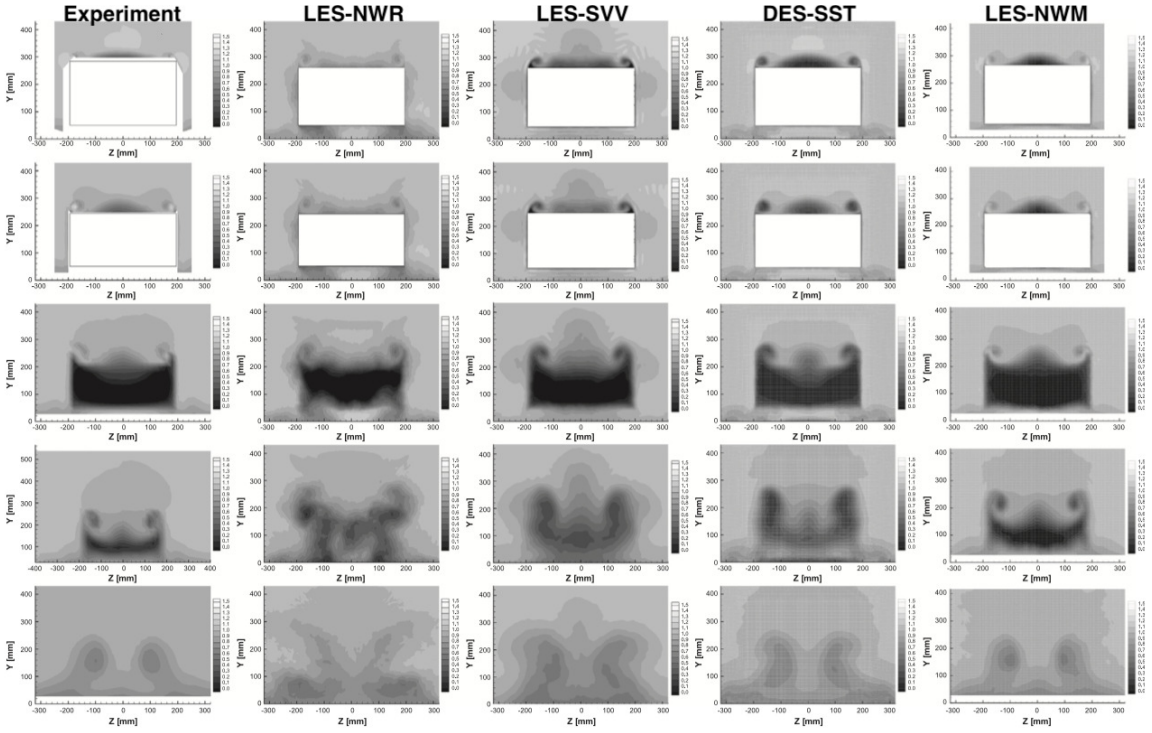


Figure 7-29: Contours of the mean streamwise velocity U in YZ-planes in the wake of the Ahmed body with slant angle of 25°. From left to right the experimental measurements of Lienhart et al. [2002] and the results of LES-NWR, LES-SVV, DES-SST and LES-NWM, respectively. From top to bottom, the rows correspond to the locations $X/L_l = 0.036$, $X/L_l = 0$, $X/L_l = 0.074$, $X/L_l = 0.190$, $X/L_l = 0.48$, respectively, with the origin x = 0 located at the slant end of the body. Serre et al. [2013]

In the LES-SVV case presented, the LES numerical solver is based on a multi-domain Chebyshev-Fourier pseudo-spectral method presented in detail at Minguez et al. [2008]. The time scheme is globally second-order accurate, with a BDF2 implicit treatment of the diffusion terms and a RK4 explicit one of the convection terms, through a semi-Lagrangian method. The geometry is defined by the volume pseudo-penalization proposed in Pasquetti et al. [2008] in 21×10^6 points grid. The spectral vanishing viscosity technique is used introduce some artificial viscosity in the high-frequency range of the spectral approximation which accounts for the unresolved turbulent dissipation. The LES-SVV methodology was the only to correctly captures the reattachment of the flow over the slant among the cases presented on Serre et al. [2013], illustrated in Figure 7-30. This is a good indicative of the potential in the LES-SVV methodology.

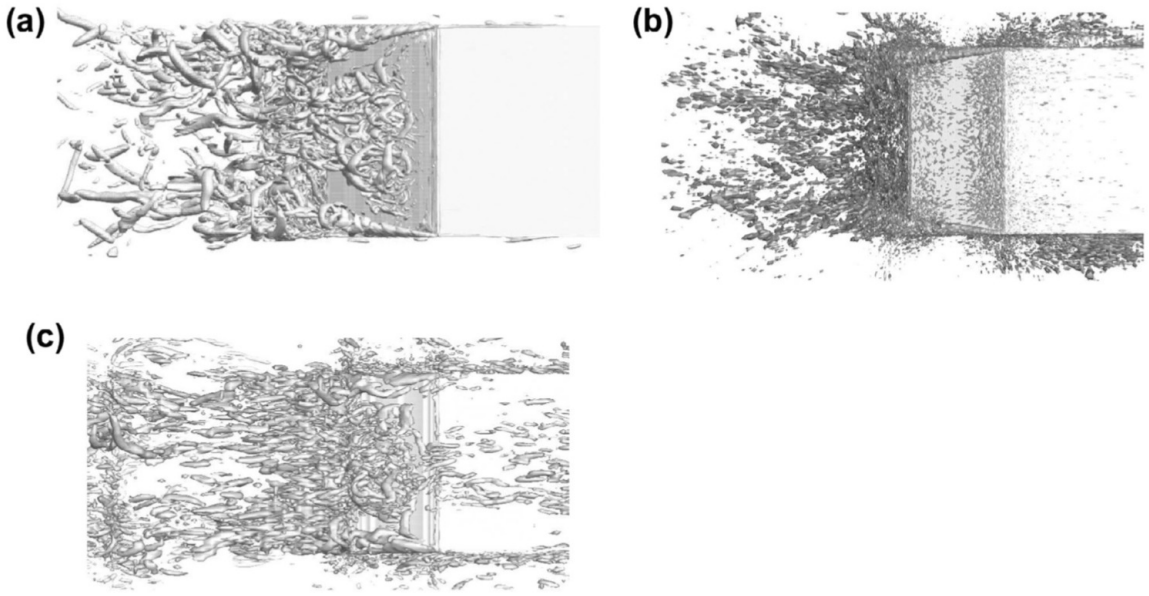


Figure 7-30: Top views showing iso-surfaces of the Q-criterion (Q = 60) indicating the vortex development over the slant: (a) DES-SST, (b) LES-NWR, (c) LES-SVV. Reproduction of Serre et al. [2013]

Considering the drag coefficient, both LES-NWR and DES-SST overestimated the value in around 16%; the LES-NWM presented a difference around 6%, which is reliable for industrial applications. The LES-SVV model better modelled the flow behaviour compared to previous models, however the drag difference was around 44%. An explanation for this could be by not correct solving the turbulent boundary layer in the simulation. This difference may be explained by having insufficient numerical dissipation due to the nature of the method and low solution polynomial order. The studies presented on this thesis aims to improve the confidence level of LES-SVV simulations for industrial applications.

7-2-3 Wake dynamics and flow structures

Bluff body flows are characterised by large regions of separated flow. The variation of the slant angle on the Ahmed body leading to different flow dynamics on that surface, influencing the wake behind the body. Free shear layers detaching from the body walls can interact, creating vortical wakes, a combination of separated flow and vortices on the flow downstream of the bluff body. When studying wake dynamics, we are interested first on identifying dominant flow structures, such as vortices and how they interact further downstream as stated by Bearman [1993]. Vortical wakes can trigger a highly unsteady flow downstream of the bluff body which might increasing the turbulence level of the flow.

The most common method to characterise the wake dynamics and identify oscillatory behaviour is by determining the Strouhal number. More advanced and complete techniques to study wake dynamics include Dynamic mode decomposition (DMD) and Proper Orthogonal Decomposition (POD). DMD computes a set of modes each of which is associated with a fixed oscillation frequency and decay/growth rate. POD was introduced as an attempt to decompose turbulence into a set of deterministic functions or POD modes, each capturing some portion of the total fluctuating kinetic energy, giving some idea about the flow structure.

A particular wake behaviour is found for the Ahmed body squared back, in which the slant angle is zero. At this Ahmed body slant configuration, the wake has a bi-stable behaviour, identified as a random displacement of the wake between preferred off-centre locations, according to Dalla Longa et al. [2019]. This behaviour was first verified for the Ahmed body squared back with laminar flow by Grandemange et al. [2012], where above a critical Reynolds number, the wake is no longer instantaneous symmetric, setting itself as one of the two possible asymmetric states, depending on the experiment initial conditions.

Analysing the same Ahmed body squared back considering turbulent flow at high Reynolds number, similar symmetry breaking flow is observed, however for this flow condition, there is a wake switching between different asymmetric states, as verified by Grandemange et al. [2013] and Dalla Longa et al. [2019]. Such a complex and unstable flow still poses a challenge for both experimental and computational simulations.

We selected the Ahmed body with slant angle of 25° as the validation case because the flow over this body is fully characterised and validated. This case however still challenges computational simulations due to a complex flow structure, combining flow separation and a pair of vortices over the slant.

7-3 Numerical Simulation of Ahmed Body with Spectral/hp Element Method

7-3-1 Objectives

The Ahmed body case with slant angle of 35° have extensive literature on flow phenomena and aerodynamic properties validation, even considering simplified CFD methods such as the steady RANS. The Ahmed body shape considering slant angle of 25° is still a challenge for computational simulations, even with some good improvements presented by the use of hybrid RANS-LES and LES models.

This part of the work focuses on the correlation study between a computational and physical model of an Ahmed Body with slant angle of 25°. Physical test conditions and tunnel test section dimensions are considered similar from the wind tunnel experiment performed by Strachan et al. [2007] which considers the Reynolds number $Re = 1.7 \times 10^6$ and moving ground condition.

Simulations employing RANS solution are able to predict with good accuracy the drag coefficient, even for cases with complex flow topology, such as the slant angle of 25°. The correlation level is around 95% compared to experimental results, however the flow physics does not agree, usually under-estimating the flow features, as previously presented on 7-2-2. Attempts considering more refined methodologies such as DES and LES provide better correlation with experiments when comparing the flow structures, but aerodynamic quantities values are less accurate.

The solution proposed for the CFD simulations performed combines an implicit LES-SVV solution with a spectral/hp element method. This method combines both classical mesh refinement (h), with higher polynomial order (P) for higher fidelity modelling available on the code Nektar++. The CG-SVV with DG mimicking Kernel works as a filter for high frequencies in order to stabilize the solution for high Reynolds numbers, as previously presented in section 6-1.

Two relatively coarse mesh configurations are evaluated considering different h-refinements which are referred as *Original* and *Refined* meshes, denoted with (-A) and (-R) respectively in the naming convention. In each of those meshes, three surface curvature discretisation are evaluated: P_M of 4^{th}, 5^{th} and 6^{th} order. To make use of the flexibility of the spectral/hp element method, we selected polynomials expansion P_N with accuracy order higher than 3^{rd} for two main reasons: evaluate the capability of the code Nektar++ to handle high-order polynomial solutions for 3D geometries and the second reason is to achieve similar number of degrees of freedom (DOF) of a LES simulation case on a coarse mesh. The polynomial expansions here proposed and evaluated are: P_N of 4^{th}, 5^{th} and 6^{th} order for accuracy.

Results are compared with the main reference experiment of Strachan et al. [2007] for the aerodynamic quantities, as it considers rolling road simulation. For the flow structures, however, we consider Strachan's postulate for the upper body by using Lienhart et al. [2002] experiment. The experiment of Lienhart et al. [2002] represents with higher accuracy the real flow behaviour over the slant since it doesn't have a support fixing the body from the top, influencing the flow. We additionally present a comparison of the full Ahmed body with the proposed methodology of using through a symmetry plane. We aim to evaluate the differences in the main aerodynamic coefficients as well as in the flow behaviour.

7-3-2 Simulation configuration

The present study is performed taking into account the Ahmed body model with slant angle of 25° as the baseline model. As this research is focused in automotive applications, we aim to reproduce the closest boundary conditions of a vehicle moving on a road. One of the main experimental references that evaluates the Ahmed body in moving ground conditions is the work from Strachan et al. [2007]. We selected this study as the baseline for our simulation setup, using same Reynolds number, similar test section domain and moving ground. In what

follows, we will use a coordinate system with X the streamwise direction, Z the spanwise direction and Y the vertical direction for all Ahmed body simulations.

The geometry of the domain was generated on a Computer Aided Design (CAD) software and exported in $STEP203$ format, with the Ahmed body in full scale dimensions, as presented in Figure 7-10 and 7-1-4. The wind tunnel test section dimensions are the same of Strachan's study, which are 1,660 mm × 2,740 mm and total length of 4,096 mm, equivalent to four Ahmed body lengths L_l. Only half of the model was created, and a symmetry plane was employed. This kind of model allows that all the proposed cases to be solve in a short computational time and it is also a common practice on the automotive and motor racing industries.

The Ahmed body model is placed on a vertical distance $h = 50$ mm from the ground, as in the original experiment of Ahmed et al. [1984] and Strachan et al. [2007]. The model has its rear end on the coordinate $X = 0$ of the virtual domain, following similar model position used in Strachan et al. [2007]. Wind tunnel inlet is positioned at $X = -2L_l$ and outlet at $X = 2L_l$ with a total X length of $4L_l$, which represents the wind tunnel length. Using appropriate boundary conditions for spectral/hp element method, this domain is reasonable for the current study.

Mesh is generated with the software NekMesh following the pipeline presented on 6-2-3. The first input requirement for the mesh generation is to provide the CAD geometry in STEP format combined with the appropriate domain type. The domain type selected for all simulations in this research is 3-dimensional (3D) with prismatic boundary layer on the external surfaces. Four numerical parameters are required to generate the high-order mesh, which are minimum and maximum mesh element sizes (h), a sensitivity factor to the curvature parameter (EPS) and order of the polynomial for the high-order mesh P_M. The system uses a curvature-based refinement and smoothness algorithms to obtain mesh sizing automatically.

The following parameters are required for the boundary layer generation in the mesh configure file (MCF): surface id where the boundary layer will be generated; boundary layer total thickness L_{BL}, also defined as the macro-prism layer height; number of layers N_{BL} in which the macro-prism layer will be divided; and boundary layer growth rate GR.

Mesh refinement regions are also specified on the volumetric mesh in different regions of the domain, aiming to add extra resolution and smoother mesh size transition in order to avoid problematic elements. The study here presented considered two different mesh configurations in terms of h-refinements, defined as *Original* and *Refined* meshes, based on the same CAD geometry and with same boundary layer setup. The possibility of evaluating two different meshes in terms of elements resolution complements the polynomial order. For 3D cases, both resolution refinement approaches should be combined to reach the best solution in a reliable time.

The study also proposes the evaluation of three high-order meshes for both *Original* and *Refined* cases, considering the first P_M of 4^{th} order, as previous reference studies from Turner et al. [2017]. In addition to previous reference, we propose increasing the polynomial resolution of the curved elements P_M to both 5^{th} and 6^{th} order. The latter was selected to use for complex wing elements, according to a confidential study. We aim to evaluate the sensitivity of the curved high-order mesh when applied to the Ahmed body. This bluff body geometry has several sharp transitions, but also has a curved surface on the frontal stagnation.

Two h-refinement zones are applied for all Ahmed body simulations. The first h-refinement zone is created over the Ahmed Body full length, referred as Ahmed body refinement, ranging from 0.3 L_l before and 0.3 L_l after the end of the body. The second h-refinement, referred as wake refinement is applied on the wake region, intercepting the first region in -0.3 L_l before the end of the body, to 1.3 L_l after the end of the body. The wake refinement and overlap with smaller elements are applied in order to fully capture the flow phenomena in the separation region. Mesh refinement regions considering the *Original* mesh are illustrated in Figure 7-31 on the plane $Z = 0$.

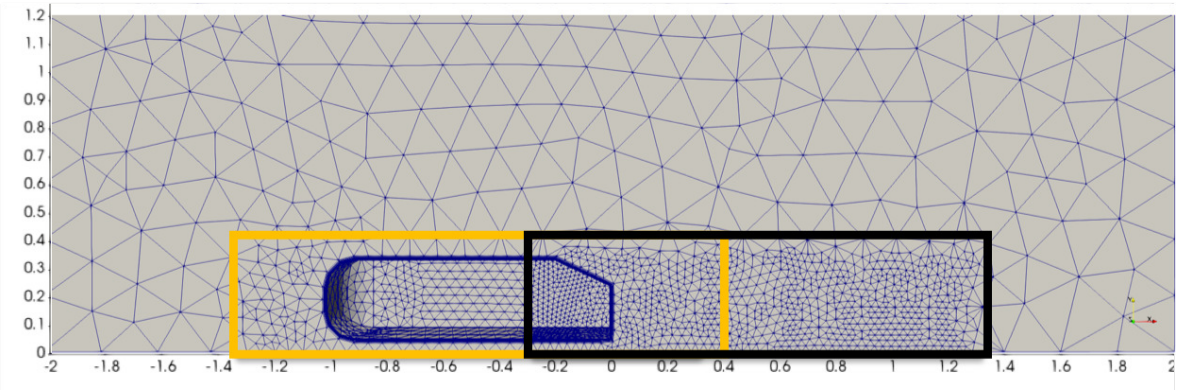


Figure 7-31: Plane view $Z = 0$ indicating the location of the refinement boxes on the Ahmed body model for the *Original* mesh case. The Ahmed body refinement region is indicated in yellow and the wake refinement region is indicated in black.

Once the refinement regions are presented, we indicate the mesh parameters for the proposed mesh cases. The *Original* mesh is generated with a total number of elements N_{EL} for half model around 94,000 mesh elements, where around 14,000 are prismatic elements N_P and 80,000 are tetrahedra elements N_T. The mesh configuration parameters on NekMesh, typically found in the automotive industry, are presented below in function of L_l, which the length of the Ahmed body as previously defined.

- Min length $h_{min} = 0.01\ L_l$;
- Max length $h_{max} = 0.2\ L_l$;
- EPS = 0.1;
- Mesh order P_M: 4^{th}, 5^{th} and 6^{th};
- Boundary Layer total thickness (macro-prism layer) $L_{BL} = 0.022\ L_l$;
- Boundary Layers split number $N_{BL} = 10$;
- Boundary Layer growth rate $GR = 1.6$;
- Ahmed Body h-refinement zone length = $0.05\ L_l$;
- Wake h-refinement zone length = $0.03\ L_l$;

The first two parameters are the minimum and maximum length of the elements on the volumetric mesh to be generated, where the minimum size is imposed on the surface of the Ahmed body model. The maximum length applies for the far-field domain, such as the inlet, outlet and walls. Maximum length values are based on current RANS mesh strategies on both racing and automotive industries as presented on Magazoni et al. [2015] and Buscariolo et al. [2015]. The EPS value is the default sensitivity parameter to have a smooth curvature over complex geometries. Mesh order represents the high-order polynomial to increase the mesh curvature accuracy on the CAD surface. The first P_M order selected is 4^{th}, same as Turner et al. [2017] study, followed by generation of two additional high-order meshes with P_M of 5^{th} and 6^{th} order respectively.

What follows next are the settings for the boundary layer over the selected surfaces. We first input the boundary layer total height L_{BL}, composed by prismatic elements. The L_{BL} value is calculated based on the turbulent boundary layer equation, presented on 7-1. Based on the Reynolds number proposed for the Ahmed body simulations and its turbulent flow behaviour, the macro or total boundary layer thickness is 0.022 L_l.

$$L_{BL} = \frac{0.37 \times B}{Re^{\frac{1}{5}}} \tag{7-1}$$

where L_{BL} is the boundary layer total thickness and B is the reference length.

The number of layers N_{BL} and growth rate GR are the next parameters to be input. They were calculated in order to have a y^+ value around 1 on the first quadrature point when applying the high-order polynomial expansions for the solution P_N.

The last settings on the NekMesh script are for the mesh element size on the refinement zones previously presented. The refinement zone generation should be organized from the coarser to the most refined size. In this case, we start from the Ahmed body refinement zone with element size around $0.05L_l$ to the wake refinement considering element size around $0.03L_l$. In our case, the overlapped slant region has element size of the wake refinement zone.

As previously presented, we proposed a h-type mesh refinement case, referred as *Refined* mesh, to evaluate the sensitivity to the mesh parameter (h) in terms of the convergence and solution stability. This new mesh density on plane $Z = 0$, together with the refinement box are illustrated in Figure 7-32.

For this additional case, the boundary layer setup, domain and refinement zones dimensions were kept the same from the *Original* mesh. The number of elements generated N_{EL} for half model is around 335,000 mesh elements, where around 35,000 are prismatic elements N_P and 300,000 are tetrahedra elements N_T. The *Refined* mesh setup is presented as follow:

- Min length $h_{min} = 0.0075\ L_l$;
- Max length $h_{max} = 0.2\ L_l$;
- Mesh order P_M: 4^{th}, 5^{th} and 6^{th};
- Ahmed Body h-refinement zone length = $0.035\ L_l$;
- Wake h-refinement zone length = $0.02\ L_l$;

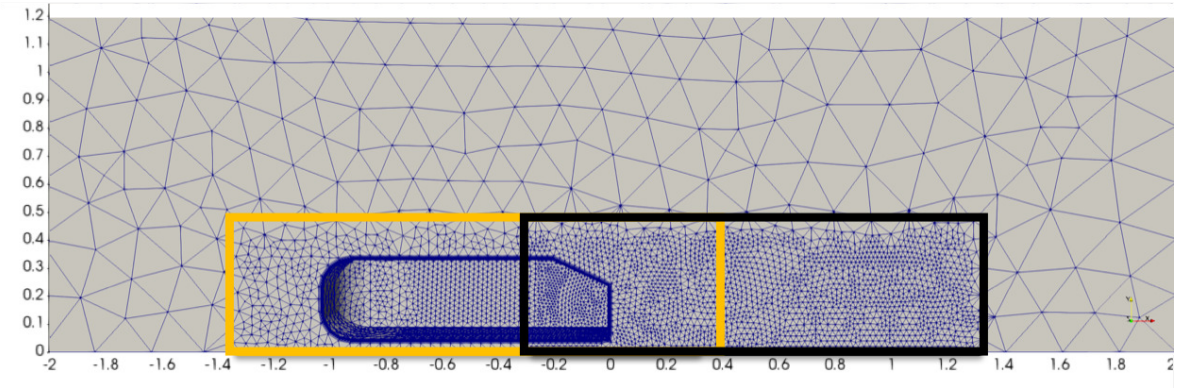


Figure 7-32: Plane view $Z = 0$ indicating the location of the refinement boxes on the Ahmed body model for the *Refined* mesh case. The Ahmed body refinement region is indicated in yellow and the wake refinement region is indicated in black.

Once the six high-order meshes are generated, high fidelity numerical simulations are performed, using the implicit LES simulations based on a spectral/hp element method. The selected the Nektar++ open source software for all simulations in this research. The solution on each element is approximated by a high-order polynomial, as presented on 5-3-2. As previously presented, three polynomial expansions P_N are selected and evaluated for each of the six meshes, in total eighteen cases were evaluated.

We can estimate the number of degrees of freedom (DOF) on each mesh case based on the number of elements on the mesh and the polynomial expansion of the solution P. The equations for converting the total number of prismatic N_{prism} and tetrahedra N_{tet} elements into DOFs are presented below:

$$DOF_{prism} = N_{prism} \times (\frac{P_N \times P_N \times (P_N + 1)}{2}) \tag{7-2}$$

$$DOF_{tet} = N_{tet} \times (\frac{P_N \times (P_N + 1) \times (P_N + 2)}{6}) \tag{7-3}$$

$$DOF_{total} = DOF_{prism} + DOF_{tet} \tag{7-4}$$

where DOF_{prism} is the total number of DOFs of all prismatic elements on a mesh, DOF_{tet} is the total number of DOFs of all tetrahedra elements on a mesh and DOF_{total} is total number of DOFs on a certain mesh.

As previously mentioned, we selected three polynomial expansion for the solution accuracy P_N and mesh order P_M, which are 4^{th} ($P_N = 4$), 5^{th} ($P_N = 5$) and 6^{th} ($P_N = 6$) order for each. The total number of DOFs for *Original* and *Refined* meshes evaluated are presented on Table 7-1, presented in millions of DOF.

From Equations 7-2 and 7-3, the mesh order P_M is not connected the total number of DOFs, as it only influence on the accuracy of CAD surface curvature representation however the polynomial expansion P_N increase the resolution of *Original* and *Refined* meshes, which are

Table 7-1: Resolution of the proposed simulations, showing total number of DOF (in Million) for each case evaluated, at different polynomial expansions accuracy P_N.

		$P_N = 4$	$P_N = 5$	$P_N = 6$
Original Mesh (-A)	$P_M = 4$	2.16	3.85	6.24
	$P_M = 5$	2.16	3.85	6.24
	$P_M = 6$	2.16	3.85	6.24
Refined Mesh (-R)	$P_M = 4$	7.40	13.13	21.21
	$P_M = 5$	7.40	13.13	21.21
	$P_M = 6$	7.40	13.13	21.21

relatively coarse compared to industrial cases. Comparing the number of DOFs of both *Original* and *Refined* mesh cases, we observe that the resolution increases almost 3 times when changing P_N from 4 to 6. The spectral/hp method main advantage is shown here, where a coarse mesh will have its resolution increased when the solution is performed, reaching similar levels as very refined meshes.

Solution convergence for all simulation here and further presented are controlled by keeping the Courant–Friedrichs–Lewy (CFL) condition around 1.0. This condition is required in order to correct propagate the information between the mesh and avoid negative numerical viscosity. The CFL condition for this research is proposed by Karniadakis and Sherwin [2013] and is determined by Equation 7-5:

$$CFL = max_1^{N_{hp}} 0.2 \Delta t V^{max} P_N^2 \tag{7-5}$$

where V^{max} is the maximum local velocity on a standard element of the mesh. In order to keep the CFL number condition, a low time step is required. The Δt required for simulations considering $P_N = 4$ is $\Delta t = 1 \times 10^{-4}$, for $P_N = 5$ the time step is reduced to $\Delta t = 5 \times 10^{-5}$ and finally for all $P_N = 6$ cases the time step employed is $\Delta t = 2.5 \times 10^{-5}$.

Considering the total length of the domain of $4L_l$, the total simulated time is 7 convective time units (CTU). The unit CTU refers to the number of times flow passes over a reference length, in this case the Ahmed body axial length L_l. CTU for all Ahmed bodies evaluated is defined as $CTU = U_\infty t_U / L_l$, where t_U is the total simulation time. Free stream velocity U is normalized to 1 in order to match the Reynolds number previously stated and set as the inlet boundary condition. The outlet is set as a high-order outflow condition, as proposed by Dong et al. [2014], which is applied to stabilize the solution avoiding flow reflection effects, thus the domain dimension become affordable. The virtual wind tunnel floor is set with the same velocity of the free stream to reproduce moving ground condition. The top and outer side wall as well as the Ahmed body are set as no slip condition and a symmetry condition applied to the inner wall, as shown on schematic Figure 7-33.

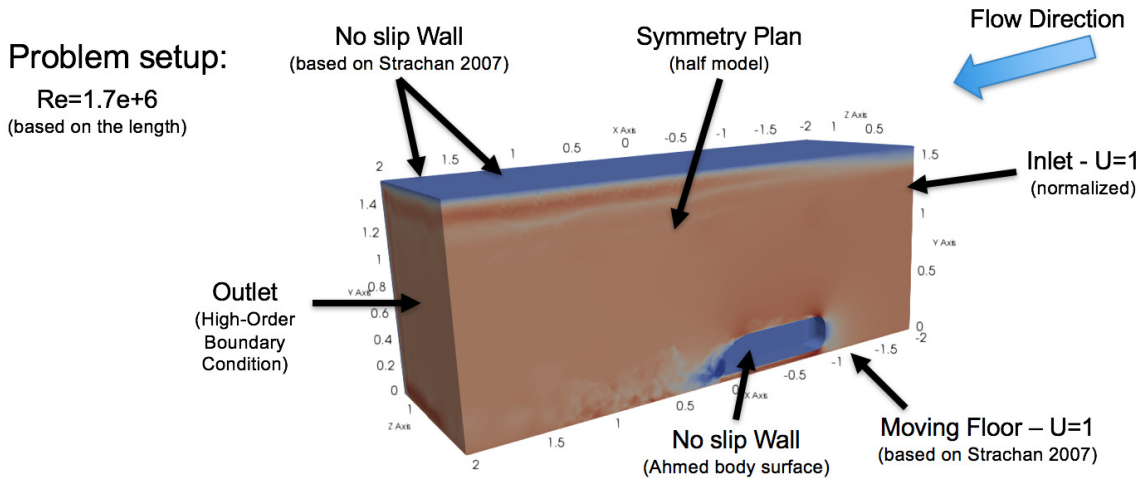


Figure 7-33: Mesh discretization considering normalized length of $1L$ for the body.

With the load cases set, simulations were performed on Imperial College's HPC at the CX2 cluster. The computational power used for each case required 18 nodes with 24 cores each, in a total of 432 computer processing units (CPUs) with 96Gb of RAM per node. Results are presented in the next section.

7-3-3 Results and analysis

For the Ahmed body with slant angle of 25°, we first present a comparative study between full model and half symmetric model, as motivated in Section 3-2. Both simulations follow similar meshing strategies and same solution criteria. The main focus is to compare averaged results for flow structures, aerodynamic quantities and required computational time.

Next, we present the details of the results for the half model. We first compare values regarding lift and drag coefficients for the cases evaluating at different mesh order P_M and the polynomial expansion order P_N over the *Original* (-A) and *Refined* (-R) mesh. This is followed by a comparison between the flow structures with experimental data in some planes on the slant and downstream. The same naming convection as in Section 6-3 for simulation configurations is used throughout.

Comparative results of iLES simulations with half (symmetric) models for exterior aerodynamics

Aiming to show the reliability of the results using symmetric models, we now present a comparison between full and half symmetric models. The comparison is performed using the NM66-R setup on half and full model. The standard for meshing and choice of domain size, as well as the boundary conditions are the same for both models. All results presented are the values averaged from the 5^{th} to the 7^{th} CTU, where the aerodynamic quantities behaviour become stable. The vortical structures in this type of vortex-dominated automotive flow

also become evident, with minor changes during the averaged period. Even though the wake structure needs longer average to converge, the focus of this research is the flow close to the body, where the results indicate that the most energetic structures of the flow and aerodynamic quantities results are reliable.

In terms of results for aerodynamic quantities, presented in Table 7-2, drag and lift coefficients are similar between the two cases. For the full model, the drag coefficient agreement compared to the experimental result improved while the lift coefficient show higher deviation. However, these variations between results are considered acceptable.

Table 7-2: Drag and lift averaged coefficient for the half symmetric and full body models, comparing with experimental values obtained from Strachan et al. [2007].

Case Model	**Average** C_D	**Average** C_L	**Difference Drag %**	**Difference Lift %**
Half symmetric	0.260	0.279	-13	1
Full body	0.266	0.273	-11	-2
Experiment	**0.298**	**0.280**		

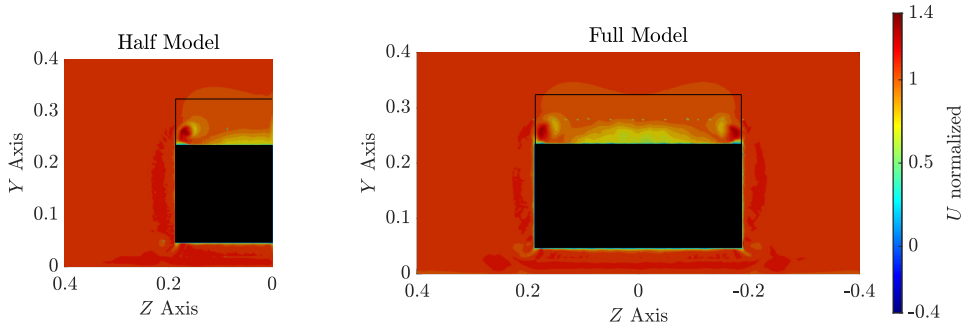
Next, we provide a flow comparison between averaged velocities from the 5^{th} to the 7^{th} CTU. Velocity comparison for U, V and W velocities on planes $X/L_l = 0$ and $X/L_l = 0.096$ are presented as in Figure 7-34, Figure 7-35 and Figure 7-36 respectively.

For normalized U, we observe similar velocity contours and shape for the slant vortex on planes $X/L_l = 0$ and $X/L_l = 0.096$. It is possible to observe a slight under-prediction on the slant of the half model. The wake over the slant on plane $X/L_l = 0$ has similar contours in both cases however is apparently bigger in the full model. This effect is less intense on plane $X/L_l = 0.096$, where only two small additional peaks are observed close to mid-span of the full model.

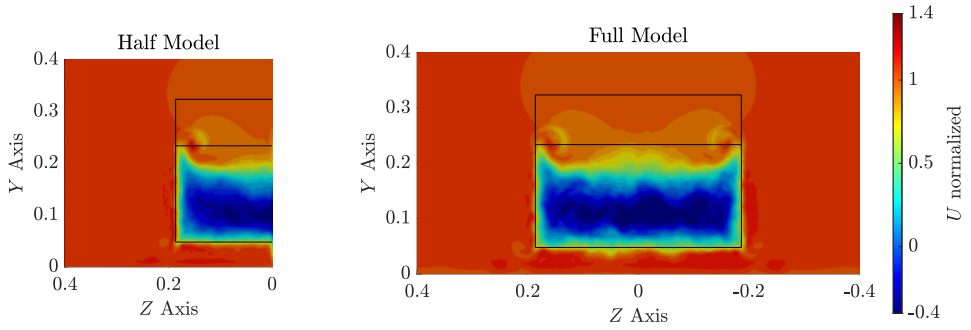
For vertical velocity V, results show good agreement for the velocity contours near the slant and lower side vortices, with similar shape and intensities when comparing half and full models. The only point of notice is that for the half model, rear wake on plane $X/L_l = 0.096$ seems slightly under-predicted.

Aiming to understand the influence of the spanwise velocity when the symmetry condition is applied, an additional plane over the slant ($X/L_l = -0.096$) is presented for the W velocity field. We observe that results for the plane $X/L_l = -0.096$ on the slant are qualitatively well-correlated between the half and full bodies for the same section. On the top of the slant close to $Z = 0$, the colour gradient matches in both cases, as well as the slant vortex. Moving further downstream to plane $X/L_l = 0$, the slant vortex is still in good agreement whereas we observe perturbations close to $Z = 0$ on the full model which are partially reproduced on the half model. On the last plane at $X/L_l = 0.096$, we observe once again the good qualitative agreement between half and full models contour on the upper slant region. For the lower side vortex, we found a good qualitative agreement between both cases, similar W velocity contours in all cases.

From U, V and W velocity contours, simulation results from the half and full models demonstrate an overall good qualitative agreement in terms of flow structures close to the body.



(a) Plane X/L_l=0

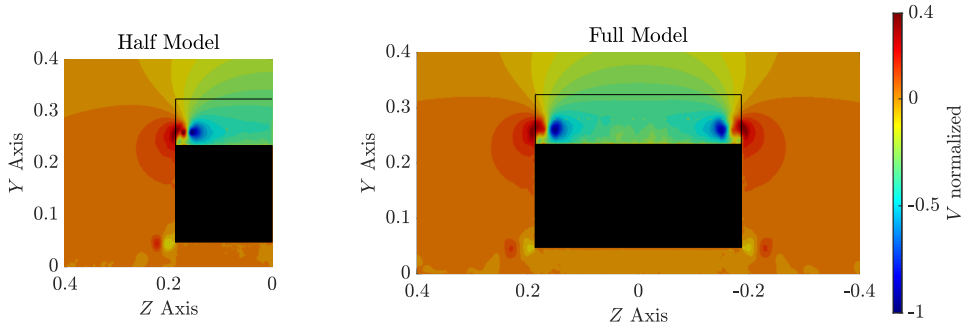


(b) Plane X/L_l=0.096

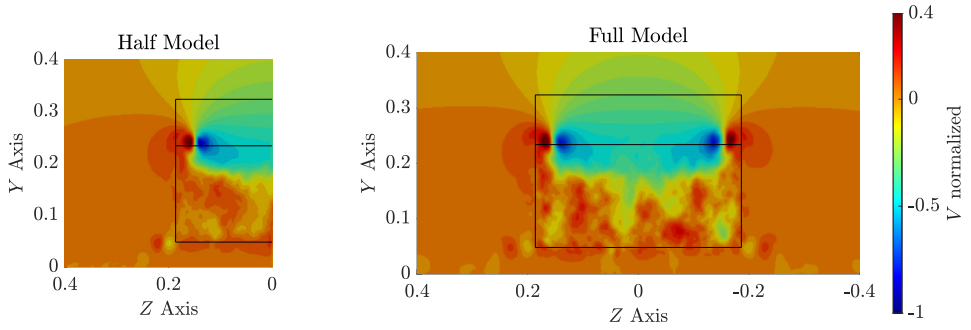
Figure 7-34: Comparison of normalized time-averaged U velocity for the symmetric model (left) against full model (right) on planes $X/L_l = 0$ (top) and $X/L_l = 0.096$ (bottom).

Downstream the Ahmed body, main flow features are still in good agreement at $X/L_l = 0.096$. At this location, the turbulent wake is slightly different on half model for V and W velocities compared to full model. Due to the short averaging period, the wake structures would not be symmetric, however the main flow features, such are the vortices, are represented. The quasi-symmetric behaviour of the wake require a longer average period, increasing the simulation time. However, from the experience of the author, there would be small influences on the main flow features and aerodynamic quantities for automotive application. The focus of this research is the flow close to the body and aerodynamic quantity values, which explain this approach.

Lastly, we compare the total computational time required for both simulations to reach 7 CTUs. Simulations for both models were performed at Imperial College London CX2 HPC facility, with 432 CPU cores for each case. The required time for half symmetric model is 80.4 hours whereas a full body model requires approximately 2.25 times of that, more than the expect 2 times due to more calculations and required computational power, reaching 179.5 hours in total. This drastic increase in computation time may directly impose constraints in the feasibility of certain numerical studies, when the allowed single wall time of the HPC is limited.



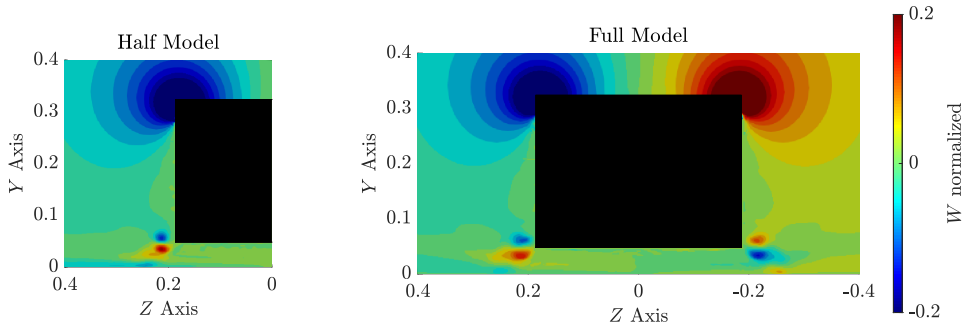
(a) Plane X/L_l=0



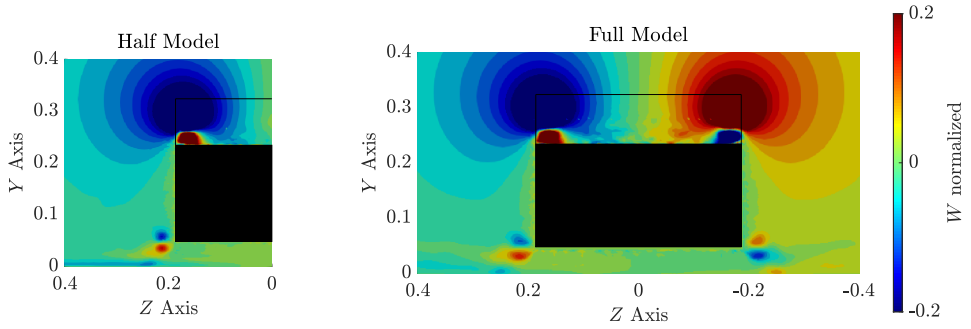
(b) Plane X/L_l=0.096

Figure 7-35: Comparison of normalized V velocity for the symmetric model (left) against full model (right) on planes $X/L_l = 0$ (top) and $X/L_l = 0.096$ (bottom).

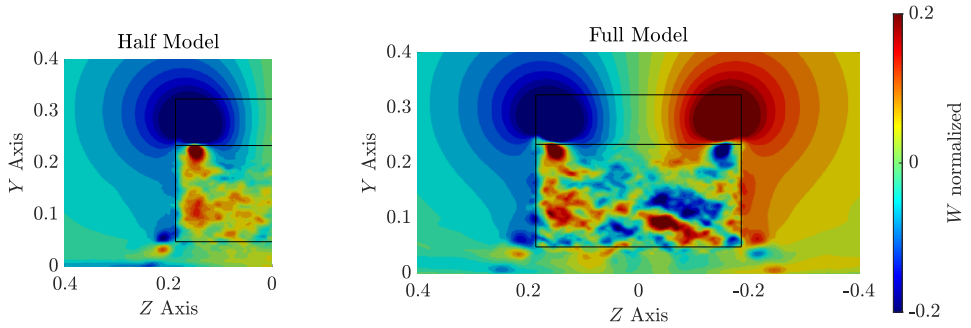
The outcome of this comparison indicates good agreement between the aerodynamic coefficients between half and full models. Flow structures are better correlated closer to the body, even at the symmetry plane. Further downstream, some asymmetry is noticed mostly on W velocity contours but should have limited consequences on the reliability of the study. Therefore, we conclude that the symmetry boundary condition provided suitable results for *LES* simulations of the geometries studied in this research.



(a) Plane X/L_l=-0.096



(b) Plane X/L_l=0



(c) Plane X/L_l=0.096

Figure 7-36: Comparison of normalized W velocity for the symmetric model (left) against full model (right) on planes $X/L_l = 0$ (top) and $X/L_l = 0.096$ (bottom).

Ahmed body drag and lift coefficient correlation results

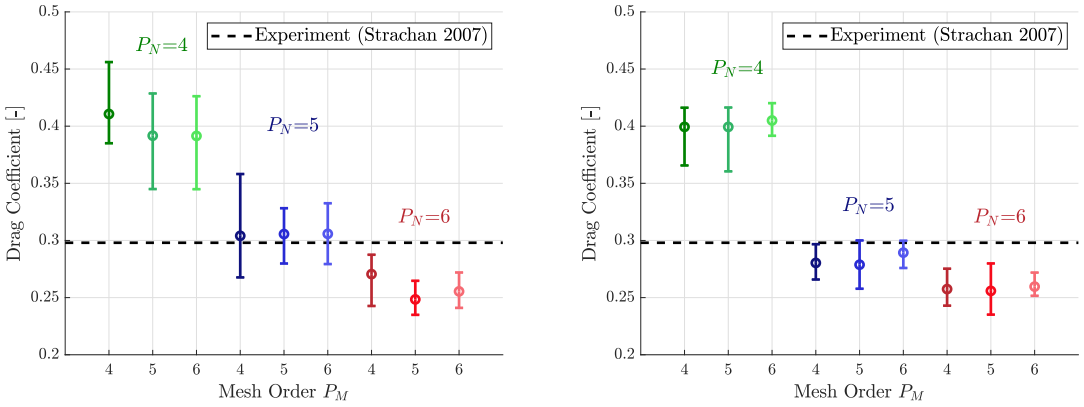
We now compile quantitative results for the nine combinations of high-order meshes with polynomial expansions for the *Original* mesh and additional nine cases for the *Refined* mesh in total eighteen cases, considering half body. A summary is presented on Table 7-3 for the time-averaged drag and lift coefficients obtained in all simulations. For the coefficients of drag and lift, results were averaged from the 5^{th} to the 7^{th} CTU.

Table 7-3: Drag and lift averaged coefficient for the *Original* and *Refined* meshes considering evaluated P_M and P_N high-order, comparing with experiments from Strachan et al. [2007].

Simulation Case	**Average** C_D	**Average** C_L	**Difference Drag %**	**Difference Lift %**
NM44-A	0.411	0.164	38	-41
NM54-A	0.304	0.266	2	-5
NM64-A	0.257	0.256	-11	-9
NM45-A	0.392	0.116	31	-59
NM55-A	0.306	0.285	3	2
NM65-A	0.248	0.258	-15	-8
NM46-A	0.391	0.115	31	59
NM56-A	0.306	0.284	3	1.5
NM66-A	0.255	0.263	-12.5	-7
NM44-R	0.399	0.253	34	-10
NM54-R	0.280	0.289	-6	3
NM64-R	0.257	0.284	-12.5	2
NM45-R	0.399	0.253	34	-10
NM55-R	0.279	0.285	-6	2.5
NM65-R	0.256	0.271	-12.5	-3
NM46-R	0.405	0.252	34	-10
NM56-R	0.289	0.275	-5.5	3.5
NM66-R	0.260	0.279	-13	1
Experiment	**0.298**	**0.280**		

In order to better visualize the results of both drag and lift coefficient from the *Original* and *Refined* mesh cases, we present the averaged quantities (dotted line) with minimum and maximum deviation comparing with experimental results (dashed line) fromStrachan et al. [2007]. The drag coefficient summary is presented in Figure 7-37 and the lift coefficient summary in Figure 7-38.

An important aspect to mention is that the mesh order P_M and solution order P_N are independent and values of both can be freely combined. Higher order of the P_M polynomial are used to improve the reproduction of complex surfaces by curving the elements, whereas P_N adds more DOFs to the solution. The first feature to be noticed on this drag coefficient analysis is that the mesh order P_M only influences the results of the first case presented (NM44) comparing to NM54 and NM64, indication that the curvature is not enough represented on the *Original* mesh with using P_M of 4^{th} order. For the other cases, the deviation on the



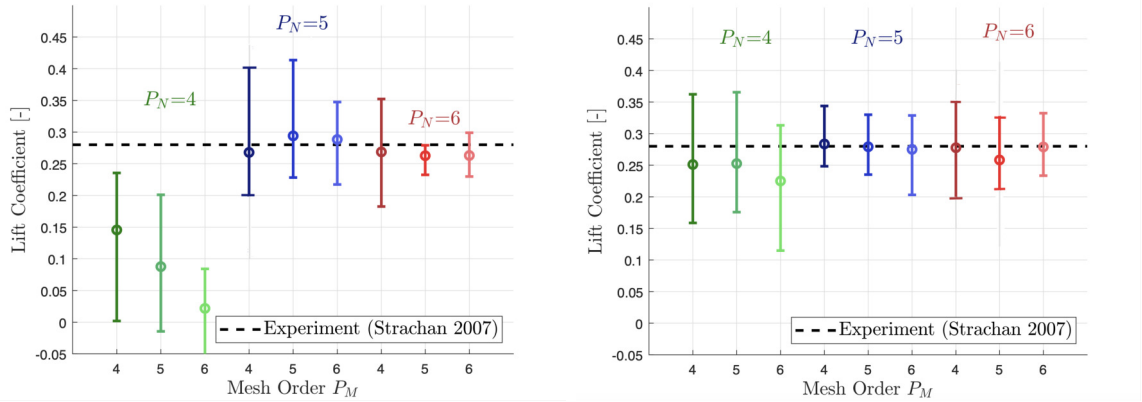
(a) Original Mesh **(b)** Refined Mesh

Figure 7-37: Drag coefficient comparison for *Original* and *Refined* mesh cases, considering proposed high-order meshes and polynomial basis.

results are smaller than 2%. Between the high-order mesh cases of 5^{th} and 6^{th} order, for further simulations we selected to build high-order meshes considering 6^{th} order.

From drag results presented on Table 7-3 and Figure 7-37, we observe that all mesh combinations cases considering $P_N = 4$ over-predict the drag coefficient by more than 30%, a value similar to the ones found on *RANS* simulations. When increasing the resolution of the simulation by using $P_N = 5$ there is an enhancement on the drag coefficient results, with highest deviation of 6% of the experiment. For this cases we also observe that results for the *Original* mesh are slightly under-predicted, however when we use the same expansion on the *Refined* mesh, the drag coefficient results become slightly over-predicted. Analysing the last set of results for $P_N = 6$, it is possible to notice that all cases evaluated are consistent, indicating that the 6^{th} order is enough to solve the drag quantity on the meshes evaluated, with maximum deviation of 13% from experiments. From the results presented, we conclude that $P_N = 5$ is the minimum polynomial expansion accuracy required to represent the problem. Results presented also correlates with state-of-the-art simulations methodology for the Ahmed body as presented by Serre et al. [2013] using wall-modelled *LES*. Comparing with previous LES-SVV study performed by Minguez et al. [2008], the gap of 44% is improved, highlighting how this new proposed methodology is efficient for bluff body geometries. One point that should be considered is that for the experimental results from Strachan et al. [2007], the Ahmed Body was fixed on the top of the wind tunnel by an aerodynamic profile strut, as previously stated, which can influence the flow and drag force measured, even algebraically removing the strut influence on the drag.

Evaluating the lift coefficient performance, we observe that cases considering $P_N = 4$ are able to predict the results with maximum deviation of 10% compared to experimental results when using the *Refined* mesh. However, the *Original* mesh with the same solution order is not able to predict the lift coefficient, indicating that the mesh resolution is too coarse to correctly predict this quantity. Results for both $P_N = 5$ and $P_N = 6$ on both the *Original* and the *Refined* meshes presented a maximum difference of 5% when compared with experiments. For the cases considering $P_N = 6$, we can observe the improvements in lift accuracy when using



(a) *Original* Mesh **(b)** *Refined* Mesh

Figure 7-38: Lift coefficient comparison for *Original* and *Refined* mesh cases, considering proposed high-order meshes and polynomial basis.

the *Refined* mesh, resulting in the best agreement in terms of lift among all cases proposed.

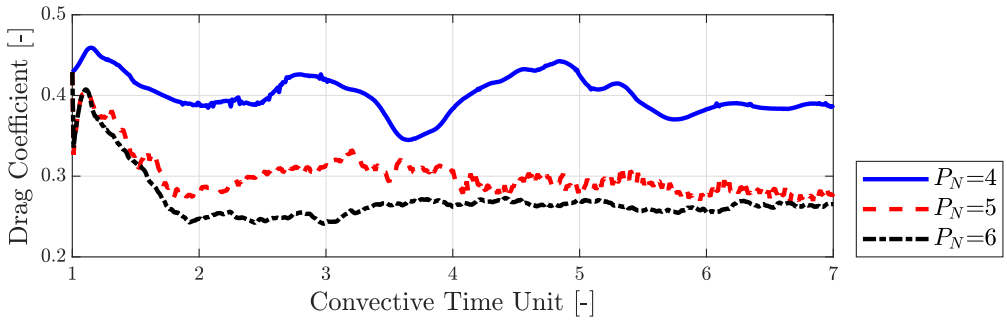
We conclude that analysing both drag and lift coefficients prediction, *Refined* mesh cases presented results which correlated closer to the experimental references. As previously mentioned, the high-order mesh doesn't heavily influence the results once the main features of the body are sharp-edges. In terms of the polynomial expansion accuracy, the best agreement for drag coefficient was reached with $P_N = 5$ and for the lift coefficient, $P_N = 6$ has the best agreement. However, we verified that only $P_N = 6$ present consistency for the quantities when the mesh resolution increased from *Original* to *Refined*, demonstrating the reliability in simulation results. The use of *Refined* mesh case combined with $P_N = 6$ also imposes $y^+ \leq 1$ for the boundary layer, providing the best representation of the flow close the walls, among all proposed solutions for this base mesh design.

Ahmed body force results convergence

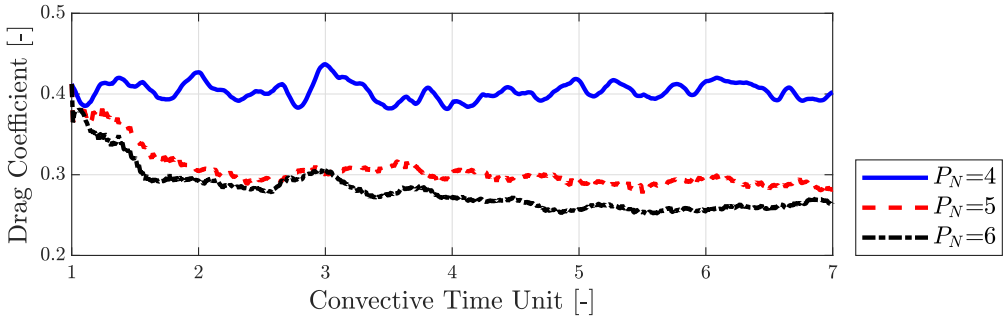
We present now the convergence of both drag and lift forces. For each solution, the simulation was warm-started with the solution obtained for the $P_N = 4$ case simulated up to 1 CTU using the same mesh design. For example, the NM66-R case was started from NM46-R solution at one CTU. This is to skip the repetitive computation for the period that the iLES-SVV solution is still stabilizing. Drag force convergence graph for the *Original* and the *Refined* meshes are shown in Figures 7-39a and 7-39b respectively.

Convergence profiles in Figures 7-39a and 7-39b show that the *Refined* mesh fluctuation on the drag force are smaller compared to the results of the *Original* mesh. Using the *Refined* mesh, we observed that $P_N = 4$ cases presented an improvement in terms of both fluctuations and results, with the number of elements increases by 3.5 times. However, neither cases had enough resolution to converge to the correct solution.

Solution with $P_N = 5$ using the *Original* mesh seems to have some unstable fluctuations on the results, indicating that the mesh may also not have sufficient resolution or computational



(a) *Original* Mesh



(b) *Refined* Mesh

Figure 7-39: Instantaneous drag coefficient convergence for the *Original* and the *Refined* mesh cases, considering all high-order meshes and polynomial expansions evaluated.

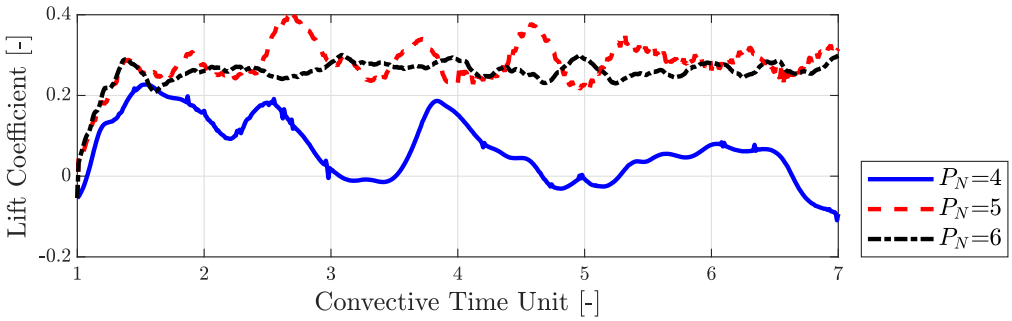
time to yield a stable solution. On the other side, *Refined* mesh results for $P_N = 5$ and $P_N = 6$ seems to converge to the same solution, as presented in Figure 7-39b.

Lift force convergence profiles for *Original* and *Refined* meshes are presented in Figures 7-40a and 7-40b respectively below.

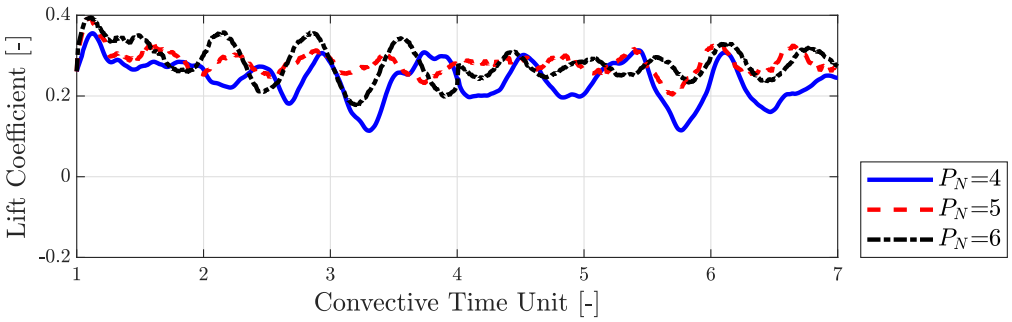
The lift force convergence profile of the *Original* mesh shown in Figure 7-40a presented unstable behaviour for $P_N = 4$ and $P_N = 5$ cases, indicating that although lift coefficient averaged values look closer to experimental reference in the case of $P_N = 5$, there is no physical convergence of the quantities by reaching a cyclical behaviour, an usual characteristic of automotive flows, due to lack of simulation resolution. Cases considering $P_N = 6$ had a stable behaviour, even presenting a cyclical behaviour. When evaluating lift force results convergence profile of the *Refined* mesh shown in Figure 7-40b, for all cases considering, stability of the lift force profile improved compared to the *Original* mesh cases, with the cyclical behaviour becoming more evident.

Ahmed body flow structures comparative results

We now present a comparison of the flow structures and flow behaviour on the simulations performed. As we previously explained, the results are shown for both *Original* and *Refined* cases with polynomial expansion P_N of 4^{th}, 5^{th} and 6^{th} accuracy order but considering only high-order mesh P_M of 6^{th} order.



(a) *Original* Mesh



(b) *Refined* Mesh

Figure 7-40: Instantaneous lift coefficient convergence for the *Original* and the *Refined* mesh cases, considering all high-order meshes and polynomial expansions evaluated.

This study has moving ground for all configuration but doesn't have the upper strut as needed in some wind-tunnel experiments. We present comparative flow behaviour evaluation using Lienhart et al. [2002] flow results over the slant as the main experimental reference, to remove the influence caused by the strut on the flow.

The first comparison presented is the vertical velocity V normalized with the free stream velocity U_∞. LDA measurements by Lienhart et al. [2002] and simulation results considering *Original* and *Refined* meshes at the three polynomial expansion P_N evaluated at the end of the slant at $X/L_l = 0$ on plane ZY, are shown in Figure 7-41.

Firstly, the results indicate that all simulation cases were able to capture a vortical structure on the end of the slant. The profile of the negative part of the vortex closely correlates to Lienhart et al. [2002], with an elongated profile on the spanwise direction toward the middle of the slant. Taking a close look on *Original* mesh contour results for the vertical velocity on different resolutions, we conclude that $P_N = 4$ is only able to indicate a weak vortex on the slant and not able to capture the correct intensity and distribution. Increasing the resolution to $P_N = 5$, the solution correctly captures the flow vertical velocity, however the vortex strength is still under-predicted. The NM66-A results can capture all positive velocity contours, however with a smaller area size for the highest vertical velocity, compared to experimental results from Lienhart et al. [2002].

Contour results for the NM46-R indicate a similar result observed for the NM56-A, with better correlation in shape and scale due to the additional h-refinement. With NM56-R, the

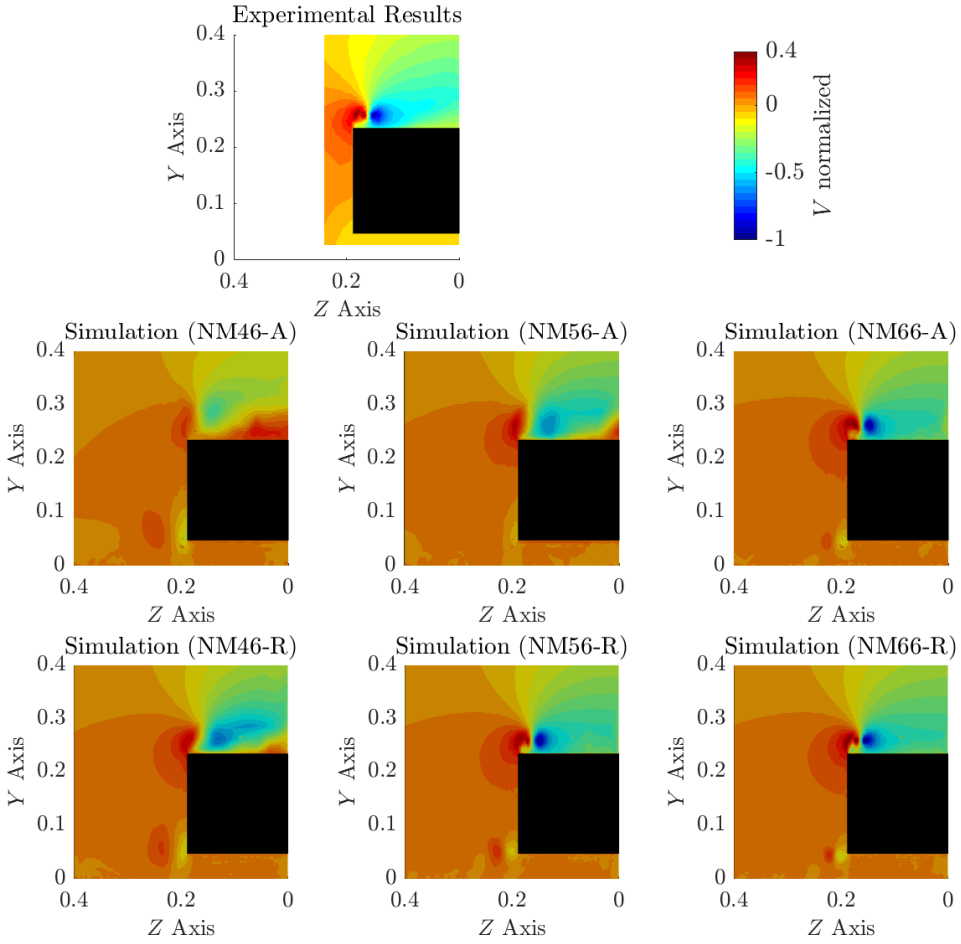


Figure 7-41: Comparison of normalized vertical velocity (V) between experiments of Lienhart et al. [2002] (top) and computational simulations on plane ZY at $X/L_l = 0$.

correlation level increases, capturing the full contour of the negative portion of the vortex; however, with some shape distortion. Moving to the last case evaluated, the NM66-R simulation has the best agreement in terms of vertical velocity with experiments, by capturing both the positive and negative parts of the velocity also closely matching the shape.

Moving further downstream of the Ahmed body, we now present a comparison of the normalized U on the plane ZY at $X/L_l = 0.077$ in Figure 7-42, aiming to identify the wake structures on the flow.

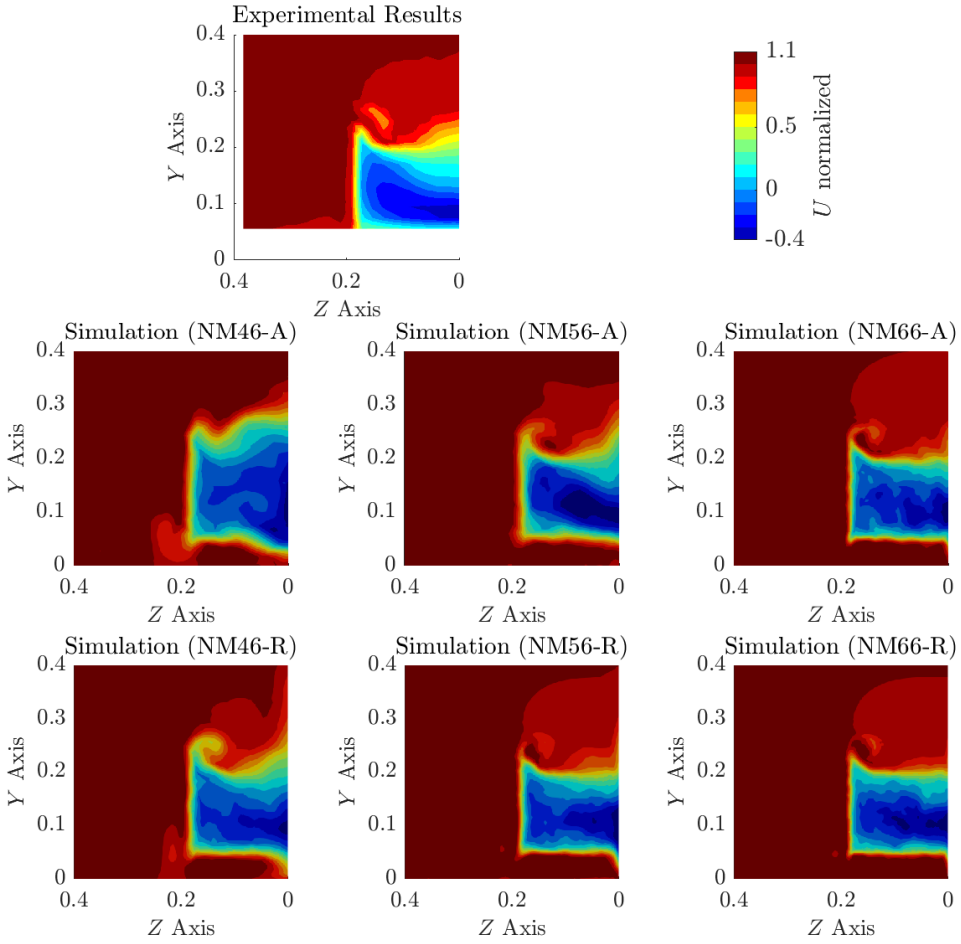


Figure 7-42: Comparison of normalized streamwise velocity U between experiments of Lienhart et al. [2002] (top) and computational simulations on plane ZY at $X/L_l = 0.077$.

From the figure, it is clear that both NM46-A and NM46-R are not able to reproduce the flow structures found on experimental references, where the *Original* mesh is not even able to capture the vortex rolling once it separates at the end of the slant as the y^+ values are much higher than 1. The *Refined* mesh contour seems to converge to the correct shape of the flow structures, however still under-predicted in terms of intensity. This under-prediction of flow main structures due to mesh conditions close to the walls are potential causes leading to over-predicted aerodynamic quantities seen in Section 7-3-3.

When analysing $P_N = 5$ cases for both meshes, we clearly see enhancements however structures captured by *Original* mesh is still evolving with time and acquiring the experimental reference's shape. The NM56-R simulation captured the correct shape and location of the flow structures, even the detail of the vortex on the top corner and transition on the middle; however, with slight under-prediction of the vortex intensity. At this point, we observe

that flow results for $P_N = 5$ cases are approaching the experiments, especially for the *Refined* mesh. The increment of resolution from *Original* to *Refined* mesh with also influenced the aerodynamic quantities measured, by mainly changing the drag coefficient from slightly over-predicted to slightly under-predicted.

Flow structure result for $P_N = 6$ on the *Original* mesh once again provides the best agreement with experiments from Lienhart et al. [2002] by reproducing the velocity profile and similar shape on the vortical structure and at the rear wake at $X/L_l = 0.077$, however with some discrepancies on the vortex intensity and velocity distribution on the rear wake. Increasing the resolution in terms of h-refinement from *Original* to *Refined* mesh, we realise flow structures are better captured due to higher number of DOFs in the simulation, however aerodynamic quantities are only slightly affected. We can conclude that 6^{th} order accuracy polynomial expansion is the required resolution for the proposed meshes. Up to this moment, NM66-R case provided the best agreement for flow structures, although the drag coefficient is slightly under-predicted. We suspect the lower values obtained is due to the absence of the upper strut on the Ahmed body, an auxiliary structure necessary for experimental measurements using a moving ground, as used by Strachan et al. [2007] to obtain the reference drag coefficient.

In order to understand the flow behaviour over the slant and complement previously discussed results, we present wall shear stress lines analysis. The expected flow behaviour is the vortex shedding from the very beginning of the top left corner combined with a separation bubble growing in size. As the separation moves inwards on the spanwise direction, this bubble size becomes constant, with a flow reattachment around the middle of the slant, as presented in Figure 7-43. The same features can be observed in our simulation results for all proposed cases are presented in Figures 7-44 and 7-45.

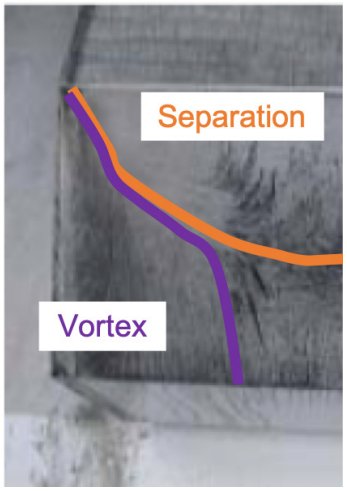
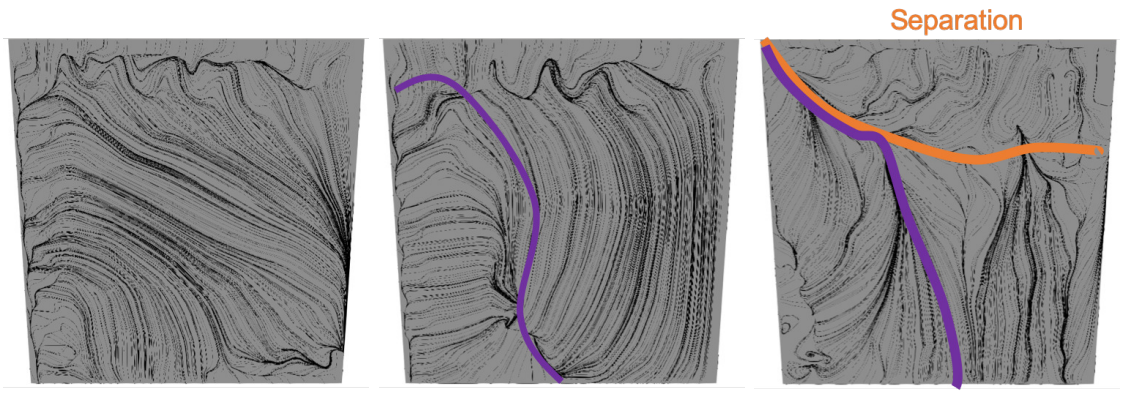


Figure 7-43: Wall shear stress lines experimental results on the slanted surface on the Ahmed body, with highlighted regions: vortex (purple) and flow separation (orange). Adaptation from Lienhart et al. [2002].

To better visualize the flow structures acting over the slant, we provided comparative figures considering the vortex acting area, defined in purple and the separation area, highlighted in orange. Results on wall shear stress lines for the *Original* mesh confirms that 4^{th} order



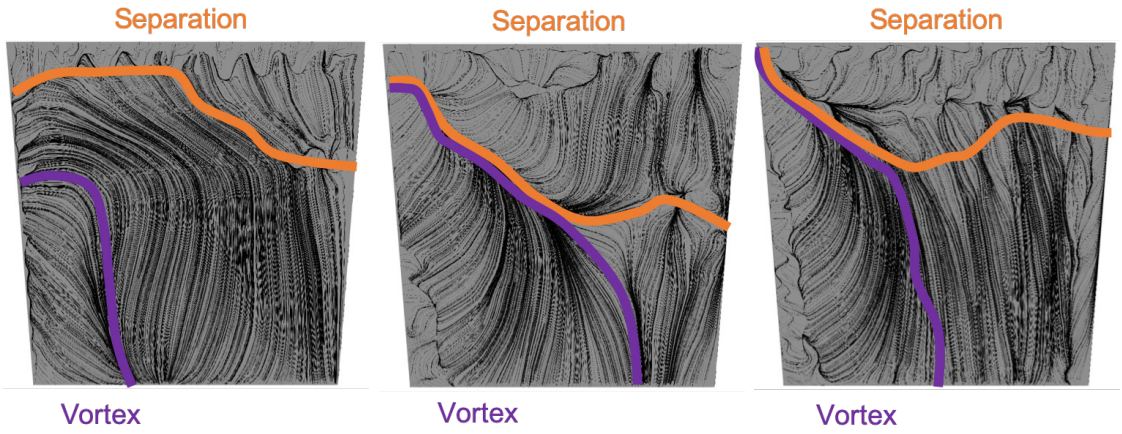
(a) NM46-A **(b)** NM56-A **(c)** NM66-A

Figure 7-44: Comparison of wall shear stress lines over the slanted surface on the Ahmed body using the *Original* mesh with different P orders.

accuracy polynomial expansion is unable to capture the slant vortex, however 5^{th} and 6^{th} order accuracy polynomials do identify this structure. The last case also captures the separation bubble over the slant, as highlighted in Figure 7-44. Following similar analysis for the *Refined* mesh cases seen in Figure 7-45, 4^{th} order accuracy polynomials partially captures the slant vortex, starting only after passing 40% of the slant length. Once again, $P_N = 5$ and $P_N = 6$ clearly capture the slant vortex and the separation bubble over the slant with higher resolution when compared with the *Original* mesh by the line density. The differences between $P_N = 5$ and $P_N = 6$ also indicate that $P_N = 5$ starts capturing the vortex at a location slightly backwards, around 10% behind of the slant edge. The delay in flow development justifies why the diffuser vortex doesn't get energetic for this configuration as it gets on $P_N = 6$. The conclusion obtained from the wall shear stress lines indicates that both mesh design cases considering $P_N = 6$ were able to replicate the experimental profile, capturing the vortex shedding, separation bubble and reattachment on the slant.

We conclude that *Refined* configuration, combined with polynomial expansion of 6^{th} order accuracy (NM66-R) is the most suitable configuration to replicate the Ahmed body under moving ground condition. This is due to its high-resolution in capturing flow features similar to the experiments, and consistency on predicting the aerodynamic quantities.

A solution resolution comparison between the proposed cases is presented in Figure 7-46. Iso-surfaces of Q-Criterion at 100 (Q-Crit = 100) are plotted on a lateral view of the Ahmed body. Results for the *Original* mesh show a gradual increment on the turbulent scales captured, when increasing the polynomial order of the solution. Coarse flow structures are observed for *Original* mesh with $P_N = 4$ and $P_N = 5$ resolutions, while increasing the polynomial order to 6^{th} order provides a good resolution increment. With the additional h-refinement on the *Refined* mesh, $P_N = 4$, $P_N = 5$ and $P_N = 6$ clearly improved the resolution. Flow structures are better defined however still too coarse for $P_N = 4$, and NM56-R resolution seems similar to the NM66-A case. The highest resolution is obtained with $P_N = 6$ with *Refined* mesh, where the lower side vortex is well-captured and doesn't get diffused as in previous cases. This resolution is required for further exploration of the lower side vortex and its interaction.



(a) NM46-R **(b)** NM56-R **(c)** NM66-R

Figure 7-45: Comparison of wall shear stress lines over the slanted surface on the Ahmed body using the *Refined* mesh with different P orders.

Computational costs

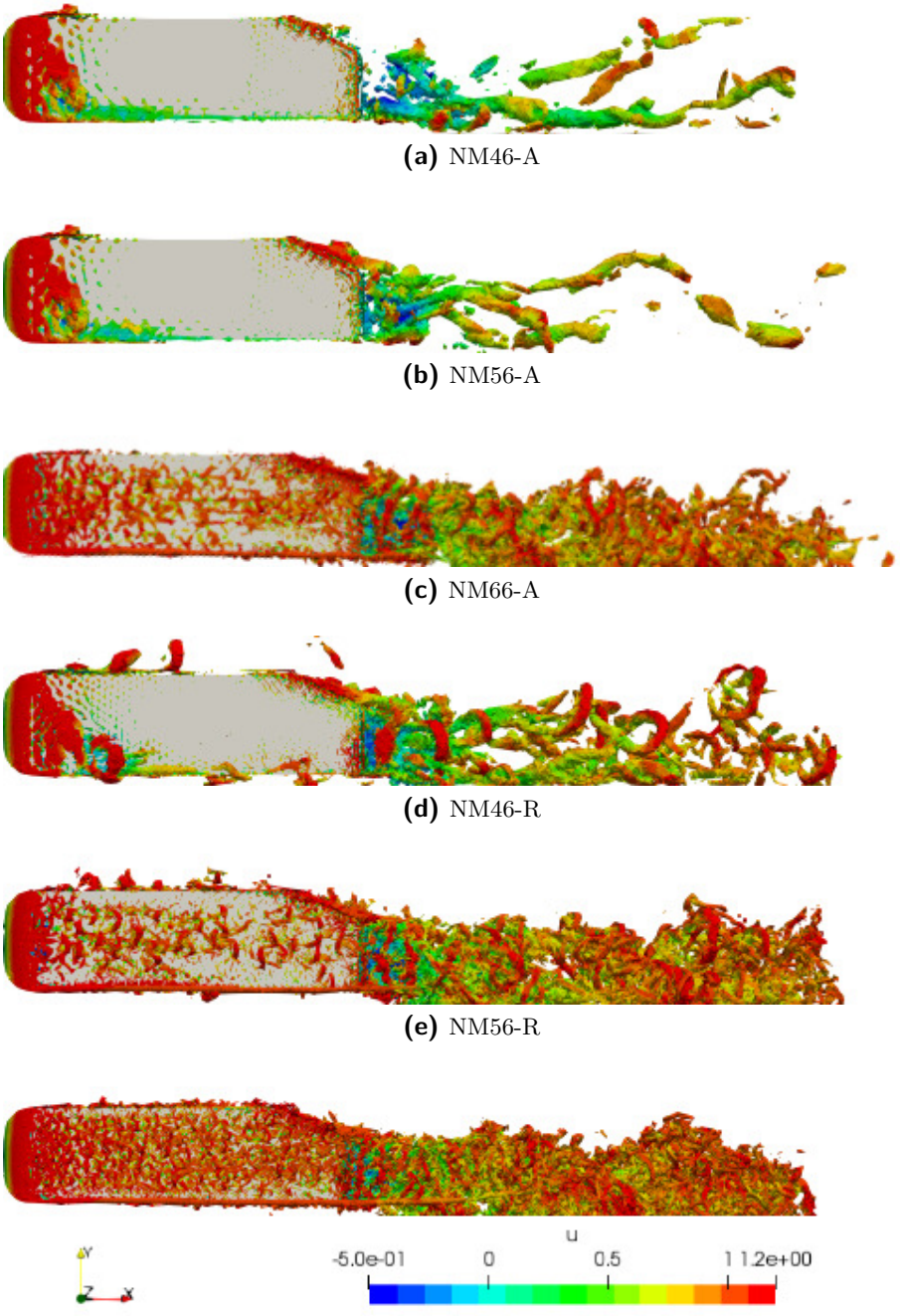
As previously reported, simulation cases for the Ahmed body are running using the Imperial College CX2 cluster. Complex cases are required to be executed using 18 nodes, each node containing 24 cores, in a total of 432 CPU cores. We present in Table 7-4 the total time required for each of the simulations to reach 7 CTU.

We notice that the resolution increment of 3.7 times from *Original* to *Refined* mesh has different impact on computational time. The computational time increased 3.7 times for $P_N = 4$ and $P_N = 5$ resolutions and approximately 2.9 times for $P_N = 6$, comparing *Original* to *Refined* mesh cases. The required time-step to keep the CFL condition around 1.0 also impacts on the computational time, increasing the simulation cost for higher resolution cases. To keep this CFL condition the required time step for $P_N = 6$ is four times smaller than the $P_N = 4$ and two times smaller than the $P_N = 5$.

Table 7-4: Required computational time in hours for different Ahmed body simulations to reach 7 CTUs at Imperial College CX2 cluster with 432 CPUs.

		$P_N = 4$	$P_N = 5$	$P_N = 6$
Original Mesh (-A)	$P_M = 4$	1.8	8.5	27.5
	$P_M = 5$	1.8	8.5	27.5
	$P_M = 6$	1.8	8.5	27.5
Refined Mesh (-R)	$P_M = 4$	6.7	31.6	80.4
	$P_M = 5$	6.7	31.6	80.4
	$P_M = 6$	6.7	31.6	80.4

The number of solution DOFs for $P_N = 6$ is around three times more than the same mesh with $P_N = 4$. Considering both the time step and number of DOFs size conditions previously stated, the case considering *Refined* mesh with $P_N = 6$ should to be at least twelve times more expensive than its correspondent $P_N = 4$, as shown in table 7-4. As expected, the most expensive solutions provide the best flow validation results.



(a) NM46-A

(b) NM56-A

(c) NM66-A

(d) NM46-R

(e) NM56-R

(f) NM66-R

Figure 7-46: Simulation resolution comparison by iso-contours 3D plots of Q-Criterion (Q-Crit = 100) coloured by U velocity, for *Original* and *Refined* meshes at different polynomial expansion proposed.

7-4 Conclusions

The results for the aerodynamic quantities indicate that for a simplified geometry such as the Ahmed body, once passing a threshold value, further increasing the mesh order has small influence on the results. For this type of bluff bodies, most of the relevant flow structures are generated from sharp edges of the geometry, such as the slant. The only curved surface is the frontal stagnation, where we see enhancements on capturing the curvature as the P_M increases. We select to have the highest high-order mesh resolution ($P_M = 6^{\text{th}}$ order) as our reference for curvature mesh also to summarize force convergence and flow structures studies here presented.

The force convergence plots indicate that except for the $P_N = 4$ case, *Refined* mesh results are stable for drag force. However the *Original* mesh can only yield stable results for the $P_N = 6$ case. For the lift force, similar behaviour is found, where *Refined* mesh results have a clearly defined oscillating profile, especially with $P_N = 5$ and $P_N = 6$. The *Original* mesh indicates a slight oscillating trend for the same cases, however still unstable. When convergence analysis is combined with numerical results, the outcome we have so far for the best methodology are between *Original* and *Refined* meshes with $P_N = 5$ and $P_N = 6$ resolution, respectively for drag and lift coefficients. A point to consider is that for $P_N = 5$, we noticed that increasing the h-refinement from *Original* to *Refined*, the result changed from over-predicted to under-predicted. Results for drag considering $P_N = 6$ resolution maintained similar value for both meshes, indicating consistency.

We also point out that the reference used for the aerodynamic quantities (Strachan et al. [2007]) has an upper support over the body to allow the moving ground condition, which the upper support contributions for the drag forces being empirically deducted from the obtained total value. However, the influences on flow features will still remain, possibly leading to weaker vortices over the slant when comparing to results without the support. Following the suggestion of Strachan et al. [2007], we are comparing aerodynamics quantity results with his study (moving ground with strut) and flow visualization with results from Lienhart et al. [2002] (static ground without strut).

Finally analysing the flow structures on V and U velocities, *Refined* mesh with $P_N = 5$ and $P_N = 6$ cases qualitatively closely correlate to experimental results, with better definition of flow structures and larger contour spectrum. Especially for $P_N = 6$ resolution, capturing similar shape of the experimental reference of Lienhart et al. [2002]. Complementing previous results, wall shear stress plots also indicate that best correlation is found for $P_N = 6$ resolution cases, indicating the separation bubble in the beginning of the slant and vortex generation on the outer side, rolling over the slant.

The main conclusion here presented is that the minimum resolution for this mesh setup to reproduce similar features and aerodynamic quantities is the *Refined* configuration combined with 6^{th} high-order mesh ($P_M = 6$) and polynomial expansion of 6^{th} order accuracy ($P_N = 6$). The *Refined* configuration combined with polynomial expansion of 6^{th} order accuracy leads to $y^+ \leq 1$ over the body walls, giving support to previous statement.

7-5 List of publications

7-5-1 Paper contributions

Buscariolo, F.F., Meneghini, J.R., Assi, G.R.S., Sherwin, S.J., Spectral/hp iLES-SVV simulation methodology study on an Ahmed Body squared back, SAE Paper, No 2018-36-0320, Society of Automotive Engineers, 2018.

Buscariolo, F.F., Meneghini, J.R., Assi, G.R.S., Sherwin, S.J., Spectral/hp methodology study for iLES-SVV on an Ahmed Body, Spectral and High Order Methods for Partial Differential Equations ICOSAHOM 2018, accepted.

7-5-2 Presentations and poster sessions

Spectral/hp methodology study for SVV-LES on an Ahmed body (presentation), 7^{th} Conference on Bluff Body Wakes and Vortex-Induced Vibrations - BBVIV 7, 2018.

Spectral/hp methodology study for iLES-SVV on an Ahmed Body (presentation), International Conference on Spectral and High Order Methods - ICOSAHOM 2018.

Chapter 8

Ahmed Body with Diffuser

Following the Ahmed body validation study, we now present a computational study on rear underbody diffusers. The diffuser study is proposed using the Ahmed body as the base bluff body, considering two body styles: 0° slant angle and 25° slant angle. Simulations using uDNS/iLES methodologies, based on spectral/hp element method, are selected to perform the diffuser study. We present an introduction to the concept and development of rear underbody diffusers, a comprehensive literature review on the topic with both experimental and computational studies, followed by the simulation setup and results. The study aims to evaluate the flow behaviour and structures on the rear wake and on diffuser surface, drag and lift coefficients and pumping effect for all configurations proposed.

8-1 Background

Aerodynamics was in focus of the automotive industry since 1930s, with main researchers based on the motor racing teams. The main focus of automotive aerodynamics studies and optimizations until the middle 1960s were on drag reduction by changing the surface design and reducing frontal area. This led most of Formula One racing vehicles to have streamlined forms, increasing their straight-line final speed, however acceleration and cornering speed improvements were still a challenge. It started to change in 1966 when Jim Hall Chaparral 2E car first appeared on the Can-Am racing Series. The Chaparral 2E incorporated inverted wings to generate downforce, as shown in Figure 8-1.

The development of the wing concept was the main focus of most Formula One teams until Jim Hall again introduced a new concept with side skirts, sealing the lateral portion of the underbody from the free stream. The side skirts were combined with electric-powered fans on the Chaparral 2J, as shown in Figure 8-2. The fan working on a sealed environment creates a suction effect, leading to low pressures on the whole underbody, increasing the downforce. As this concept included moving devices, it was also banned and until today, movable parts, except the Drag Reduction System (DRS) are not allowed.

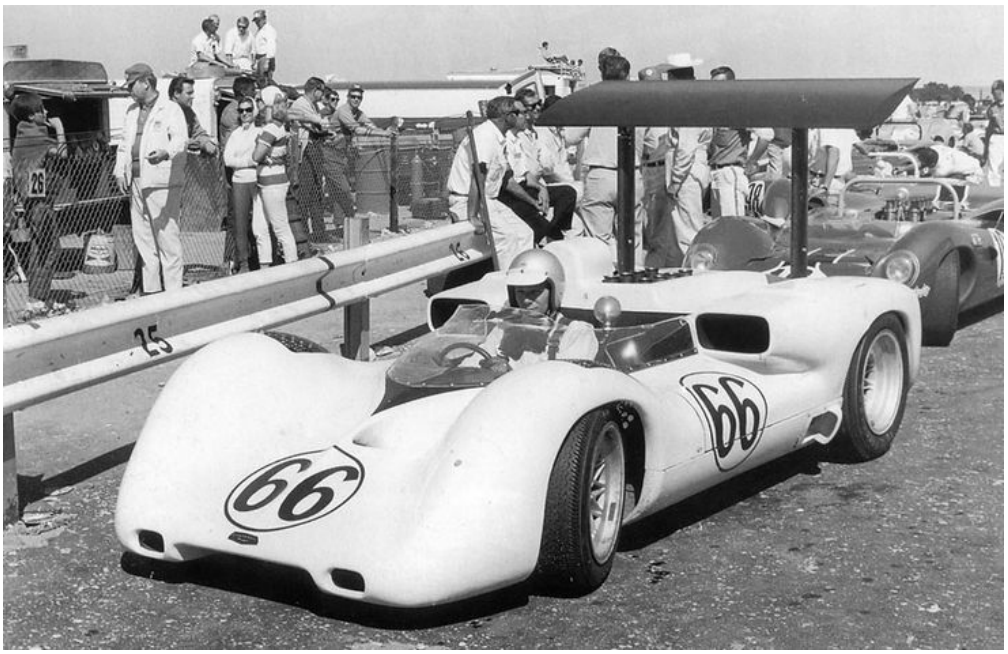


Figure 8-1: The Chaparral 2E car, designed by Jim Hall. Reproduction from https://www.gettyimages.ie/

The main find of Jim Hall's skirt/fan suction system is that the underbody could also be used to increase downforce. Considering the large area of the underbody, engineers started to change its geometry to generate negative pressure. This additional downforce source considerably increased acceleration and vehicle stability. Colin Chapman took advantage of the downforce that could be generated by the underbody and introduced the ground effect concept for the first time in a race car, when design the Lotus 78 Formula One car.

Ground effect can be defined as the engineered use of the ground influence when a vehicle is moving close to the road, in order to improve aerodynamic properties. According to Ehirim [2018], the ground-effect phenomenon associated with road and race cars is governed by the Bernoulli principle, which states that an increase in velocity of an inviscid flow simultaneously occurs with a decrease in static pressure. For ground vehicles, a flow interaction occurs between the car components such as underbody and the road surface. Considering racing vehicles that have components such as front wing and underbody both designed to create downforce by employing inverted wing curvatures, moving in ground proximity, the airflow between the components and road surface is constrained. The constrained airflow accelerates causing a drop of the static pressure generating suction surface of the underbody. This results in an increase of the negative lift vector, generating downforce on the components.

The design of the Lotus 78 proposed by Colin Chapman had the whole central structure shaped as an inverted wing and the two sides of the car were sealed by lateral sliding skirts. This configuration sealed the side portion of the underbody by touching the road and generating low pressures over a very large area, enabling large downforce levels. Optimized underbody geometry combined with sliding skirts in contact with the ground of the Lotus 79 provided the perfect combination in terms of downforce. Lotus 78 and 79 won the world



Figure 8-2: The Chaparral 2J car designed by Jim Hall considering the dual-fan on the rear and side skirts scheme. Reproduction from http://www.grandprixhistory.org/

championship in 1978 and both designs are shown in Figure 8-3.

According to Katz [2006], the sliding skirts were not trouble free, where irregular road track surface resulted in sealing problems due to loss of the contact between the skirt and the road and consequently loss of downforce. This issue caught the attention of the engineers and race commissioners once a 20 mm gap between the skirt and the road could result in the loss of 50% of the downforce and could impact the safety of the vehicles. This led to the banning of all sliding seals in 1983 and nowadays the only part of the vehicle allowed to be in contact with the ground are the tires. The underbody of the vehicle shaped as an inverted aerofoil was still able to provide additional downforce even without the sliding skirts.

Additional solutions to replace the skirts started to be developed such as improving exterior geometries or using additional aerodynamic devices. Among the new aerodynamic conceptual parts, we highlight the rear underbody diffusers or diffuser, as presented in next section.

8-1-1 Introduction

Diffusers can be defined as aerodynamic devices designed to extract the underbody flow, acting as an expansion chamber, and smoothly re-inserting it at the base pressure of the vehicle. Initially, diffusers were considered additional parts to be assembled on the rear part of the underbody. However, current racing and high-performance road vehicle incorporate the diffuser with the underbody design aiming to maximize the vehicle performance. Figure 8-4 shows an application example of the diffuser to a race car: the 2018 McLaren MCL-33 Formula One car .

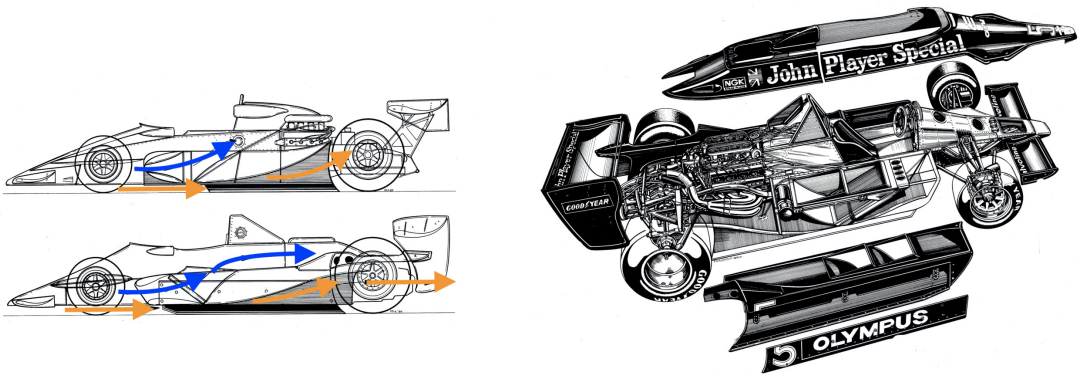


Figure 8-3: Lotus John Player Special 78 (top) and Lotus John Player Special 79 (bottom) Formula One cars. Reproduction from https://racingengineering.tumblr.com/



Figure 8-4: Rear view of the McLaren MCL-33 Formula One car, highlighting its rear underbody diffuser. Reproduction from www.motorsport.com

An easy analogy to illustrate the operation principle of a diffuser relies on Venturi's experiment. Air flow enters the constrained cross section of the vehicle's underbody where its relative velocity increases. This higher velocity flow moves along the underbody until reaching the diffuser area to be re-inserted into the free stream. Following the Bernoulli principle, presented in Equation 8-1, increasing the flow velocity on the underbody represents lowering the pressure on that region and consequently additional downforce.

$$p_{air} - p_{underbody} = \frac{\rho}{2}(\boldsymbol{v}_{underbody}^2 - \boldsymbol{v}_{air}^2) \tag{8-1}$$

where ρ is the density of the fluid, $\boldsymbol{v}_{air}$ is the free stream velocity U_∞, $\boldsymbol{v}_{underbody}$ is the flow velocity at the underbody, p_{air} is the static pressure on the free stream and $p_{underbody}$ is the pressure acting on the underbody.

It was also noticed a downforce increment for the vehicle when applying the diffuser up to certain angles. The flow mechanism on how this additional source of downforce is generated remained unknown until the work of Cooper et al. [1998].

The pioneer research work on diffusers, performed by Cooper et al. [1998], focused on the aerodynamic behaviour of plane-walled, single-plane-expansion, underbody diffusers. Diffusers

were assembled in a proposed squared-back automotive bluff body, as presented in Figure 8-5, incorporating similar features of previous geometries from Morel [1978] and Ahmed et al. [1984]. The main purpose of the study was to understand the physics of automotive underbody diffusers in ground proximity. Different angles and lengths of diffusers were evaluated at both moving-ground and fixed-ground conditions.

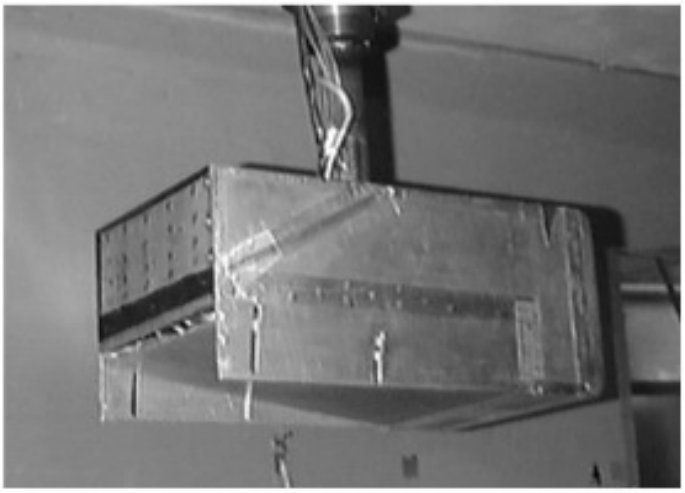


Figure 8-5: Automotive bluff body proposed by Cooper et al. [1998] for proposed diffuser studies. Reproduction from Cooper et al. [1998].

The study of Cooper et al. [1998] identified three important characteristics on a body underbody diffuser. The first is the diffuser pumping effect, characterized by a negative peak of pressure coefficient at the diffuser inlet. The pumping effect exists due to the increment of area ratio along with the diffuser length, we observe a static pressure increment, however, the static pressure at the diffuser outlet is the same as the body's base pressure (atmospheric pressure). To keep the flow continuity and compensate the fixed diffuser outlet base pressure, air flow needs suddenly increase its velocity at the diffuser inlet generating an additional low-pressure area. Thus, the diffuser acts as similar a pumping device, where the low-pressure area at the diffuser inlet is responsible for increasing underbody velocity, generating more downforce, compared to the case without diffuser. The expected pumping effect is presented in Figure 8-6 on the bluff body proposed by Cooper et al. [1998].

The second characteristic is the interaction with the ground, or ground effect. As the ground clearance between the floor and the underbody becomes smaller, the flow velocity increases on the lower portion of the model. The flow acceleration reduces the static pressure on the underbody and at the diffuser inlet, creating an additional suction effect. Later references noticed that there is a separation area at the diffuser inlet due to the sharp edge transition and will be further presented.

The third characteristic is the angled upsweep, which generates vortices on the diffuser side up to a certain critical angle. These vortices create an upwash of the flow, aiding flow attachment and increasing downforce. Cooper et al. [1998] didn't perform flow visualization measurements, concentrating most of the efforts on quantitative results. Lift coefficient results in Figure 8-7 demonstrate that an underbody diffuser can significantly increase downforce

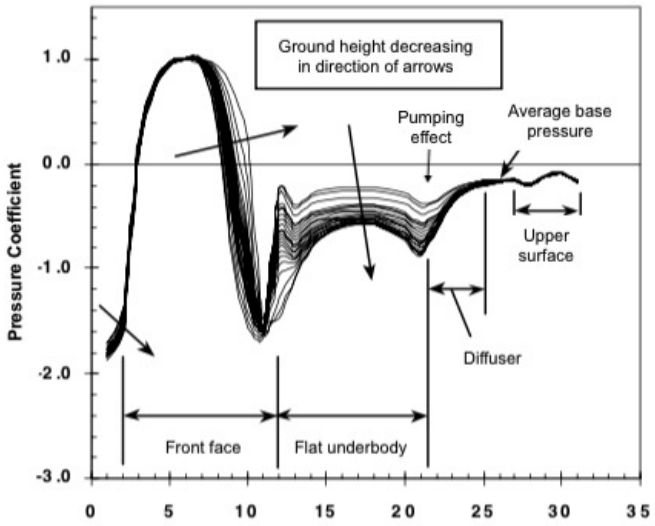


Figure 8-6: The pumping effect is demonstrated by Cooper et al. [1998] on the middle plane for diffuser angle of 9.64° and at different ground heights and moving ground. Reproduction from Cooper et al. [1998].

when compared to baseline. The ground height also influences in the downforce increment, saturating the at approximately $h/H = 0.06$ for most of the diffuser angles evaluated. Drag coefficient also increases as the ground height is reduced, reaching similar peak values as the lift coefficient at approximately $h/H = 0.06$ as presented in Figure 8-8.

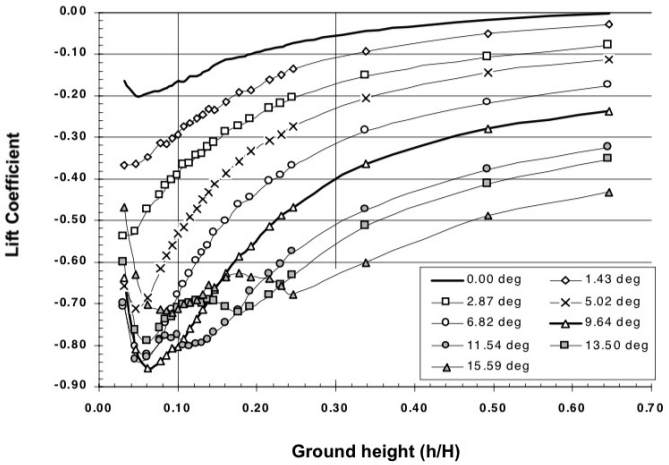


Figure 8-7: Lift coefficient values at different ground heights h/H and moving ground condition for proposed diffuser angles from Cooper et al. [1998] study. Reproduction from Cooper et al. [1998].

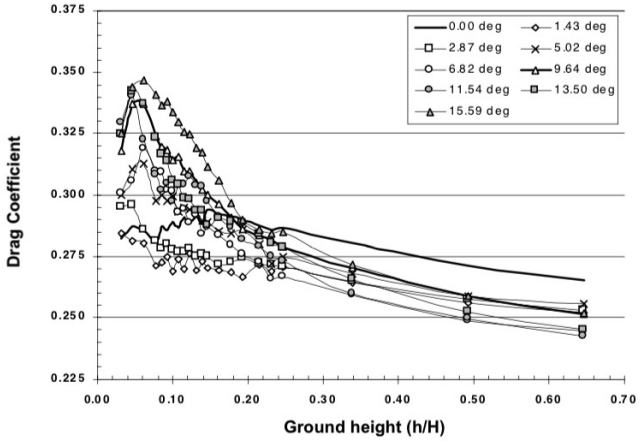


Figure 8-8: Drag coefficient values at different ground heights h/H and moving ground condition for proposed diffuser angles from Cooper et al. [1998] study. Reproduction from Cooper et al. [1998].

The moving ground influence was also investigated by Cooper et al. [1998] compared to static floor. Downforce increments are higher when the floor is moving for ground heights h/H values smaller than 0.22 as seen in Figure 8-9. The case considering diffuser angle of 9.64° has a different trend from the baseline and diffuser angle of 2.87° when the ground height higher than 0.22. The fixed ground condition presented higher downforce increments than the moving ground, which is not verified for the other two cases. We highlight the importance of the moving ground condition when studying underbody components to reproduce the real road operation condition. The moving ground might have small influence in the overall performance; however, it is critical for automotive underbody development and automotive flows close to the ground.

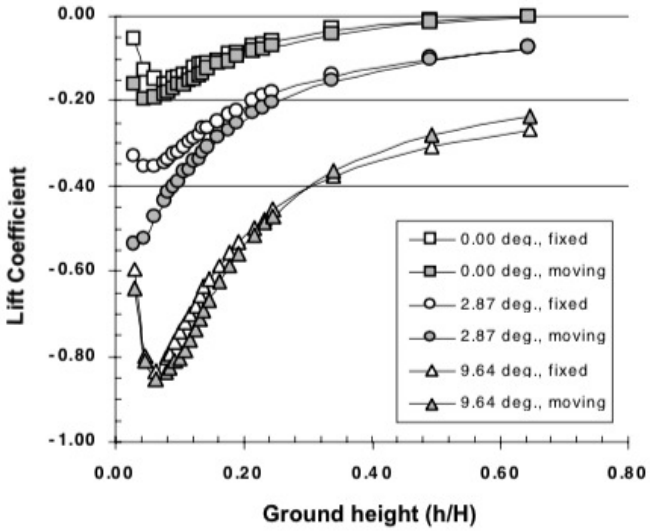


Figure 8-9: Lift coefficient comparative analysis between moving and fixed ground condition at different ground heights h/H. Reproduction from Cooper et al. [1998].

This additional source of downforce provided by the diffuser is desirable for racing tracks with elevate number of curves, were additional grip is required. High-performance road cars also took advantage of the diffuser development. Seeking for additional grip and curve stability performance, the incorporation of diffusers helped engineers reaching this objective. Figure 8-10 shows the concept of underbody diffuser applied to the McLaren P1 high-performance car.



Figure 8-10: Rear view of the McLaren P1 hyper-car, highlighting its rear underbody diffuser.

Wright [1982] states that the front wing is responsible for about 30% of the overall lift, the underbody accounts for 40% and the rear wing for about 35%. In terms of drag contribution for open-wheel race cars, the rear wing accounts for about 30%, the wheels for 40%. It is important to get further understanding of individual contribution of each component, in order to improve the performance of the vehicle.

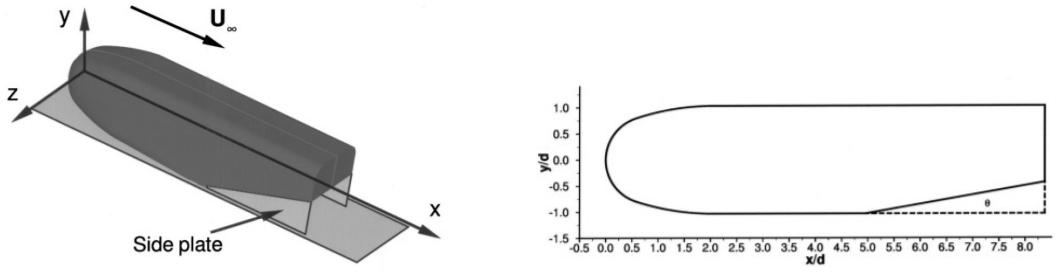
As the diffuser accounts for a significant portion of the downforce produced by the underbody and has a potential use for drag coefficient reduction, this component was selected to be studied. We incorporated the diffuser without endplates on a well-studied Ahmed body bluff

body in order to fully understand its flow behaviour and force contributions and provide an additional literature test case. Next, we present relevant literature on diffusers.

8-1-2 Literature review

We present the main references in terms of diffuser studies for automotive bluff bodies, contemporaneous from the work of Cooper et al. [1998]. An interesting fact is that most authors generate their own bluff body for their studies. Limited literature is available on previously know bluff bodies with diffuser, such as the Ahmed body.

A generic rounded-front automotive bluff body was proposed by Senior and Zhang [2001], considering a rear diffuser with angle of 17° and diffuser length of 514.5 mm. The model main dimensions are: length of 1,315 mm; height of 324 mm; width of 314 mm. The diffuser extends for 41% of the length of the body presented in Figure 8-11.



(a) 3D details **(b)** Side view

Figure 8-11: Generic rounded-front bluff body used for automotive studies, considering diffuser. Ruhrmann and Zhang [2003]

The wind tunnel measurements were performed at 20 m/s for the flow velocity, focusing on forces and pressure measurements. Flow feature results found that the diffuser flow in ground effect is characterized by a diffuser vortex combined with flow separation at this diffuser angle. Four distinct regions of diffuser performance related to the model ground height were identified as presented in Figure 8-12. First region a defined from $h/Wd = 0.76$ to $h/Wd = 0.38$, where Wd is half of the body width, is referred as downforce enhancement. In this region, flow on the diffuser surface is symmetric with a small separation area at the diffuser inlet. The second region b is referred as maximum downforce, ranging from $h/Wd = 0.38$ to $h/Wd = 0.217$. This region has similar flow behaviour as the first region, except for the formation of a separation bubble at the centre of the diffuser. The third and fourth regions, c and d, are referred both as the downforce reduction and low downforce regions. Both regions start from $h/Wd = 0.217$ and are characterized by an asymmetric and separated flow behaviour at the inlet and surface of the diffuser causing downforce reduction. Flow features observed in each region by Senior and Zhang [2001] are presented in Figure 8-13, where the diffuser inlet is on top and diffuser outlet is in the bottom. This is the first reference to report flow visualization on the diffuser surface.

The work from Ruhrmann and Zhang [2003] was based on the previous reference, focusing on forces and pressures measurements using the same bluff body proposed by Senior and

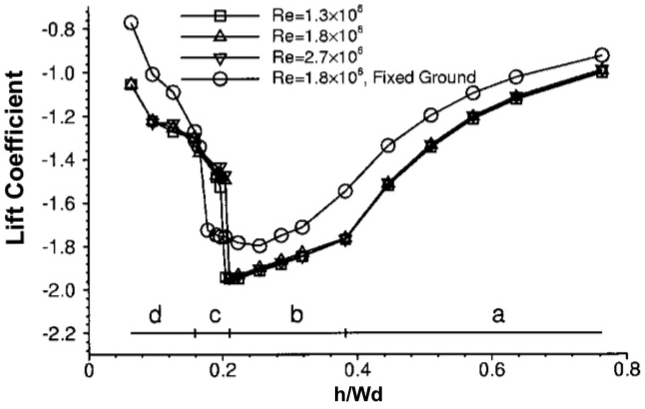


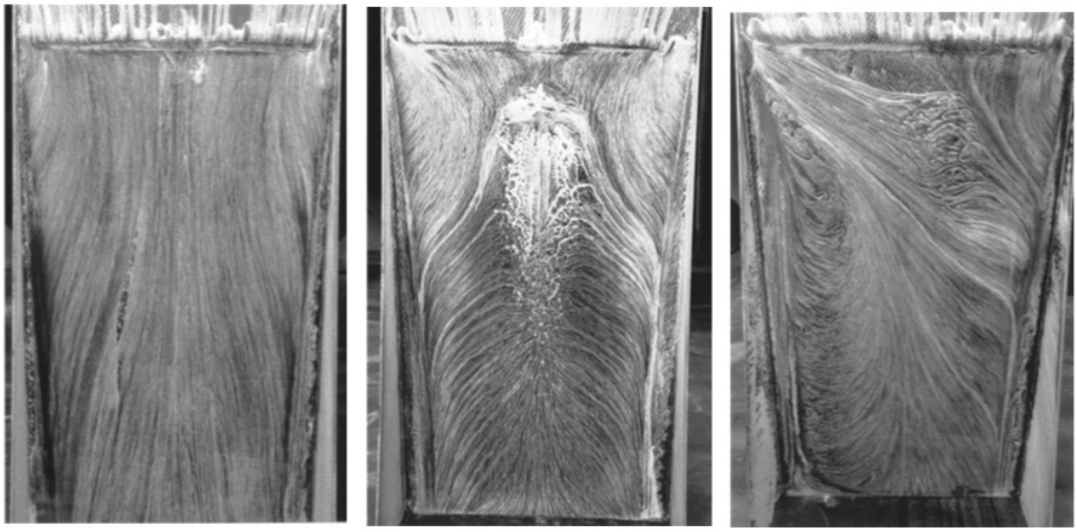
Figure 8-12: Lift coefficient and proposed performance region division based on the ground height h/Wd for a generic automotive bluff body equipped with 17° diffuser. Reproduction from Senior and Zhang [2001].

Zhang [2001]. Five different diffuser angles were evaluated in this case: 5°, 10°, 15°, 17° and 20° at wind-tunnel velocity of 30 m/s. Within this new set of experimental results, a further downforce reduction region *e* was identified after the low force region *d*. This region *e* appeared on the diffuser angle of 15° because the lowest ground height evaluated is smaller than the one used in Senior and Zhang [2001] and is presented in Figure 8-14.

Results shows once again that the downforce produced by the diffuser is dependent on the ground height. The flow behaviour on the diffuser surface is also related to the inclination angle of the diffuser. Flow visualization taken at the maximum downforce region and presented in Figure 8-15 show attached flow and two vortices on the 5° diffuser. The 10° diffuser shows an unsteady separation bubble on the centre of the diffuser, with further flow reattachment close to its outlet. Last case considering diffuser angle of 15° indicates an unsteady structure on the surface of the diffuser causing diffuser vortex breakdown. The main contribution of this work was the identification o different flow behaviours when the diffuser angle changes. Within this, the diffuser could be designed to obtain the best compromise between downforce and drag.

The PhD thesis of Jowsey [2013], which was summarized in the paper Jowsey and Passmore [2010], the author created a simple diffuser-equipped bluff body to investigate the performance of plane and multi-channel diffusers using force, pressure measurements and PIV techniques for flow visualization. The focus concentrated on the angle and ground height evaluation where ten diffuser angles (from 7° to 25° in increments of 3° and also 0° and 30°) and eight ride heights were investigated on a scale wind tunnel, considering moving and static ground and some studies on Reynolds number sensitivity.

The results for the plane diffuser showed similar trends in lift and drag presented in current literature of increased both downforce and drag with decreasing ride height to a saturation point, followed by a sharp decreased in downforce due to ground proximity. The optimum angle for downforce was found to be between 13° and 16°, with the pressure measurements highlighting local separation present at the diffuser inlet above 13° and a completely stalled



(a) Region a **(b)** Region b **(c)** Region c and d

Figure 8-13: Diffuser flow analysis considering four performance regions as proposed by Senior and Zhang [2001]. Reproduction from Senior and Zhang [2001].

flow behaviour for diffuser angle above 25°. The presence of a vortex and an underbody upwash within the diffuser were confirmed by PIV visualization for all cases. The intensity of the vortex at 25° is much weaker than lower angles with signs of asymmetry. As the ride height was increased the vortex strength increased and reduced levels of separation were also observed.

Multiple-channel diffusers results showed similar trends in lift and drag to the plane diffusers, and increased downforce production for the 16° and 19° diffuser angles. Area pressure measurements indicated that the gains occurred through improved diffuser pumping and pressure recovery in both the inside and outside channels. In the PIV data, all the multi-channel diffusers exhibited a similar flow field distribution to the plane diffuser. The multi-channel diffusers exhibited reduced levels of separation due to the presence of the splitter plates, improving attachment and increasing downforce, especially for the two-channel case. This study offered significant contribution to diffuser literature, especially for complex diffuser, such as the multi-channel ones. It would be even more interesting if the study was performed with a well-established automotive bluff body.

The work from Ehirim [2018] combines experimental and computational investigations were conducted into generic automotive bluff body equipped with a diffuser and side plates in ground-effect condition. Passive flow-control methods such as bumps, and wing profiles are applied to the diffuser aiming to enhance the diffuser's performance.

In the first part of the study, the author confirmed reported observations from previous studies in a newly proposed bluff body. Downforce generated by the diffuser in proximity to a ground plane is influenced by the peak suction at the diffuser inlet and subsequent static pressure-recovery towards the diffuser exit. When the ride height is reduced, it was found the same four flow behaviours reported by the study of Senior and Zhang [2001]. When

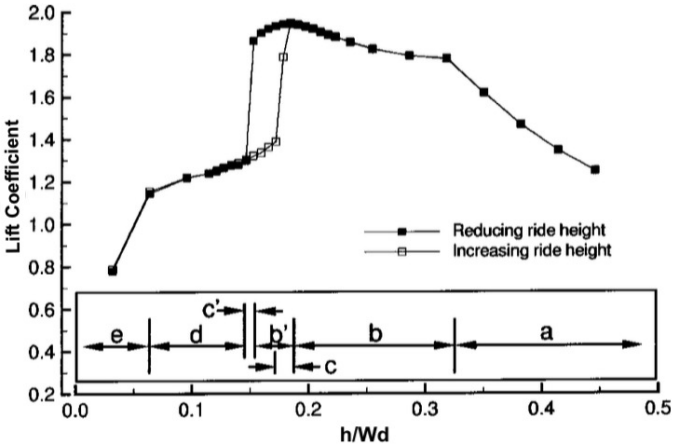


Figure 8-14: Lift coefficient and proposed performance region division by Ruhrmann and Zhang [2003]. Reproduction from Ruhrmann and Zhang [2003].

applying the proposed passive flow-control geometries, it was found that they induced a second-stage pressure-drop and recovery near the diffuser exit. This behaviour was due to the radial pressure gradient induced on the diffuser flow by the suction surface curvature of the passive devices. As a result of this aerodynamic phenomenon, the diffuser generated across the flow regimes additional downforce, and a marginal increase in drag due to the profile drag induced by the devices. Correlation CFD simulations generally agreed with experimental results, with slight increasing on the drag deviation when the body gets closer to the ground. This works combined both experimental and computational techniques, however the focus was experimental to identify the flow behaviour. Once again, the author decided to design a completely new bluff body to perform the measurements. The computational study is based on a commercial code solution using RANS, URANS and IDDES, in which the main contributions are in terms of the experiments, once no novel techniques were used for the CFD cases.

Studies considering the Ahmed body with diffuser were mostly performed by using CFD simulation and we now present main references. Huminic and Huminic [2010] numerically simulated the flow around the Ahmed body for the rear slanted upper surface of 35° and a simplified underbody diffuser, without endplates. The study was conducted in order to investigate the influence of the diffuser on the main aerodynamic quantities. The study proposes different geometric configurations, combining different diffuser lengths with diffuser angle variation. A commercial code is used for both mesh generation and simulation processing using a simplified $RANS\ k-\omega\ SST$ model. The use of $RANS$ methodology for complex flow phenomena, would not be the most recommended as previously presented. The conclusion of the study indicates that there is a continuous and well-predictable variation of lift and drag coefficients for diffuser angle up to 7°. For angles above this value, flow separates, generating vortices and unstable behaviour and we believe that the simulation methodology is not reliable enough to characterize the phenomena.

Continuing the previous work, Huminic and Huminic [2012] present a similar study, considering the Ahmed body with slant angle of 35° with a rear underbody diffuser but adding

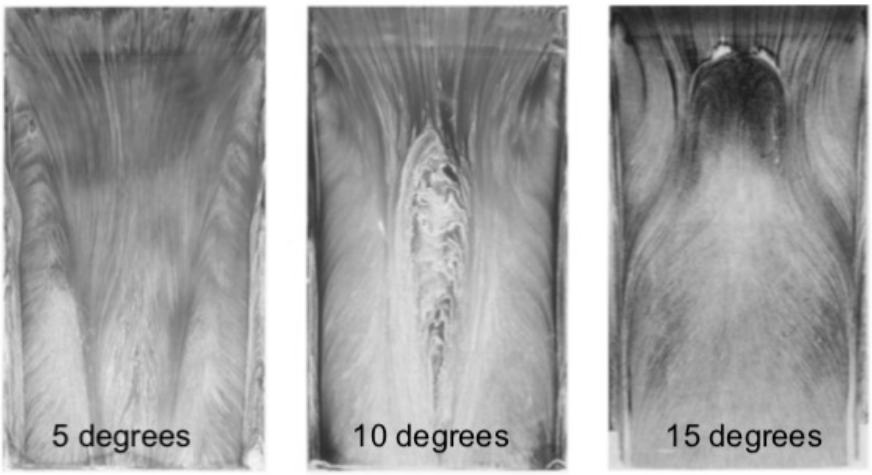
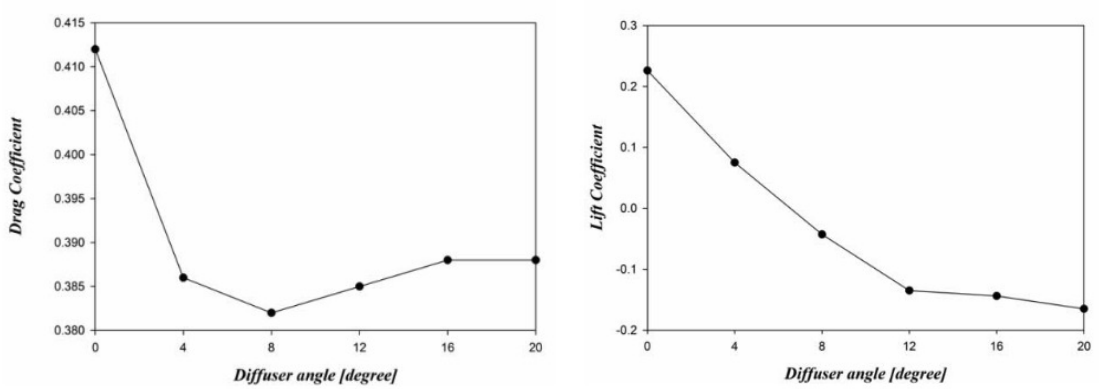


Figure 8-15: Surface flow visualization on the diffuser surface at maximum downforce region for 5°, 10° and 15° diffuser angles. Flow from up to down at $h/Wd = 0.584$. Reproduction from Ruhrmann and Zhang [2003].

wheels and wheelhouses. The simulation methodology was the same used in the previous work Huminic and Huminic [2010]. Results show that by adding wheels and wheelhouses to the current Ahmed Body with slant angle of results 35° both drag and lift coefficients increase mainly due to the vortices originated from the wheels and its rotation. By applying and underbody diffuser to this new Ahmed Body with wheels, results show that both drag and lift are reduced up to a certain limit in the length and angle of the diffuser.

Computational references on the Ahmed body with diffuser performed *RANS* simulations for all studies presented. The *RANS* methodology is able to provide good agreement in terms of drag coefficient, however they usually under-predict complex flow features as presented in Section 3-1. Correctly capturing the flow physics of the Ahmed body requires refined simulation methodologies (Guilmineau et al. [2017]). Flow structures on the Ahmed body diffuser appear to be similar to the ones presented by Ruhrmann and Zhang [2003] and Senior and Zhang [2001]. As an indication of the *RANS* methodology limitation, previous studies concentrated efforts on reporting only aerodynamic quantities values. Thus, lift coefficient prediction is also affected when using this simulation methodology as demonstrated by Guilmineau et al. [2017].

Moghimi and Rafee [2018] performed an experimental and numerical study on an Ahmed body equipped with diffuser. Both experiments and simulations were performed at a low Reynolds number of $Re = 9.31 \times 10^4$ considering a 10% scale half Ahmed body with slant angle of 25°. A diffuser with fixed length (not mentioned) was investigated at different angles ranging from 0° (baseline case) to 20°, in increments of 4°, following similar diffuser configurations from Lai et al. [2011]. Computational studies also employed the *RANS* methodology combined with the *SST* turbulence model, similar to Aulakh [2016]. Initial assessments present validation of the numerical model with references however using different boundary conditions for the ones proposed in the study. A mesh sensitivity study is next presented, and results indicate small changes for the drag coefficient. The lift coefficient variation, however, reaches 19% difference with an additional increment of 10% in h-mesh elements. The study doesn't detail the mesh



(a) Drag coefficient **(b)** Lift coefficient

Figure 8-16: Aerodynamic coefficient results in function of diffuser angle. Reproduction from Moghimi and Rafee [2018].

strategy and the number of elements used for each case reported.

The performance of the diffuser is summarized in Figure 8-16. Drag coefficient has decreased for angles up to 8° as presented in Figure 8-16a. For higher diffuser angles, drag coefficient values increase, reaching similar level of 4° or slightly above. Best drag coefficient performance for diffuser angle of 8° is justified by the back that flow is still attached to the diffuser. Lift coefficient increased downforce for all evaluated diffuser angles, as shown in Figure 8-16b, reaching maximum value at 20°. Diffuser pumping effect on the inlet was observed for the cases, as previously highlighted by Cooper et al. [1998].

From the study above, we first notice that the model scale factor is extremely reduced compared to other experiments. The small model is more sensitive to geometric imperfections, introducing additional source of error. The Ahmed body model used by Moghimi and Rafee [2018] seems to have a radius connecting the top and side walls, as well as, the slant also looks slightly rounded, as indicated in Figure 8-17. It's not presented on the study if the same geometry used on the wind tunnel was scanned and used for CFD studies. We point out that the main best practice for computational studies in the automotive industry, is to perform simulations with full scale models.

Once again, *RANS* methodology is used for the numerical solution of a complex flow problem in unstable conditions. When comparing the experimental results with the numerical simulations in this study, we found a 8.3% difference for the drag and 12.1% for the lift coefficients for the baseline model. The difference is similar when comparing the case with diffuser angle of 8°, where the drag difference is 6.8% but the lift coefficient difference reached 24.7%. Using static ground condition and low Reynolds number configuration is also not very suitable when studying diffusers, specially the static ground condition. The research doesn't make clear if we keep increasing the diffuser angle, we will have the same downforce increment, also not studied in previous references.

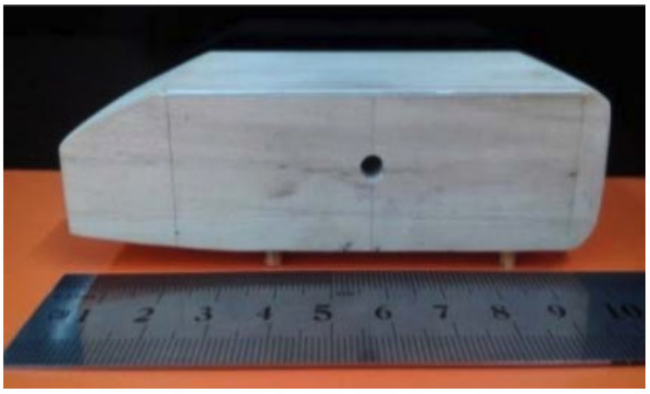


Figure 8-17: Half Ahmed body scale model proposed by Moghimi and Rafee [2018] in a reference with a ruler. Reproduction from Moghimi and Rafee [2018].

8-1-3 Objectives

We now propose a computational study to explore detailed features of the near-ground vortices, and to examine the potential benefits of implementing underbody diffusers on a classical Ahmed body geometry. The Ahmed bodies used in the study are with the squared-back and a slant angle of 25°, representing respectively station-wagons (attached flow) and performance cars (vortex generation with flow detachment).

In this study, the length of the underbody diffuser is set to be the same as the Ahmed Body slant length, with diffuser angles (DA) ranging from 10° to 50°, in increments of 10°. An additional case considers diffuser angle of 5°, a setting commonly found in racing vehicles. Proposed cases were simulated following the spectral/hp element methodology developed for the Ahmed body validation as well as the boundary conditions, as presented in the previous chapter.

By proposing different diffuser angles to be evaluated on the Ahmed body, this study has well-established objectives. The first objective is to quantify the diffuser influence on both drag and lift coefficients values and the relationship between drag and downforce generation.

Next, we aim to identify the flow structures and possible different flow regimes close to the diffuser. We present comparison of U, V and W velocities as well as contours of Q-Criterion and surface wall shear stress for all proposed cases. As presented in Chapter 8-1-2, we have an indication of which flow structures should be found, however the absence of the endplate might lead to new findings.

The third objective is to evaluate the influence of the exterior geometry in the overall performance of the diffuser. By selecting the Ahmed body squared-back and 25° slant angle to perform the diffuser angle variation study, we aim to investigate how the dynamics of the flow changes.

The last objective is related to identify the origin of the lower side vortex and how its trajectory changes as the diffuser angle increases. We also highlight here the importance of a high-resolution solution, to capture this vortex. Next, the proposed Ahmed body geometries are detailed.

8-1-4 Geometry

Based on the same principle of the classical Ahmed body where the slant length remains fixed and the angle changes, we proposed similar condition for the diffuser. Diffuser length L_d is set to be always the same as the upper slant length L_s of 222 mm, regardless of the inclination of the diffuser angle θ. This length is selected to make it possible to use the classical Ahmed body geometry for a complementary study on diffusers and also to compare the flows structures on the upper slant with the new ones find in the diffuser.

We proposed two geometries based on the classical Ahmed body shape equipped with rear underbody diffuser, presented in Figures 8-18 and 8-19. The first one is based on the Ahmed body squared back or 0° slant angle, representing hatchback or station wagon vehicles. The second one considers the slant angle of 25°, representing fastback and racing vehicles cars with rear wings, due to the nature of the vortical flow on the slant, as previously presented on Chapter 7.

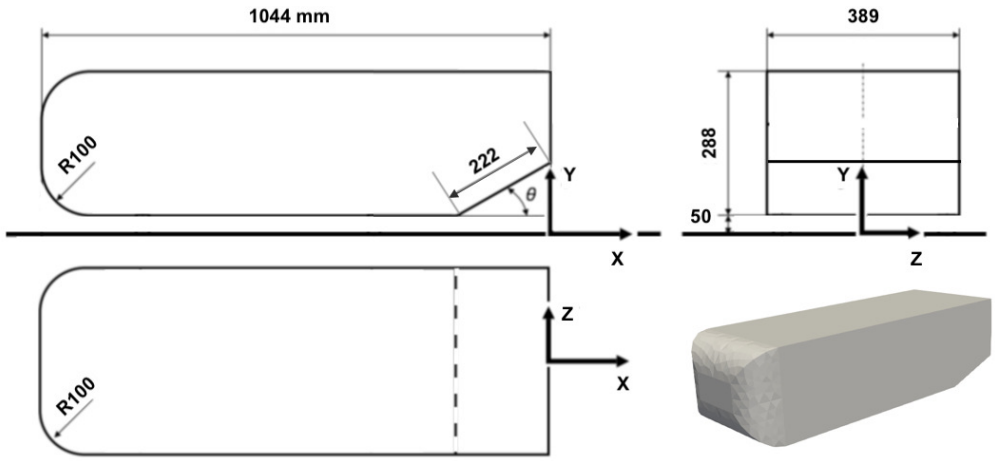


Figure 8-18: Schematic drawing of the Ahmed body squared-back equipped with rear underbody diffuser.

The full domain and Ahmed body position follow similar setup as proposed in the previous chapter for the classical Ahmed body. We present next, details for the simulation setup in this study.

8-2 Simulation configuration

In this study, we use similar simulation parameters and setup as presented in Chapter 7-3-2. The Reynolds number for all diffuser cases is set to $Re = 1.7 \times 10^6$, based on the body total length L_l. We employ similar conditions as employed by Strachan et al. [2007] also considering moving floor simulation.

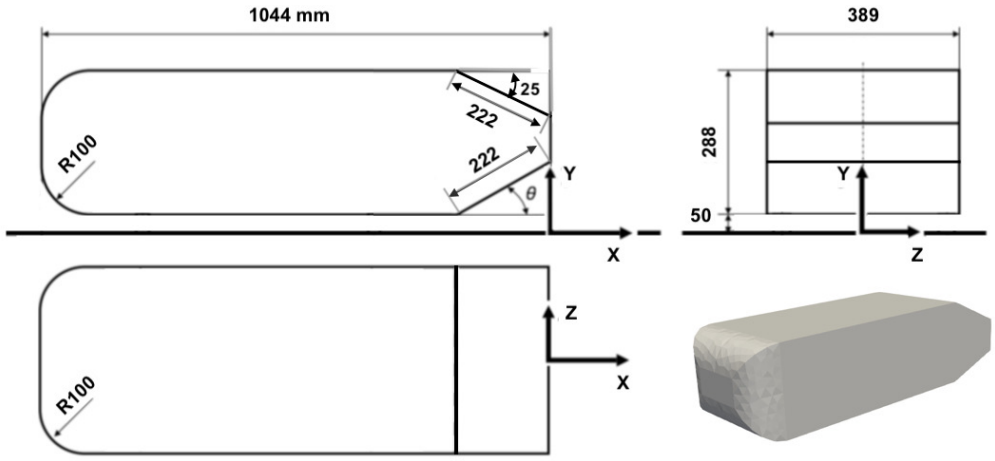


Figure 8-19: Schematic drawing of the Ahmed body with slant angle of 25° equipped with rear underbody diffuser.

The boundary conditions for the computational study are summarized as follows:

- Ahmed bodies with diffuser are set as wall with no-slip condition;
- A half model of the geometry is used;
- Symmetry condition imposed at $Z = 0$;
- Uniform velocity profile at the inlet;
- High order outflow condition at the outlet (as proposed by Dong et al. [2014]);
- A moving ground condition on the floor with speed U in the X direction, as used by Strachan et al. [2007].
- Simulations are performed for 7 CTUs.
- 432 CPUs used for each diffuser case simulation.

The high-order mesh for all cases presented in this work are generated by NekMesh (Turner [2017]), following its complete pipeline, without using the commercial software, as presented in Figure 6-5. As defined and explained on Chapter 7-3-2, we select high-order polynomials for both P_M and P_N of 6^{th} order accuracy to have the most reliable flow representation.

The volumetric mesh also incorporates two refinement zones applied over the Ahmed body length as illustrated with Figure 8-20, similar to the mesh study performed by Buscariolo et al. [2020]. The refinement zones are aimed to help capturing the flow phenomena over the slant and diffuser areas as well as the flow features on the far field, based on a h refinement approach of the spectral/hp element method.

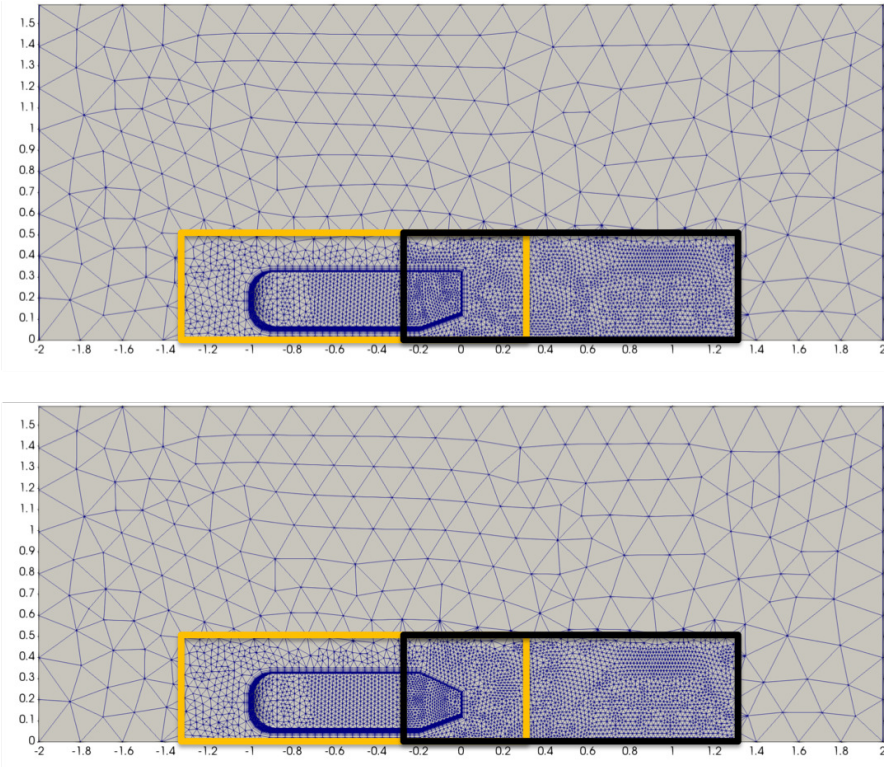


Figure 8-20: Mesh refinement regions on both Ahmed bodies squared back (top) and with slant angle of 25° (bottom). Refinement region highlighted in yellow is defined as the Ahmed Body refinement and region highlighted in black is defined as Wake Refinement.

For both Ahmed body squared-back and with slant angle of 25°, meshing configuration parameters and boundary layer setups follow similar procedure and values as proposed for the *Refined* mesh in chapter 7-3-2. Similar to the classical Ahmed body, *Refined* mesh generated approximately $N_{EL} = 335,000$ elements for each diffuser case proposed. Within the use of 6^{th} order P-refinement on the spectral/hp element method for the solution, the mesh resolution increases to 21.2 million DOFs per variable. We next present results for the diffuser study on both Ahmed body styles.

8-3 Results and analysis

The key findings of the study are presented as follows. We first present a comparison of drag and lift coefficients when different diffuser angles changes for both Ahmed body styles. Both quantities are averaged from the 5^{th} to the 7^{th} convective length where we assure to have a fully converged physical solution. Values are presented for the different diffuser angles for both Ahmed Bodies with squared-back and 25° slant inclination. Flow structures comparison for planes $X/L_l = 0$ and $X/L_l = 0.096$, representing flow close to the body, focusing on vortical structures and wall shear stress lines averaged from the same period are also presented in order to complement the findings. Iso-contours 3D plots of Q-Criterion (QCrit = 100) presented are instantaneous on the 7^{th} convective length (CTU).

8-3-1 Aerodynamic quantities results

Drag coefficient results

We first present results for the averaged drag coefficient with both Ahmed body slant angles in Figure 8-21. Ahmed body squared back results shows that the drag coefficient initially rises as the diffuser angle increases, reaching the maximum drag coefficient value at the diffuser angle of 30°. This drag rising trend suddenly break for diffuser angles higher than 30°, where results for further angles are similar to the diffuser with 20° inclination. Such behaviour for the drag coefficient indicates similar trends as earlier verified in studies on Ahmed body slant angle variations of Ahmed et al. [1984], Lienhart et al. [2002] and Strachan et al. [2007]. The drag breaking point for the diffuser angle being similar to slant angle is an indication of flow structure change on the diffuser region and is further discussed. For all diffuser angles tested, the averaged drag coefficient calculated are higher than the baseline squared-back body without diffuser. We conclude that any diffuser added to this baseline case has a penalty in terms of drag performance, following similar trend as the slant change for the original Ahmed body experiment. The wake flow generated in all cases has a quasi-symmetric profile, with diffuser flow structures interacting with the base pressure wake. These flow interactions generate additional drag loses higher when compared to the squared-back case which has a bi-stable wake profile.

The drag coefficient results for Ahmed body with 25° slant angle show different trend from previous case: diffuser application has no negative impact on drag coefficient performance. Applying the diffuser with angles of 5°, 10° and 20° angle leads to drag reduction with the optimum angle for at 10°. For the other diffuser angles, the drag coefficient recovers to similar value of the baseline case without diffuser. For this case, we also notice that the drag enhancement region might be related to flow behaviour change on the diffuser region.

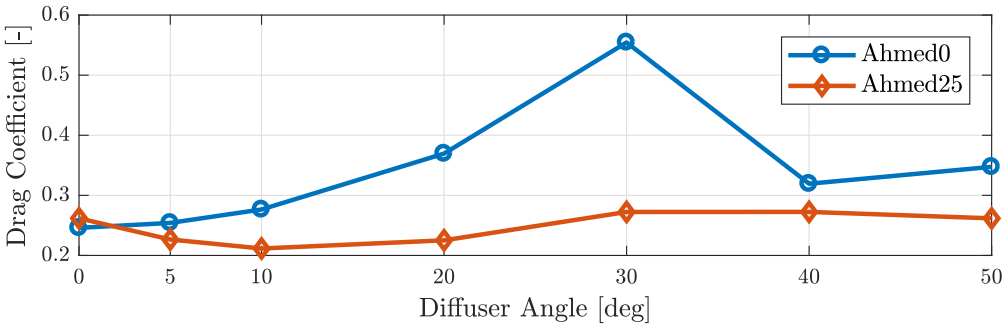


Figure 8-21: Drag coefficient comparative results for Ahmed Body squared-back (blue line) and 25° slant inclination (orange line), considering baseline configuration and evaluated diffuser angles: 5°, 10°, 20°, 30°, 40° and 50°.

Summarizing, we noticed that the slant angle of the Ahmed body influences the drag coefficient performance when adding a diffuser. The two Ahmed body slant angle cases evaluated, squared-back and 25°, had different behaviours due to their body shapes and different base pressure values. The Ahmed body squared-back always presented drag increment when adding a diffuser. In a real vehicle, this device would increase fuel consumption level and need

further analysis for its implementation. The Ahmed body with slant angle of 25° equipped with diffuser has no drag penalties. Drag performance enhancement is achieved considering diffuser angles of 5°, 10° and 20°. In this case, the use of diffuser is recommended for overall performance improvement. Next, we evaluate the lift performance of the diffuser for the same baseline cases.

Lift coefficient results

Analysing the lift coefficient results for the Ahmed body squared back, downforce enhancement is obtained as the diffuser angle increases from 0°, reaching maximum downforce value at 30°. The trend breaking phenomenon is once again observed for the downforce for diffuser angles higher than 30°. The downforce values for both diffuser angles higher than 30° are similar to the diffuser of 5°, indicating saturation in terms of downforce increment performance.

Lift coefficient results for the Ahmed body with 25° slant inclination shows similar trend of previous squared-back results. One interesting point to notice is the positive lift on the baseline case without diffuser, which might compromise gripping on performance and race cars. By implementing the diffuser, downforce performance starts to increase, where the first proposed diffuser angle of 5° take the lift coefficient to zero. The downforce enhancement happens until the diffuser angle of 20°, where the maximum performance is reached. The diffuser loses its performance when observing lift coefficient results for 30° and above. The diffuser angle of 30° has performance similar to the 5° whereas the 40° and 50° diffusers have similar performance as the baseline. Lift coefficient results previously discussed for both Ahmed body cases are presented in Figure 8-22.

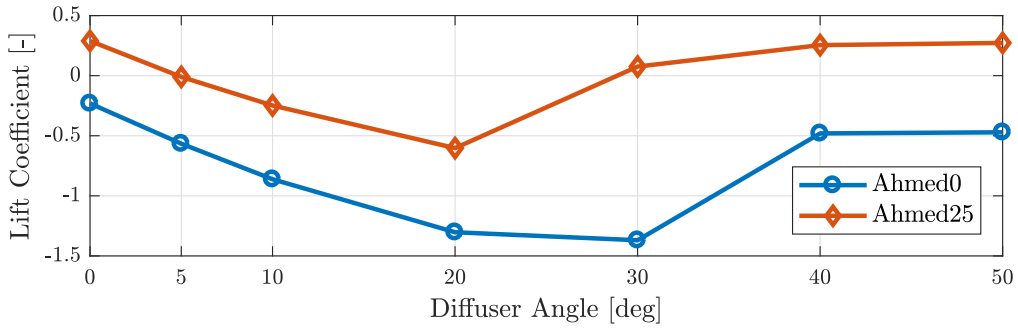


Figure 8-22: Lift coefficient comparative results for the Ahmed Body squared-back (blue line) and 25° slant inclination (orange line) considering standard configuration and evaluated diffuser angles: 5°, 10°, 20°, 30°, 40° and 50°.

Summarizing lift coefficient results presented, downforce increases as the diffuser is applied in all cases for the Ahmed body squared-back. The maximum downforce performance is reached with the diffuser of 30°. We observe similar trend break as seen for the drag coefficient for diffuser angles above 30°. The conclusion is that, for Ahmed body with a squared back, the drag and negative lift coefficient increments are directly related. Both share the same breaking trend at the diffuser angle of 30°, where maximum drag and downforce values are

observed. The final statement is that a diffuser applied to an Ahmed body squared-back increases both drag, and downforce compared to baseline.

Analysing lift and drag coefficient results combined, it is not possible to find the same trend as the Ahmed body squared-back. The window of interest although, lies on the same diffuser angles range, from 5° to 40°, where there is an indication of different flow regimes. We observe that the maximum downforce increment is achieved using the diffuser angle of 20°, whereas the maximum drag coefficient is found using the diffuser of 30°. Unlike the first case, increasing the diffuser angle leads to better drag performance compared to baseline. A possible explanation is that the flow over the inclined slant interacts with the diffuser flow to reduce the rear wake. The slant vortex, which is a very dominant flow structure, has a tendency to merge with the diffuser vortex, whenever this feature is present. This merged vortex reduces the rear wake, improving the drag performance. Once the diffuser vortex is not present, the drag value recover similar values as the case without diffuser.

8-3-2 Flow Features Analysis

Comparative results for the flow structures found on the Ahmed body equipped with diffuser are now presented. The main comparisons are presented for two planes, one at $X/L_l = 0$, where the end of the Ahmed body is placed and another one further downstream at $X/L_l = 0.096$, in order to evaluate how the flow structures develop as they separate from the body. Contours of Q-criterion, U (streamwise), V (vertical) and W (spanwise) velocities are provided for the cited planes, aiming to identify flow structures and define its interactions with the rear wake. We also provide a flow topology comparison on the diffuser surface by plotting wall shear stress lines. Results for the Ahmed body squared-back are firstly presented, followed by the Ahmed body with 25° slant angle. We define the simulation cases by the abbreviation of diffuser angle, DA, followed by the inclination angle (e.g. diffuser angle of 30° is defined as DA30). All plane views presented are observed from downstream.

Ahmed body squared-back with diffuser

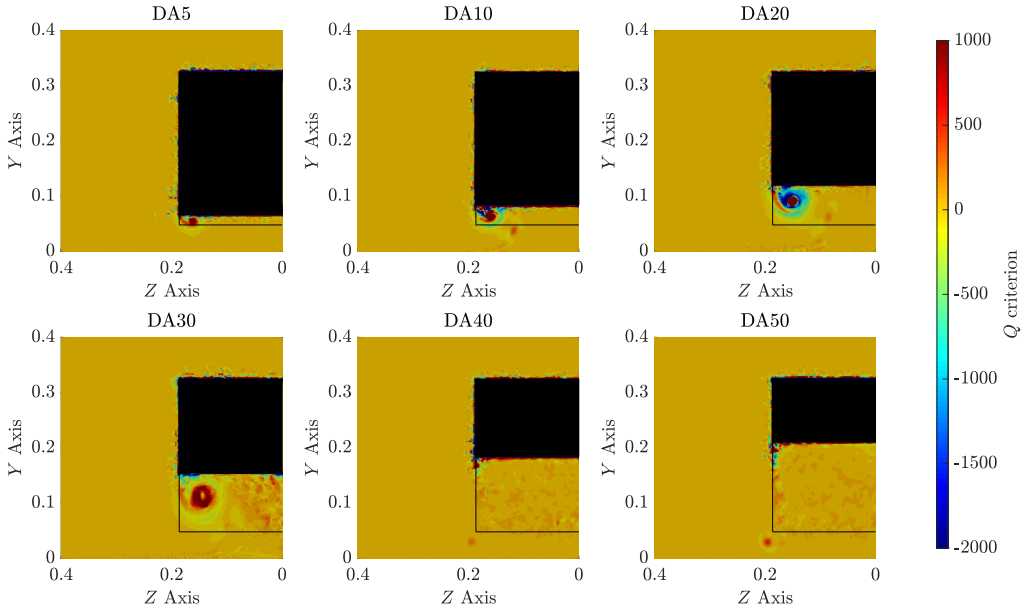
We now present the flow analysis for the Ahmed body squared-back with diffuser. The first analysis of Figure 8-23a indicates that there is a vortex arising from side part of the diffuser up to the angle of 30°. The vortex intensity and core size increase as the diffuser angle gets more inclined. A wake structure can also be noticed for the DA30 case, indicating that there is separated flow on the diffuser. This behaviour is similar to the classical Ahmed body slant variation experiment for slant angles ranging from 12.5° to 30°. For diffuser angles above 30° only a few details are observed, such weak vortices on the lower part, which will be further discussed. There is an indication of fully separated flow, however the Q-Criterion image alone is not conclusive.

Moving downstream to plane $X/L_l = 0.096$, shown Figure 8-23b, the main difference noticed is on DA30 case where the diffuser vortex was ingested by the rear wake. The diffuser vortex in cases DA5, DA10 and DA20 are weaker and shifting both upwards and in the spanwise direction towards the symmetry plane.

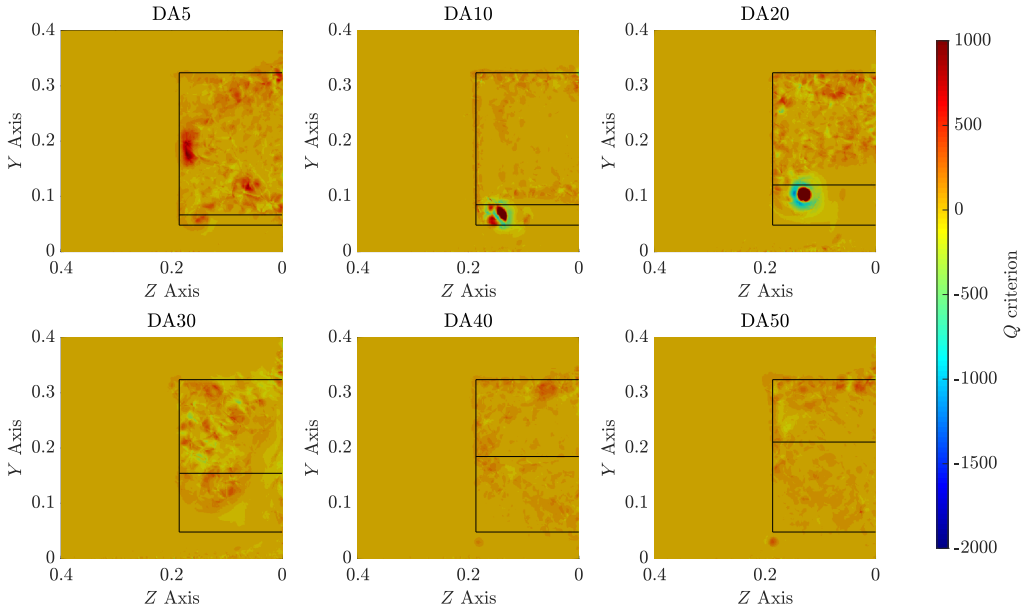
Flow separation is noticed for DA40 and DA50 case on plane $X/L_l = 0$ and shown in Figure 8-24a. The large negative velocity area indicates that the flow is already separated at the outlet

of the diffuser. A more intense contour of negative U velocity is observed on DA50 when comparing to DA40, explaining the higher drag for the former. We also notice a negative velocity area on DA30 at mid-span, showing flow separation combined with vortex generation. With both flow features, the DA30 case can be characterized as a highly complex flow.

The evolution of the flow structures on the plane $X/L_l = 0.096$ is presented in Figure 8-24b. Low velocity zones are located on the base pressure area of the body, with a different contour position for DA30. The DA30 shifts the base wake upward as it moves on the inner spanwise direction. The diffuser vortex intensity seems to create this translation effect and further results are present to explain the phenomenon.



(a) Plane $X/L_l = 0$



(b) Plane $X/L_l = 0.096$

Figure 8-23: Contours of Q-Criterion for the Ahmed body squared-back considering diffuser angle of 5° (DA5), 10° (DA10), 20° (DA20), 30° (DA30), 40° (DA40) and 50° (DA50) for planes $X/L_l = 0$ and $X/L_l = 0.096$.

From normalized vertical velocity V contours in Figure 8-25, we extract the diffuser vortex rotation direction. From the downstream view, the diffuser vortex rotates anti-clockwise, as the most inner spanwise vortex component has positive vertical velocity and the outer negative.

DA30 vertical velocity contour on plane $X/L_l = 0.096$ explain the wake moving upwards on the spanwise direction from Figure 8-24b. There is a strong positive vertical velocity zone at the mid-span behind both the diffuser and back of the Ahmed body.

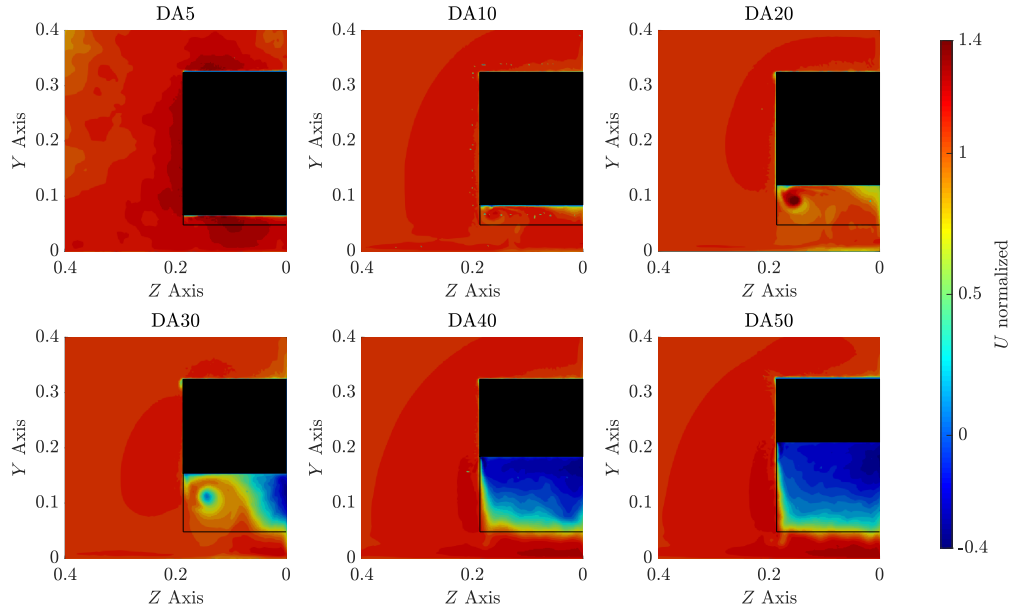
Lastly, we present results for spanwise velocity W in Figure 8-26. Intensity and shape of the diffuser vortex is shown in Figure 8-26a for plane $X/L_l = 0$, where we observe that the intensity and size increases as the angle of the diffuser get steeper from DA5 to DA30. The counterclockwise rotation is also confirmed, as the top part of vortex component has positive W, while the lower has negative. An increment of the spanwise velocity is noticed close to the surface of the diffuser comparing DA40 with DA50.

On the plane $X/L_l = 0.096$, the diffuser vortex starts to get diffused, as the wake effects downstream influence the vortex behaviour. This effect is observed for diffuser angles ranging from 5° to 20°. Contours of W on the DA30 case shows a flow structure similar to a vortex, generated by the combination of the rear wake and the diffuser vortex. This combined structure leads DA30 to have both highest drag and lift coefficients.

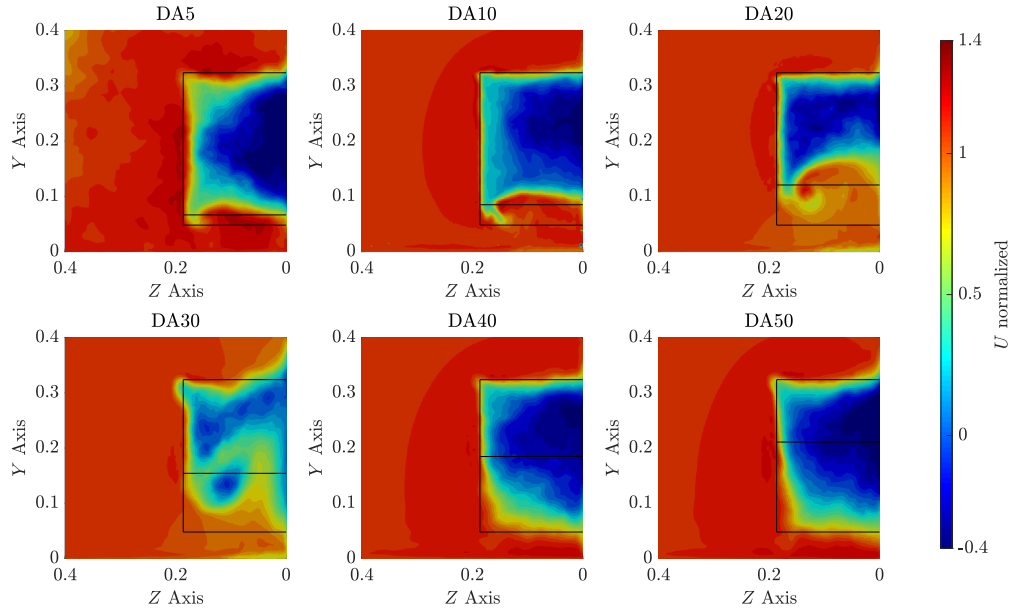
Results for the wall shear stress lines for the diffuser cases are evaluated. The bottom view of the diffuser, with flow direction coming from the top in presented in Figure 8-27. We define the terms diffuser inlet as the top face of the diffuser, and diffuser outlet as the bottom face.

From previous results, the diffuser flow structure has a vortex up to the DA30 and separated flow from DA40 onward. Analysing results in Figure 8-27, we found different flow behaviours on the diffuser surface, detailed as follows. The DA5 and DA10 cases have the side diffuser vortex touching the diffuser surface up to the mid-span. There is a clearly defined separation area at the diffuser inlet, corresponding to a low-pressure area. When applying an effective diffuser, the low-pressure area at the diffuser inlet is generated in order to keep the flow continuity. The diffuser recovers pressure on its length due to the inclination and consequently change of cross-section area, until reaching the outlet at a fixed base pressure region. We also observe that the separation area increases from DA5 to DA10 and the flow remains attached on the diffuser surface until reaching the diffuser outlet for both cases. Comparing the diffuser performance, DA10 provides more downforce than DA5, where the main change is the size of the flow separation area. A combination of both separated flow on the diffuser surface and diffuser vortex is observed for the DA30 case. The diffuser vortex size increases, reaching almost mid-span distance at the diffuser outlet, while fully separated flow is also observed on the diffuser surface. The case considering DA20 lies between DA30 and DA10 or DA5 diffuser flow regimes.

The DA20 case presents diffuser vortex, with defined separation area at the diffuser inlet followed by a small separation bubble. The flow then reattaches to the diffuser surface and follow this pattern until reaching the diffuser outlet. Similar behaviour is observed by Senior and Zhang [2001], Jowsey [2013] and Ehirim [2018]. The cases considering extreme diffuser angles (DA40 and DA50), had no previous references, however the low performance is expected. Results show a chaotic behaviour on their surfaces due to the separated flow and an additional separation is observed at the diffuser outlet. A complimentary analysis is presented further in this section.

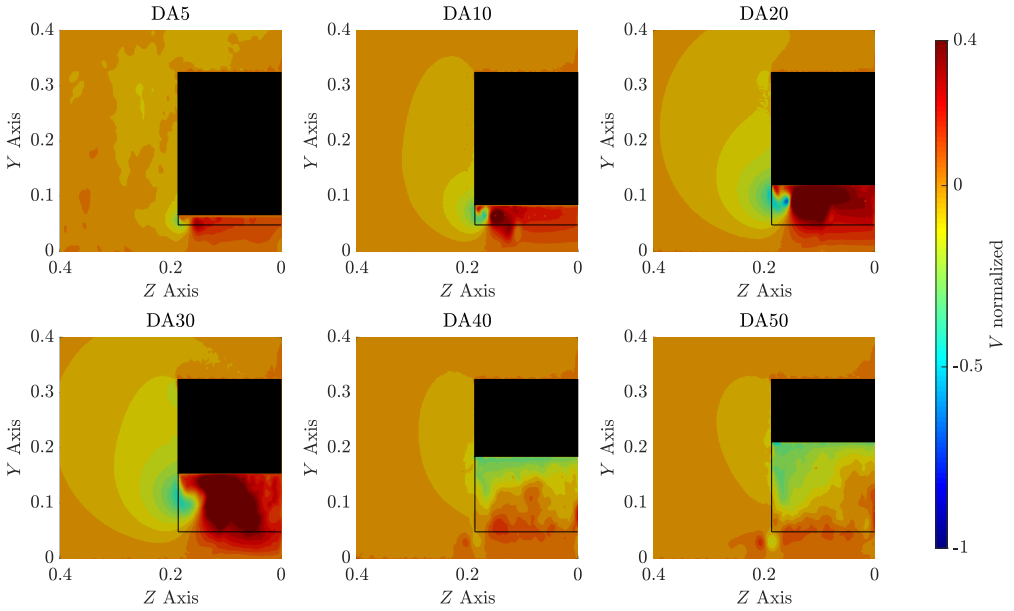


(a) Plane $X/L_l = 0$

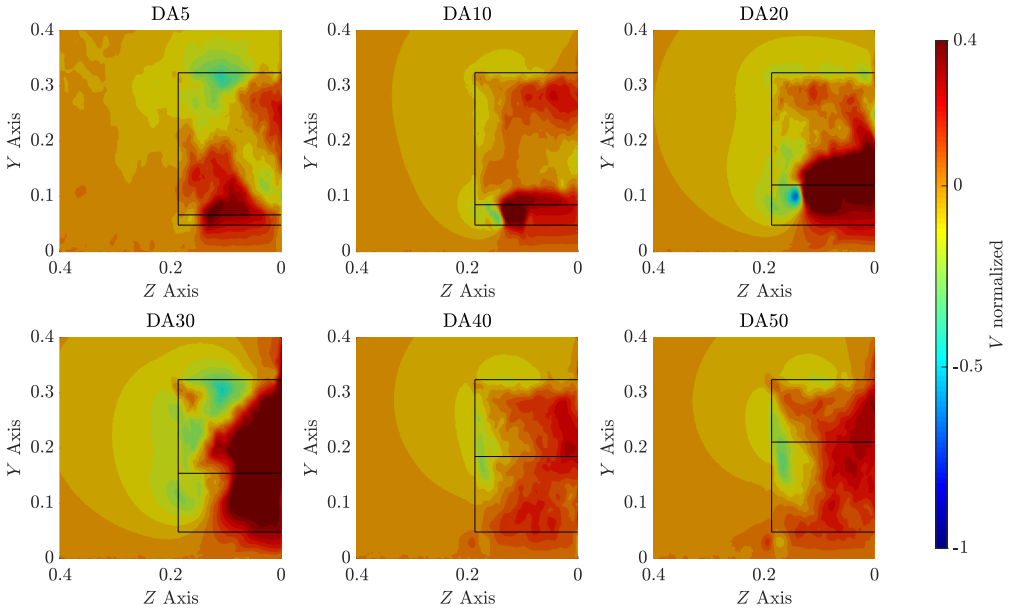


(b) Plane $X/L_l = 0.096$

Figure 8-24: Contours of normalized streamwise velocity U for the Ahmed body squared-back considering diffuser angle of 5° (DA5), 10° (DA10), 20° (DA20), 30° (DA30), 40° (DA40) and 50° (DA50) for planes $X/L_l = 0$ and $X/L_l = 0.096$.

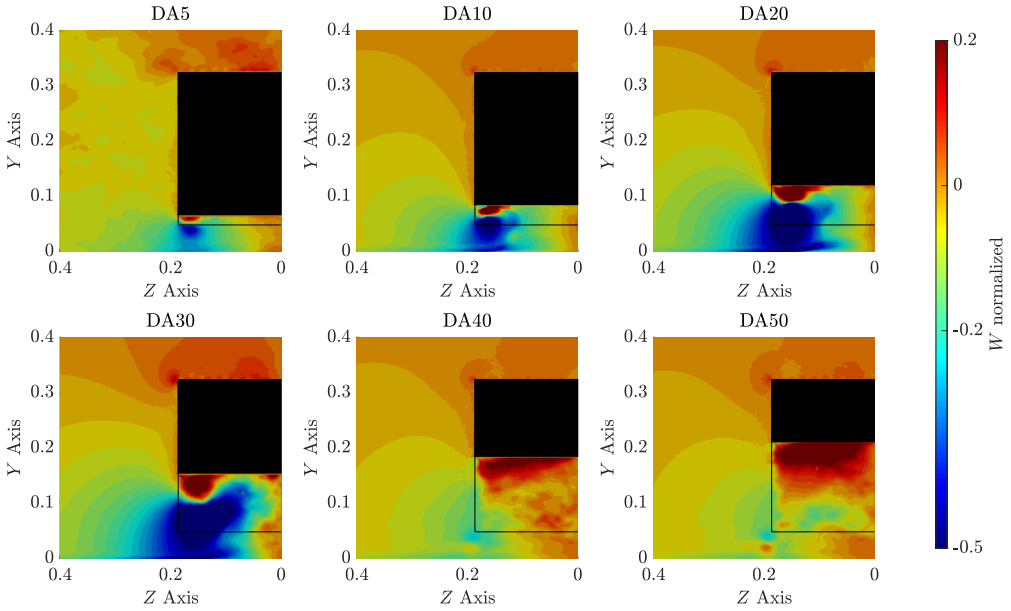


(a) Plane $X/L_l = 0$

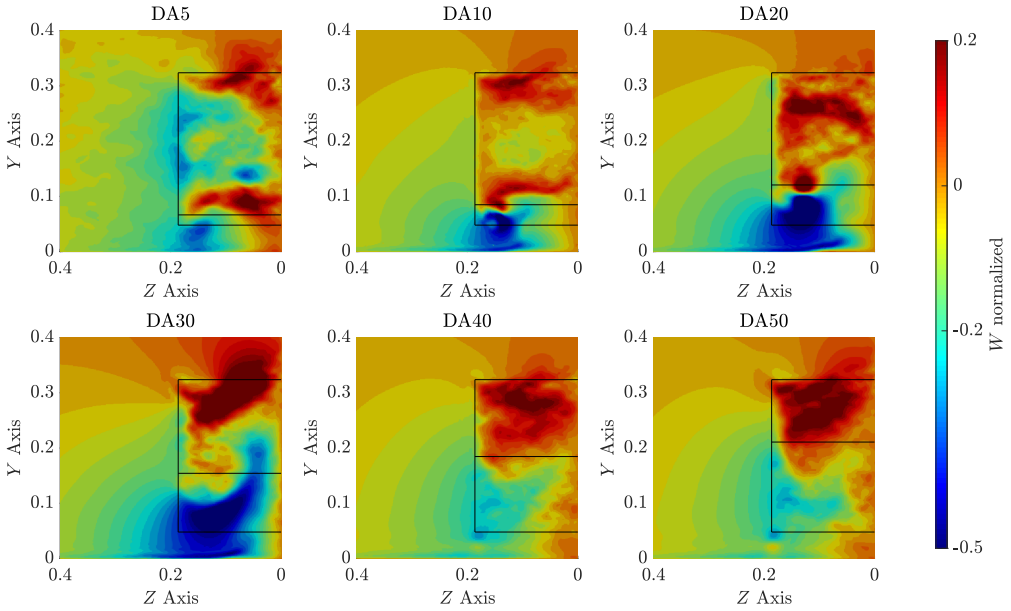


(b) Plane $X/L_l = 0.096$

Figure 8-25: Contours of normalized vertical velocity V for the Ahmed body squared-back considering diffuser angle of 5° (DA5), 10° (DA10), 20° (DA20), 30° (DA30), 40° (DA40) and 50° (DA50) for planes $X/L_l = 0$ and $X/L_l = 0.096$.

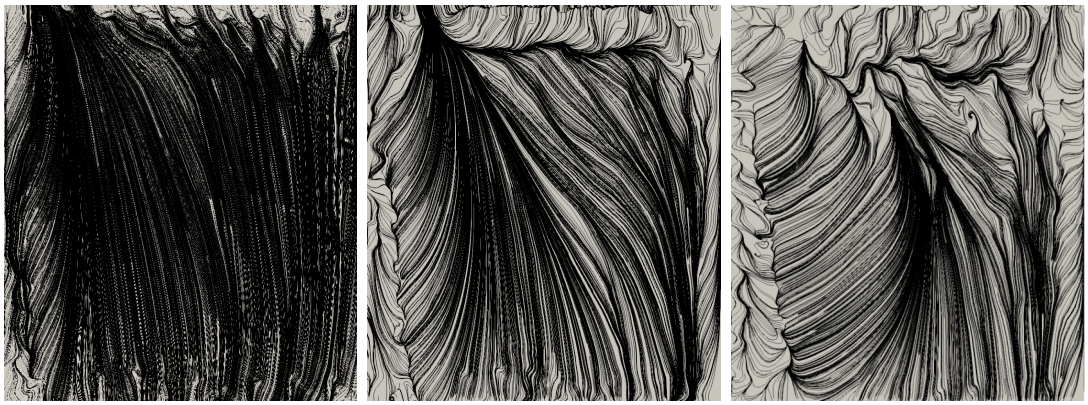


(a) Plane $X/L_l = 0$

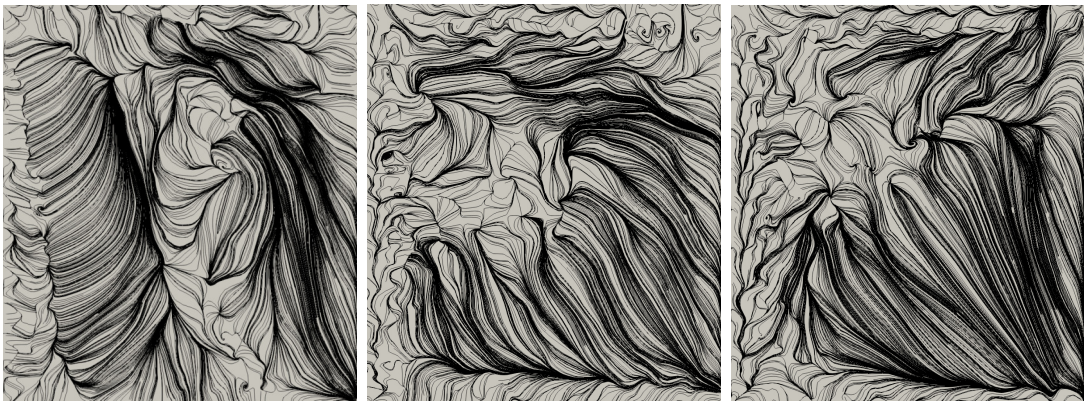


(b) Plane $X/L_l = 0.096$

Figure 8-26: Contours of normalized spanwise velocity W for the Ahmed body squared-back considering diffuser angle of 5° (DA5), 10° (DA10), 20° (DA20), 30° (DA30), 40° (DA40) and 50° (DA50) for planes $X/L_l = 0$ and $X/L_l = 0.096$.



(a) DA5 **(b)** DA10 **(c)** DA20



(d) DA30 **(e)** DA40 **(f)** DA50

Figure 8-27: Time-averaged wall shear stress lines (black) on the diffuser surface for the Ahmed body squared-back considering the proposed diffuser angles: 5° (DA5), 10° (DA10), 20° (DA20), 30° (DA30), 40° (DA40) and 50° (DA50), bottom view, incoming flow direction from top.

The last result presented for the Ahmed body squared-back in Figure 8-28 is the pressure coefficient (C_p). Results for C_p curves are extracted on a parallel line closer to the lower surface of the Ahmed body at $Z/L = 0.0479$, converting full Ahmed body length from $X/L_l = -1$ to $X/L_l = 0$. The diffuser pumping effect, as previously explained, was first observed by Cooper et al. [1998], characterised by a negative C_p peak at the diffuser inlet. This lower C_p is also associated with the flow on the underbody to be faster, with a consequent downforce performance improvement. Similar behaviour is observed on our simulation cases of DA5, DA10 and DA20, with increase of low pressure on the flat underbody and pressure recover on the diffuser length. DA30 case doesn't have an evident peak, however an almost flat area as the flow becoming fully separated on the diffuser. The diffuser is still effective on this case. For diffuser angles higher than 30°, C_p shows no evidence of pressure reduction on the underbody.

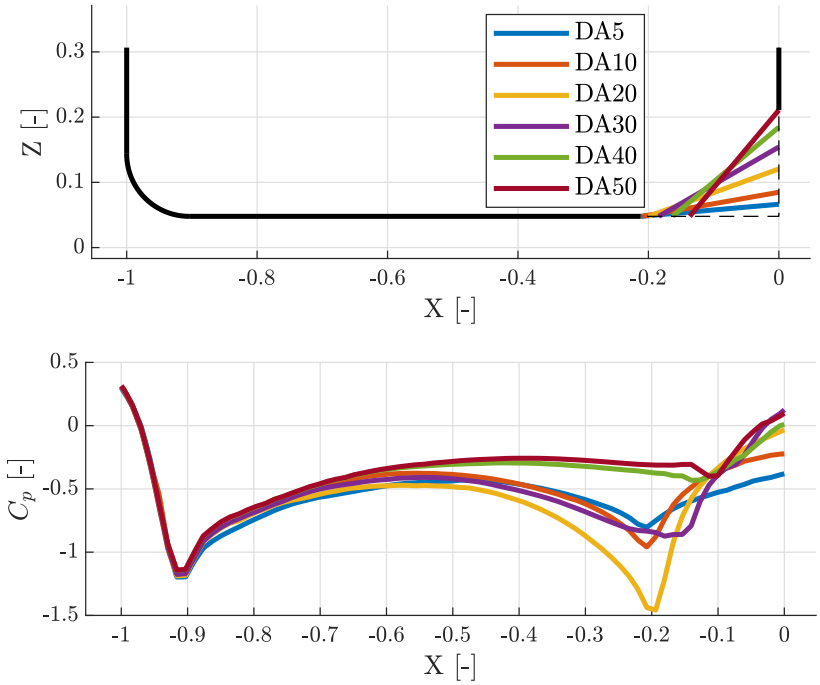


Figure 8-28: Pressure coefficient (C_p) distribution for proposed diffuser angles though the whole Ahmed body squared-back length.

Ahmed body 25° slant inclination flow

We now analyse flow the structures found for the Ahmed body with slant angle of 25° equipped with the proposed underbody diffuser angles. The slant vortex is clearly defined in all diffuser angles evaluated. As previously presented, contours of Q-Criterion for planes $X/L_l = 0$ and $X/L_l = 0.096$ are shown in Figure 8-29. The diffuser vortex appears on DA5, DA10 and DA20 together with an additional small intensity vortex on the plane $X/L_l = 0$. The diffuser vortex has similar intensity and size as the slant vortex in the DA20 case. The other three

diffuser cases, DA30, DA40 and DA50 have no evidence of the diffuser vortex but only the same weak vortex, originated on the frontal part of the Ahmed body, which will be detailed next.

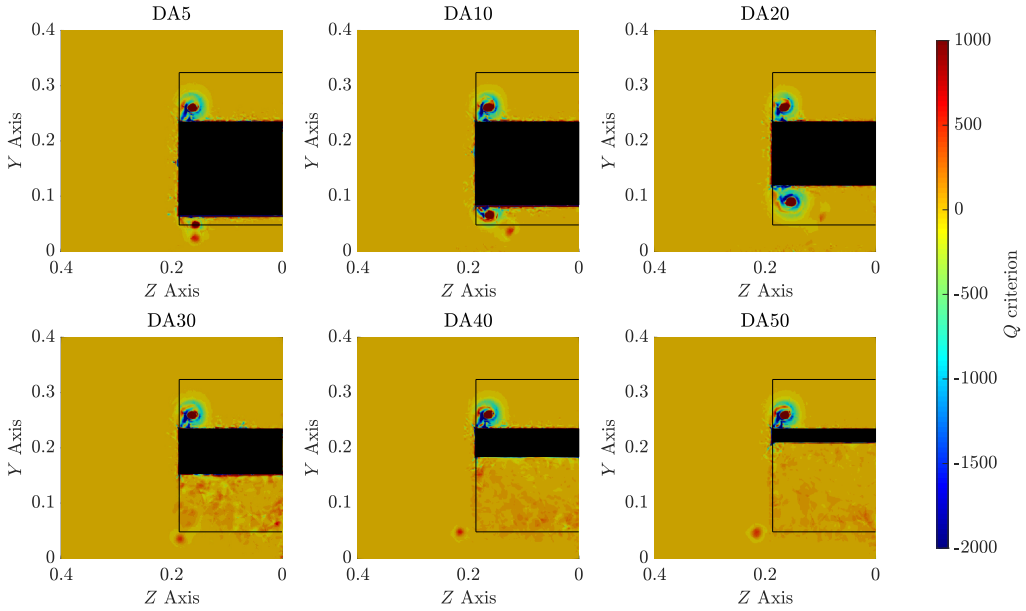
Further downstream on plane $X/L_l = 0.096$, the vortical system have moved inward in the spanwise direction on the first three cases. The last three cases indicate that the lower side vortex got weaker as it moved downstream.

Contours of normalized U for the planes $X/L_l = 0$ and $X/L_l = 0.096$ are presented in Figure 8-30. The velocity gradient on the upper slant changes as the diffuser angle becomes more inclined up to DA20 on plane $X/L_l = 0$, however the three other cases from DA30 to DA50 have similar velocity profiles. As for the diffuser, attached flows can be seen for diffuser angle up to 20°, whereas for higher angles, a significant wake contribution can be seen from the fully separated flow from the diffuser.

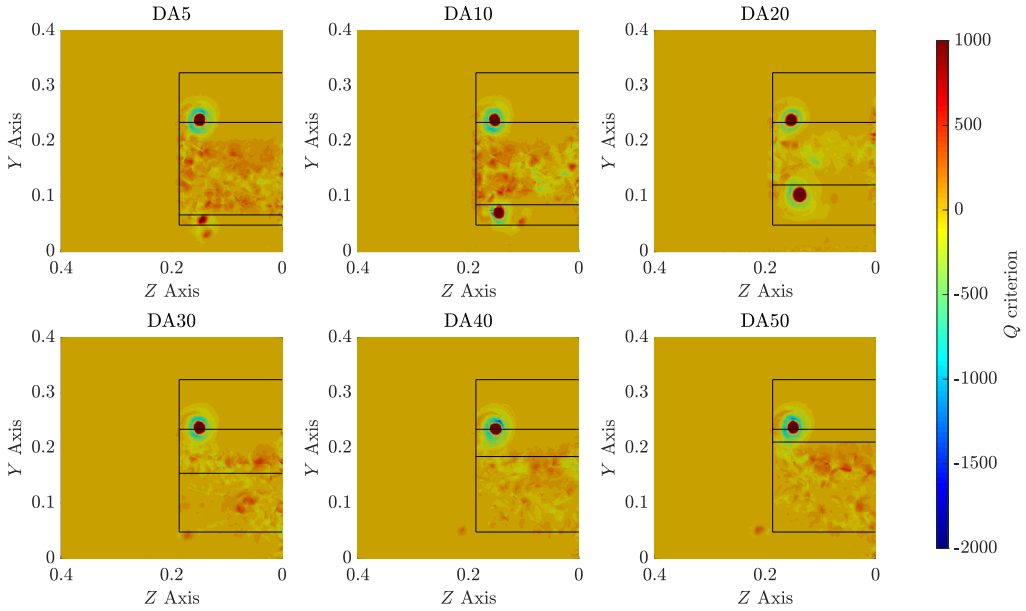
Moving downstream, normalized U on plane $X/L_l = 0.096$ shows the evolution of the turbulent wake and vortices for the different diffuser cases. Base pressure turbulent wake with the slant and diffuser vortices are the main structures seen on cases DA5 and DA10. The U velocity contours on this plane for the DA20 case shows a very small negative velocity zone, indicating a very energetic wake, together with the slant and diffuser vortices moving downstream. Moving to DA30 case, wake profile and vortical system is similar to DA40 and DA50 except by the fact of a distortion on the lower outer area of the diffuser. At this point, the flow distortion could be caused by a vortical flow structure and further plots will provide evidence to confirm this assumption.

Normalized vertical velocity V is analysed and presented in Figure 8-31. On plane $X/L_l = 0$, we observed similar contour on the slant as the experimental reference defined on the Ahmed validation study of Lienhart et al. [2002]. When analysing the diffuser area, a pair of vortices is identified at similar spanwise coordinates but different heights on DA5 case, characterized by a positive and negative velocity regions converging to a point. From bottom to top, the lower side vortex and the diffuser vortex are in the same region, however it is not possible to assure they are merging at this point. Only the diffuser vortex is observed for DA10 and DA20, following the same identification principle exposed for DA5 case, once again this vortex has anti-clockwise rotation direction. The case considering diffuser angle at 30° (DA30) also has an indication of two vortices, however only the lower side vortex (bottom) can be confirmed at this point. For the last cases, DA40 and DA50 shows the lower side vortex with similar intensity in both cases and a slightly different V velocity distribution on the diffuser, with higher velocities in the most inclined diffuser.

Moving to plane $X/L_l = 0.096$, the inner spanwise component of the slant vortex is shifting downwards, once this flow structure starts to interact with the wake. On the diffuser area of DA5, the pair of vortices is merged into one single structure, with high V velocity on the positive component of the new merged vortex. DA10 and DA20 cases maintain only one single diffuser vortex structure, moving slightly up and into the spanwise direction. The DA30 case still maintain the lower side vortex in similar position as in plane $X/L_l = 0$ and the additional structure seem not to behave as a vortex however this statement will be further confirmed. The diffuser wake structure is still similar on DA40 compared to DA50, where the main difference relies on a low velocity zone at the mid-span of the diffuser, caused by the interference of slant vortex on the diffuser wake. Further analysis is made for the spanwise velocity.

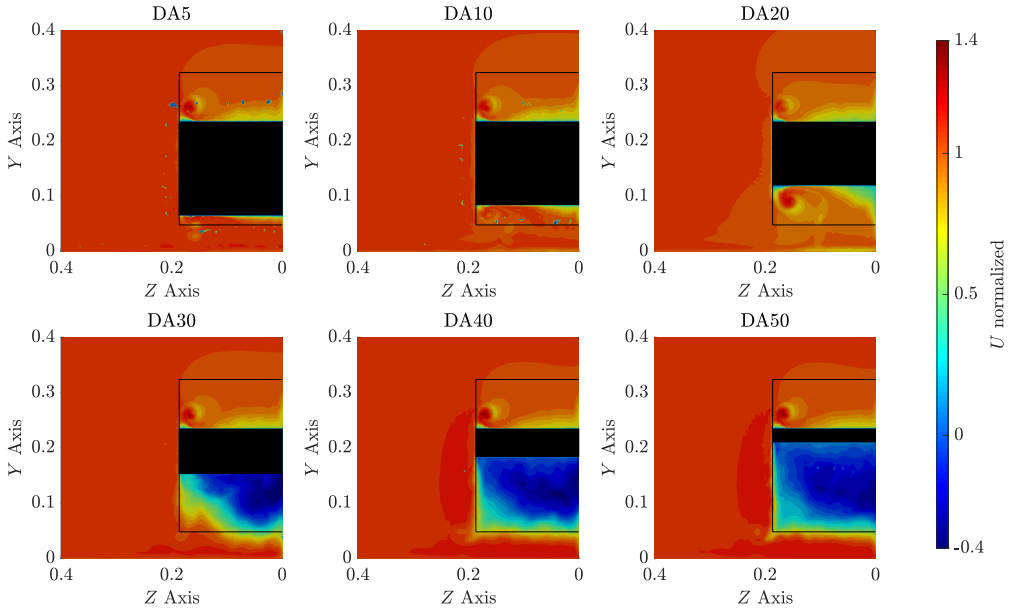


(a) Plane $X/L_l = 0$

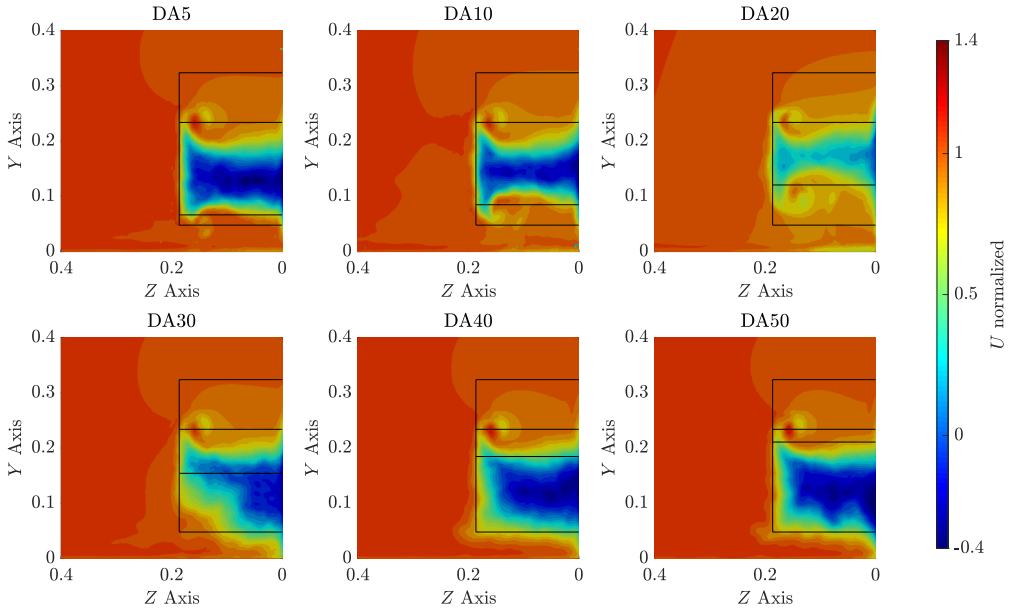


(b) Plane $X/L_l = 0.096$

Figure 8-29: Contours of Q-Criterion (QCrit = 100) for the Ahmed body with slant angle of 25° considering diffuser angle of 5° (DA5), 10° (DA10), 20° (DA20), 30° (DA30), 40° (DA40) and 50° (DA50) for planes $X/L_l = 0$ and $X/L_l = 0.096$.



(a) Plane $X/L_l = 0$



(b) Plane $X/L_l = 0.096$

Figure 8-30: Contours of normalized streamwise velocity U for the Ahmed body with slant angle of 25° considering the proposed diffuser angles: 5° (DA5), 10° (DA10), 20° (DA20), 30° (DA30), 40° (DA40) and 50° (DA50) for planes $X/L_l = 0$ and $X/L_l = 0.096$.

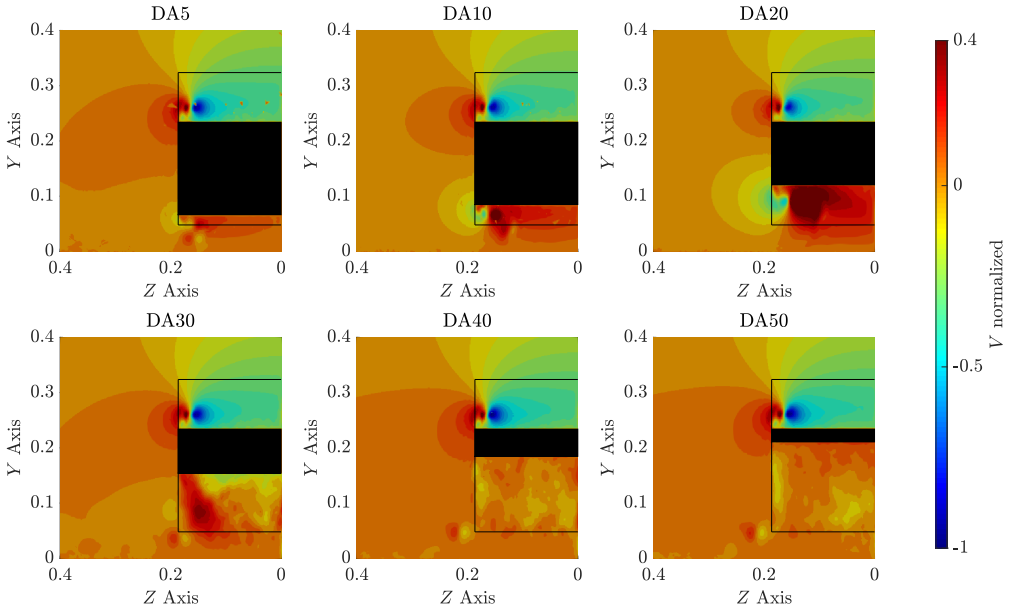
The flow structure analysis on planes downstream of the Ahmed body with slant angle of 25° is concluded by presenting contours of normalized spanwise velocity W in Figure 8-32. The slant vortex on plane $X/L_l = 0$ presented earlier has very similar shape and intensity for both positive and negative velocity components for all cases. The diffuser vortex alone is observed in cases DA10 and DA20, where velocity components increase in size and intensity, reaching the maximum level in the last case. Two vortices with positive and one large negative W velocity component is observed in the DA5, related to both lower side vortex (bottom) and diffuser vortex (top), previously explained. A complex W velocity contour is observed on the diffuser region in DA30, DA40 and DA50 cases, with the lower side vortex at different intensity in DA30 when compared to both DA40 and DA50. The intensity change might be caused by influence of the stronger wake, shifting the lower side vortex inwards the spanwise direction.

On plane $X/L_l = 0.096$, the same slant vortex W velocity components with slightly decreased intensity and moved downwards in the inner spanwise direction. On the diffuser region, the diffuser vortex has similar behaviour of the slant vortex for the first three proposed cases, except by the fact of upwards movement. The diffuser wake has an unsteady behaviour when analysing the last three diffuser angles proposed. The lower side vortex loses some intensity compared to plane $X/L_l = 0$, maintain its definition in DA30 and getting partially diffused in DA40 and DA50 cases.

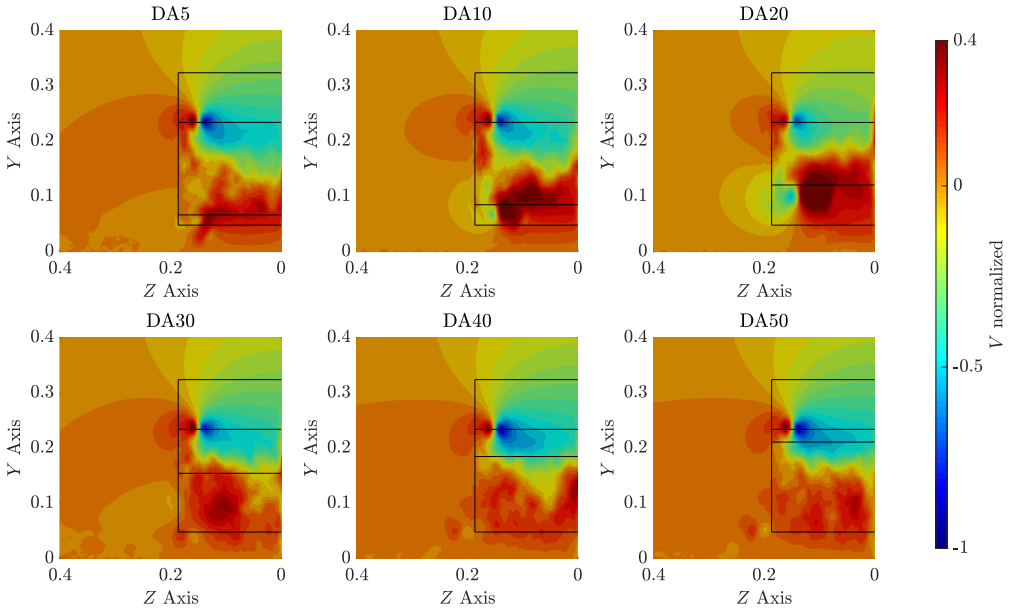
Wall shear stress lines on the surface of each diffuser cases evaluated are now presented in Figure 8-33. This analysis follows similar terminology and setup as presented for the Ahmed body squared-back.

The flow structure on the diffuser indicates a vortex touching the diffuser surface up to angle of 20° (DA20) and separated flow from DA30 onward. Results in Figure 8-33 shows three flow behaviour on the diffuser surface as the previous Ahmed body squared-back, detailed as follows. The DA5 and DA10 cases have the side diffuser vortex touching the diffuser surface together with a separation area at the diffuser inlet. The flow remains attached on the surface until reaching the outlet. Separated flow on the diffuser surface and diffuser vortex is observed in the DA20 case, with a partial reattachment at the outlet. The last three proposed diffuser angles of 30° (DA30), 40° (DA40) and 50° (DA50) have a fully separated flow all over the diffuser surface.

Pumping effect analysis on the Ahmed body with 25° slant angle is presented in Figure 8-34. Negative C_p peaks at the diffuser inlet are observed on DA5, DA10 and DA20 cases, similar as the Ahmed body squared-back. Pressure reduction on the underbody and pressure recovering effects are also present in the same three cases, following similar trends in the literature. These facts highlight a characteristic pressure behaviour when the diffuser is effective in producing downforce. Similar as the C_p findings for the Ahmed body squared-back, for diffuser angles higher than 30°, C_p have no evidence of pressure reduction on the underbody, indicating that these diffusers are not efficient for downforce increment.

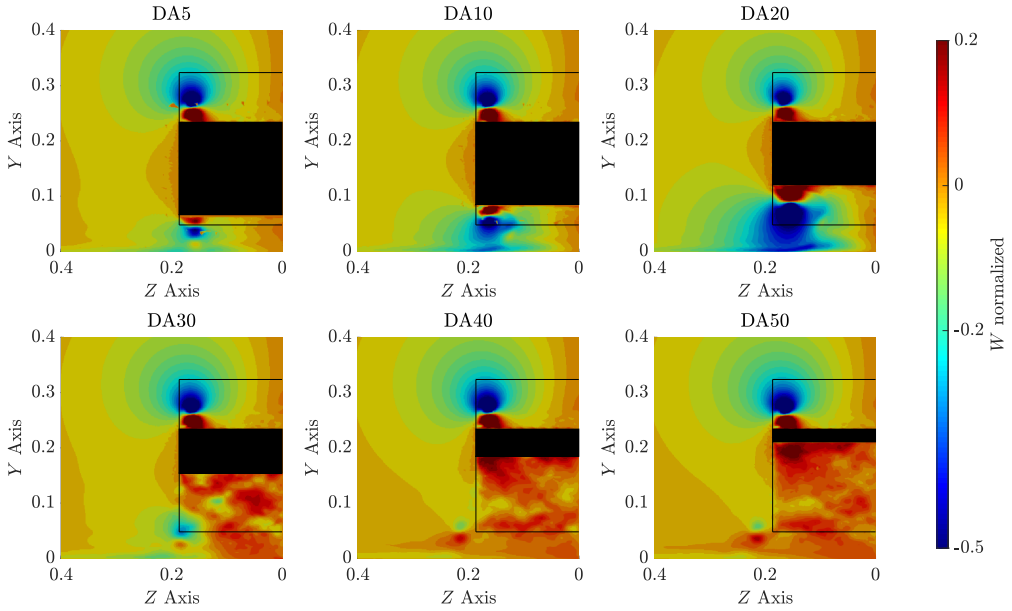


(a) Plane $X/L_l = 0$

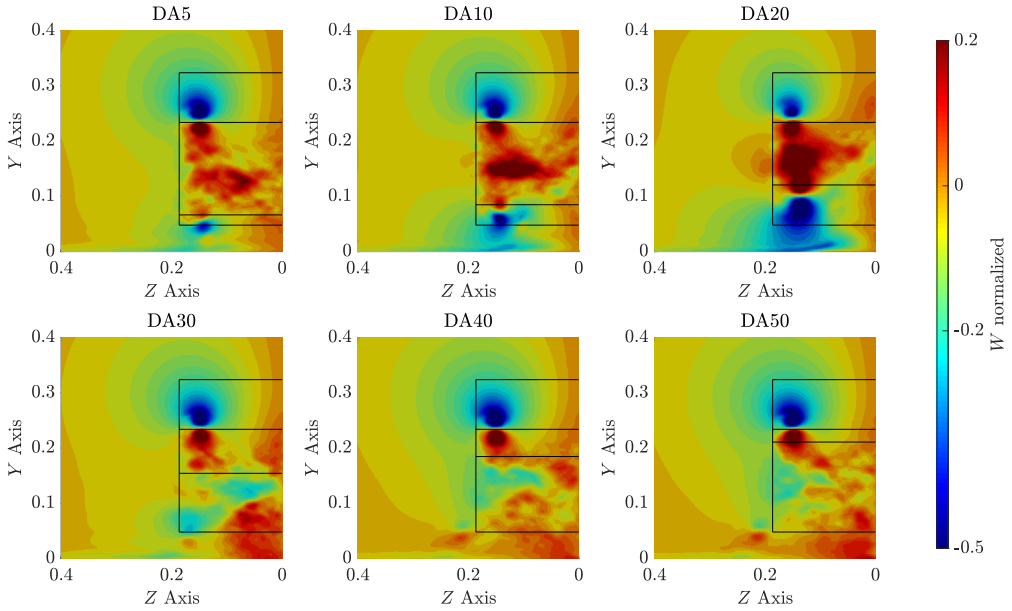


(b) Plane $X/L_l = 0.096$

Figure 8-31: Contours of normalized vertical velocity V for the Ahmed body with slant angle of 25° considering the proposed diffuser angles: 5° (DA5), 10° (DA10), 20° (DA20), 30° (DA30), 40° (DA40) and 50° (DA50) for planes $X/L_l = 0$ and $X/L_l = 0.096$.

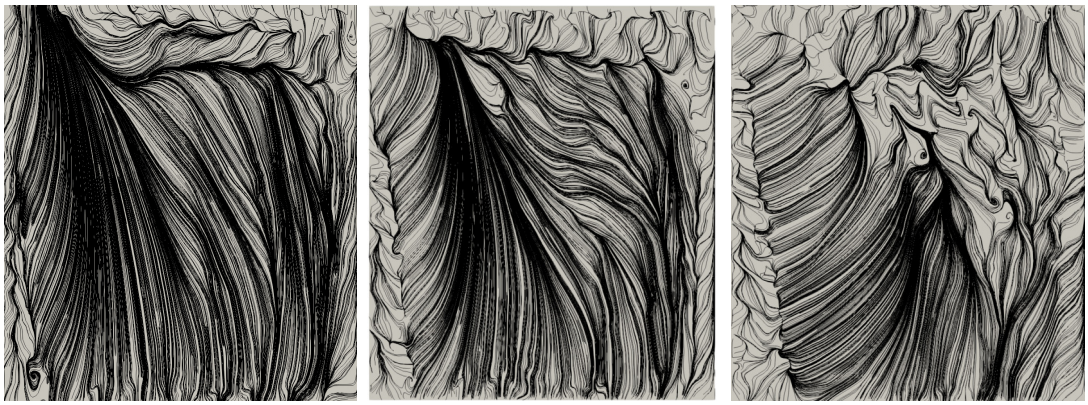


(a) Plane $X/L_l = 0$

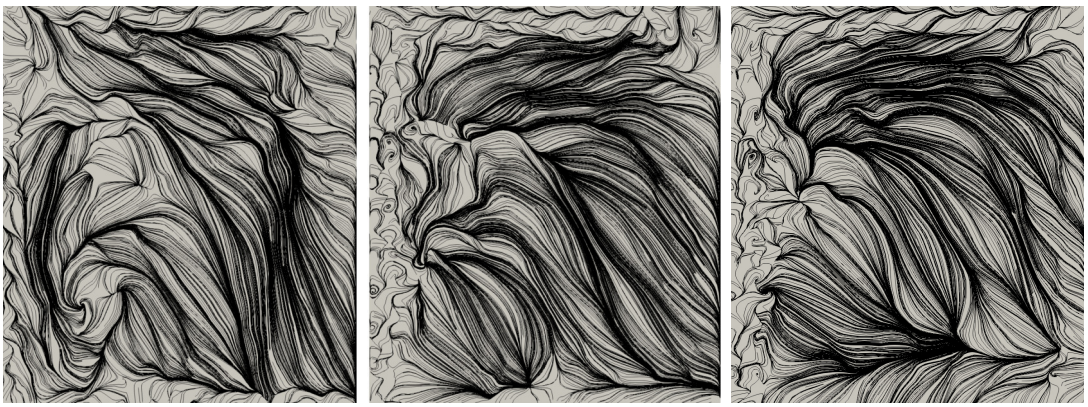


(b) Plane $X/L_l = 0.096$

Figure 8-32: Contours of normalized spanwise velocity W for the Ahmed body with slant angle of 25° considering the proposed diffuser angles: 5° (DA5), 10° (DA10), 20° (DA20), 30° (DA30), 40° (DA40) and 50° (DA50) for planes $X/L_l = 0$ and $X/L_l = 0.096$.



(a) DA5 **(b)** DA10 **(c)** DA20



(d) DA30 **(e)** DA40 **(f)** DA50

Figure 8-33: Time-averaged wall shear stress lines (black) on the diffuser surface for the Ahmed body with slant angle of 25° considering the proposed diffuser angles: 5° (DA5), 10° (DA10), 20° (DA20), 30° (DA30), 40° (DA40) and 50° (DA50), bottom view, incoming flow direction from top.

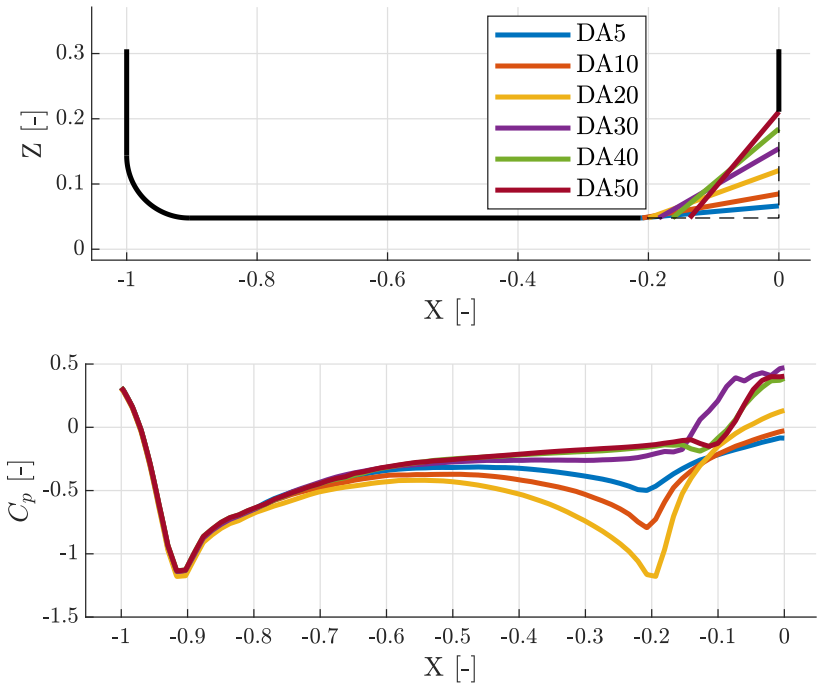


Figure 8-34: Pressure coefficient (C_p) distribution for proposed diffuser angles though the whole length of the Ahmed body with 25° slant.

Ahmed body lower side vortex

We now present an analysis of the 3D flow structures for the Ahmed body squared-back equipped with diffuser. The first step is highlighting one interesting flow structure on the Ahmed body: the lower side vortex. The original study from Ahmed (Ahmed et al. [1984]) as well as the flow visualization experiments from Lienhart et al. [2002] have no information regarding this flow structure. The lower side vortex was first noticed when performing first experiments on the Ahmed body without the ground fixing supports. The first thought suggests that the lower vortex generation is related to the type of ground simulation used.

Krajnović and Davidson [2004] identified the lower side vortex using *LES* simulations with a virtual model without the ground fixing support and static ground condition. Further experimental study of Strachan et al. [2007] found the same lower vortex phenomena using a model fixed from the top with moving ground condition. We conclude that the generation of the lower side vortex is related to the installation method of the model in the wind tunnel. The ground fixing supports used by Ahmed et al. [1984] influence the lower side vortex generation, preventing it to reach the rear area of the body.

Capturing the lower side vortex depends also on the simulation resolution, as observed from contours of Q-Criterion on the plane $X/L_l = 0$, presented in Figure 8-35. The indication of this flow structure first appears on the case considering *Original* mesh with $P_N = 6$ and *Refined* mesh with $P_N = 5$. The lower side vortex is clearly defined only when using *Refined* mesh with $P_N = 6$, increase the confidence level of using this resolution in this research case. The additional computational time required for the *Refined* mesh with $P_N = 6$ cases, presented in Section 7-3-3, receives an extra justification to be the most suitable in this Ahmed body study.

The lower side vortex is a secondary flow feature compared to the slant vortex and wake; however, it becomes important when studying the underbody flow and potential changes. Controlling and tracking the vortices path over the vehicle is one of the key challenges in motorsports, especially in Formula One. Our main goal in this research is to offer the highest resolution results, independent of the computational time, for all cases studied in order to fully capture the flow structures.

The lower side vortex origin is presented on the Ahmed body with slant angle of 25°, using *Refined* mesh and $P_N = 6$ polynomial expansion accuracy in Figure 8-36. The lower and lateral angled surfaces junction at the front part of the Ahmed body are the poins of origin of the lower side vortex: the connection between the two curved surfaces created a sharp edge feature for floe separation, generating the lower side vortex when close to the ground.

Bottom view of the Ahmed body squared-back at different diffuser angles showing iso-contours of Q-Criterion (QCrit = 100) are presented in Figure 8-37. The lower side vortex is shifting in the inner spanwise direction for DA5 up to DA30. The offset of the lower side vortex in the spanwise direction is related to the presence of the diffuser vortex. The counterclockwise rotation and higher intensity of the diffuser vortex are the main reasons of the lower side vortex shifting. The separated flow behaviour without the diffuser vortex in cases DA40 and DA50 do not affect the lower side vortex trajectory.

No vortex merging between the diffuser and the lower side vortices is seen, as they are in different vertical position. Secondary vortices are seen for the cases DA10, DA20 and DA30, as part of the lower side vortex being powered by the moving ground.

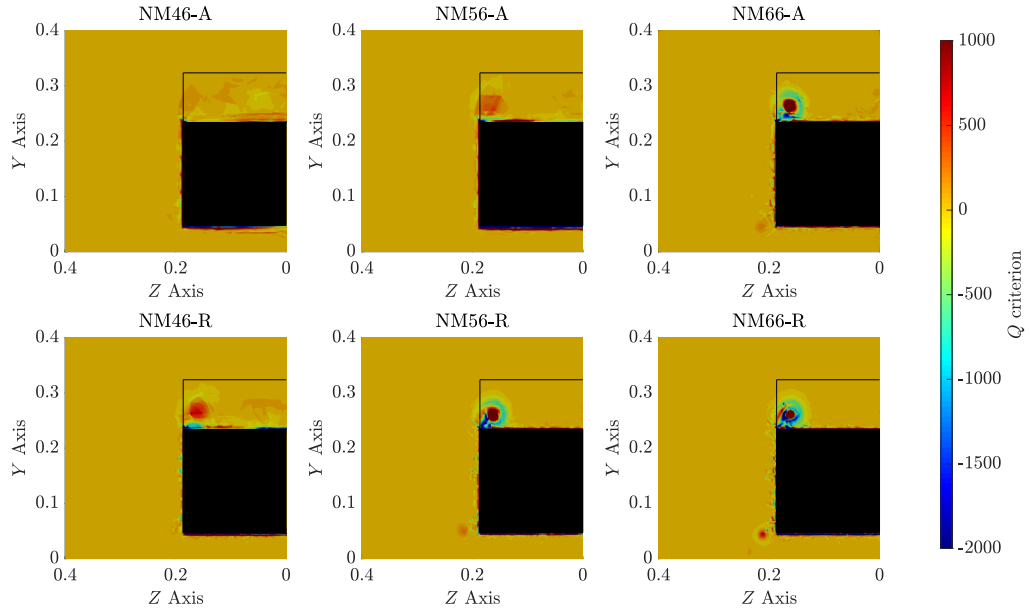


Figure 8-35: Contours of Q-Criterion on the plane $X/L_l = 0$ for the proposed Ahmed body with slant angle of 25° simulation resolutions without diffuser. The lower side vortex is observed at approximate coordinates $Y = 0.05$ and $Z = 0.2$ for cases with enough resolution.

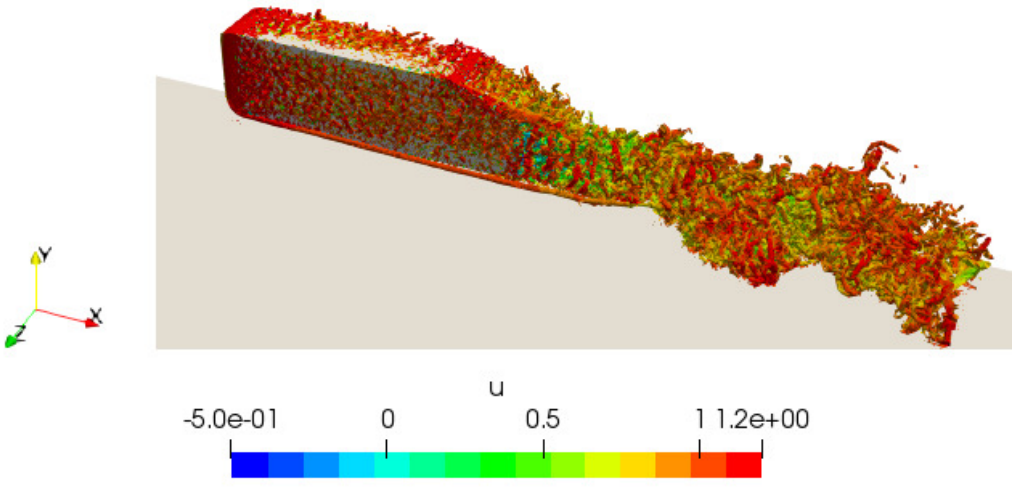
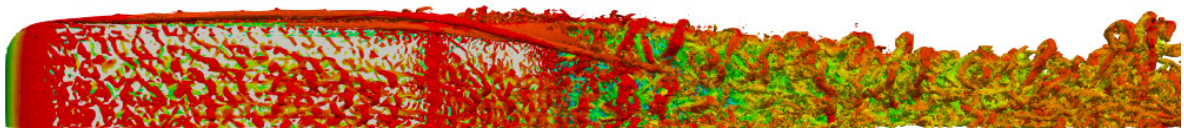
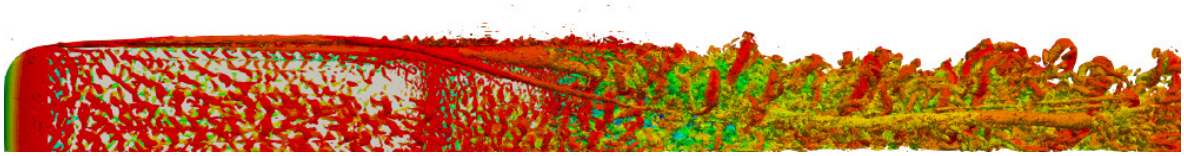


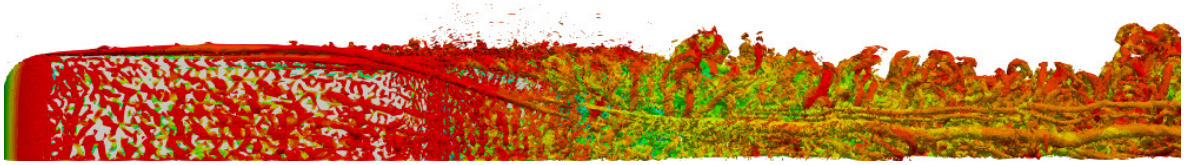
Figure 8-36: Lower side vortex origin by iso-surface contours of Q-Criterion (QCrit = 100) coloured by U.



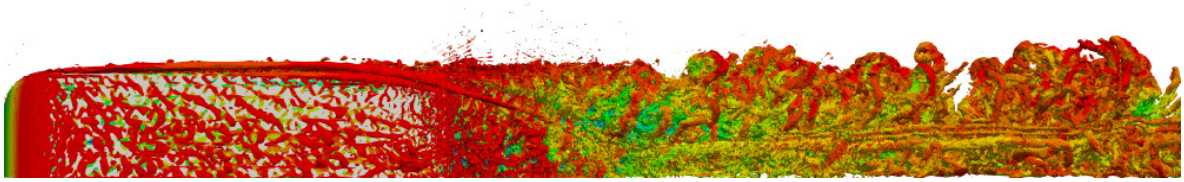
(a) DA5



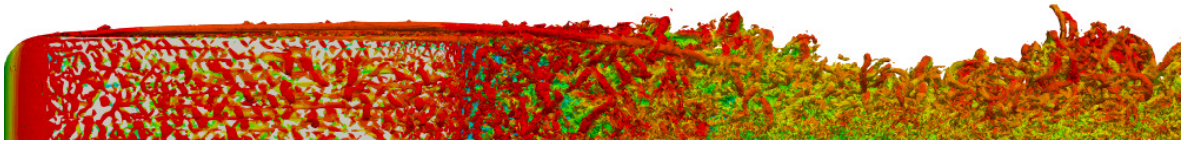
(b) DA10



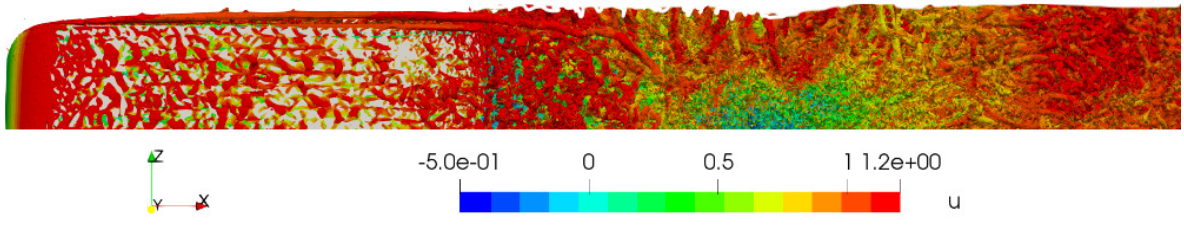
(c) DA20



(d) DA30



(e) DA40



(f) DA50

Figure 8-37: Iso-contours of Q-Criterion (QCrit = 100), coloured by U, of the bottom view of the Ahmed body squared-back. The following proposed diffuser angles are presented: 5° (DA5), 10° (DA10), 20° (DA20), 30° (DA30), 40° (DA40) and 50° (DA50).

Similar bottom view results for the Ahmed body with slant angle of 25° considering different diffuser angles are presented in Figure 8-38. From the iso-contours of Q-Criterion (QCrit = 100) coloured by U, we observe the same lower side vortex behaviour shifting inwards in the spanwise direction. The lower vortex shifting only happens with the existence of the diffuser vortex, from DA5 to DA20 in this case. Both vortices move further downstream independently without merging on DA5, DA10 and DA20 cases. On the DA20 case, the lower side and diffuser vortices merge, creating a single structure that propagates further downstream. For fully separated flow at higher diffuser angles, we observe similar behaviour from previous analysis: the chaotic turbulent wake on the diffuser area maintains the lower side vortex original trajectory.

8-4 Conclusions

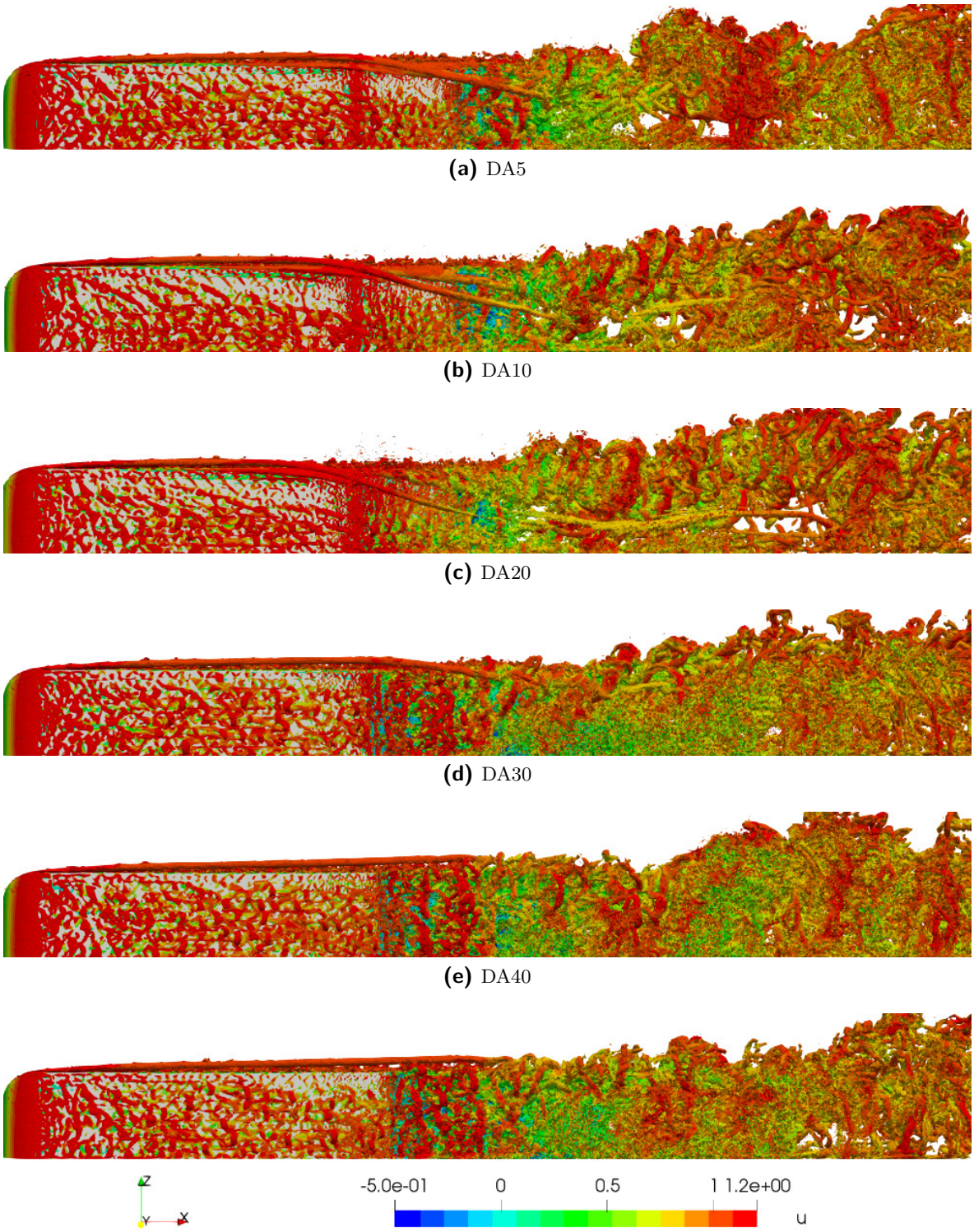
A parametric study on diffusers is conducted on the Ahmed body at two slant cases: squared-back and 25° angle. The first is proposed as a possible test case by using a classical Ahmed body flipped upside down. The diffuser length is fixed with the same dimension of the slant and cases are evaluated at a Reynolds number of $Re = 1.7 \times 10^6$ and moving ground condition. The diffuser angles proposed range from 10° to 50° in increments of 10°, including one additional angle of 5° for both cases.

Results for the Ahmed body squared-back indicate two different flow behaviours. The first behaviour, observed in diffuser angles up to 30°, indicate that downforce increment leads to higher drag coefficient. Flow structure for this regime is composed of a lateral vortex and fully attached flow on the diffuser surface for angles up to 20°. The critical angle has the same diffuser vortex however the flow is partially separated on the rest of the diffuser surface. The second flow regime is found for diffuser angles higher than 30°. At this second flow regime, downforce increment efficiency is lost, and the flow is fully separated on the diffuser surface.

For diffuser angles up to 20° on the Ahmed body with 25° slant angle, downforce increases while the drag coefficient is reduced. Maximum downforce is observed at 10°. The flow structure is also composed by the diffuser vortex and attached flow on the diffuser surface, however only for the 5° and 10° diffuser angles. The diffuser vortex is also observed in the 20° case but the flow is mostly separated. Like the squared-back case, the highest drag coefficient value is observed for the 30° angle, and flow structure from this case onward is fully separated.

The same pumping effect observed by Cooper et al. [1998] study, characterised by underbody flow velocity increment, is found at the diffuser inlet area whenever the diffuser is effective in downforce generation. We also conclude that the exterior geometry, such as the slant angle, influences the diffuser performance in terms of aerodynamic quantities and flow structure.

The lower side vortex on the Ahmed body is a flow structure originated on the lower front stagnation, travelling downstream beside the body and close to the floor. The final trajectory of the lower side vortex relates to the diffuser flow behaviour. When the flow is fully separated on the diffuser surface, the lower side vortex trajectory is maintained on the side of the Ahmed body with further dissipation on the far wake. For the other diffuser flow behaviours, diffuser vortex with either attached or partially separated flow, the lower side vortex trajectory moves inward the spanwise direction. We also observe that this structure gets more energetic and is longer conserved.



(a) DA5

(b) DA10

(c) DA20

(d) DA30

(e) DA40

(f) DA50

Figure 8-38: Iso-contours of Q-Criterion (QCrit = 100), coloured by U, of the bottom view of the Ahmed body with slant angle of 25°. The following proposed diffuser angles are presented: 5° (DA5), 10° (DA10), 20° (DA20), 30° (DA30), 40° (DA40) and 50° (DA50).

8-5 List of publications

8-5-1 Paper contributions

Buscariolo, F.F., Assi, G.R.S., Sherwin, S.J., Computational study on an Ahmed Body equipped with simplified underbody diffuser, Journal of Wind Engineering and Industrial Aerodynamics, submitted.

8-5-2 Presentations and poster sessions

UK Turbulence Consortium - UKTC 2018, presentation on turbulent flows: Spectral/hp methodology study for SVV-LES on an Ahmed body.

11^{th} International Symposium on Turbulence and Shear Flow Phenomena - TSFP11 2019, poster presentation with the title: Diffuser study on a squared-back Ahmed body using spectral/hp iLES-SVV simulations.

Part IV

Imperial Front Wing

Chapter 9

Imperial Front Wing

The third part of this research focuses on the development, experimental test and CFD analysis of a new standard test case using a Formula One front wing, named Imperial Front Wing or IFW. This part of the research was developed in collaboration with McLaren Racing for the application of high-fidelity methods on industrial cases.

Here we first introduce the concept of using front wings for race cars. This is followed by the illustration of the full geometry, experimental setup and the CFD simulation configurations using uDNS/iLES with spectral/hp element method. The results presented includes aerodynamic quantities, as well as comparison studies between the experimental results and the simulation solutions.

9-1 Background

The use of race car incorporated inverted wings started in 1966 with Jim Hall Chaparral and his 2E car in the Can-Am racing Series, aiming to increase downforce, as presented in Section 8-1. The use of wings in Formula One stared in the 1968 season when teams started to implement aluminium wing profiles to increase downforce as stated by Jowsey [2013]. Lotus firstly introduced a simplified front wing and a spoiler with an inverted wing profile on its Lotus 49B model. The use of the wing required stiffer suspension springs to support the additional force, especially on high-speed conditions. The new Lotus 49B configuration proposed by Collin Chapman and Maurice Philippe was introduced during the 1968 Monaco Grand Prix and is presented in Figure 9-1.

Following the success of Lotus, other teams such as McLaren, Brabham and Ferrari proposed full width wings mounted on struts high above the driver. To avoid stiffening the suspension springs, wings were now attached to the suspension, as mentioned by Katz [2006]. An example of this type of assembly is shown in Figure 9-2 for the 1968 McLaren M7A.

After a series of accidents mainly involving race cars with wings assembled on the suspension, the use of wings was banned for the rest of the season and reintroduced in 1969 under new



Figure 9-1: Inverted rear wing profile and reduced front wing configuration on the 1968 Lotus 49B. Reproduction from www.favcars.com

design regulations. The new regulations defined the limit wing size and location, in order to avoid unstable driving conditions and prevent more accidents. Having evolved over time, similar rules are still used today.

9-1-1 Introduction

Race cars are designed to reach maximum performance in all systems. In order to challenge the race teams, the *Fédération Internationale de l'Automobile* - FIA provide new design rules every year, pushing the technological development to the limits. External aerodynamics is one of the key performance differentiators in Formula 1: a mere 1-2% improvement in aerodynamics performance can mean the difference of being first or tenth. As a result, aerodynamics has become one of the main design focus for Formula One performance and clearly involves challenging fluid mechanics.

For open wheel racing cars, the front wing is a key aerodynamic feature whose role is twofold: the generation of load on the front axle (i.e. downforce), and secondly, as presented in Figure 9-3, the production of a vortical system to control the flow downstream, and in particular to limit the negative effect of the front wheel wake on the rest of the car.

The front wing became one of the most complex system in current race vehicle designs, once it is now composed by an assembly of different aerodynamic elements. Examples of aerodynamic elements are the flaps, turning vanes and endplates seem on the McLaren MCL-33 front wing, presented in Figure 9-4. The main function of the aerodynamic elements is to guide and control the flow around the car, balancing both downforce distribution and drag increment over the car. The front wing can generate up to 40% of the total downforce on a Formula One car, which also balances the downforce distribution over the car.

Formula One complex geometry cases are of great interest of the automotive aerodynamics due to its complexity and novelties. Although there are a number of Formula One test cases in the open literature Zerihan and Zhang [2000]; Zhang and Zerihan [2003]; Ahmed et al. [2007], these have typically been constructed to be visually similar to existing racing cars but



Figure 9-2: Dual wing configuration on the 1968 McLaren M7A, where the front wing is assembled on the front suspension. Reproduction from www.pinterest.com

have no experimental validation. Furthermore, to the best of our knowledge these test cases have not been developed by a Formula One team.

In this work we propose a test case, referred to as the Imperial Front Wing (IFW) model, which is based on the McLaren MP4-17D race car front end, developed in partnership with McLaren Racing. The geometry was previously investigated experimentally by Pegrum [2007] in the Donald Campbell wind tunnel and initially simulated by Lombard [2017]. The geometry consists of a multi-element wing in ground effect, leading to the generation of a series of interacting vortical structures, thereby creating a highly complex flow environment downstream of the wing, as shown in Figure 9-3. Accurately modelling these vortices and their interactions, by capturing their relative position and strength, is of utmost importance for a successful front wing design. With this challenging geometry, presented in next Section, we propose a new standard test case also aiming to test the accuracy of CFD code applied to complex automotive flows.

9-1-2 Geometry

The IFW posed an interesting test case for automotive and motorsport aerodynamics as it represents a Formula One front wing. The geometry is based on the McLaren MP4-17D Formula One race car, as presented in Figure 9-5.

Its geometry is mainly composed of a three-element front wing: main wing element, intermediate wing element and flap, with an endplate attached to a simplified nose cone. We present the main dimensions of the IFW in Figure 9-6.

Despite looking simpler than present-day front wings, which have benefited from another fifteen years of development, the IFW captures the essential aerodynamic features of a front wing configuration. It still poses significant aerodynamic challenges in accurately estimating the aerodynamic loads, the locations of transition lines, the generation and shedding pattern of multiple vortices and their respective strengths.

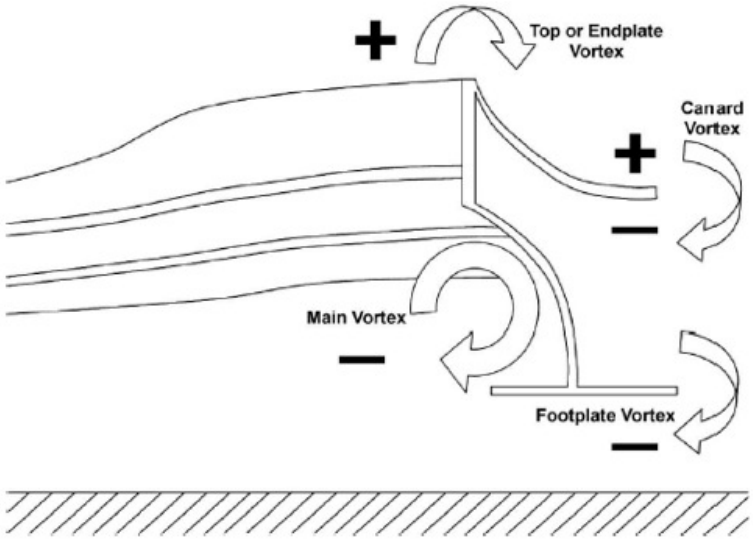


Figure 9-3: Topology of the complex vortex system downstream of the front wing with the three main vortices rotation direction. Reproduced from Pegrum [2007].



Figure 9-4: Front wing detail of the McLaren MCL-33 (2018). Reproduction from www.motorsport.uol.com.br



Figure 9-5: McLaren MP4-17D Formula One car. Reproduction from www.somefoi.com

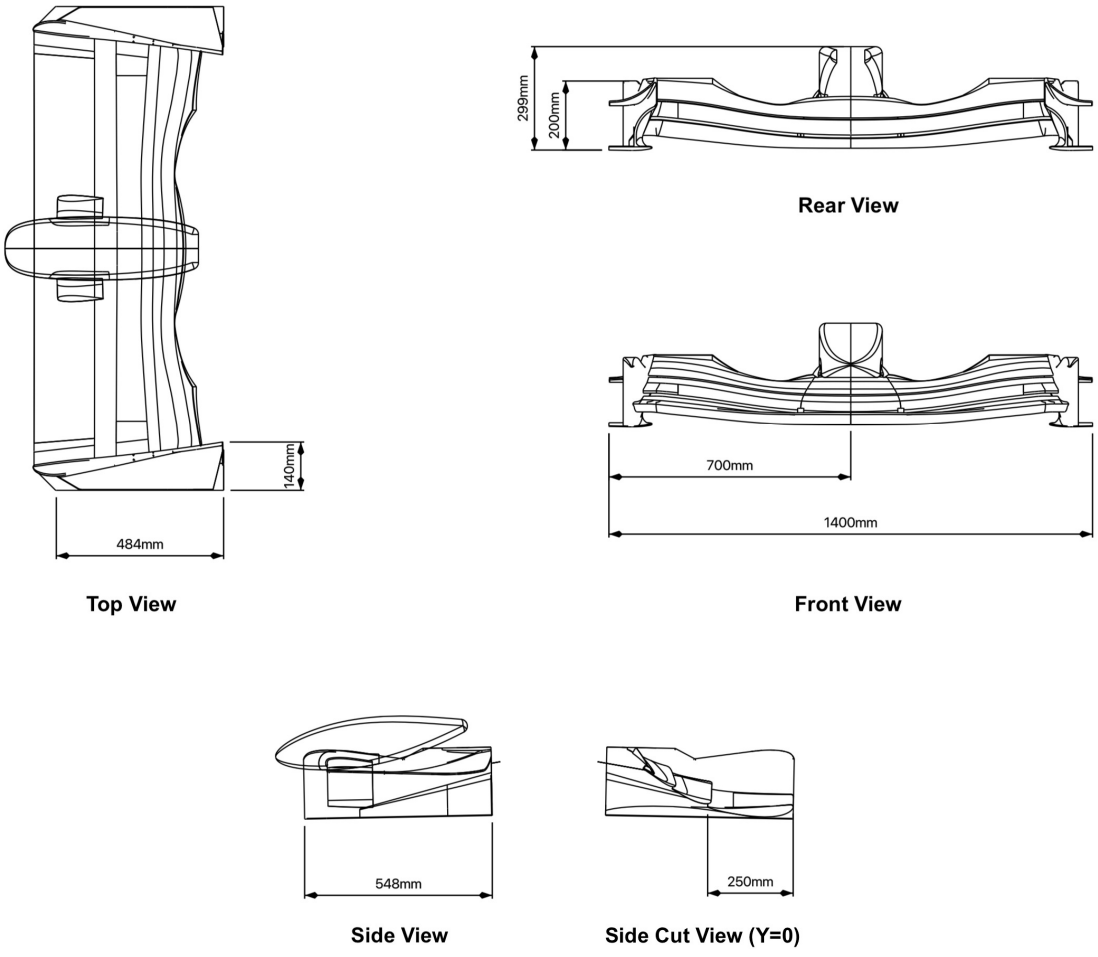


Figure 9-6: Schematic drawing of the IFW with main dimensions (in mm).

9-1-3 Literature review

The study and development of a Formula One race car is a challenging and expensive task, therefore only few data considering real geometries are available on the literature. The main reason is due to the very specific application and the corresponding competitive nature of the motorsport industry as stated by Katz [2006]. Therefore, research results conducted into race-car aerodynamics have generally been kept confidential. The initial studies on front wings first considered generic wing profile, such as NACA aerofoils, in proximity to the ground.

Zerihan and Zhang [2000] investigated the performance characteristics and flow field phenomena of a simplified front wing in moving ground conditions. This study is considered the first to evaluate the main wing design of a Formula one car, the Tyrrell 026 race car, shown in Figure 9-7. A highly cambered single element aerofoil at 80% scale was used to investigate the effect of changing the ride height and the incidence angle. Two cases were evaluated at a Reynolds number of $Re = 2 \times 10^6$: one considering a bump in order to generate an artificial transition in the spanwise direction of wing, fixed at 10% of c; the second case is evaluated without artificial transition. The fixed transition case was considered to simulate the behaviour of debris accumulation during one race.



Figure 9-7: Tyrrell 026 race car. Reproduction of www.motorsport.com.

The main conclusions of the study indicate that as the ride height reduction is directly connected to increment in downforce levels. The lift coefficient curves for the Tyrrell main front wing profile at $AoA = 1°$ are presented in Figure 9-8. For ground clearances of less than 20% of the wing chord, downforce measured is significantly higher than the base case. Stalling behaviour is observed on the wing profile at a ride height of less than 10% of the chord, explaining the losing in downforce performance. Using a fixed transition point, it was found to significantly reduce the levels of downforce generated due to circulation loss.

The incidence angle variation changes the slope of the lift curve and its total increment, as presented in Figure 9-9. The separation points on the wing profile changes, affecting its stalling point. The additional suction due to ground effect lose effectiveness, affecting the downforce increment.

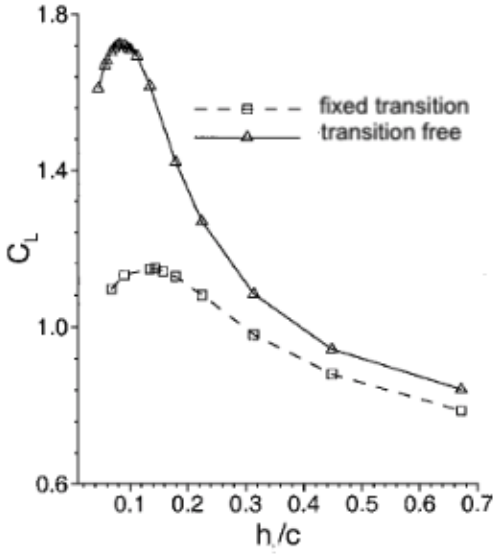


Figure 9-8: Lift coefficient results in ground effect for the Tyrrell 026 front wing at $AoA = 1°$, for the two proposed configurations: fixed transition and transition free wing. Reproduction of Zerihan and Zhang [2000].

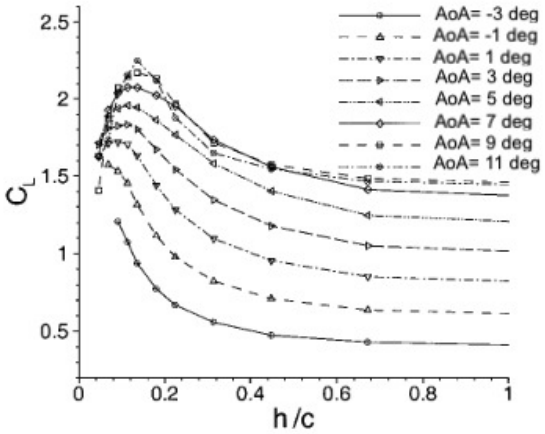


Figure 9-9: Lift coefficient results in ground effect for different AoA on the transition free wing. Reproduction of Zerihan and Zhang [2000].

This study first presented the influence of a wing profile when moving close to the ground. The main conclusions are that lower ground height is desirable up to a certain limit, when the ground effect suction saturates. The saturation of the ground effect causes the wing profile to stall and lose the performance in terms of downforce. Changing the incidence angle or *AoA* of the wing profile also influence the ground effect, causing it to reach maximum level at different ground heights. Further references increased the complexity of this first case.

Katz and Garcia [2002] evaluated a generic Formula Indy-type open-wheel race car model in a low speed, fixed ground wind tunnel. Elevated ground plane method was selected for the road simulation to allow flow visualization under the car. Results indicate that the combination of the front and rear wings together with the underbody vortex generators are responsible for most of the aerodynamic downforce. The main contributors for the drag force are the open wheels and the front and rear wings.

Focusing on front wing, results presented in Figure 9-10, indicate that the downforce increases almost linearly with the change in the flap angle, while the vehicle's total lift increment saturates at a certain point. Flow visualizations indicate that the tip vortex of the front wing reaches the rear wing in certain *AoA* configurations. The vortex travel from the front wing up to the rear wing highlights the importance of correctly capture those structures for efficient aerodynamic design. By increasing the *AoA* of the front wing main element above a critical value, the underbody flow is diverted, resulting in less downforce.

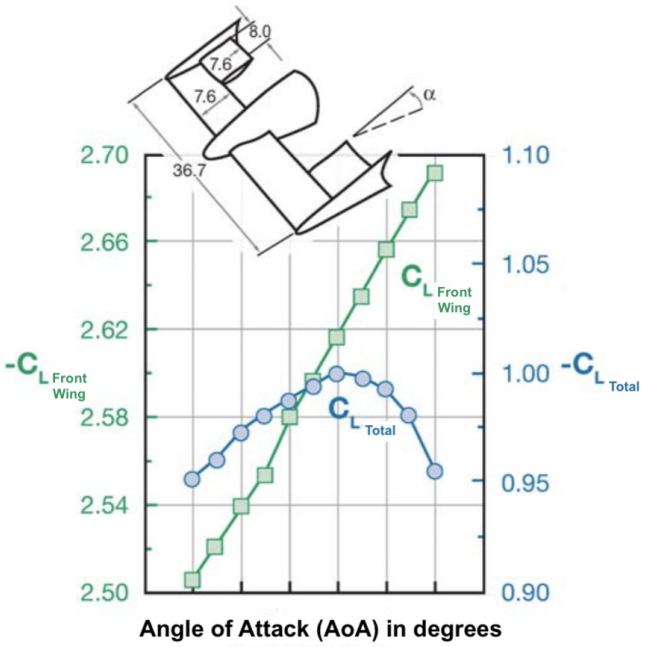


Figure 9-10: Front wing geometry and lift coefficient variation with main front wing element *AoA*. Reproduction of Katz and Garcia [2002].

The work of Zhang and Zerihan [2003] followed Zerihan and Zhang [2000] study by proposing an LDA experiment to determine the overall effect on the wake structure and the displacement of tip vortices. A double-element wing was used for the experiments, consisting of the main

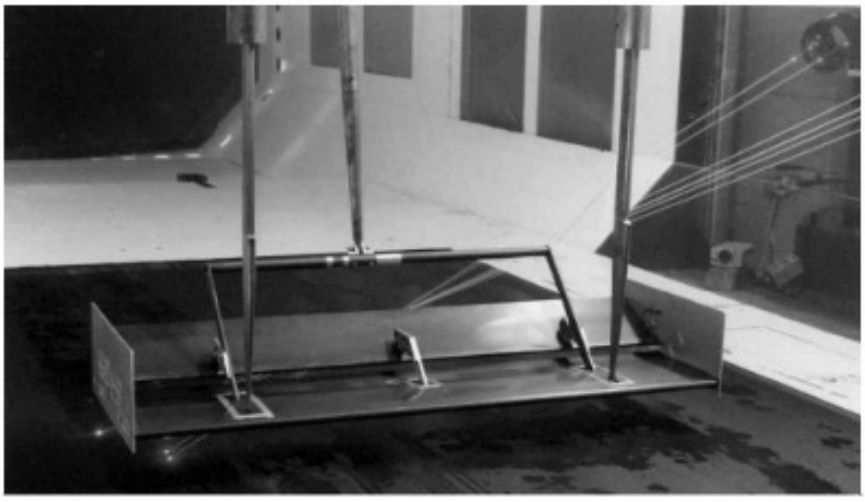


Figure 9-11: Double-element front wing assembly. Reproduction of Zhang and Zerihan [2003].

wing element with a flap element downstream, as shown in Figure 9-11. Measurements of aerodynamic quantities were taken when varying ride height and two different flaps AoA. Results showed that as the wing approached the ground, the region of separated flow and the size of the wake increased, moving towards the ground as it travelled downstream. With subsequent further reduction in ride height, the tip vortex strength increases until a critical ride height at which a loss of downforce occurred, as previously observed. The main wing element produces most of the downforce and dominates the turbulent wake development, even when considering additional elements on the wing assembly.

A summary of racing car aerodynamics is presented by Katz [2006]. The study briefly explains the significance of the aerodynamic downforce and how it improves race car performance. The author highlights that the principal race car component responsible for most downforce generation are the front wing, diffuser and rear wing. Understanding the aerodynamic interaction between the various body components is significant to improve aerodynamic performance of a race car since a complex vortical system is generated. The downforce generation from the front wing is justified using inverted wing profile with an ideal ground clearance, generating a strong ground effect. Different examples of vehicle shapes are presented in the study to demonstrate the importance of aerodynamics in motor sports.

Ahmed et al. [2007], evaluated the NACA4412 aerofoil. The experimental investigation considered six different angles of attack (AoA) ranging from 0° to 10° in increments of 2°. Seven ground clearances were evaluated for each AoA at a Reynolds number of $Re = 3.0 \times 10^5$. Results indicated suction increment on the lower surface at the smaller ground height for the angle of attack of 10°, shown in Figure 9-12. The formation of a convergent-divergent channel between the lower part of the profile and the ground, explain the downforce increment.

Drag coefficient increased with smaller ground height for all AoA evaluated as shown in Figure 9-13. The drag increment happened mainly due to modification in the pressure distribution on the lower surface of the aerofoil, causing early separation. Flow behaviour investigation was not conducted in this study as the span of the aerofoil fitted the whole width.

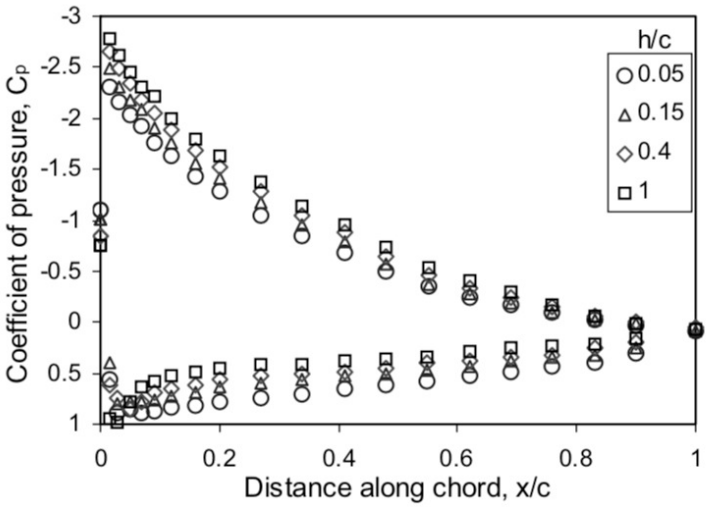


Figure 9-12: Pressure distribution on the surface of the NACA4412 aerofoil at AoA of 10°. Reproduction of Ahmed et al. [2007].

Diasinos and Gatto [2008] presents a study on a sub-scale open wheel race car inverted wing profile, aiming to represent a simplified Formula One front wing and wheel illustrated in Figure 9-14. The flow behaviour of the system as well as the isolated wheel were evaluated using LDA measurement. Static and moving ground conditions were both evaluated in the isolated wheel test. The wing-wheel system was evaluated with moving ground in two setups: wingspan 0% and 100% overlap of the wheel width. The angle of attack of the wing profile was changed from 0° to 12° in increments of 4°.

Results demonstrated that the main reason for changing wing AoA was to change the size, strength and degree of movement of the tip vortex generated from the main wing element. The intensity and strength of the tip vortex increases as the AoA also increases. At low wingspans, the vortex travels on the inside of the wheel, producing a complex asymmetric wake structure, which is not found for long span. The general rotational characteristics is in the clockwise direction when viewed from in front of the combination.

Previous studies have evaluated the performance of conceptual front wings, providing useful insights on the flow interactions. However, they are still simplified cases that do not represent a real Formula One front wing geometry without any experimental data available.

Pegrum [2007] first evaluated the behaviour of the vortex system generated by a Formula one front wing. The simplified 50% scale model of the McLaren MP4-17D front wing was evaluated in two conditions: without wheel and with rotating wheel. The investigation of the flow structure downstream of the wing was performed using PIV, total pressure wake surveys and hot-film anemometry. The analysis of the isolated front wing downstream indicated four co-rotating vortices, as shown in Figure 9-15. The four co-rotating vortices interact and merge together and these structures are influenced by the ground height of the wing.

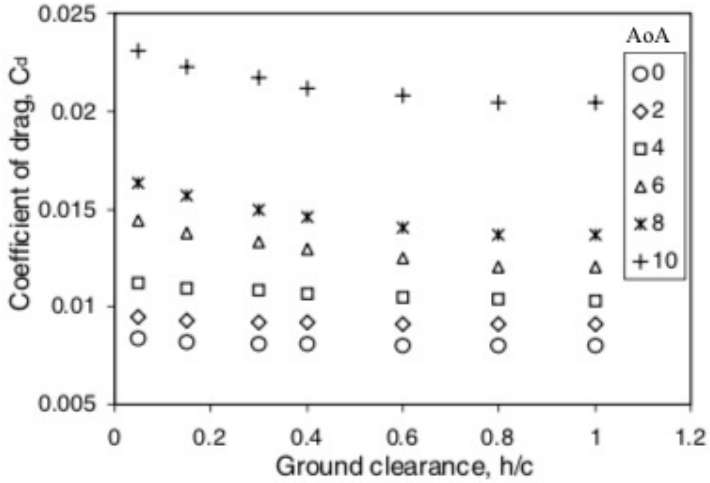


Figure 9-13: Drag coefficient results for the NACA4412 aerofoil at different ground clearances (h/c) for varying AoA. Reproduction of Ahmed et al. [2007].

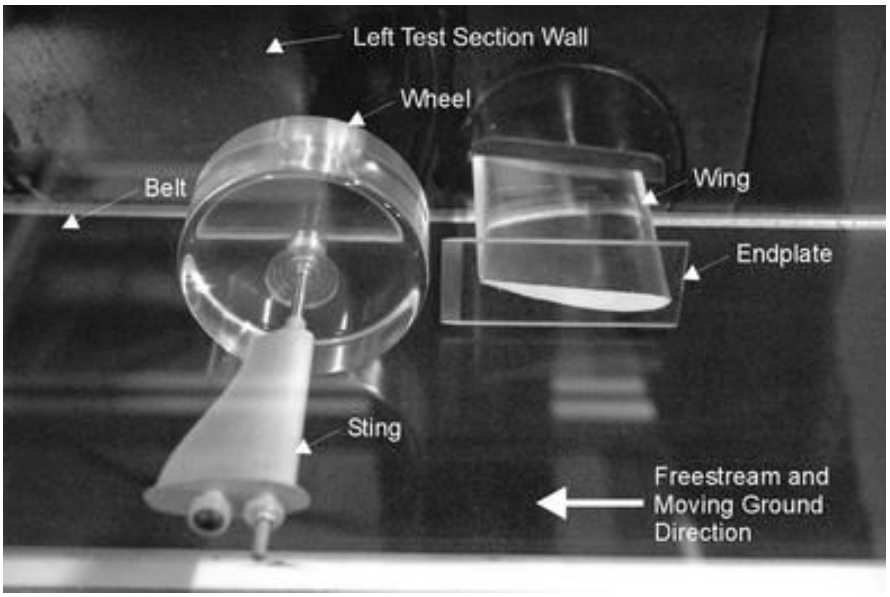


Figure 9-14: Open wheel and inverted wing profile setup configuration of Diasinos and Gatto [2008] experiment. Reproduction of Diasinos and Gatto [2008].

When the wheel is assembled together with the front wing, the vortical system substantially changes. The flow structure downstream the wing is dominated by the interaction between the main and footplate trailing vortices. The relative strength and separation of these two structures is affected by its ride height as well as by the rotating wheel. The top vortex is observed closer to the inner side part of wheel; however, it gets diffused as moving downstream. No evidence of the canard vortex was observed, indicating that it has either interacted with the other vortices or has not been able to navigate around the front of the wheel.

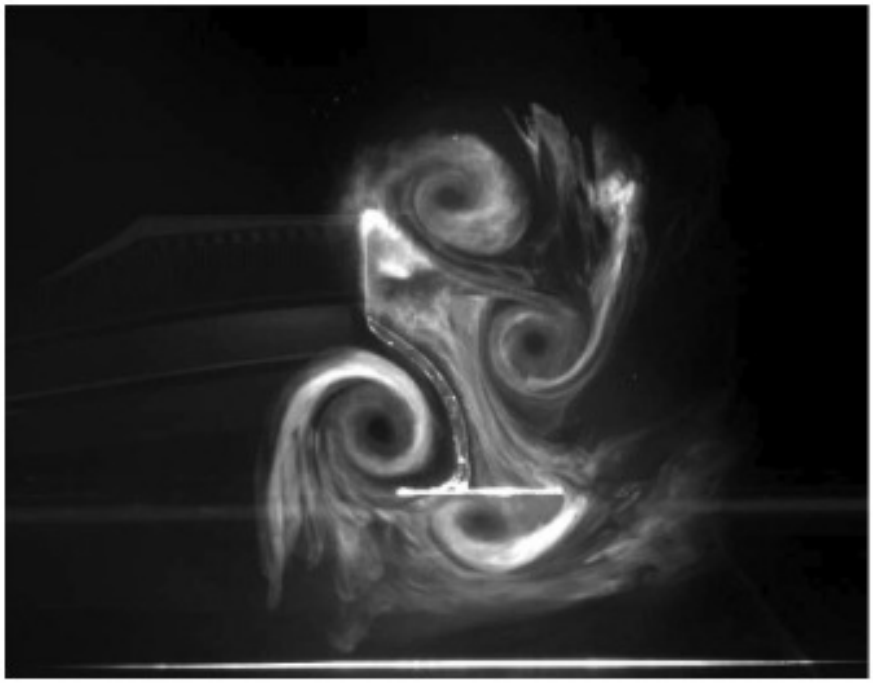


Figure 9-15: Laser smoke visualisation behind the endplate, courtesy of Jonathan Pegrum. (Pegrum [2007]).

Lombard [2017] performed a initial computational study on the MP4-17D front wing at $h/c = 0.48$, aiming to correlate with experimental study of Pegrum [2007]. Simulation results confirm the presence of the four vortices downstream the wing and similar features from experimental reference. However, we obverse further downstream the wing, reduction of the correlation level, especially in terms of vortex core location. The author suggests additional computational time for more conclusive results, as well as, a mesh convergence study. In this current work, we consider both approaches, including the use of higher P_N.

9-1-4 Objectives

The main objective of this study is to establish the IFW as a standard test case for the automotive aerodynamics community, supported by availability of experimental data. CAD geometry is also available as an open source case, in agreement with McLaren Racing. Experimental data set include measurements of surface flow visualization and averaged time-resolved PIV results.

This study also offers a comparison between the simulation results obtained from Nektar++ using various polynomial orders of the spectral/hp element method against experiment. Solutions of high accuracy were directly obtainable thanks to the implementation of novel techniques for the stabilisation of higher-order spectral/hp methods and mesh sizing as previously highlighted. We also implemented a solution mapping for spectral/hp meshes in order to warm-start for converged steady-state solutions.

9-2 Experimental test configuration

Wind tunnel experiments were performed in the 10 × 5 Wind Tunnel in the Department of Aeronautics at Imperial College London Department of Aeronautics [2019]. It is a closed loop facility with two test sections: the lower test section with dimensions 3.04 m (wide) × 1.52 m (high) × 20 m (long); the upper test section with dimensions 5.8 m (wide) × 2.7 m (high) × 18 m (long). The lower test section used for this experiment is temperature controlled with flow uniformity around 1.0% and turbulence intensity less than 0.25%, reaching 41 m/s as the maximum speed. It also incorporates a rolling road system with belt tracking and a belt-suction platen together with a 2-stage boundary layer suction upstream. Models using the rolling road system are mounted at the bottom end of a strut that extends from the ceiling as presented in Figure 9-16, showing the IFW 50% scale model. The strut can also automatically modify the ride-height of the model, without additional setup changes.

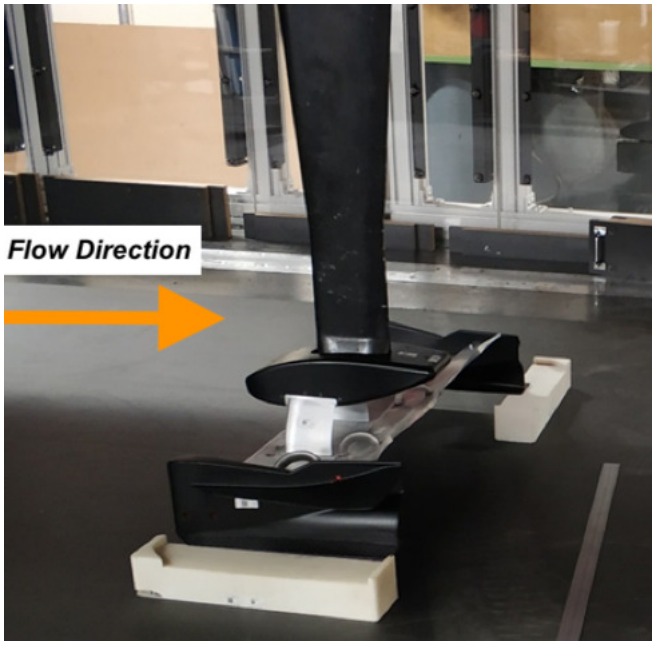


Figure 9-16: Imperial Front Wing assembly on Imperial College London 10 × 5 wind tunnel.

9-2-1 Domain parametrisation

In the following, we will use a coordinate system with X denoting the streamwise direction, Y the spanwise direction and Z the vertical direction. The trailing edge of the front wing is located at -300mm in X direction and the ground plane at -25mm in the Z direction. A 3D illustration is presented in Figure 9-17 and the wing is two-sided, and PIV measurements were only performed on the $y < 0$ endplate.

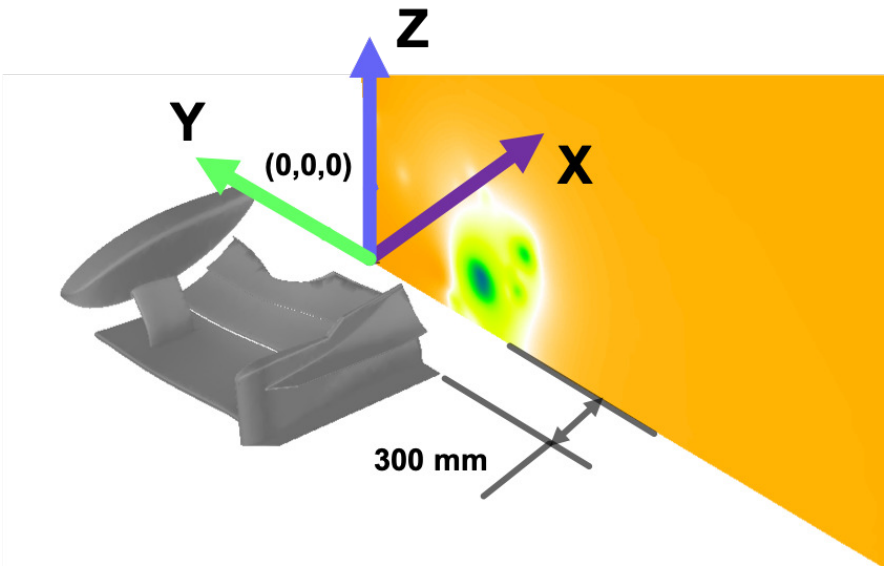


Figure 9-17: Imperial Front Wing geometry with its coordinate axis definition.

As shown in Figure 9-18, we denote by h the ride-height (i.e. the distance between the ground and the lowest part of the front wing endplate) and by c the chord length of the main element. The position of the wing in the tunnel is further characterised by a pitch angle of 1.094°.

This study uses the configuration of $h/c = 0.36$ which can be considered as a relatively low front ride height, with high ground effect and hence higher loads on the wing. The corresponding Reynolds number is $Re = 2.2 \times 10^5$, based on the main element chord - c, of 250 mm and a free stream velocity (U_∞) of 25 m/s.

9-2-2 Measurements

The experiments performed in the 10×5 wind tunnel located in the Department of Aeronautics from this study were defined, organized and part performed by the author in a collaborative work with McLaren Racing, ExaFLOW consortium and Imperial College London. The measurements consist of flow visualizations of wall-bounded streaklines using aerodynamic paint flow measurements, and time-resolved PIV on distinct planes of various locations, which are presented as follows.

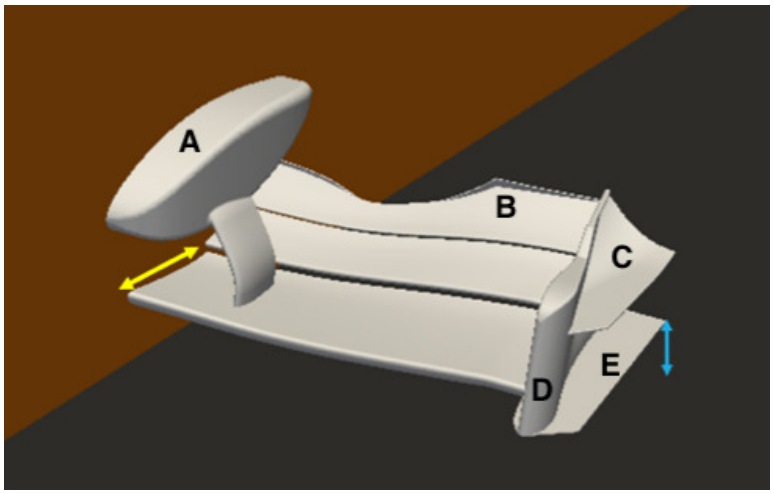


Figure 9-18: Imperial Front Wing geometry. Nomenclature: ride height h (light blue line), chord c (yellow line), main plane (dark orange), moving belt (dark grey), nose cone (A), Gurney flap (B), canard (C), endplate (D) and footplate (E).

Surface flow patterns

The first quantity of interest is the analysis of wall-bounded streaklines on the wing. To that end, flow visualization paint was applied on the wing in order to identify separation and transitional regions, at a reduced velocity of 15m/s (i.e. $Re = 1.32 \times 10^5$) to avoid operational problems with the flow visualization paint and the wind tunnel. Visualization results will be compared to wall shear stress contours from the numerical simulations at $Re = 2.2 \times 10^5$. To make the experiment easier to reproduce numerically, unlike previous experiments by Pegrum [2007], we elected not to use any transition strips, hence adopting a natural transition mechanism.

Particle image velocimetry

To capture the evolution of vortices travelling downstream, PIV measurements were performed in various iso-X planes within an interest window of 225 mm $\times$ 130 mm. The inspection plane closest to the trailing edge of the wing (located at $X = -300mm$) was at $X = -294mm$. It was not possible to get any closer to the trailing edge without being affected by laser reflections. It should however provide a good representation of the initial position of the vortical structures leaving the wing. A further four inspection planes were located respectively at $X = -250mm, -150mm, -24mm$ and $150mm$. For each plane, the total averaging time was 10 seconds, at an acquisition frequency of 250Hz. The locations of the interrogation planes (also normalised by the main element chord) are indicated in Table 9-1 and Figure 9-19 is based on the coordinate system in Figure 9-17.

The PIV setup for the IFW measurements is presented in Figure 9-20. The system considers a Litron LDY300 Nd: YLF laser at wavelength of 527 nm and beam thickness adjusted to be approximately 2 mm in thickness, combined with mirror and Dantec optics. To capture the

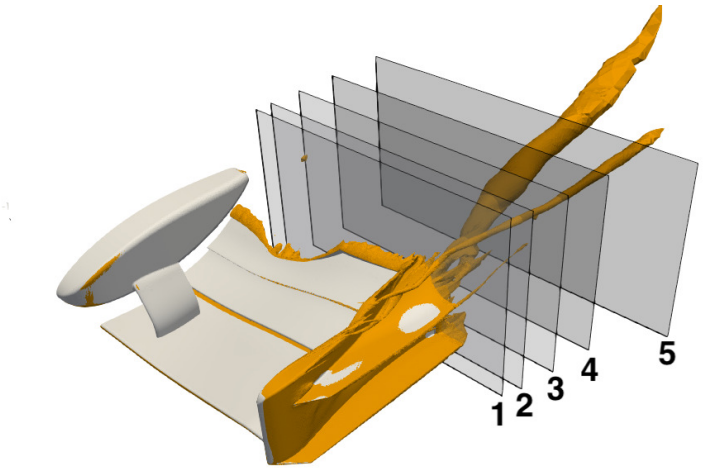


Figure 9-19: Imperial Front Wing geometry and selected PIV planes.

flow snapshots, a Phantom v641 camera with 135 mm lens was used. The camera system has a 4-megapixel sensor which is capable of capturing up to 1460 frames per second.

Polyethylene Glycol (PEG) mixed at a ratio of 1:4, was atomised by a Dantec 6-jet seeder and introduced into the test section downstream of the model. The PEG seeding, therefore, travelled along the wind tunnel's closed circuit, passing through the motors, three sets of turning vanes, heat exchange, honeycomb and screens to ensure it is uniformly mixed with the travelling air prior to hitting the laser sheet.

Calibration was performed against a custom 2D target pattern of dots output from *DaVis*, a La Vision PIV processing software, however the PIV hardware used is from Dantec. The target was aligned with the centreline of the laser beam thickness. To avoid new calibrations at every streamwise location tested, a dynamic common platform was designed in order to allow the mirror and laser optics to move, keeping the image acquisition system fixed.

The interframe time of laser pulses and camera exposures were synchronized so that PEG particles would have crossed around a quarter of the interrogation cell between image pairs. Particle images were acquired with a magnification of 0.0898 mm/pixel and the quality of the acquired images is improved by applying a 3x3 median filter and Gaussian smoothing techniques. The filtered images are finally assembled using the *DaVis* software with 32x32

Plane Number	X **[mm]**	X/c **[-]**
1	-294	-1.176
2	-250	-1.000
3	-150	-0.600
4	-24	-0.096
5	150	0.600

Table 9-1: Plane locations for PIV measurements

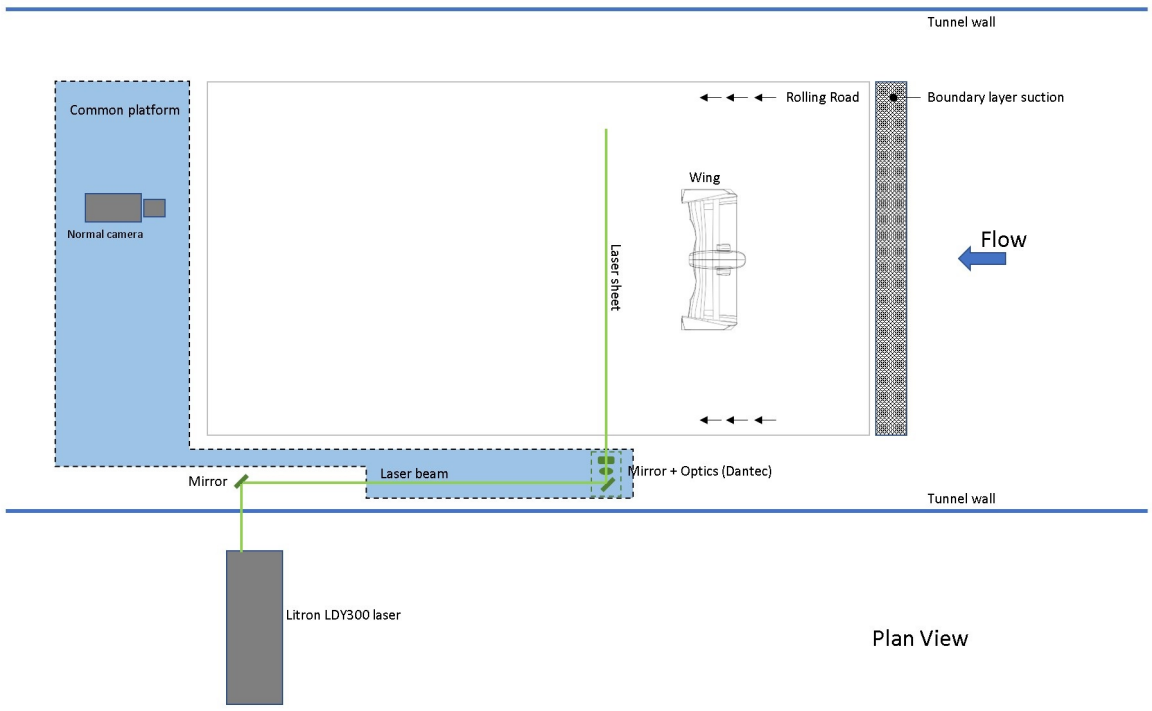


Figure 9-20: Complete PIV setup of the IFW at the 10 × 5 wind tunnel in the Department of Aeronautics at Imperial College London.

interrogation windows overlapped by 50% to deliver the final averaged velocity field, presented in this work.

The PIV measurements accuracy was attested following a calibration grid, aligned with the upper support and set in the coordinate Y=0, presented in Figure 9-21. The average period of 10 seconds is long enough to have a stable flow over the wing.

9-3 Simulation configuration

All simulations were performed using the incompressible Navier-Stokes solver which employs a velocity correction scheme Guermond and Shen [2003], similar to previously presented cases. The elliptic operators were discretised using a classical continuous Galerkin formulation whereas the advection operator on the formulation used a discontinuous Galerkin projection. Combining both CG and DG approaches allows the use a sub-stepping algorithm as proposed by Sherwin [2003], aiming faster convergence for the simulation which is employed in all IFW simulations. For simulation stability, we consider both CG-SVV with DG mimicking kernel and dealiasing techniques, as presented for the Ahmed body cases.

9-3-1 Boundary Conditions

Following similar setup from the Ahmed body simulations, the main boundary conditions for the computational study are presented as follows:

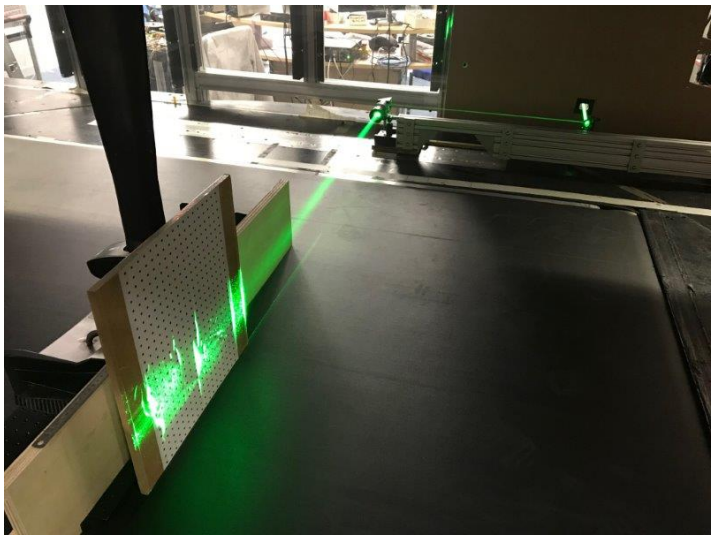


Figure 9-21: PIV calibration grid used for the IFW measurements at the 10 × 5 wind tunnel in the Department of Aeronautics at Imperial College London.

- Both front wing and nose cone are set as wall with no-slip condition;
- A half model of the geometry is used with a symmetry condition imposed at $Y = 0$;
- Uniform velocity profile is imposed at the inlet;
- A high-order outflow condition is imposed at the outlet, as proposed by Dong et al. [2014];
- A moving ground condition is imposed on the floor with speed U in the X direction.

9-3-2 Mesh Generation

The mesh domain is defined using half symmetric model of both front wing and wind tunnel. The tunnel length is 20 m longer, similar to the test section of the 10x5 wind tunnel at Imperial College London. To match same blockage condition of the experiments, half cross sectional area considered is $3m \times 3m$, the double of the half test section area of the 10x5 wind tunnel. Inlet is located at $X/c = -30$ and outlet at $X/c = 50$. The IFW then is positioned with its trailing edge at $X/c = -1.2$ and footplate at $h/c = 0.36$.

The linear mesh for the IFW study is first generated with a finite volume (FV) commercial mesher using a conformal hybrid tetrahedron/prism layout. In order to make this initial mesh suitable for higher orders, as well as to provide a mesh with an appropriate boundary layer spacing as required at higher Reynolds numbers, the mesh is then processed through NekMesh, following the hybrid mesh approach presented in Section 6-2-4.

The single 'macro' prism layer size is defined as $0.012c$ in order to have $y^+ \leq 1$. Detail of the macro boundary layer mesh on the symmetry plane around the main wing element is shown in Figure 9-22.

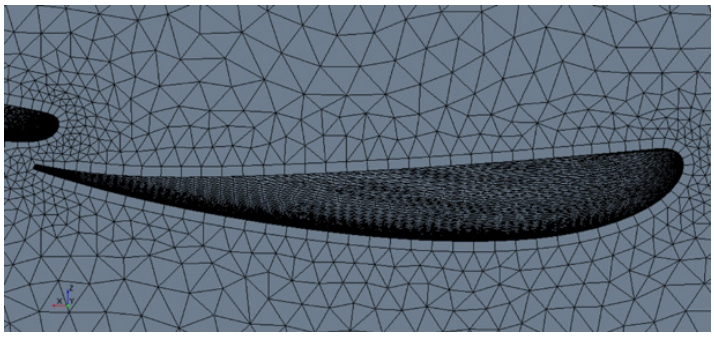


Figure 9-22: Detailed view of the macro prism layer.

Similar to the Ahmed body, we also included h-type mesh refinement boxes, shown in Figure 9-23 on plane $Y/c = -2$. The first refinement box (red) is defined to have a transition from coarse far-field mesh elements. It is defined from $X/c = -4.4$ to $X/c = 2$, height of $2.2c$ and width of $3.4c$ and is referred as far-field refinement. A second refinement box, referred as wing refinement, (light blue) is applied at the front wing region to improve number of mesh elements in the region where the IFW is located. It is initially positioned at $X/c = -4$ and $Z/c = 0.4$, extended to $X/c = -0.7$ and $Z/c = 1.9$, with total width of $3.1c$. The last refinement (orange) is applied downstream the endplate region and is referred as endplate refinement. It is applied from $X/c = -1.2$ to $X/c = 1.2$, total height of $1.6c$ and width from $Y/c = -0.45$ to $Y/c = -0.8$. The maximum mesh element size is approximately $0.8c$, while we impose the mesh element size of $0.16c$ on the far-field refinement box and $0.07c$ for both wing and endplate refinement boxes.

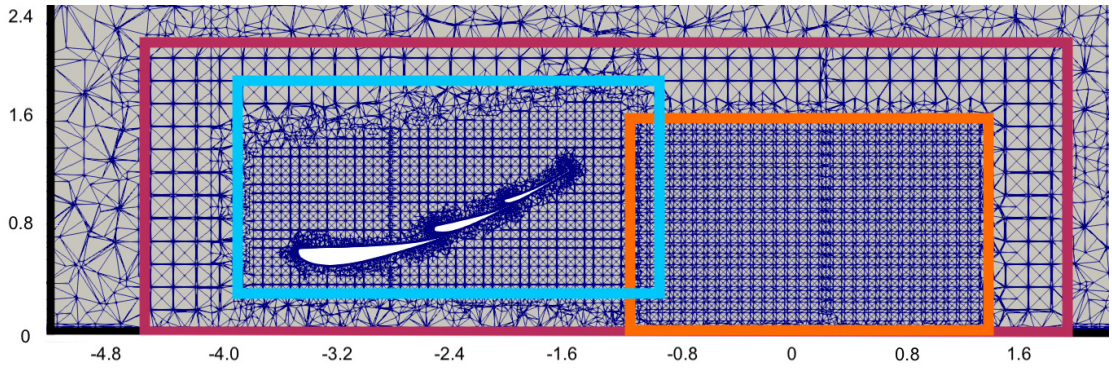


Figure 9-23: Details of the three proposed refinement boxes on the plane $Y/c = -2$. Far-field refinement box (red), wing refinement box (light blue) and endplate refinement box (orange).

We note that where a high-order element meets a CAD surface, it must be deformed in order to align with the CAD and thus faithfully represent the geometry. The use of NekMesh applies surface curvature in a manner so as to minimise the projection error as described in Turner [2017]. For all simulation cases on the IFW, the high-order mesh implemented uses a polynomial (P_M) of 6^{th} order. The final step is splitting of the macro prism layer on both the front wing and the moving ground. We subdivide the prism layer into 7 elements ($N_{BL} = 7$) using a geometrical growth rate of 1.6 ($GR = 1.6$). The parameter settings for

the mesh, together with surface and volumetric refinement criteria, are based on the Ahmed body validation and in an optimization internal study from McLaren Racing.

The estimated number of finite volume mesh elements to have a reliable *LES* simulation (N_{LES}) for IFW is approximately 70 million elements, based on the expertise of McLaren Racing. Applying the proposed spectral/hp element mesh generation strategy, we generated a coarse mesh with approximately 2.82 million elements. The coarse mesh definition from Equation 6-9 is based for a 4^{th} order polynomial accuracy for the solution. We note that this mesh is much coarser when compared with a standard finite volume models with similar solution accuracy, recalling that within each element a polynomial expansion is applied in the spectral/hp element methods. The final mesh is provided in the Nektar++ XML format and details of this format can be found under www.nektar.info or DOI 10.14469/hpc/6049.

9-3-3 Load case configuration

All simulations are conducted at a nominal velocity U of 25m/s. We have used a mixed expansion order in velocity and pressure where following Taylor-Hood elements, where we recall the pressure expansion is one order lower than the velocity expansion. Initial runs were performed at $P_N = 3$ (third order expansion in velocity and second order expansion in pressure). We then increased the resolution to $P_N = 4$, which was the lowest order to obtain reliable results for the mesh discretisation provided with this chapter and is discussed in the following sections. To complement these results, we also performed simulations of the IFW with $P_N = 5$ to evaluate the extend of resolution enhancement with an increment of the polynomial order.

Total number of mesh elements for the proposed IFW case is approximately 2.815 million, much coarser than traditional *LES* meshes. Based on equations 7-2 to 7-4, mesh resolution increases when combined with high-order polynomials for the solution. Mesh resolution reaches approximately 37.3 million DOFs for NM36 simulation and 79.2 and 144.4 million DOFs respectively for NM46 and NM56. Recall that the notation NM36 indicate $P_N = 3$ with $P_M = 6$.

To save computational time, initialisation techniques are systematically used at various stages of the simulation. We first interpolate the results of a previously converged *RANS* simulation onto the high order mesh at NM36 simulation using our developed mapping technique. This case with interpolated solution is simulated for two main element chord time units or convective time unit (CTU). The unit CTU refers to the number of times flow passes over a reference length, in this case the chord length c of the main wing element. CTU for the IFW is defined as $CTU = U_\infty t_U / c$, where t_U is the total simulation time. These results were then used to initialise the NM46 simulation. This solution was subsequently used as the initial point for higher order simulations.

9-4 Results and analysis

Before collecting the averages, we first time marched the NM46 for 8 CTU, starting from the NM36 restart. This simulation was then time marched a further 2 CTU at NM46, reaching a total of 10 CTU. Time averaging of drag and lift coefficients and downstream comparative

planes occurs from 8.4 to the 10 CTU for this case. For the 5^{th} order case (NM56) resolution, we restarted the simulation from the NM46 case at 8.4 main element time unit and ran the simulation up to the 11.75 CTU as we verified that we needed to extend further once lift was still evolving with time. The time averaging for the lift and drag at NM56 was started from different times when the signal has reached a stationary state. Therefore, the drag was averaged between the 10.5 and 11.75 CTU and the lift was averaged from 11.5 to 11.75 CTU. The comparative planes were averaged from the 8.4 to the 10 CTU, similar to the NM46.

Simulations were performed on McLaren Racing R&D cluster, while extended simulations for NM46 and NM56 were later performed on HP cluster. Since McLaren Racing cluster configuration is confidential, we present HP cluster configuration in Tables 9-2 and 9-3.

Table 9-2: EDR Infiniband technical specifications on HP cluster.

	EDR Infiniband
Product Type	ICE-XA
Product Name	SGI 8600-IP157
Board Model	X11DPT-SA-SG007 / X11DPT-SB-SG007
Processors	2 x 20 Intel(R) Xeon(R) Gold 6148 CPU @ 2.40GHz
Total Memory	192 GB/per node
Speed	2667 MHz DDR4

Table 9-3: Intel Omni-Path Cluster technical specifications on HP cluster.

	Intel Omni-Path
Product Type	ICE-XA
Product Name	SGI 8600-IP157
Board Model	X11DPT-SA-SG007 / X11DPT-SB-SG007
Processors	2 x 18 Intel(R) Xeon(R) Gold 6154 CPU @ 3.00GHz
Total Memory	192 GB/per node
Speed	2667 MHz DDR4

For each simulation resolution, we evaluated the required computational time for the flow pass one chord length c of the main wing element, based on the number of CPUs and time step, as presented in Table 9-4. We first notice that time step reduces five times as the resolution increases, in order to keep the CFL condition below one. Time per iteration is almost similar between NM36 and NM46, however NM46 simulations were performed with approximately 2.8 times more CPUS. NM36 has the best performance when analysing total wall time, however when comparing NM46 and NM56, we would expect a time increment that doesn't happen.

9-4-1 Wing loading resolution sensitivity

An easily accessible diagnostic when performing the simulations is to consider the lift and drag coefficients. We start by comparing lift/downforce coefficient, based on the main plane surface area, for NM46 and NM36 as shown in Figure 9-24. We observe there is a very distinct deviation on the lift coefficient where results for NM46 are generally powering up (producing

Table 9-4: Simulation time for one convective length using Nektar++, considering NM36, NM46 and NM56.

Load Case	CPUs	Time per time step (s)	Time Step	Length	CPU Time (h)	Total Wall Time (h)
NM36	2048	14	5e-5	0.25	38912	19
NM46	5760	13	1e-5	0.25	368640	90
NM56	5760	6	5e-6	0.25	300000	84

more negative lift) whilst the NM36 can be seen to deviate significantly with a reduction in downforce (negative lift). This point will be further discussed in section 9-4-2 when we consider the wall shear stress, however it is important to note that NM36 is an insufficient resolution for this mesh.

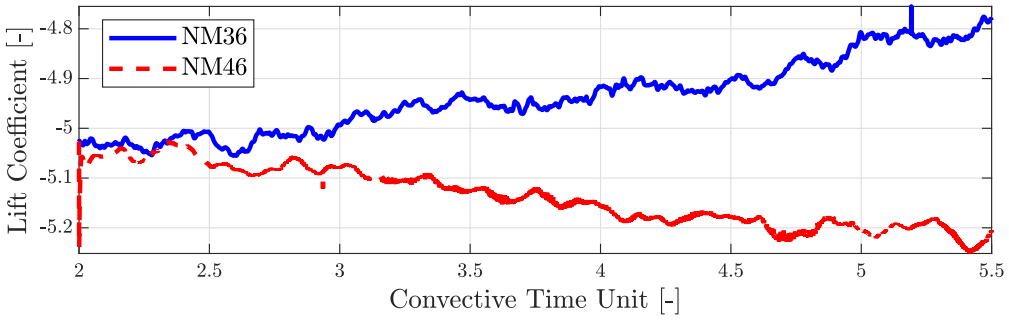


Figure 9-24: Comparative lift trend line for 3rd (NM36 - blue line) and 4th (NM46 - red-dashed line) polynomial expansions obtained from the same NM36 restart file from the 2nd to the 5.5 CTU

To demonstrate the convergence of the IFW aerodynamic load with both time and polynomial order, the time history of the drag and lift forces are shown in Figure 9-25. From this figure we see the evolution of both drag and lift coefficients for the time period from the 9 to the 10 CTU, based on the main chord for NM46 simulation. Both drag and lift coefficients are based on the surface area of the main wing element chord $c = 0.25$ and the total span of the wing $W_s = 5.6c$. The same sampling is used for both NM46 and NM56, however the wiggly behaviour of the later is explained by the fact of more scales being resolved with higher solution polynomial order, with the same time interval.

As seen from Figure 9-25, the drag and lift coefficients for NM46 simulation have converged to a relatively stationary limit cycle before the 9 CTU, having well-established behaviour throughout the time window. In contrast, the drag force for NM56 starts with an oscillatory path and gradually converging to a steady value, higher than the NM46, between the 10.5 and 11.75 CTU, as presented in Figure 9-26. Lift is still evolving all the way to the end of the averaging window. This indicates that the vortices may not have reached their maximum strength in the simulations period however we can see that there is a region between the 11.5 and 11.75 CTU that seems to have a stabilized lift behaviour. Unfortunately, limited computational resources prevented us from simulating further.

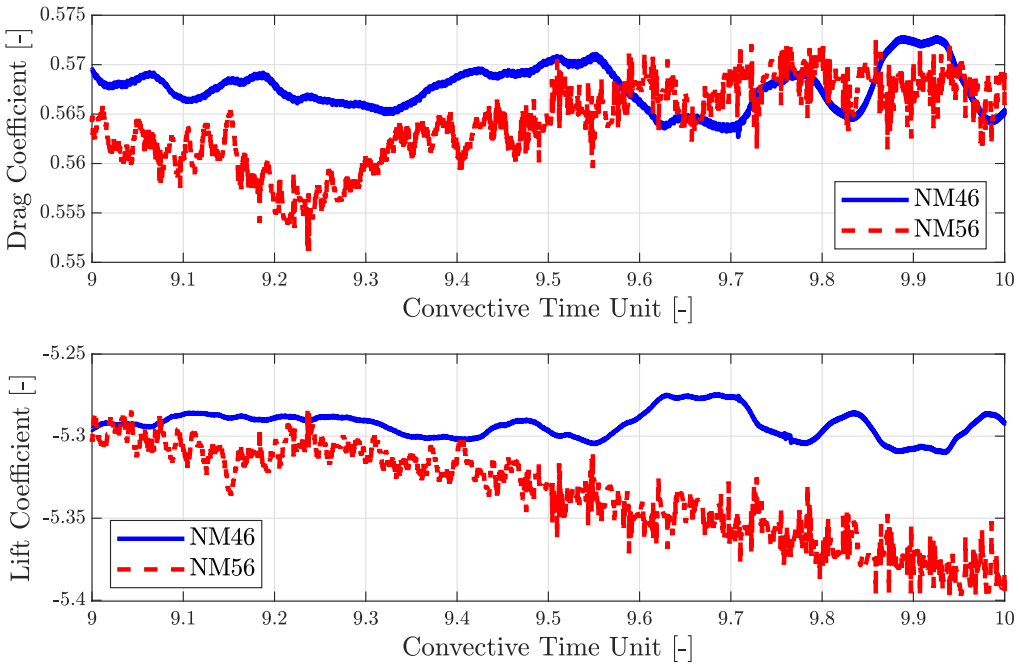


Figure 9-25: Drag (top) and Lift (bottom) coefficients history on the IFW comparing NM46 and NM56 results.

Using the above windows for averaging we observe a drag coefficient of **0.568** at NM46 and **0.575** at NM56 and a lift coefficient of **-5.30** at NM46 and **-5.54** at NM56. The gap between NM46 and NM56 for drag results is around 1.3% and 4.5% for the lift coefficient.

9-4-2 Flow Visualization

Experimental flow visualization results for IFW are shown in Figure 9-27a, 9-27b and 9-27c in bottom, top and side views respectively. For this experiment, we applied a shear-sensitive type of flow visualization aerodynamic paint on the right-hand side surface of the IFW and performed the test at a lower free stream velocity of 15 m/s. The reduced velocity was to avoid distortions in the visualization due to excessive loss of paint, as well as contamination of the wind tunnel.

In Figures 9-28 and 9-29, we compare the experimental flow visualization with the wall shear stress magnitude from the Nektar++ simulations considering instantaneous plots at 10 CTU for the NM46 and 11.75 CTU for NM56. In Figure 9-28, we first consider the bottom surface of the IFW with the simulations at NM46 and NM56 resolutions. All results show similar attachment lines on the footplate, indicating that the vortical structure positioning is likely to be consistent and the transition bubble in the main plane (first element of the cascade) is well captured. Increasing the polynomial order to NM56 leads to improvements in the prediction of the finer detailed features of the solution, better capturing the attachment line labelled 1 and also drawing out the streakier structure of the attached flow on the main element. Although it is quite hard to identify the separation zones from the experimental

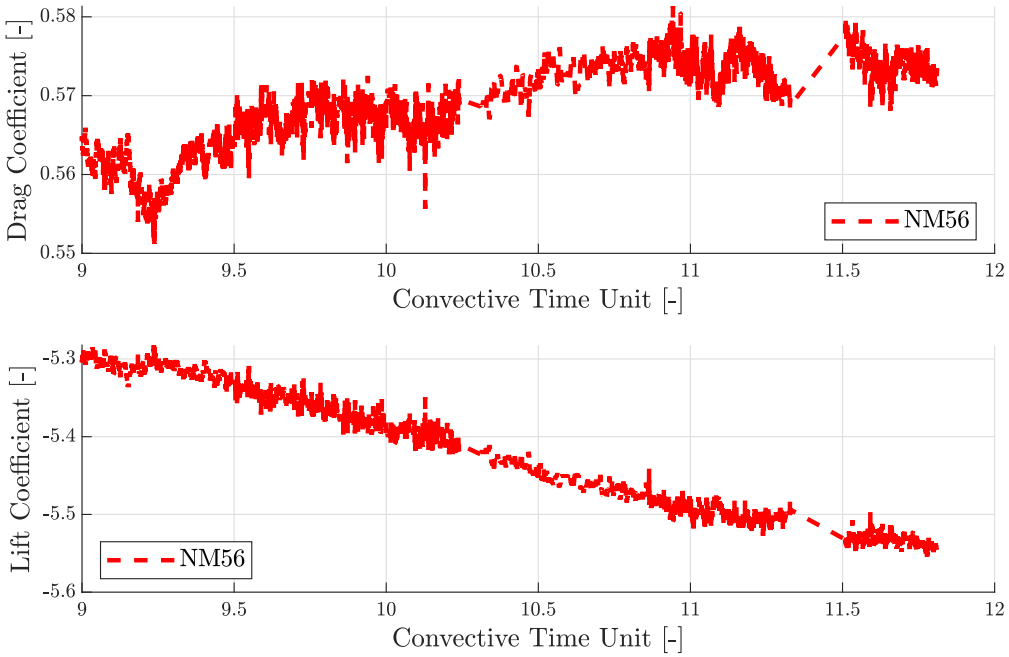


Figure 9-26: Drag (top) and Lift (bottom) coefficients history on the IFW for the NM56 results.

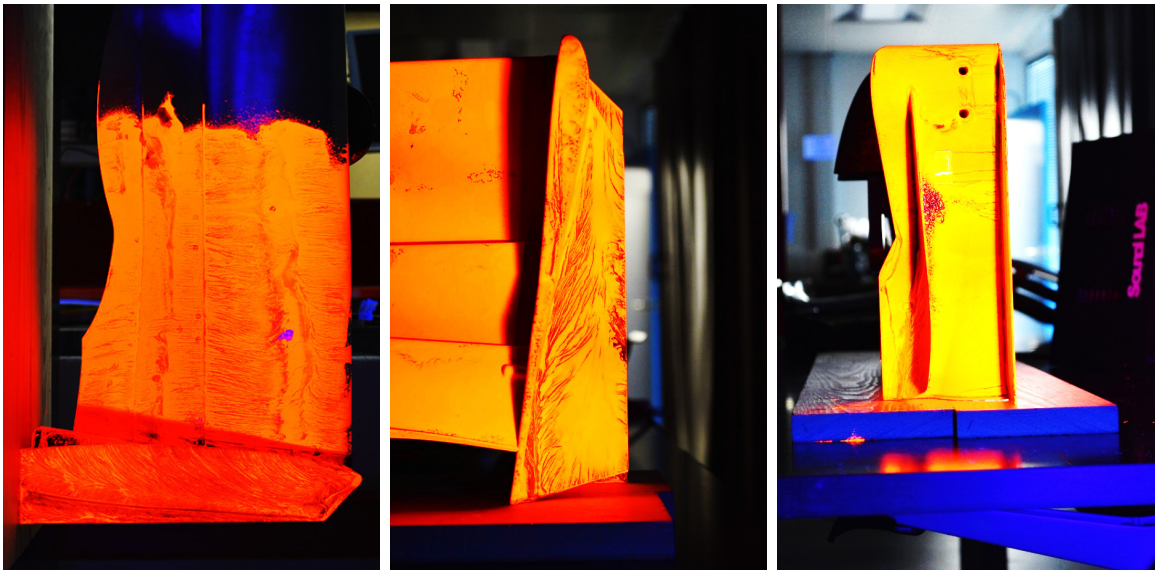
data, careful consideration of the images highlights a recirculation zone between (25-30%) of the main element chord, considering the flow moving from right to left, and this recirculation zone is relatively well captured on the main element of the Nektar++ simulations.

Figure 9-29 also demonstrates a consistent prediction of the top edge and canard attachment lines for the two simulation cases. Comparing to NM46, the simulation at NM56 has a better resolved wall shear stress, indicating the separation lines on the vane (as indicated by the number 2) and flap, showing that increasing the polynomial order has a positive effect on the quality of the near wall flow prediction.

To confirm the discrepancy of NM36 resolution in predicting the flow structures, we present the flow visualization for this resolution in Figure 9-30, where most of the flow features found on experiments and higher-order simulations previously presented such as the vane separation line (indicated by 2) are only marginally captured.

Comparing all three simulation resolutions in terms of the surface behaviour on each wing element presented on the bottom view in Figure 9-31, for the NM56 case, flow separates from the main wing element then re-attaches all along the span. However, for NM46, it does not seem to quite re-attach at the most outboard part of the main plane, where we observe a discontinued re-attachment line and increment of the separated flow region. At NM36 the flow is predominantly attached at about 2/3 of the span, similar to NM46 even with the separated flow region at the outboard part of the main wing element. At this point, NM56 presented similar flow topology as experimental results and NM46 and NM36, with similar results, slightly agreed.

On the middle wing section, the flow on the NM56 case does re-attach, indicating similar profile of the main wing element. Once again, the NM46 case manages to capture flow re-



(a) Bottom view **(b)** Top view **(c)** Side view

Figure 9-27: Flow visualization of IFW at velocity of 15m/s using Formula 1 standard aerodynamic paint.

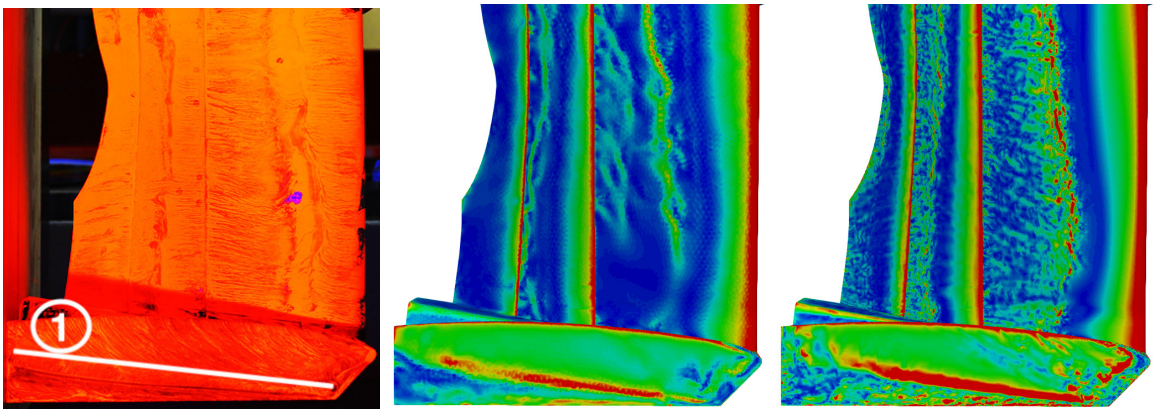
attachment but further downstream of the element, not so early and well-defined as on NM56 case. Finally, the NM36 is fully separated until the mid-span of the section, indicating that this resolution is not enough to capture the flow physics. Once again, NM56 results qualitatively well-captured the experimental results for this wing element, NM46 indicated similar flow physics with incorrect position and size and NM36 failed to represent experimental results.

Finally, for the third wing element, where the gurney flats are assembled, the flow only appears to be re-attaching in the NM56 case at the trailing edge of the wing element. On the footplate, NM56 and NM46 captures the vortex detached whereas NM36 only marginally captures this flow structure. We conclude that NM56 is the resolution required for this mesh setup to correctly capture the flow behaviour on the wing, although as we shall see in the following section, the NM46 can capture many features of the time averaged flow.

9-4-3 Comparison with PIV data

We now compare the numerical simulations against the PIV results on a few planes at different downstream locations. Firstly, we identify the relevant vortex structures in the contour plots: the main, canard and endplate vortices are the dominant flow structures on the planes presented in this work and are depicted in Figure 9-32.

In the following, we present the comparisons for the planes closest to the wing (Figure 9-33 and 9-34), the intermediate planes (Figure 9-35 and 9-36), as well as a plane in the far field (Figure 9-37), hence quantifying the prediction of the transport of vortices downstream. Both spanwise (Y) and vertical (Z) non-dimensionalised velocity components are presented. The location of each plane, as previously defined on 9-2-2, is identified in the top right sub-plot.



(a) Test bottom view **(b)** NM46 **(c)** NM56

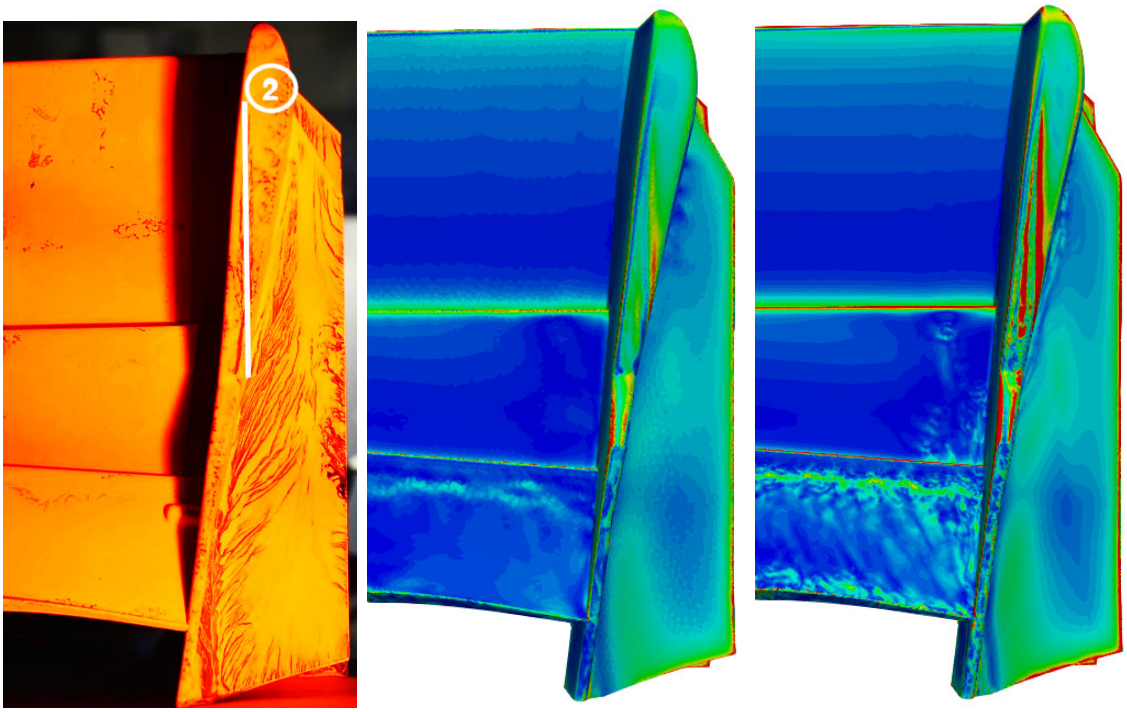
Figure 9-28: Comparison of the flow visualization and wall shear stress results for IFW (bottom view)

For each plane, we present time-averaged velocity results for the spanwise V and vertical W components, normalized by the free stream velocity U_∞.

Considering the V components shown in Figure 9-33a we observe a large blue (negative) region on top of a red triangular patch of V. These two features and their W counterparts in Figure 9-33b represent the main vortex arising from the inboard footplate of the endplate, denoting a region of counter clockwise rotating flow as we look at the plane from a downstream position: this is referred as the main vortex in the following. We also observe on the left side of Figure 9-33a two small circular regions, which are typically referred to as the canard vortex. The canard vortex is generated by the aerodynamic device mounted on the outboard side of the endplate (referred as canard) and is representative of the type of devices often introduced to provide additional load or shed vorticity. It has similar behaviour as the main vortex, with top circular region in blue (negative) and the lower portion is orange (positive), denoting similar counterclockwise rotation downstream for this vortex. The signature of this vortex is also clearly seen in V and W components shown in Figures 9-34a and 9-35a and Figures 9-34b and 9-35b.

The third relevant flow structure is observed on the top left side of Figures 9-37a and Figure 9-37b and is defined here as the top-edge or endplate vortex. In the sampling window of this image we can only observe half the vortex as indicated by the orange (positive) circular region. The endplate vortex is generated by the pressure difference across the endplate according to Pegrum [2007].

We next consider the evolution of the three vortices, tracking their position as they travel downstream. The main vortex first appears with its core at around two-thirds of the spanwise location on plane 1 and the three elements on the wing contribute to its build up. As it travels downstream, it gets diffused, as is evident from plane 3. Further downstream, by plane 5, we observe that the main vortex core has shifted inwards (towards the symmetry plane) to around half of the span, which is consistent with the induced velocity from the image vortex in the plane of the floor. There is also evidence of the vortex moving upwards from the images of vertical velocity.



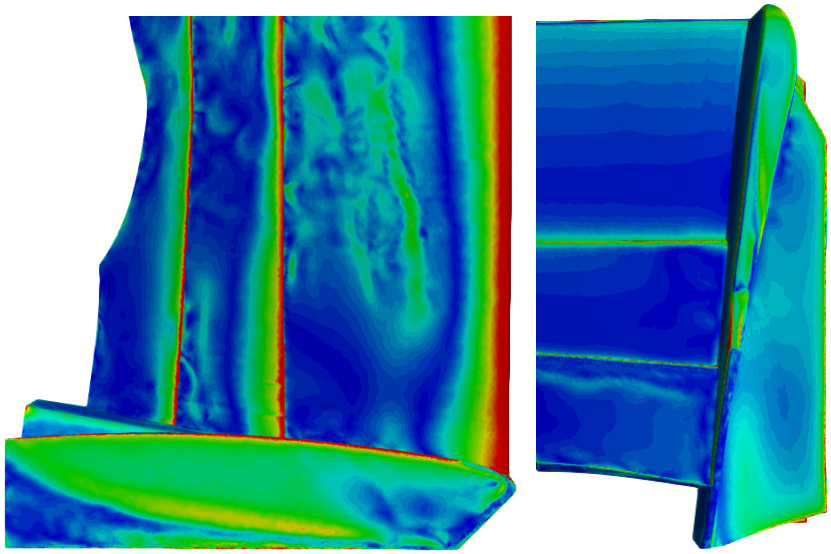
(a) Test top view **(b)** NM46 **(c)** NM56

Figure 9-29: Comparison of the flow visualization and wall shear stress results for IFW (top view)

Similarly, the canard vortex moves towards the symmetry plane, and its intensity is similar in planes 1 to 3. Further downstream in plane 5, a very distinct movement in the negative Z direction suggests that it is being ingested by the main vortex and this is perhaps most clear in the plots of the vertical velocity. For the endplate vortex, despite the absence of full results due to limitations in the PIV measurement window, we can still observe that it moves upwards in plane 3 and then downwards in plane 5, suggesting that the main vortex intensity influences the trajectory of the endplate vortex.

Figures 9-33 through 9-37 show that both NM46 and NM56 polynomial orders have captured the main vortex, despite a slight under-prediction of its strength. In addition, the secondary features such as the endplate vortex and the canard vortex are also well captured by both numerical simulations. In short, for these resolutions both spectral/hp numerical simulations demonstrated good initial agreement with experimental results in terms of core position and intensity in the initial and downstream planes.

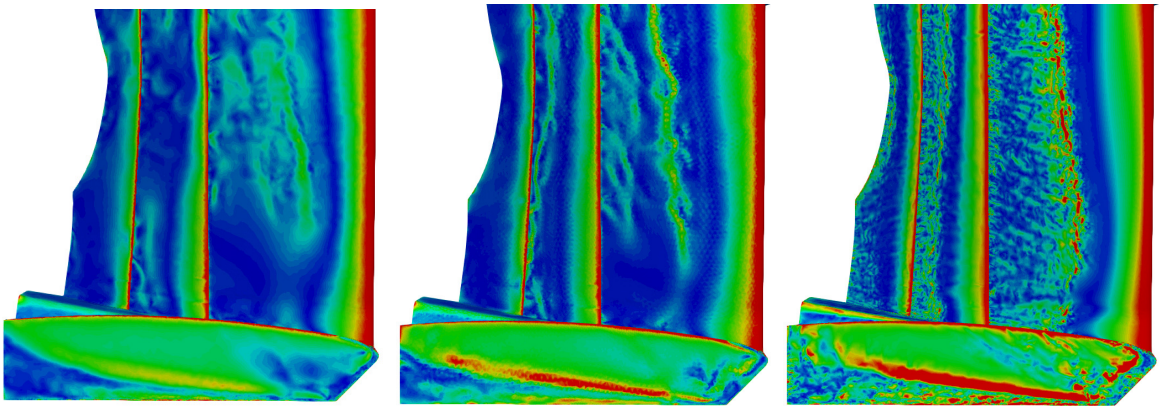
The difference between simulation results at 4^{th} and 5^{th} order can be observed in the sharper resolution of the smaller structures, which are less affected by diffusion at the higher 5^{th} order resolution. However, it is worth noting that the duration of averaging window used for NM56 is similar to NM46, at the same interval from 8.4 to 10 CTU and we are confident that the planes where NM46 shows better agreement (namely plane 3) are mostly benefiting from a longer average and a more settled solution, as can also be seen from the lift traces.



(a) bottom view **(b)** top view

Figure 9-30: Flow visualization results for IFW simulation considering 3rd polynomial expansion (NM36)

The results in the last plane, located more than one chord length away from the wing are then considered, where we recall the footplate vortex is merging into the main vortex. We would naturally expect that the numerical benefits of the high order scheme are very important here, achieving better coherence of the flow structures, through to better representation of pressure gradient and external effects. This observation highlights the attractiveness of higher order methods for racing aerodynamics, where accurate study of vortices advected along the full length of the car is required.



(a) NM36 bottom view **(b)** NM46 bottom view **(c)** NM56 bottom view

Figure 9-31: Comparative flow visualization results for IFW simulation considering 3rd (NM36), 4th (NM46) and 5th (NM56) polynomial expansion in order to highlight the major differences in resolution.

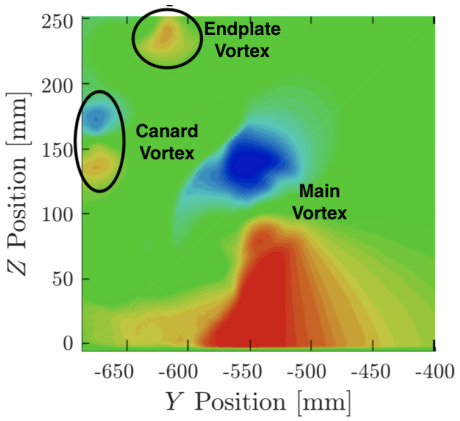
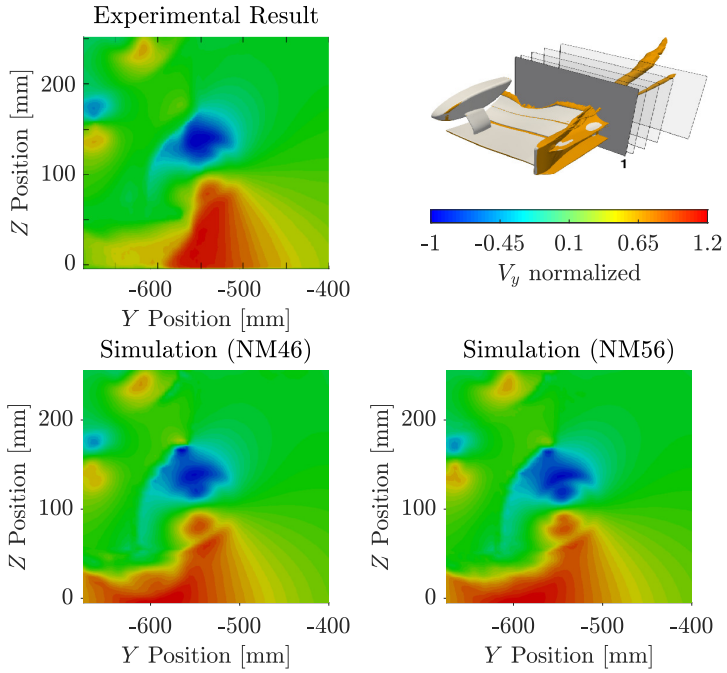
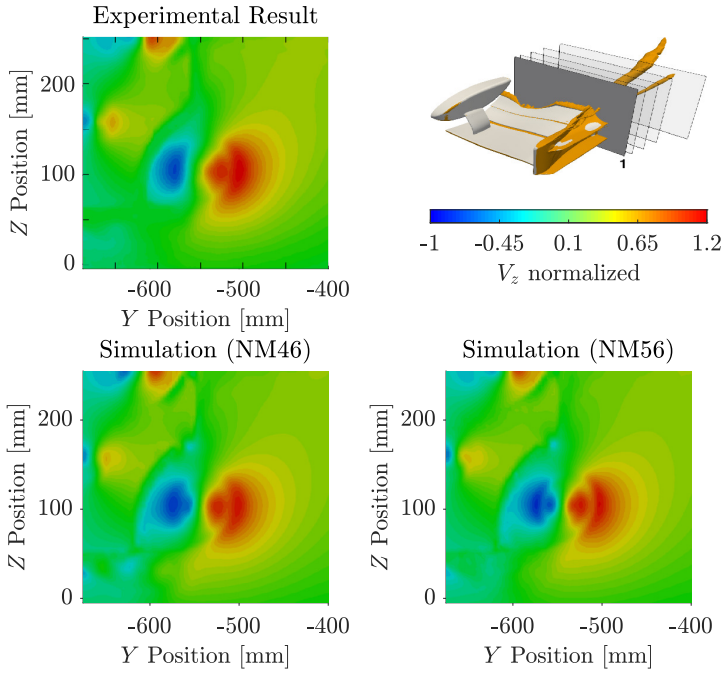


Figure 9-32: IFW vortices nomenclature definition on the V velocity plot. From top to bottom: endplate vortex (partially represented), canard vortex and main vortex.

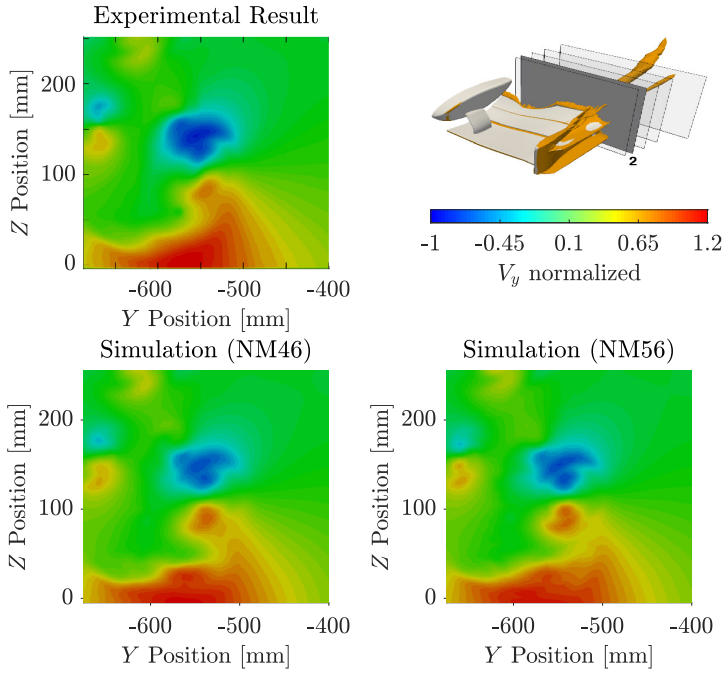


(a) Normalized V

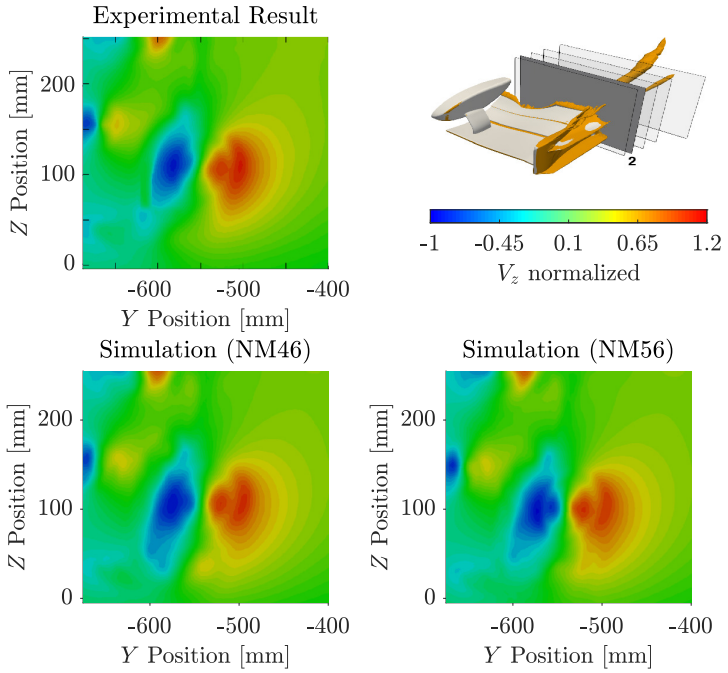


(b) Normalized W

Figure 9-33: Time-averaged normalized V and W velocity results from Nektar++ for 4th (NM46) and 5th (NM56) order polynomial expansion compared with experimental results for plane 1.

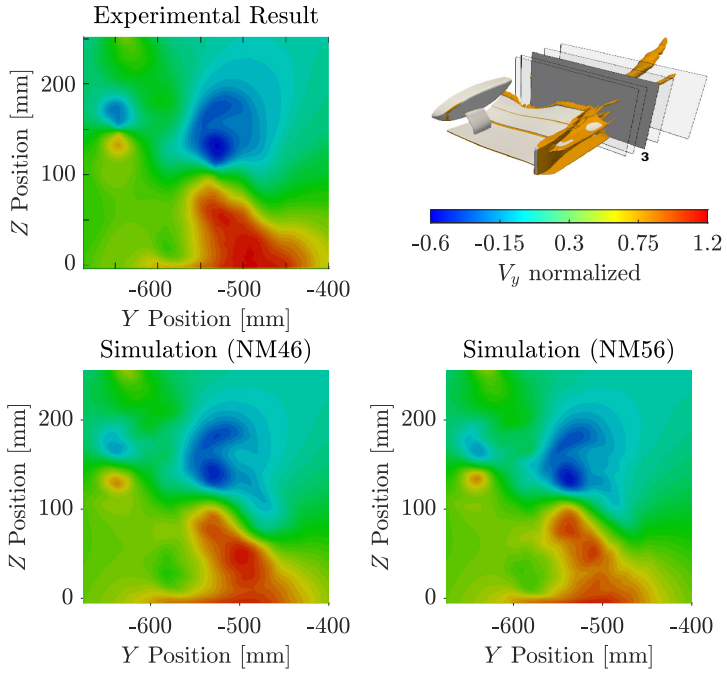


(a) Normalized V

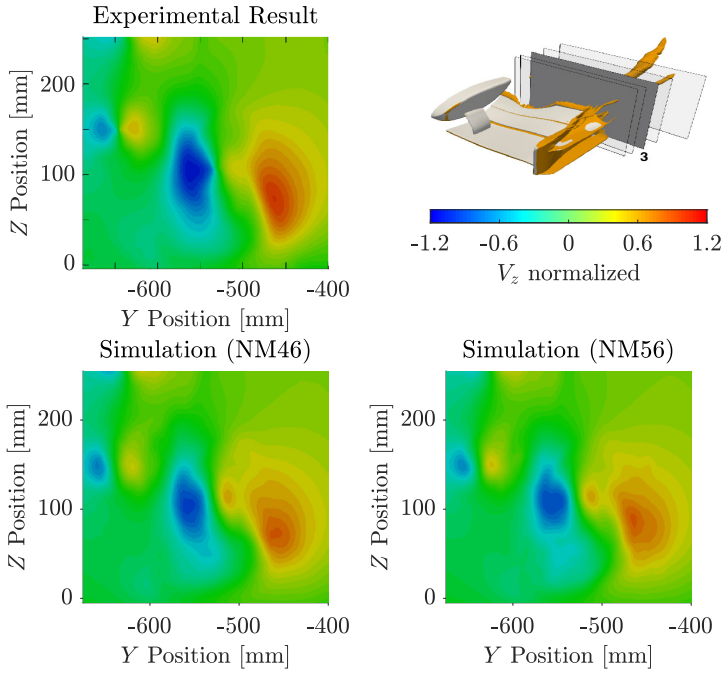


(b) Normalized W

Figure 9-34: Time-averaged normalized V and W velocity results from Nektar++ for 4th (NM46) and 5th (NM56) order polynomial expansion compared with experimental results for plane 2.

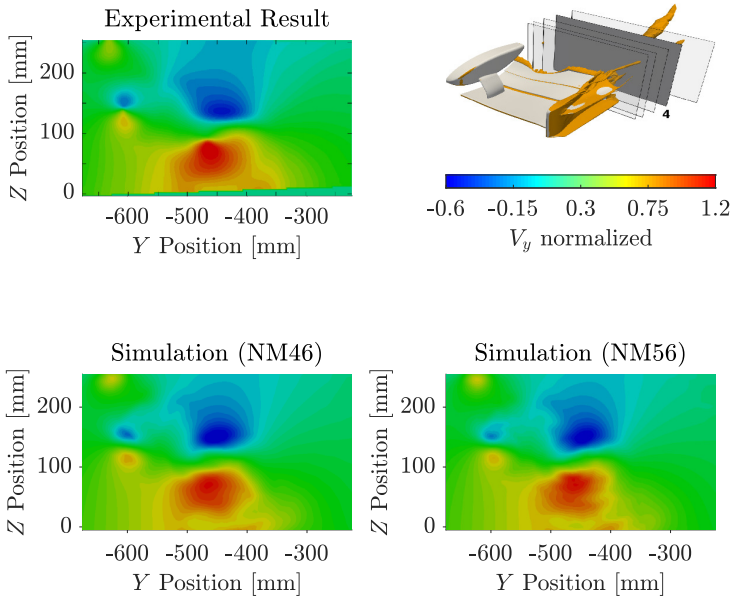


(a) Normalized V

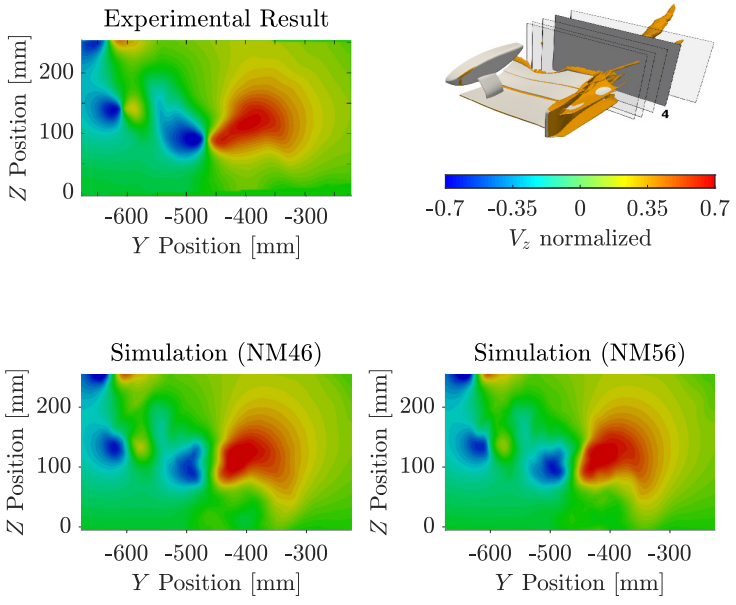


(b) Normalized W

Figure 9-35: Time-averaged normalized V and W velocity results from Nektar++ for 4th (NM46) and 5th (NM56) order polynomial expansion compared with experimental results for plane 3.

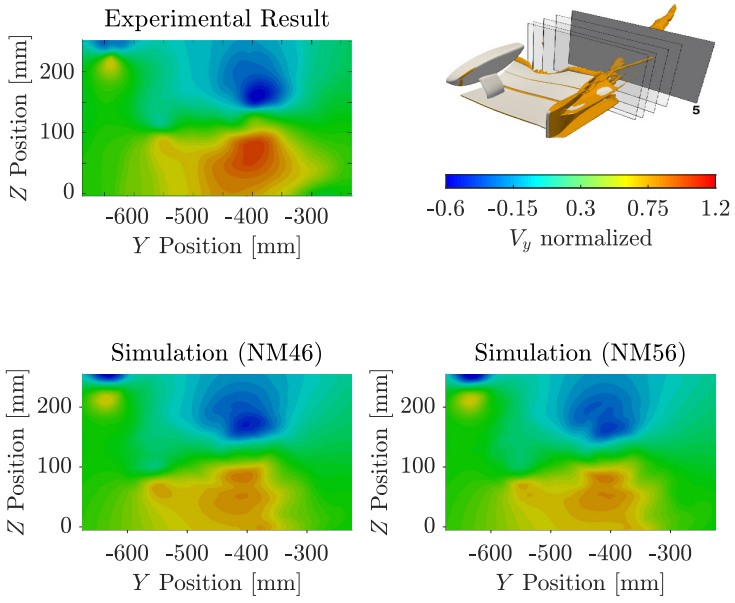


(a) Normalized V

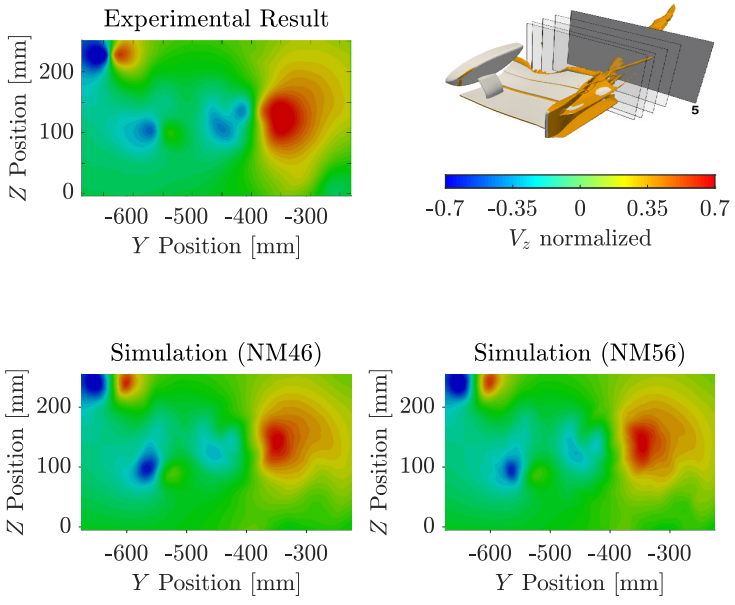


(b) Normalized W

Figure 9-36: Time-averaged normalized V and W velocity results from Nektar++ for 4th (NM46) and 5th (NM56) order polynomial expansion compared with experimental results for plane 4.



(a) Normalized V



(b) Normalized W

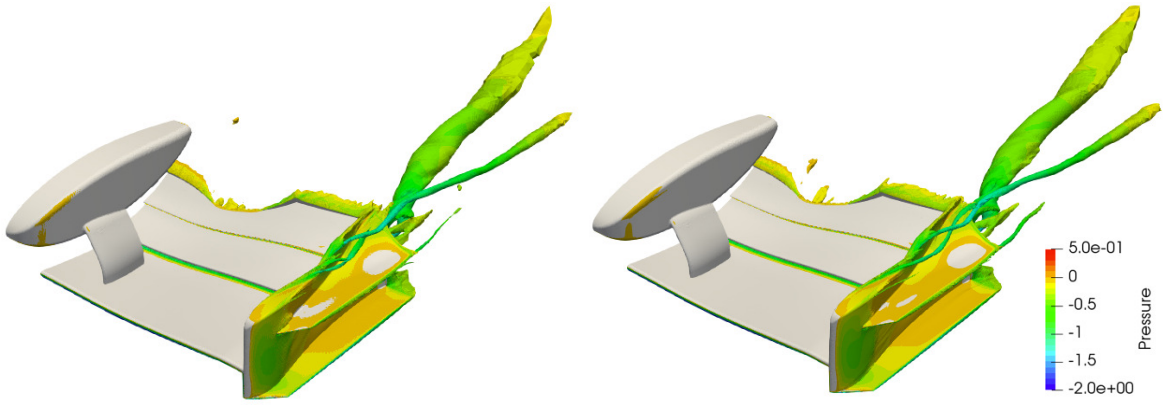
Figure 9-37: Time-averaged normalized V and W velocity results from Nektar++ for 4th (NM46) and 5th (NM56) order polynomial expansion compared with experimental results for plane 5.

9-4-4 Additional flow features

In the previous section we considered the time-averaged results, where the simulation with 5^{th} order polynomial expansion had only slightly better correlation with experimental results in terms of scales, intensity and the contour shape. These improvements are in fact the direct consequence of the better capturing a wider spectrum of flow structures, which can be highlighted when examining the instantaneous results instead.

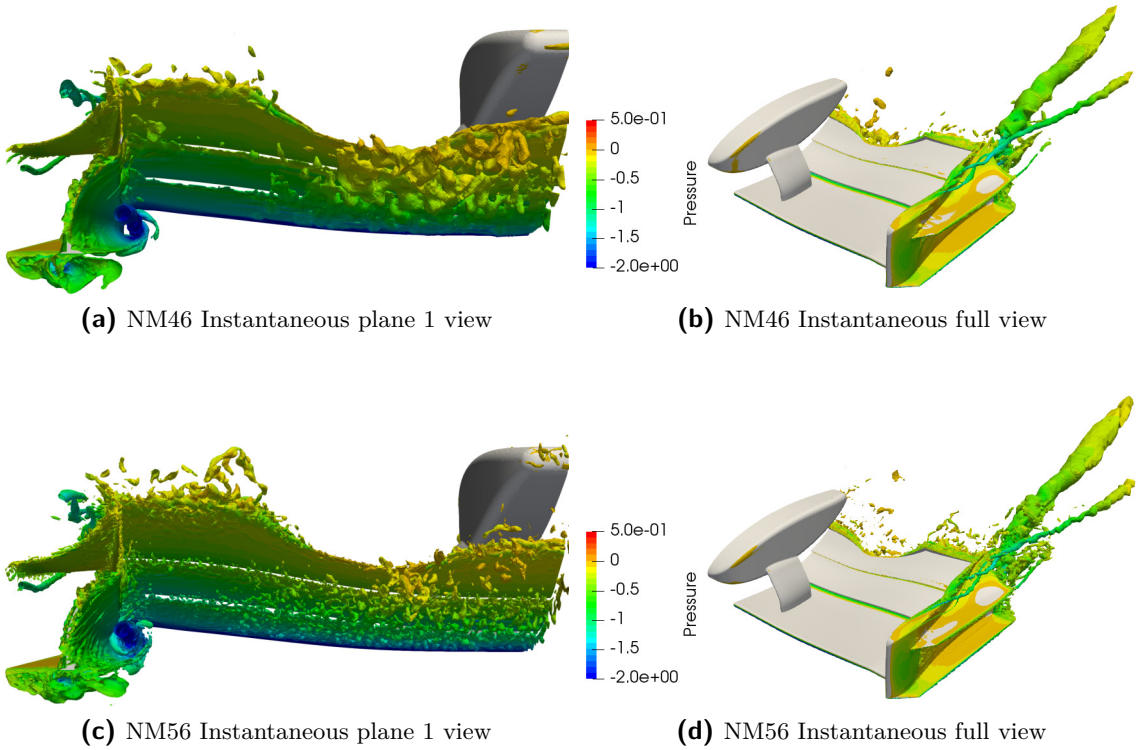
We first define $CP0$, the pressure coefficient, as: $CP0 = (p - p_\infty)/0.5\rho_\infty U_\infty^2$, where p_∞ is the free stream static pressure. Time-averaged iso-contour plots of $CP0 = 0$ over the IFW are presented in Figure 9-38. A close inspection of the effect of the increment of resolution highlights that there is some change in the strength of the smallest vortices, such as the canard vortex and the initial formation of the endplate vortex, when comparing NM46 to NM56. Once again this was evidenced by the downforce increment, which was observed when enhancing the resolution from 4^{th} to 5^{th} order.

Figure 9-39 presents instantaneous iso-contour plots of $CP0 = 0$ comparing NM46 at 10 CTU and NM56 at 11.75 CTU in two scenarios: an upstream view from plane 1 location and a top-side view of the flow and scales over the wing. Comparing flow structures results presented in Figure 9-39a with those in Figure 9-39c, we observe that NM56 does indeed capture smaller scales when compared NM46. It can also be seen that the partial flow separation visible close to the symmetry is significantly reduced when increasing the polynomial order, as was also demonstrated by the wall shear stress plots in Section 9-4-2.



(a) NM46 Averaged **(b)** NM56 Averaged

Figure 9-38: Comparison of time averaged iso-contours of $CP0 = 0$ coloured by pressure.



(a) NM46 Instantaneous plane 1 view

(b) NM46 Instantaneous full view

(c) NM56 Instantaneous plane 1 view

(d) NM56 Instantaneous full view

Figure 9-39: Comparison of instantaneous iso-contours of $CP0 = 0$ coloured by pressure.

9-5 Conclusions

This part of the study presents a new test case for the automotive fluid dynamics community supported by experimental data, the Imperial Front Wing (IFW). The IFW geometry includes multiple wing elements under ground-effect as well as other aerodynamic features such as gurney flaps, canard and foot plates, all of which are commonly used in present-day front wing designs.

In terms of the locations of the vortex cores for the main, endplate and canard vortices, induced movements in both the spanwise and vertical directions were observed, as the vortices travel downstream and interact with each other. This type of complex geometry therefore leads to relatively intricate flow features that can be challenging to simulate and therefore obtain accurate prediction of the aerodynamic loads, transition lines locations and vortex intensities. We believe that the proposed geometry is therefore an interesting, aerodynamically challenging test case for CFD validation, especially for high-fidelity methods.

In this study we have compared the results of an uDNS/iLES simulation using third (NM36), fourth (NM46) and fifth (NM56) order spectral/hp element discretisation against experimental data. High-fidelity simulations were started from the NM36 resolution, and we first presented a comparison between results on the lift coefficient for NM36 and NM46, where results indicated discrepancy since at NM46 the downforce increased with time and NM36 followed the opposite trend (decreasing downforce). Lift coefficient results for the NM46 have

converged around 8.4 CTU, whereas for NM56 it was still evolving, obtaining a stable region between the 11.5 and 11.75 CTU and downforce increased by 4.5% compared to NM46 results.

When complementing previous analysis with wall shear stress results, NM56 is the case that most closely correlates with the experimental results, capturing the re-attachment and flow features in all wing components. Results for NM46 indicate correct prediction of most of the features, except for the last wing component. The downforce increments on NM56 compared to NM46 is explained by the correct re-attachment of the flow on the wing elements, generating more downforce. For the NM36 case, flow features were marginally captured at the main wing element and the footplate and failed on capturing re-attachment on the other components, leading to the smallest downforce value and concluding that NM36 is an insufficient resolution for the proposed mesh.

The time-averaged results of NM46 and NM56 simulations are in relatively good agreement with the experimental PIV data. Consideration of the instantaneous solutions highlights that smaller scales are being captured in the higher resolution simulation, although these smaller scales are not having a significant effect on the time averaged evolution of the downstream vortices.

We conclude that the minimum resolution for this mesh to correct capture the flow characteristics of vortical structures propagating downstream of the wing is NM46. The higher resolution does however help in capturing the less energetic vortices, improving the wall-bounded streaklines resolution and has therefore played a role in capturing a better downforce prediction.

9-6 List of publications

9-6-1 Paper contributions

Buscariolo, F.F., Hoessler, J.F.A., Moxey, D., Jassim, A., Gouder, K., Basley, J., Murai, J., Assi, G.R.S., Sherwin, S.J., Spectral/hp element simulation of flow past a Formula One front wing: validation against experiments, Computer and Fluids, submitted.

Part V

Conclusions and recommendations

Chapter 10

Conclusions and recommendations for future work

This research evaluates the reliability and readiness of the academic CFD code Nektar++ to handle complex industrial cases with simulations of fully 3D complex geometries. A novel numerical stabilization technique using discontinuous Galerkin (DG) mimicking kernel-based CG-SVV (continuous Galerkin spectral-vanishing viscosity) was used to improve the stability and convergence of spectral/hp element method solution under high Reynolds numbers and complex geometries. As the result, a good correlation for automotive flows was observed when the Ahmed body comparative study results were presented, when comparing with existing experimental results. Extension to the application of a diffuser on the same Ahmed body further demonstrated the potential for the proposed methods and workflows to be used in independent analysis of industrial test cases. This capability is further verified in the development and evaluation of the Imperial front wing as a standard test case, with results of high accuracy obtained from the spectral/hp element method simulation without prior knowledge of the experimental results.

The spectral/hp element method proved to be flexible enough to build relatively coarse meshes, with high-order polynomials able to capture geometry curvatures with minimum loss of accuracy. However, we have also noticed that, for improving solution quality, traditional mesh refinement regions and size transition zone can still be beneficial. With the three test cases, we have demonstrated that the proposed new strategy for mesh generation is capable of incorporating various design considerations available for spectral/hp element method, allowing efficient and accurate simulations of complex cases using only relatively coarse grids.

In the following sections, detailed concluding remarks will be given for the application of spectral/hp element method in 3 different implementation cases: the Ahmed body, the Ahmed body with diffuser and the Imperial front wing. This is followed by recommendations and suggestions for future work.

10-1 Application of spectral/hp element method in 3D cases

Although the spectral/hp element method has been successfully implemented for canonical and some industrial simulations, significant amount of care and work were need for 3D geometries, where quasi-3D (2.5D) simulations were often employed. In addition, limitations in the method have led to restrictions on the allowable Reynolds number and the polynomial order.

One of the main contributions of this research is the development of a framework for fully 3D complex geometries simulations at high Reynolds numbers with higher order polynomials, result in textbook-like procedures that one can simply follow to obtain the desired solution. Direct use of this guideline has led to successful simulation of all 3 test cases, with the key findings and conclusions highlighted below:

- **Application of novel CG-SVV with DG mimicking kernel allows stable uDNS/iLES simulations in 3D geometries at elevated Reynolds numbers**

  Based on the outcome of all three test cases, it can be concluded that the proposed stabilization technique with DG mimicking kernel-based CG-SVV and dealiasing is successful in making the solution process for spectral/hp element method sufficiently stable. As the result, the algorithm can consistently produce results of high accuracy, with similar good convergence behaviour seen in all test cases. To our knowledge, this is the first time such fully 3D complex industrial geometries result for high Reynolds numbers has been reported for higher order simulations (up to 6) of spectral methods.

- **Use of high-order polynomials with spectral/hp element method allows accurate simulation with a coarser mesh**

  The advantages of using a higher order mesh, as well as the benefits of taking appropriate meshing strategies, are evident from the results. In all three cases, solutions of much higher accuracy were obtained using relatively coarse meshes. Although the best practices to take full advantage of the extra flexibility available in spectral/hp element method still require further investigations, the guidelines proposed in this research can be considered as a good initial estimate.

- **Efficient *LES* simulation with half models is possible for automotive flows**

  We have successfully extended the common practice in automotive industry of using half models with symmetry boundary condition in steady-state simulations (*RANS*), to scale-resolving simulations of *LES*. The method is valid when only the time-averaged flow properties are of interest, and the flow features evaluated are close to the body. Using the Ahmed body simulations, we have demonstrated more than 50% saving of computation time using half models, with only minor differences seen in the solution.

- **Computational time feasibility for high order simulations can be achieved with a combination of measures**

  With the help of only using the half model, as well as various implementations such as warm starting and solution mapping, the required computational time for all test cases have been successfully reduced to fit in the limitations of the computing infrastructure

currently available. The practice of warm staring higher order simulations with available (lower order or *RANS*) solutions provides a unique way to quickly obtain stable high order spectral/hp element solutions which otherwise would not be obtainable due computational constraints of wall time.

10-1-1 Ahmed body validation

Specifically, for the simulation of the original Ahmed body, this is the first validation of fully 3D geometries using the spectral/hp element method at high Reynolds number. The focus of the study has been in the examination of various meshing options in the proposed strategy to yield solutions with high accuracy and sufficient resolution, using the available knowledge of the flow physics from the literature. The main findings of this validation study are summarised into the following points:

- **Although lower order simulations can match the values of aerodynamic quantities, only higher order solutions correctly capture the flow physics**

  In this comparative study, when the polynomial orders are increase, the number of mesh elements remain unchanged. Based on the obtained solution, we can conclude that the number of mesh element is insufficient to obtain reliable results with the polynomial of 4^{th} order accuracy. Increase the accuracy order to 5 yield matching of aerodynamic quantities of lift and drag with experimental data, however upon close inspection of flow physics and consistency, it was found that not all flow features were correctly captured. Correlation of flow structures was only obtained with the polynomial order accuracy further increased to 6.

- **In current status of Nektar++, increase polynomial order accuracy is more efficient and effective than increasing the number of mesh elements**

  Consider the required solution resolution is equivalent to the outcome of the simulation using refined mesh and polynomials of 6^{th} order accuracy, based on the proposed relationship in section 6-2-1. It would require the number of elements to almost triple if a polynomial of 4^{th} order accuracy is to be used. However, such configuration is shown to lead to inefficient and time-consuming operations in the current framework of Nektar++. As the result, for obtaining highly accurate solution efficiently, it is recommended to use the highest polynomial order realistically possible as the starting point.

- **Even for higher order mesh, h-type mesh refinement can still be beneficial for improving solution resolution locally**

  Although increasing the polynomial orders can result in substantial improvements in solution accuracy, if is often the case that using the highest polynomial order realistically possible will still not yield the required resolution at certain regions locally. For 3D simulations using the current version of Nektar++, which requires all elements to have the same polynomial order, further increment of polynomial order is now prohibitive as the associated computational cost (due to both increase in problem dimension and reduction in allowable step sizes) now will result in sharp increases.

- **Higher order spectral/hp method with *LES* is able to capture complex flow features, assisting experimental studies**

  Flow features in unsteady regions of the domain, such as the intensity of the slant vortex for Ahmed body with slant angle of 25°, is significantly under-predicted by traditional *RANS* simulation in the literature, regardless the mesh resolution. By taking the time-averaged solution of scale-resolved simulations like the *LES*, these complex flow structures can be better preserved in comparison to method that models the process. This is also reflected in the structures seen downstream, where solutions from steady-state methods have been affected by a much stronger numerical dissipation. In addition, unlike methods in which turbulence is modelled reliably depending on the choice of many parameters, we are able to consistently obtain results of high resolution using *iLES* in the same setting. As the result, the numerical simulation with the proposed method can offer further insights into flow physics to assist design iterations, potentially reducing the workload and overheads needed for experimental studies.

10-1-2 Ahmed body with diffuser

Based on the guidelines obtained in the Ahmed body validation study, the study of the Ahmed body with diffuser aims at implementing the same simulation technique with a derived geometry that contains similar flow features. In this way, we can isolate the effects of corresponding geometry changes, and at the same time, examine whether the proposed method is sufficiently reliable to be used as a single source of information for aerodynamic design. With regards to this part of the study, we conclude the following:

- **The effects of underbody diffuser can be better evaluated using classical automotive bluff body geometries**

  In current literature, studies of diffusers are often made using non-standard bluff bodies, which often does not have well established solution for the base geometry. The effect of diffusers on the obtained flow solutions are often difficult to isolate from other influencing factors related to experimental setup and simulation quality. On the other hand, after decades of research, the aerodynamic quantities and flow features of classical automotive bluff bodies are well known and agreed by researchers across the field. By taking our validated numerical method for Ahmed bodies, and apply to the simulation of Ahmed bodies with diffusers, we are able provide a comprehensive set of results regarding the effectiveness and flow features of the diffuser.

- **The performance of diffuser can be influenced by the geometry of the reference body**

  Distinctive differences have been identified from the study with the two Ahmed bodies. Changing from a squared back to the one with slant angle of 25°, the effect of the diffuser on the vehicle during downforce production has changed from drag penalty to drag reduction. However, the downforce generation performance breaking point is shown to happen at a smaller diffuser angle of 20 degrees, whereas for the squared back, downforce can be sustained up to a diffuser angle of 30 degrees which has a lower base pressure. From the results, we conclude that the exterior geometry of the vehicle will

greatly influence the diffuser performance in terms of downforce and drag. Therefore, one should not expect to obtain an optimal diffuser angle for all design cases, and an integrated approach for vehicle aerodynamics should be taken.

- **Flow structures obtained are in agreement with literature**

  Although there is no direct reliable reference on the flow structures of Ahmed bodies with diffusers, our simulation outcome showed similar flow features in agreement with experimental and numerical studies on generic bluff bodies with diffusers. When downforce increment is predicted, the flow on the diffuser region is characterized by a vortical structure combined with either attached or partially separated flow on the surface. As the diffuser angle gets steeper, the vortex increases its intensity up to a critical breakdown angle.

- **Pumping effect is observed when diffuser provides downforce increase**

  Existing studies on diffusers have all demonstrated a so-called 'pumping' effect, a low-pressure region caused by the flow acceleration with the change in geometry curvature. For our simplified diffuser, this suction zone is concentrated near the sharp corner of the diffuser inlet, contributing to the increase in downforce.

- **Strong interactions between the lower side vortex trajectory and the diffuser flow behavior**

  For Ahmed bodies without diffuser, there has been a pair of lower side vortices developed from the lower stagnation point. With the inclusion of the simplified diffuser, we have observed the strengthening of this lower vortex when travelling downstream, as long as the diffuser is producing downforce. After the breaking angle, flow becomes fully separated on the diffuser, and the lower side vortex is observed to quickly dissipate.

10-1-3 Imperial front wing

Unlike the Ahmed body validation study where a simplified bluff body was simulated with priory knowledge regarding flow features and behaviour, the experimental study and the uDNS/iLES-SVV simulation for the Imperial front wing were conducted in parallel. This simulation case can therefore be considered as an ultimate test for the proposed methodology and process pipeline in offering reliable high accuracy result for complex geometries of industrial level. Based on the results of this case study, we are able to conclude that

- **High-fidelity uDNS/iLES-SVV simulation using spectral/hp element method is obtainable with the proposed approach for complex industrial geometries**

  Subsequent analysis comparing the simulation and experimental results showed good agreement between both independent studies regarding the flow structures at various planes near the body and downstream. We have determined that the minimum required polynomial accuracy order to be 4^{th} for correlating the flow velocity fields at various planes, and additional resolution is required by increase the polynomial accuracy order to 5^{th} to match the details in flow visualization.

- **Based on a real race car, IFW is a potential standard test case for automotive and motorsport CFD validation**

  With geometry consisting of a multi-element wing in ground effect, leading to the generation of a series of interacting vortical structures, the IFW captures the essential aerodynamic features of a front wing configuration. This poses significant aerodynamics challenges in accurately estimating the aerodynamic loads, the locations of transition lines, the generation and shedding pattern of multiple vortices and their respective strengths. To our knowledge, there current exist no such test cases supported by open CAD geometry and the availability of experimental data publicly.

An important remark is the possibility to use relatively coarse meshes, considering number of elements similar to a RANS case to perform iLES simulations. Whenever a steady-state solution is not enough to have the correct physics, similar mesh can be used to increase the complexity of the simulation, leading to more refined solutions. The solution polynomial order increment to increase simulation resolution doesn't require additional mesh generation or re-work, which is also very desirable on industrial applications.

10-2 Recommendations and further work

As a future work for the study of Ahmed body and the Imperial front wing, we would suggest to increase the polynomial order of the solution to evaluate the influence of the extra resolution. The main goal is to obtain the limiting situation where meaningful improvements can no longer be observed with both increase in polynomial order and further refinement of the mesh. Such comprehensive study will also help to establish the Pareto front for 3D simulations with the proposed method, providing guideline for best practices in trading-off solution accuracy with computational complexity. Another point of interest for this test is to examine the current stabilization technique when polynomial orders becomes even higher, as the use of higher order polynomials often lead to larger numerical challenges, e.g. the controlling of errors due to limited machine precision.

The work on Ahmed body with the diffuser would be complemented with some additional studies. The first suggestion is to perform a similar study on the diffuser angles considering the diffuser endplates. The use of end plates constrains the flow on the diffuser and this study would be interesting in order to compare the changes in aerodynamic quantities as well as how the flow structures. Another suggestion is the experimental validation of the proposed models, specially the Ahmed body squared-back with diffuser, aiming to verify the findings of this study. As for the IFW study, we are still carrying on with experiments to obtain the aerodynamic quantities measurements and stereo-PIV measurements for the proposed planes. The additional data will provide extra validation features. Another project contemplates a future application of the proposed methodology to simulate flow around a Formula One car.

Suggestions for additional applications of Nektar++ and the spectral/hp element method on 3D geometries can be categorized into two areas. Firstly, we believe that it is still valuable to study existing benchmark cases, for example other automotive bluff bodies like the Windsor body, to provide a more robust verification of the method under various conditions.

At the same time, trial implementation of the toolchain and design flow in actual industrial design activities will generate valuable experiences for continued development of Nektar++ into an industry-ready software.

Bibliography

Adams, N. and Hickel, S. [2009], Implicit large-eddy simulation: Theory and application, *in* 'Advances in turbulence XII', Springer, pp. 743–750.

Adams, N., Hickel, S. and Franz, S. [2004], 'Implicit subgrid-scale modeling by adaptive deconvolution', *Journal of Computational Physics* **200**(2), 412–431.

Ahmed, M., Takasaki, T. and Kohama, Y. [2007], 'Aerodynamics of a naca4412 airfoil in ground effect', *AIAA journal* **45**(1), 37–47.

Ahmed, S., Ramm, G. and Faltin, G. [1984], Some salient features of the time-averaged ground vehicle wake, Technical report, SAE Technical Paper.

Aulakh, D. [2016], 'Effect of underbody diffuser on the aerodynamic drag of vehicles in convoy', *Cogent Engineering* **3**(1), 1230310.

Baldwin, B. and Lomax, H. [1978], Thin-layer approximation and algebraic model for separated turbulentflows, *in* '16th aerospace sciences meeting', p. 257.

Barnard, R. [2001], *Road vehicle aerodynamic design-an introduction*.

Bearman, P. [1993], Challenging problems in bluff body wakes, *in* 'Bluff-Body Wakes, Dynamics and Instabilities', Springer, pp. 1–10.

Boussinesq, J. [1877], *Essai sur la théorie des eaux courantes*, Impr. nationale.

Buscariolo, F. [2009], Estudo de diferentes tipos de solo em túnel de vento através de simulação numérica., Master's thesis, Universidade de São Paulo.

Buscariolo, F., Assi, G., Meneghini, J. and Sherwin, S. [2020], Spectral/hp methodology study for iles-svv on an ahmed body, *in* 'Spectral and High Order Methods for Partial Differential Equations ICOSAHOM 2018', Springer, p. to be released.

Buscariolo, F., Magazoni, F., Maruyama, F., Alves, J. and Volpe, L. [2015], Windows opening influence on the drag coefficient of a hatchback vehicle, Technical report, SAE Technical Paper.

Buscariolo, F., Magazoni, F., Wolf, M., Maruyama, F., Alves, J. and Della Volpe, L. [2016], Analysis of turbulence models applied to CFD drag simulations of a small hatchback vehicle, Technical report, No. 2016-36-0201, SAE Technical Paper.

Buscariolo, F. and Mariani, A. [2010], Analysis of different types of wind tunnel's ground configuration using numerical simulation, sae paper, Technical report, No. 2010-36-0078I, Society of Automotive Engineers.

Cantwell, C., Moxey, D., Comerford, A., Bolis, A., Rocco, G., Mengaldo, G., De Grazia, D., Yakovlev, S., Lombard, J.-E., Ekelschot, D. et al. [2015], 'Nektar++: An open-source spectral/hp element framework', *Computer Physics Communications* **192**, 205–219.

Cooper, K., Bertenyi, T., Dutil, G., Syms, J. and Sovran, G. [1998], The aerodynamic performance of automotive underbody diffusers, Technical report, SAE Technical Paper.

Dalla Longa, L., Evstafyeva, O. and Morgans, A. [2019], 'Simulations of the bi-modal wake past three-dimensional blunt bluff bodies', *Journal of Fluid Mechanics* **866**, 791–809.

Department of Aeronautics, I. C. L. [2019], '10x5 wind tunnel'.
URL: *www.imperial.ac.uk/aeronautics/facilities/10x5-wind-tunnel*

Diasinos, S. and Gatto, A. [2008], 'Experimental investigation into wing span and angle-of-attack effects on sub-scale race car wing/wheel interaction aerodynamics', *Experiments in Fluids* **45**(3), 537.
URL: *https://doi.org/10.1007/s00348-008-0499-z*

Dong, S., Karniadakis, G. E. and Chryssostomidis, C. [2014], 'A robust and accurate outflow boundary condition for incompressible flow simulations on severely-truncated unbounded domains', *Journal of Computational Physics* **261**, 83–105.

Ehirim, O. [2018], Aerodynamics and performance enhancement of a ground-effect diffuser, PhD thesis, Cranfield.

Fu, C., Uddin, M. and Robinson, A. [2018], 'Turbulence modeling effects on the CFD predictions of flow over a nascar gen 6 racecar', *Journal of Wind Engineering and Industrial Aerodynamics* **176**, 98–111.

Garnier, E., Mossi, M., Sagaut, P., Comte, P. and Deville, M. [1999], 'On the use of shock-capturing schemes for large-eddy simulation', *Journal of computational Physics* **153**(2), 273–311.

Gordon, W. and Hall, C. [1973], 'Transfinite element methods: blending-function interpolation over arbitrary curved element domains', *Numerische Mathematik* **21**(2), 109–129.

Grandemange, M., Cadot, O. and Gohlke, M. [2012], 'Reflectional symmetry breaking of the separated flow over three-dimensional bluff bodies', *Physical review E* **86**(3), 035302.

Grandemange, M., Gohlke, M. and Cadot, O. [2013], 'Bi-stability in the turbulent wake past parallelepiped bodies with various aspect ratios and wall effects', *Physics of Fluids* **25**(9), 095103.

Graysmith, J., Baxendale, A., Howell, J. and Haynes, T. [1994], Comparisons between CFD and experimental results for the ahmed reference model, *in* 'RAeS conference on vehicle aerodynamics, Loughborough', pp. 30–1.

Grinstein, F. and Fureby, C. [2004], 'From canonical to complex flows: Recent progress on monotonically integrated les', *Computing in Science & Engineering* **6**(2), 36.

Guermond, J.-L. and Shen, J. [2003], 'Velocity-correction projection methods for incompressible flows', *SIAM Journal on Numerical Analysis* **41**(1), 112–134.

Guilmineau, E. [2008], 'Computational study of flow around a simplified car body', *Journal of wind engineering and industrial aerodynamics* **96**(6), 1207–1217.

Guilmineau, E., Deng, G., Leroyer, A., Queutey, P., Visonneau, M. and Wackers, J. [2017], 'Assessment of hybrid rans-les formulations for flow simulation around the ahmed body', *Computers & Fluids* .

Guilmineau, E., Deng, G. and Wackers, J. [2011], 'Numerical simulation with a des approach for automotive flows', *Journal of Fluids and Structures* **27**(5), 807–816.

Gupta, K., Lung, S. and Ibrahim, A. [2015], Numerical CFD simulation and test correlation in a flight project environment, *in* 'ASME 2015 International Mechanical Engineering Congress and Exposition', American Society of Mechanical Engineers, pp. V001T01A008–V001T01A008.

Hoessler, J. [2011], Direct numerical simulations and stability analysis of vortex-dominated flows around complex geometries, PhD thesis, Imperial College London.

Howell, J. and Le Good, G. [2005], Vortex drag for a simple bluff body at incidence in ground proximity, Technical report, SAE Technical Paper.

Howell, J. and Le Good, G. [2008], The effect of backlight aspect ratio on vortex and base drag for a simple car-like shape, Technical report, SAE Technical Paper.

Howell, J., Sheppard, A. and Blakemore, A. [2003], Aerodynamic drag reduction for a simple bluff body using base bleed, Technical report, SAE Technical Paper.

Hucho, W. and Sovran, G. [1993], 'Aerodynamics of road vehicles', *Annual review of fluid mechanics* **25**(1), 485–537.

Huminic, A. and Huminic, G. [2010], Computational study of flow in the underbody diffuser for a simplified car model, Technical report, No. 2010-01-0119, SAE Technical Paper.

Huminic, A. and Huminic, G. [2012], Numerical flow simulation for a generic vehicle body on wheels with variable underbody diffuser, Technical report, No. 2012-01-0172, SAE Technical Paper.

Jones, W. and Launder, B. [1972], 'The prediction of laminarization with a two-equation model of turbulence', *International journal of heat and mass transfer* **15**(2), 301–314.

Jowsey, L. [2013], An experimental study of automotive underbody diffusers, PhD thesis, © Lydia Jowsey.

Jowsey, L. and Passmore, M. [2010], 'Experimental study of multiple-channel automotive underbody diffusers', *Proceedings of the Institution of Mechanical Engineers, Part D: Journal of Automobile Engineering* **224**(7), 865–879.

Kapadia, S., Roy, S., Vallero, M., Wurtzler, K. and Forsythe, J. [2004], Detached-eddy simulation over a reference ahmed car model, *in* 'Direct and large-eddy simulation V', Springer, pp. 481–488.

Karamanos, G. and Karniadakis, G. [2000], 'A spectral vanishing viscosity method for large-eddy simulations', *Journal of Computational Physics* **163**(1), 22–50.

Karniadakis, G. E., Israeli, M. and Orszag, S. [1991], 'High-order splitting methods for the incompressible navier-stokes equations', *Journal of computational physics* **97**(2), 414–443.

Karniadakis, G. and Sherwin, S. [2013], *Spectral/hp element methods for computational fluid dynamics*, Oxford University Press.

Katz, J. [1995], *New directions in race car aerodynamics: designing for speed*, Bentley Publishers.

Katz, J. [2006], 'Aerodynamics of race cars', *Annu. Rev. Fluid Mech.* **38**, 27–63.

Katz, J. and Garcia, D. [2002], 'Aerodynamic effects of indy car components', *SAE Transactions* pp. 2322–2330.

Kelly, K., Provencher, L. and Schenkel, F. [1982], The general motors engineering staff aerodynamics laboratory-a full-scale automotive wind tunnel, Technical report, SAE Technical Paper.

Kirby, R. and Karniadakis, G. [2003], 'De-aliasing on non-uniform grids: algorithms and applications', *Journal of Computational Physics* **191**(1), 249–264.

Kirby, R. and Sherwin, S. [2006], 'Stabilisation of spectral/hp element methods through spectral vanishing viscosity: Application to fluid mechanics modelling', *Computer methods in applied mechanics and engineering* **195**(23-24), 3128–3144.

Kolmogorov, A. [1941], 'The local structure of turbulence in incompressible viscous fluid for very large reynolds numbers', *Cr Acad. Sci. URSS* **30**, 301–305.

Krajnović, S. and Davidson, L. [2004], Large-eddy simulation of the flow around simplified car model, Technical report, SAE Technical Paper.

Lai, C., Kohama, Y., Obayashi, S. and Jeong, S. [2011], 'Experimental and numerical investigations on the influence of vehicle rear diffuser angle on aerodynamic drag and wake structure', *International Journal of Automotive Engineering* **2**(2), 47–53.

Lienhart, H., Stoots, C. and Becker, S. [2002], Flow and turbulence structures in the wake of a simplified car model (ahmed model), *in* 'New Results in Numerical and Experimental Fluid Mechanics III', Springer, pp. 323–330.

Littlewood, R. and Passmore, M. [2010], The optimization of roof trailing edge geometry of a simple square-back., Technical report, SAE Technical Paper.

Littlewood, R. and Passmore, M. [2012], 'Aerodynamic drag reduction of a simplified square-back vehicle using steady blowing', *Experiments in fluids* **53**(2), 519–529.

Littlewood, R., Passmore, M. and Wood, D. [2011], 'An investigation into the wake structure of square back vehicles and the effect of structure modification on resultant vehicle forces', *SAE International Journal of Engines* **4**(2), 2629–2637.

Lombard, J.-E. [2017], A high-fidelity spectral/hp element LES study of Formula 1 front-wing and exposed wheel aerodynamics, PhD thesis, Imperial College London.

Lombard, J.-E., Moxey, D., Sherwin, S., Hoessler, J., Dhandapani, S. and Taylor, M. [2015], 'Implicit large-eddy simulation of a wingtip vortex', *AIAA Journal* **54**(2), 506–518.

Magazoni, F., Buscariolo, F., Maruyama, F., Alves, J. and Volpe, L. [2015], Aerodynamic shape improvement for driver side view mirror of hatchback vehicle using adjoint optimization method, Technical report, No. 2015-36-0156, SAE Technical Paper.

Makowski, F. and Kim, S.-E. [2000], Advances in external-aero simulation of ground vehicles using the steady rans equations, Technical report, SAE Technical Paper.

Mengaldo, G., De Grazia, D., Moxey, D., Vincent, P. and Sherwin, S. [2015], 'Dealiasing techniques for high-order spectral element methods on regular and irregular grids', *Journal of Computational Physics* **299**, 56–81.

Menter, F. [1994], 'Two-equation eddy-viscosity turbulence models for engineering applications', *AIAA journal* **32**(8), 1598–1605.

Minguez, M., Pasquetti, R. and Serre, E. [2008], 'High-order large-eddy simulation of flow over the "ahmed body" car model', *Physics of fluids* **20**(9), 095101.

Moghimi, P. and Rafee, R. [2018], 'Numerical and experimental investigations on aerodynamic behavior of the ahmed body model with different diffuser angles.', *Journal of Applied Fluid Mechanics* **11**(4).

Morel, T. [1978], Aerodynamic drag of bluff body shapes characteristic of hatch-back cars, Technical report, SAE Technical Paper.

Moura, R. [2017], On the use of spectral element methods for under-resolved simulations of transitional and turbulent flows, PhD thesis, Imperial College London.

Moura, R., Mengaldo, G., Peiró, J. and Sherwin, S. [2017], 'On the eddy-resolving capability of high-order discontinuous galerkin approaches to implicit les/under-resolved dns of euler turbulence', *Journal of Computational Physics* **330**, 615–623.

Moura, R., Sherwin, S. and Peiró, J. [2016], 'Eigensolution analysis of spectral/hp continuous galerkin approximations to advection–diffusion problems: Insights into spectral vanishing viscosity', *Journal of Computational Physics* **307**, 401–422.

Moxey, D., Green, M., Sherwin, S. and Peiró, J. [2015], 'An isoparametric approach to high-order curvilinear boundary-layer meshing', *Computer Methods in Applied Mechanics and Engineering* **283**, 636–650.

Orszag, S. [1970], 'Analytical theories of turbulence', *Journal of Fluid Mechanics* **41**(2), 363–386.

Pagliarella, R. [2009], 'On the aerodynamic performance of automotive vehicle platoons featuring pre and post-critical leading forms'.

Pasquetti, R., Bwemba, R. and Cousin, L. [2008], 'A pseudo-penalization method for high reynolds number unsteady flows', *Applied Numerical Mathematics* **58**(7), 946–954.

Pegrum, J. [2007], Experimental study of the vortex system generated by a Formula 1 front wing, PhD thesis, Imperial College London.

Perry, A., Almond, M., Passmore, M. and Littlewood, R. [2016], 'The study of a bi-stable wake region of a generic squareback vehicle using tomographic piv'.

Pope, S. [2001], *Turbulent flows*, Cambridge University Press.

Ruhrmann, A. and Zhang, X. [2003], 'Influence of diffuser angle on a bluff body in ground effect', *Transactions-American Society of Mechanical Engineers Journal of Fluids Engineering* **125**(2), 332–338.

Schlüter, J. [2004], 'Influence of axisymmetric assumptions on large eddy simulations of a confined jet and a swirl flow', *International Journal of Computational Fluid Dynamics* **18**(3), 235–245.

Senior, A. and Zhang, X. [2001], 'The force and pressure of a diffuser-equipped bluff body in ground effect', *Transactions-American Society of Mechanical Engineers Journal of Fluids Engineering* **123**(1), 105–111.

Serre, E., Minguez, M., Pasquetti, R., Guilmineau, E., Deng, G., Kornhaas, M., Schäfer, M., Fröhlich, J., Hinterberger, C. and Rodi, W. [2013], 'On simulating the turbulent flow around the ahmed body: A french–german collaborative evaluation of les and des', *Computers & Fluids* **78**, 10–23.

Serson, D. [2017], Numerical study of wings with wavy leading and trailing edges, PhD thesis, Imperial College London / Poli-USP.

Sherwin, S. [2003], A substepping navier-stokes splitting scheme for spectral/hp element discretisations, *in* 'Parallel Computational Fluid Dynamics 2002', Elsevier, pp. 43–52.

Sherwin, S. and Karniadakis, G. E. [1995], 'A triangular spectral element method; applications to the incompressible navier-stokes equations', *Computer methods in applied mechanics and engineering* **123**(1-4), 189–229.

Sherwin, S. and Peiró, J. [2002], 'Mesh generation in curvilinear domains using high-order elements', *International Journal for Numerical Methods in Engineering* **53**(1), 207–223.

Shewchuk, J. [2002], 'Delaunay refinement algorithms for triangular mesh generation', *Computational geometry* **22**(1-3), 21–74.

Si, H. [2015], 'Tetgen, a delaunay-based quality tetrahedral mesh generator', *ACM Transactions on Mathematical Software (TOMS)* **41**(2), 11.

Smagorinsky, J. [1963], 'General circulation experiments with the primitive equations: I. the basic experiment', *Monthly weather review* **91**(3), 99–164.

Smith, A. and Cebeci, T. [1967], Numerical solution of the turbulent-boundary-layer equations, Technical report, DOUGLAS AIRCRAFT CO LONG BEACH CA AIRCRAFT DIV.

Spalart, P. [1997], Comments on the feasibility of les for wings, and on a hybrid rans/les approach, *in* 'Proceedings of first AFOSR international conference on DNS/LES', Greyden Press.

Spalart, P. and Allmaras, S. [1992], A one-equation turbulence model for aerodynamic flows, *in* '30th aerospace sciences meeting and exhibit', p. 439.

Strachan, R., Knowles, K. and Lawson, N. [2007], 'The vortex structure behind an ahmed reference model in the presence of a moving ground plane', *Experiments in fluids* **42**(5), 659–669.

Tadmor, E. [1989], 'Convergence of spectral methods for nonlinear conservation laws', *SIAM Journal on Numerical Analysis* **26**(1), 30–44.

Turner, M. [2017], High-order mesh generation for CFD solvers, PhD thesis, Imperial College London.

Turner, M., Moxey, D., Peiró, J., Gammon, M., Pollard, C. and Bucklow, H. [2017], 'A framework for the generation of high-order curvilinear hybrid meshes for CFD simulations', *Procedia engineering* **203**, 206–218.

Turner, M., Moxey, D., Sherwin, S. and Peiró, J. [2016], Automatic generation of 3d unstructured high-order curvilinear meshes, ECCOMAS proceedings.

Wilcox, D. [1988], 'Reassessment of the scale-determining equation for advanced turbulence models', *AIAA journal* **26**(11), 1299–1310.

Wright, P. [1982], 'The influence of aerodynamics on the design of formula one racing cars', *International Journal of Vehicle Design* **3**(4), 383–397.

Xu, H., Cantwell, C., Monteserin, C., Eskilsson, C., Engsig-Karup, A. and Sherwin, S. [2018], 'Spectral/hp element methods: Recent developments, applications, and perspectives', *Journal of Hydrodynamics* **30**(1), 1–22.

Zerihan, J. and Zhang, X. [2000], 'Aerodynamics of a single element wing in ground effect', *Journal of aircraft* **37**(6), 1058–1064.

Zhang, X. and Zerihan, J. [2003], 'Aerodynamics of a double-element wing in ground effect', *AIAA journal* **41**(6), 1007–1016.